Elastic-Plastic Design Sensitivities based on Variational Analysis and Applications in Optimal Specimen Design

Dissertation

Jan Liedmann

Elastic-Plastic Design Sensitivities based on Variational Analysis and Applications in Optimal Specimen Design

von der Fakultät Architektur und Bauingenieurwesen
der Technischen Universität Dortmund
zur Verleihung des akademischen Grades
Doktor-Ingenieur (Dr.-Ing.)
genehmigte Dissertation

von
Jan Liedmann, M.Sc.

Dortmund, September 2021

Kontakt

M. Sc. Jan Liedmann
Institut für Baumechanik, Statik und Dynamik
Fakultät Architektur und Bauingenieurwesen
Technische Universität Dortmund
August-Schmidt-Str. 8, D-44227 Dortmund
Email: jan.liedmann@tu-dortmund.de
URL: *https://www.bauwesen.tu-dortmund.de/bm*
ORCID: 0000-0001-8759-6940

Prüfungskommission

Erster Referent (first referee):	Prof. Dr.-Ing. Franz-Joseph Barthold
Zweiter Referent (second referee):	Prof. Dr.-Ing. Michael Brünig
Vorsitz (committee chair):	Prof. Dr.-Ing. Ingo Münch

Tag der Einreichung (thesis submission):	04.06.2021
Tag der mündlichen Prüfung (thesis defense):	16.09.2021

Abstract

Advancing technological progress places high demands on engineering structures and materials. It is important to keep the production costs low and at the same time to ensure the highest level of safety in practical use. Logistical and ecological aspects also play an important role. The right choice and utilization of the potential of the used materials is extremely important in this context. Computer-aided optimization of components and materials is assigned to the field of structural optimization, which enables improvements of mechanical structures with regard to selected properties and at the same time taking important restrictions into account. For this, the design to be changed must be defined and the desired objective values and constraints have to be formulated mathematically. On the one hand, this requires knowledge of the stress and strain intensity occurring in the analyzed component and, on the other hand, the mechanical processes within the used material must be well understood and captured by mathematical models. Especially unfavorable phenomena, such as plastic yielding, damage or fatigue, which can ultimately lead to structural failure, are worth to be analyzed in detail. The development of models to describe mechanical phenomena is a longstanding scientific tradition and is constantly being further developed. The performance of scientific experiments is essential in this context and should be tailored to the mechanical phenomenon to be investigated.
This thesis is about the shape optimization of biaxial test specimen for damage characterization of ductile metallic materials. Ductile damage and the driving micromechanical mechanisms highly depend on the stress state. Therefore, the shape of the biaxial specimen should be changed in such a way that certain and as homogeneous stress states as possible arise during the tests. For this purpose, an efficient computer-aided model is prepared that covers large elastoplastic deformations and, as part of a gradient-based optimization process, provides the necessary sensitivity information with regard to the change in shape of the specimen. The determination of the sensitivity information is carried out using a variational approach and requires deep understanding of the governing equations of the mechanical model. For validation of the resulting optimal geometries, experiments are carried out and monitored using digital image correlation. Furthermore, high-resolution images of the fracture surfaces, which were recorded using a scanning electron microscope, are examined in order to draw conclusions about the state of stress shortly before failure.

Kurzfassung

Voranschreitender technologischer Fortschritt fordert hohe Ansprüche an ingenieurtechnische Strukturen und Materialien. Dabei ist es wichtig, die Produktionskosten gering zu halten und gleichzeitig höchste Sicherheit in der praktischen Anwendung zu gewährleisten. Auch logistische und ökologische Aspekte spielen eine wichtige Rolle. Die richtige Wahl und Ausnutzung des Potentials der verwendeten Materialien ist in diesen Zusammenhängen enorm wichtig. Die computergestützte Optimierung von Bauteilen und Materialien ist dem Gebiet der Strukturoptimierung zuzuordnen, welche es ermöglicht, mechanische Strukturen hinsichtlich gewählter Eigenschaften zu verbessern und gleichzeitig wichtige Einschränkungen zu berücksichtigen. Dafür muss das zu verändernde Design definiert und gewünschte Zielwerte und Nebenbedingungen mathematisch formuliert werden. Dies erfordert zum einen Wissen über den Grad der Beanspruchung des analysierten Bauteils und zum anderen müssen die mechanischen Vorgänge innerhalb des verwendeten Materials gut verstanden und im Rahmen mathematischer Modelle abbildbar sein. Vor allem ungünstige Phänomene, wie z.B. plastisches Fließen, Schädigung oder Ermüdung, die letztendlich zum Strukturversagen führen können, sind es wert detailliert analysiert zu werden. Die Entwicklung von Modellen zur Beschreibung mechanischer Phänomene ist langjährige wissenschaftliche Tradition und wird stets weiterentwickelt. Die Durchführung wissenschaftlicher Experimente ist in diesem Zusammenhang unabdinglich und sollte auf das zu untersuchende mechanische Phänomen zugeschnitten sein.
In dieser Arbeit geht es um die Formoptimierung biaxialer Versuchskörper zur Charakterisierung von Schädigung duktiler metallischer Werkstoffe. Duktile Schädigung und die treibenden mikromechanischen Mechanismen sind abhängig vom Spannungszustand. Daher soll die Form der Biaxialprobe so verändert werden, dass sich während der Versuche bestimmte und möglichst homogene Spannungszustände einstellen. Hierzu wird ein effizientes computergestütztes Modell aufbereitet, das große elastoplastische Deformationen berücksichtigt und im Rahmen eines gradientenbasierten Optimierungsverfahrens die benötigten Sensitivitätsinformationen bezüglich der Formänderung der Probe liefert. Die Bestimmung der Sensitivitätsinformationen erfolgt mittels eines variationellen Ansatzes und erfordert tiefes Verständnis der Grundgleichungen des mechanischen Modells. Zur Validierung der resultierenden optimalen Geometrien werden Experimente durchgeführt und mittels digitaler Bildkorrelation aufgezeichnet. Anschließend werden hochauflösende Bilder der Bruchflächen untersucht, die mittels eines Rasterelektronenmikroskops aufgenommen wurden, um Rückschlüsse auf den Spannungszustand kurz vor dem Versagen zu ziehen.

Vorwort

"Life is and will ever remain an equation incapable of solution, but it contains certain known factors".

– Nikola Tesla

Diese Dissertation entstand während meiner Tätigkeit am Lehrstuhl für Baumechanik der Fakultät für Architektur und Bauingenieruwesen der Technischen Universität Dortmund.

Ich danke meinem sehr geschätzten Betreuer Professor Franz-Joseph Barthold für die Möglichkeit, diese Dissertation schreiben zu können, sowie für seine professionelle Anleitung und wertvollen Ratschläge während der unzähligen Diskussionen.

Weiter danke ich Professor Michael Brünig für das rege Interesse an meiner Dissertation und für die Bereitschaft, als Zweitgutachter tätig zu werden, sowie für die Möglichkeit, die Labore des Lehrstuhls für Baumechanik der Universität der Bundeswehr München zu nutzen.
Aus der kurzen, aber wertvollen Zeit während meines Aufenthalts in München konnte ich viel mitnehmen. Allen voran möchte ich mich bei Steffen Gerke bedanken, für die nahtlose Integration ins Team, die unzähligen Ratschläge und die herzliche Gastfreundschaft. Für ihr Engagement und ihre Hilfsbereitschaft bei der Durchführung der Experimente bedanke ich mich bei Moritz Zistl, Janek Tix und Sanjeev Koirala, sowie bei Wolgang Saur für die Unterstützung bei der Bedienung des Rasterelektronenmikroskops.

Bei allen Mitarbeitern des Instituts Baumechanik, Statik und Dynamik bedanke ich mich für die immer angenehme Arbeitsatmosphäre, alle spannenden Dienstreisen und die gegenseitige Hilfsbereitschaft. Danke an Wojciech Kijanski und Nikolai Gerzen für die ununterbrochene Unterstützung seit Beginn meiner Promotionszeit.

Besonderer Dank gilt meiner Familie für die bedingungslose Unterstützung in allen Lebensphasen. Meiner lieben Caro danke ich speziell für ihre Geduld und besondere Rücksichtnahme in stressigen Phasen.

Dortmund, September 2021 Jan Liedmann

Contents

Chapter 1

Introduction

This introducing chapter gives an overview on the topics tackled in this thesis. The main scope, that is, the optimization of specimen design in the context of plasticity and ductile fracture, is motivated and classified into the scientific context. The arising problems that need to be solved are formulated and the main solution methods are presented. Relevant literature and the state of the art are reviewed in detail.

Contents

1.1 Motivation

Demands on materials and engineering structures are growing in modern times. While high performance is required, lightweight structures and cost efficiency play an important role. In addition, environmental pollution must be limited in production and use. The development of better and better engineering structures requires deep knowledge on the behavior of the deployed materials and the underlying micromechanical mechanisms. Exploiting the full potential of materials as well as specific structures while ensuring these important restrictions always state challenging optimization problems within the designing process. Successfully managing these requirements leads to high performant and efficient constructions in the sense of costs, lightweight, strength or service lifetime of a construction tailored for its specific demands.

In this thesis, focus lies on ductile metals, especially aluminium alloys that are widely used in different engineering disciplines such as civil engineering or the automotive and aerospace industries, cf. e.g. [121, 195], not least because of its excellent strength to weight ratio, which makes it an excellent choice for transportation vehicles such as cars, ships, trains and air- or spacecrafts. In Fig. 1.1 some visual impressions on industrial usage of aluminium alloys are given. In these industries, especially the safety and security of civilians and passengers is the ultimate asset. Thus, fulfilling construction efficiency in terms of the above named aspects is strongly restricted by limitations of critical phenomena like fatigue, wear behavior, irreversible plastic deformations or material damage and failure. In this context computer aided simulations play a key role to be able to predict these phenomena and even more important to avoid or at least limit their occurrence to ensure safe and substantial constructions. This holds true not only for the final use of the construction but also and especially for the manufacturing process.

In the past decades, various research has been investigated into understanding mechanical mechanisms triggering these phenomena and the development of complex models predicting them. This requires systematic analysis of the material behavior by means of reproducible tests and corresponding specimens geared towards this objective for the development and validation of constitutive models. In recent years, various constitutive models incorporating damage and failure mechanisms have been presented, cf. e.g. [25, 36, 105], where the choice of the parameters characterizing damage is of great importance. In addition to isotropic damage models that are based on scalar variables, cf. [99, 146], anisotropic concepts using tensor-valued variables have also been developed e.g. in [41, 184]. In order to be able to cover a wide range of applications, an efficient continuum damage model has been presented in [38]. Here, different damage mechanisms that depend on the stress state, i.e. for instance growth and coalescence of pores or formation of micro-shear cracks as well as their interaction, and their influence on the damage and failure behavior can be taken into account.

In this context, systematic experiments are essential to calibrate and validate the damage model. Here, the geometry of the test specimen plays an important role. Frequently used standard test specimen are usually designed in a way that predefined stress states are generated. For example, tensile specimens with different notches cause increasing stress triaxialities with decreasing notch radius, cf. [9, 38, 58]. Shear stress states can be achieved with one-dimensional specimens with single and double joints, see e.g. [38, 58, 70, 144]. As the leading damage mechanism and therefore the overall damage behavior changes at

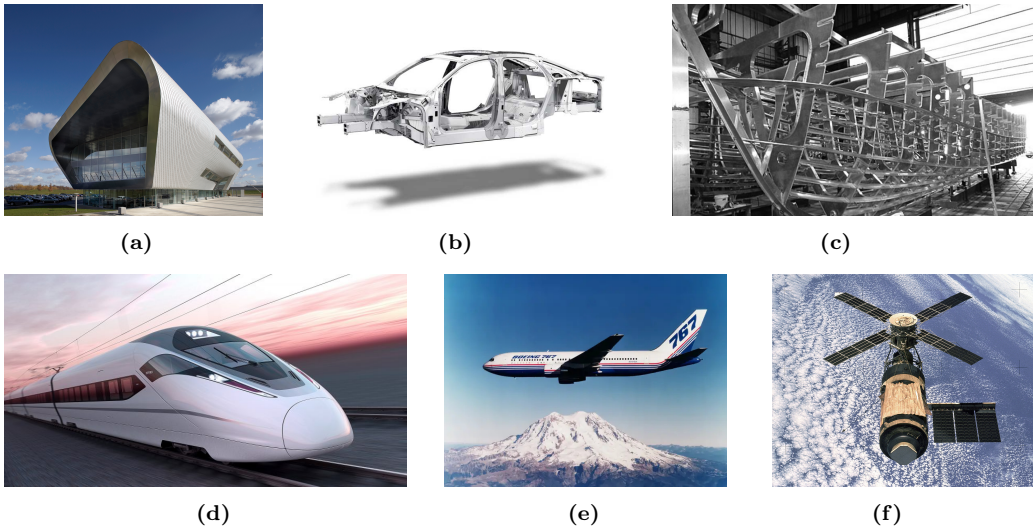

Figure 1.1: Examples of industrial use of aluminium alloys: (a) Farnborough Airport, UK [177] (b) aluminium car body [7] (c) aluminium ship construction [92], (d) highspeed train CRH1A-A [106], (e) Boeing 767 [84], (f) Skylab space station [131].

different stress states, specimen geometries covering a wide range of specifically generated stress states are convenient. First suggestions for this have been made for instance with the butterfly specimen, cf. [128], which shows significant stress gradients in the damage and cracking areas. Cruciform specimens have the advantage that it is possible to generate different stress states with just one geometry. In this context, new biaxial cruciform specimen geometries have been proposed, cf. [37, 40, 59, 60, 61, 62], of which especially the X0-specimen is subject of investigations in this work. In Fig. 1.2 the X0-specimen geometry is illustrated. For the X0-specimen, the localization of deformations and thus also the damage area is predefined by notches in thickness direction and a wide range of stress states can be generated through the variation of the loading conditions. However, for accurate and practicable macroscopic characterization of the damage behavior in terms of experimentally determined parameters, the corresponding stress state dependent micromechanical damage mechanisms have to be separated. Thus, distinct and preferably homogeneous stress states are demanded.

1.2 Goals and scope

This motivates the main objective of this thesis, i.e. the shape optimization of the X0-specimen with the aim of gaining distinct and preferably homogeneous stress states in terms of the stress triaxiality. This on the one hand serves as verification of the theoretical and computational developments founding this work. On the other hand, it emphasizes the added value of investigating into optimal specimen design by constituting a proof of concept in this context. However, the development of an efficient and accurate computa-

tional method required to reach the main goal constitutes the most challenging task and is therefore the main topic within this thesis. The outcome can not only be used within the scope of optimal specimen design but constitutes a general computational package for the structural design optimization considering elastoplastic material beahvior at finite strains. To achieve this, several tasks have to be accomplished.

Firstly, the overall optimization problem and the corresponding solution procedure have to be developed. This includes mathematical formulation of the problem in terms of design controlling quantities and objective quantities as well as potential restrictions. Furthermore, mathematical solution algorithms have to be chosen that provide adequate and computationally efficient solutions, i.e. gradient based solutions are demanded.

Secondly, the computational simulation model has to be implemented that captures large elastoplastic deformations and delivers reliable structural analysis results at reasonably computational cost while avoiding involuntary numerical defects. Thus, an iterative solution method has to be implemented to search for thermomechanical equilibrium described by a geometrically and physically nonlinear equation system.

Thirdly, the gradient information of the solution with respect to the defined design parametrization has to be determined. Because of their computational efficiency, analytical methods are preferable to numerical methods. Therefore, governing equations of the implemented structural analysis problem have to be linearized for consistent determination of design sensitivity information within the iterative solution procedure.

Finally, the developed computational method has to be applied to the X0-specimen shape optimization problem. Therefore, the computational geometry model has to be set up and the mathematical optimization problems have to be defined. The solutions have to be experimentally verified by comparison of the measurements with the initial basis X0-specimen geometry.

The latter of the mentioned tasks of course demands the accomplishment of successfully coupling the three first mentioned computational tasks, of which the determination of the design sensitivity information constitutes the most challenging and most important in view of the scientific novelty.

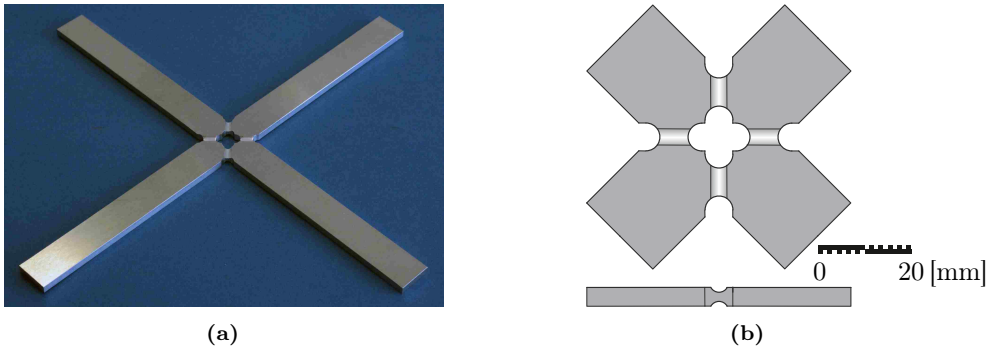

Figure 1.2: X0-specimen: (a) photography, (b) sketch.

1.3 Methodology and state of the art

Reaching the main goals of this thesis requires combinations of different research fields. This combination should expediently result in an efficient computational method that forms the framework of design optimization of general elastoplastic structures. Therefore, the method has to provide information on the elastoplastic structural deformation behavior, as well as its sensitivity regarding geometrical shape and constitutive design. In the following the employed methods from different scientific fields are introduced.

Structural mechanics. Structural mechanics deals with numerical computations of deformations, strains, forces and stresses within structures subjected to given loading scenarios. In this context, from a mathematical point of view, partial differential equations (PDEs) have to be solved subject to certain boundary conditions leading to a so-called boundary value problem (BVP). Here, the finite element method (FEM) has well established in structural solid mechanics as a numerical method for solving PDEs during the past decades. Briefly, the anlayzed structure is spatially divided into a finite number of so-called finite elements within a discretization process. The entirety of all finite elements forms the finite element mesh that constitutes the numerical solution domain. Fundamental details on structural mechanics and the finite element method can e.g. be found in [21, 31, 33, 47, 80, 172, 190, 191, 198, 199, 200]. The constitutive properties of the analyzed material is governed by the chosen constitutive material law that numerically describes the relation between occurring strains and the material's thermomechanical response. Based on the class of the material and the phenomena that are to be analyzed, various different assumptions and approaches exist that capture mulitphysical and multiscale effects. In this thesis, focus lies solely on elastoplastic deformations, see e.g. [42, 110, 118, 126, 127, 133, 159, 160, 172]. However, the shape optimization of the X0-specimen is motivated by the idea of tailoring specimen design to experimental damage characterization. That is, the final results aid the development and calibration of constitutive damage models in which the choice of the damage characterizing parameters are of great importance, as e.g. [25, 36, 105]. Due to the assumption of plastic incompressibility within the chosen elastoplastic model used within this thesis, it is convenient to utilize advanced element formulations to avoid volumetric locking effects, see e.g. [93]. In this work, the so-called $\overline{F}$ method, see e.g. [49, 55, 172] is conducted because of its simplicity and efficiency.

Structural optimization. Methods from *structural optimization* (SO) are often used for assistance in design processes. Utilizing SO, it is possible to computationally identify the best choice of structural design suited to its demands. Here, mathematical optimization algorithms are utilized to optimize selected structural properties depending on the mechanical behavior by changing its design in terms of topology, shape or material design. Thus, it can be seen as a combination of mathematical optimization and structural mechanics. Some fundamental works providing an excellent overview on structural optimization are for instance [10, 23, 29, 45, 76, 151]. As the topology of the X0-specimen is predefined and is not considered to change, topology optimization is not topic of this work. However, the interested reader is referred to e.g. [1, 24, 86, 136, 156, 157, 183], where besides solid mechanical problems also multi-physical effects are considered. In this thesis, focus lies on shape optimization. Here, in contrast to rearrange the material distribution within a fixed

design space as in topology optimization, only the outer contour of the structure's geometry is considered to change. That is, neither additional holes can be created, nor can existing holes be completely closed. Basics on shape optimization can e.g. be found in [13, 18, 28, 29, 171, 201]. Structural optimization in the context of specimen optimization has been topic of investigations in several works. For instance in [90] the stress concentration in the transition zone of a uniaxial tensile test specimen is conducted. The relationship between the geometric shape and the identification of material parameters has been discussed in [22, 144]. Optimizing the shape of biaxial specimens is, however, much more complex and demanding, cf. e.g. [56, 112], since large, inelastic deformations occur in biaxial tests of ductile metal sheets, which must be taken into account in the constitutive model and the numerical calculations. Specimen shape optimization considering elastic material behavior has been e.g. tackled in [51], where Powell's method [139] is used to search for the optimum solution, or in [11], in which the direct multi-search method (DMS) has been used. In [130] a multi-attribute decision making (MADM) method has been conducted to find an optimum specimen design out of a limited number of alternatives. Some other contributions connected with optimal cruciform specimen design are for instance [2, 44, 79, 82, 96, 107, 111, 193, 194, 196, 197]. All of the deployed methods have in common that they are derivative-free. Within the scope of this work a gradient based optimization strategy considering finite elastoplastic deformations is followed, see e.g. [103, 104, 185, 186, 187]. This ensures efficiency and accuracy of the results. However, additionally to the elastoplastic structural response, sensitivity information regarding changes of shape and constitutive design is required.

Design Sensitivity analysis. Design sensitivity analysis (DSA) describes a research field that deals with the determination of changes of quantities of interest regarding chosen design parametrizations, see for instance [12, 14, 32, 43, 77, 89, 125, 138, 171, 180, 201] for a broad overview of different methods and approaches. The different methods differ in theoretical and computational effort. Analytical methods usually require higher theoretical cost. However, this often pays off with highly efficient computational procedures in return. Within the main scope of this thesis, the quantity of interest is the stress state, which depends on the elastoplastic structural and material behavior. The analytical derivation of gradient information utilizing the variational approach developed in [18] is used in this thesis to formulate compact sensitivity relations naturally embedded into the general structural mechanical framework. This approach is based on an enhanced kinematic viewpoint that allows rigorous separation of geometrical and physical quantities and therefore facilitates the analytic derivations by means of variational calculus. This has been frequently shown in several works in the context of optimal structural design, see e.g. [14, 63, 116] in the context of hyperleasticity, [124] and [175] in the context of structural dynamics and the theory of porous media, [87, 88] in the context of multiscale material design and [103, 104] in the context of finite strain elastoplasticity. For the latter especially the pioneering works [185, 186, 187] have served as basic requisite in the formulation of variational design sensitivity information of elastoplastic structures, as well as for the work at hand.

Experimental investigations. Although the main focus in this work lies on the mentioned computational aspects, as the results of the computational method will be experimentally verified, some remarks on experimental methods should not be missing. The experiments with the cruciform X0-specimen are performed with the biaxial testing machine LFM-BIAX 20 kN produced by Walter+Bai, Switzerland. The used material is the aluminium alloy $AlMgSi_1$ (EN AW 6082-T6). During the experiments the deformation behavior is monitored by means of a digital image correlation (DIC) system Q-400 provided by Limess/Dantec. Therefore, six cameras are used, each equipped with 6.0 Mpx and 75 mm lenses. After final fracture, the fracture surfaces are analyzed utilizing scanning electron microscopy (SEM), which provides detailed visualizations up to magnitudes of 1 000 000 x. The experimental equipment is located at the laboratories of the Institut für Mechanik und Statik and the Institut für Werkstoffe des Bauwesens at the Universität der Bundeswehr München. The opportunity to use this equipment for presentation of the results in this work is gratefully appreciated. For further details on the experimental techniques the interested reader is referred to [59, 60, 61, 62], in which the same evaluations have been covered as in this work utilizing a similar experimental setup.

1.4 Outline

The overall scope of this work is reflected by the outline. The above mentioned deployed methods are step by step described in detail.

Chapter 2 provides basic preliminaries and introduces the mathematical notation. Additionally, the deployed hard- and software components and their use for different stages of the overall method are explained.

Chapter 3 presents the notation of general constrained optimization problems within the scope of structural optimization. The specific terms and methods used in this context are explained and the computational treatment is outlined.

Chapter 4 summarizes fundamentals in continuum thermomechanics and solution algorithms based on the finite element method. The elastoplastic constitutive model is presented with consistent linearizations needed for the FEM based solution procedure using Newton's method. Additionally, remarks on volumetric locking in connection with plastic incompressibility are given and the $\overline{F}$-method is exploited for remedy.

Chapter 5 is concerned with the sensitivity analysis. The variational approach is outlined and detailed continuous derivations of all necessary quantities are presented. Therefore, an enhanced kinematic viewpoint is exploited that enables naturally embedding the acquired sensitivity information into the structural mechanical framework.

Chapter 6 aims at transforming the continuously derived sensitivity information into a compact discrete matrix formulation. Discrete design parametrizations are introduced and the resulting discrete equations are systematically allocated to the different stages of the computational algorithm within the finite element method.

Chapter 7 represents the final proof of practicability and accuracy of the developed computational method. First, the developed method is used to identify constitutive parameters of the exploited elastoplastic constitutive model to fit the local material response. Subsequently, the shape optimization of the X0-specimen is performed and results are opposed with data acquired by the experimental investigations.

Chapter 8 finally summarizes the theoretical and computational developments in this thesis and draws conclusions on the findings. Within a closing outlook, hints on future investigations concerning the addressed research fields are given.

To provide a smooth general flow of reading, lengthy derivations and specific implementation details that are helpful in view of replication of the results presented in this thesis are given in the appendix.

Appendix A gives detailed information on lengthy derivations of important variations in the context of structural and sensitivity analysis.

Appendix B explains details on the numerical treatment in context of the FEM and gives specific hints on implementations utilizing `MATLAB`.

Appendix C presents further evaluations of SEM images at different magnitudes of the specimens fracture surfaces to improve the overall impression of the microscopic texture.

Chapter 2

Preliminaries

In this chapter the general notational conventions used in this thesis are introduced. Differences in tensor notation of continuous quantities and matrix notation of discrete quantities are outlined. Additionally, an overview of the hardware components and software tools used for numerical investigations is given.

Contents

2.1 Notation

Throughout this whole work symbolic tensor notation is used, unless in special cases, which are indicated separately. To distinguish between the tensorial order of quantities, different typographies are utilized. The convention in Tab. 2.1 summarizes the typographic notation. Vectors are bold face italic. Given an n-dimensional vector space with an arbitrary covariant basis $\{\boldsymbol{g}_1, \boldsymbol{g}_2, \dots, \boldsymbol{g}_n\}$, the expression $\boldsymbol{v} = v^i\, \boldsymbol{g}_i$ represents a vector with contravariant coefficients v^i and basis vectors $\boldsymbol{g}_i$. Second order tensors are written upright bold face and sans serif, e.g. $\mathsf{T} = T^{ij}\, \boldsymbol{g}_i \otimes \boldsymbol{g}_j$. Third order tensors have the same topographic style as second order tensors, but are additionally underscored $\underline{\mathsf{T}} = T^{ijk}\, \boldsymbol{g}_i \otimes \boldsymbol{g}_j \otimes \boldsymbol{g}_k$. Fourth order tensors are blackboard bold characters $\mathbb{T} = T^{ijkl}\, \boldsymbol{g}_i \otimes \boldsymbol{g}_j \otimes \boldsymbol{g}_k \otimes \boldsymbol{g}_l$. In most cases, quantities are given w.r.t. a Cartesian basis with basis vectors $\boldsymbol{e}_i$ or $\boldsymbol{E}_i$. As a Cartesian basis is orthonormal by definition, the distinction of co- and contravariance is not necessary. This simplifies the notation of operations between the mentioned quantities as follows. Note that Einstein's summation convention applies.
Single contraction is either denoted as dot product for vectors or omitted for higher order tensors and double contraction is denoted as colon, e.g.

$$\boldsymbol{u} \cdot \boldsymbol{v} = u_i v_i; \quad \mathsf{T}\,\boldsymbol{v} = \mathsf{T} \cdot \boldsymbol{v} = T_{ij} v_j\, \boldsymbol{e}_i \quad \text{and} \quad \mathbb{A} : \mathsf{T} = A_{ijkl} T_{kl}\, \boldsymbol{e}_i \otimes \boldsymbol{e}_j. \tag{2.1}$$

Special transpositions of third or fourth order tensors are denoted as superscripts, e.g.

$$\mathbb{T}^{\overset{23}{\mathsf{T}}} = T_{ikjl}\, \boldsymbol{e}_i \otimes \boldsymbol{e}_j \otimes \boldsymbol{e}_k \otimes \boldsymbol{e}_l, \tag{2.2}$$

which represents the transposition of the second and third bases of a fourth order tensor. For instance, the special fourth order projection tensors that map a second order tensor to itself or its symmetric and deviatoric contribution, respectively, can be written as

$$\begin{aligned}
\overset{4}{\mathbb{I}} &= (\mathsf{I} \otimes \mathsf{I})^{\overset{23}{\mathsf{T}}} = (\delta_{ik}\, \delta_{jl})\, \boldsymbol{e}_i \otimes \boldsymbol{e}_j \otimes \boldsymbol{e}_k \otimes \boldsymbol{e}_l, \\
\mathbb{I}^{\mathsf{sym}} &= \frac{1}{2} \left((\mathsf{I} \otimes \mathsf{I})^{\overset{23}{\mathsf{T}}} + (\mathsf{I} \otimes \mathsf{I}^{\mathsf{T}})^{\overset{23}{\mathsf{T}}} \right) = \frac{1}{2} (\delta_{ik}\, \delta_{jl} + \delta_{il}\, \delta_{jk})\, \boldsymbol{e}_i \otimes \boldsymbol{e}_j \otimes \boldsymbol{e}_k \otimes \boldsymbol{e}_l, \\
\mathbb{I}^{\mathrm{dev}} &= \mathbb{I}^{\mathsf{sym}} - \frac{1}{3}\, \mathsf{I} \otimes \mathsf{I} = \left(I^{\mathsf{sym}}_{ijkl} - \frac{1}{3}\, \delta_{ij}\, \delta_{kl} \right) \boldsymbol{e}_i \otimes \boldsymbol{e}_j \otimes \boldsymbol{e}_k \otimes \boldsymbol{e}_l.
\end{aligned} \tag{2.3}$$

In some equations, the special product $\overset{\mathrm{ij}}{*}$ is used, which denotes a single contraction of the i-th basis of a fourth order tensor with the j-th basis of a second order tensor, i.e.

$$\mathbb{T} \overset{21}{*} \mathsf{A} = T_{ijlm} A_{jk}\, \boldsymbol{e}_i \otimes \boldsymbol{e}_k \otimes \boldsymbol{e}_l \otimes \boldsymbol{e}_m. \tag{2.4}$$

This notation has been introduced in [103] and is notational convenient in some cases, as it allows compact representations of complicated terms, e.g. tensor-valued derivatives of physical quantities defined in the current configuration that are *pulled-back* to the reference configuration.

Table 2.1: Typographic convention.

	Example	Typography
Scalar	S, s, α	italic
Vector	$\boldsymbol{V}$, $\boldsymbol{v}$, $\boldsymbol{\nu}$	bold face, italic
2nd order tensor	$\mathbf{T}$, $\mathbf{t}$, $\boldsymbol{\beta}$	bold face, upright, sans serif
3rd order tensor	$\underline{\mathbf{M}}$, $\underline{\mathbf{m}}$, $\underline{\boldsymbol{\gamma}}$	underscored, bold face, upright, sans serif
4th order tensor	$\mathbb{A}$, $\mathbb{a}$, $\mathbb{\Sigma}$	blackboard
Matrix	$\boldsymbol{K}$, $\boldsymbol{k}$, $\boldsymbol{\eta}$	bold face, italic, sans serif

Table 2.2: Tensor operations.

Operation	Symbol	Example
Single contraction	$\cdot$ or " "	$s = \boldsymbol{u} \cdot \boldsymbol{v}$; $\mathbf{A} = \mathbf{B}\,\mathbf{C}$
Double contraction	:	$s = \mathbf{A} : \mathbf{B}$; $\mathbf{S} = \mathbb{C} : \mathbf{E}$
Special single contraction	$\overset{\text{ij}}{*}$	$\mathbb{S} = \mathbb{A} \overset{21}{*} \mathbf{B}$
Dyadic product	$\otimes$	$\mathbf{T} = \boldsymbol{a} \otimes \boldsymbol{b}$

2.1.1 Continuous variations and function spaces

Total variations of functionals are indicated with the δ symbol. Partial variations receive an extra subscript indicating the direction of the derivative. Given a three field functional $J(\boldsymbol{u},\boldsymbol{s},\boldsymbol{h})$, with $\boldsymbol{u} \in \mathcal{U}$, $\boldsymbol{s} \in \mathcal{S}$ and $\boldsymbol{h} \in \mathcal{H}$ that is generally nonlinear in all three arguments, where $\mathcal{U}, \mathcal{S}$ and $\mathcal{H}$ are Hilbert spaces, its total variation is given by the sum of its partial variations

$$\delta J(\boldsymbol{u},\boldsymbol{s},\boldsymbol{h}) = \delta_u J(\boldsymbol{u},\boldsymbol{s},\boldsymbol{h};\delta\boldsymbol{u}) + \delta_s J(\boldsymbol{u},\boldsymbol{s},\boldsymbol{h};\delta\boldsymbol{s}) + \delta_h J(\boldsymbol{u},\boldsymbol{s},\boldsymbol{h};\delta\boldsymbol{h}), \tag{2.5}$$

where the partial variations are defined as the *Gâteaux* or *directional derivatives*

$$\begin{aligned}
\delta_u J &= \lim_{\epsilon\to 0} \frac{1}{\epsilon}\,[J(\boldsymbol{u}+\epsilon\,\delta\boldsymbol{u},\boldsymbol{s},\boldsymbol{h}) - J(\boldsymbol{u},\boldsymbol{s},\boldsymbol{h})] = \frac{\mathrm{d}}{\mathrm{d}\epsilon}\,J(\boldsymbol{u}+\epsilon\,\delta\boldsymbol{u},\boldsymbol{s},\boldsymbol{h})\bigg|_{\epsilon=0}, \\
\delta_s J &= \lim_{\epsilon\to 0} \frac{1}{\epsilon}\,[J(\boldsymbol{u},\boldsymbol{s}+\epsilon\,\delta\boldsymbol{s},\boldsymbol{h}) - J(\boldsymbol{u},\boldsymbol{s},\boldsymbol{h})] = \frac{\mathrm{d}}{\mathrm{d}\epsilon}\,J(\boldsymbol{u},\boldsymbol{s}+\epsilon\,\delta\boldsymbol{s},\boldsymbol{h})\bigg|_{\epsilon=0}, \\
\delta_h J &= \lim_{\epsilon\to 0} \frac{1}{\epsilon}\,[J(\boldsymbol{u},\boldsymbol{s},\boldsymbol{h}+\epsilon\,\delta\boldsymbol{h}) - J(\boldsymbol{u},\boldsymbol{s},\boldsymbol{h})] = \frac{\mathrm{d}}{\mathrm{d}\epsilon}\,J(\boldsymbol{u},\boldsymbol{s},\boldsymbol{h}+\epsilon\,\delta\boldsymbol{h})\bigg|_{\epsilon=0},
\end{aligned} \tag{2.6}$$

with also $\delta\boldsymbol{u} \in \mathcal{U}$, $\delta\boldsymbol{s} \in \mathcal{S}$ and $\delta\boldsymbol{h} \in \mathcal{H}$. The partial variations are linear w.r.t. the respective direction of the derivative, which is indicated by the argument following a semicolon. The resulting operators are called semi-linear forms, as for a fixed set $\{\widehat{\boldsymbol{u}},\widehat{\boldsymbol{s}},\widehat{\boldsymbol{h}}\}$ they are linear forms, e.g. $\delta_u J(\widehat{\boldsymbol{u}},\widehat{\boldsymbol{s}},\widehat{\boldsymbol{h}};\delta\boldsymbol{u}) = \delta_u J : \mathcal{V} \to \mathbb{R}$. Partial variations of semi-linear forms result in semi-bilinear forms, which consequently for a fixed set $\{\widehat{\boldsymbol{u}},\widehat{\boldsymbol{s}},\widehat{\boldsymbol{h}}\}$ become

bilinear forms. For instance, given a semi-linear form $R(\boldsymbol{u},\boldsymbol{s},\boldsymbol{h};\boldsymbol{v})$, with $\boldsymbol{v} \in \mathcal{V}$, its partial variation w.r.t. $\boldsymbol{u}$ is given by $\delta_u R(\widehat{\boldsymbol{u}},\widehat{\boldsymbol{s}},\widehat{\boldsymbol{h}};\boldsymbol{v},\delta\boldsymbol{u}) = \delta_u R : \mathcal{V} \times \mathcal{V} \to \mathbb{R}$. Linear and bilinear operators can be expressed in matrix form, i.e. e.g.

$$R(\widehat{\boldsymbol{u}},\widehat{\boldsymbol{s}},\widehat{\boldsymbol{h}};\boldsymbol{v}) = \boldsymbol{v}^{\mathsf{T}}\,\boldsymbol{R} \quad \text{and} \quad \delta_u R(\widehat{\boldsymbol{u}},\widehat{\boldsymbol{s}},\widehat{\boldsymbol{h}};\boldsymbol{v},\delta\boldsymbol{u}) = \boldsymbol{v}^{\mathsf{T}}\,\boldsymbol{K}\,\delta\boldsymbol{u}. \tag{2.7}$$

For details on the function spaces and the notation using linear and bilinear operators, see e.g. [43, 77, 89, 171].

2.1.2 Discrete quantities

For the numerical implementation of a continuum theory, a discretization of the relevant quantities is necessary. In this work, the finite element method (FEM) is utilized. For reasons of simplicity and efficiency the so called Voigt notation is commonly used to reduce the order of arrays. For instance, the coefficients of a second order tensor $\mathbf{A} = A_{ij}\,\boldsymbol{e}_i \otimes \boldsymbol{e}_j$ can be represented by a matrix

$$\boldsymbol{A} = \left[A_{ij}\right], \quad \text{for } i,j = 1,2,3 \tag{2.8}$$

or by a column matrix (vector) using the convention

$$\boldsymbol{A} = \begin{bmatrix} A_{11} & A_{21} & A_{31} & A_{12} & A_{22} & A_{32} & A_{31} & A_{32} & A_{33} \end{bmatrix}^{\mathsf{T}} \tag{2.9}$$

for general nonsymmetric coefficients, or by

$$\boldsymbol{A} = \begin{bmatrix} A_{11} & A_{22} & A_{33} & 2\,A_{12} & 2\,A_{23} & 2\,A_{31} \end{bmatrix}^{\mathsf{T}} \tag{2.10}$$

if the coefficients are symmetric. Note that there are exceptional cases in which the vector representation is handled differently, cf. e.g. the vector representation of the mechanical stress tensor in Eq. 6.44. In these cases, the vector notation will be explicitily stated. In the same manner, matrix representations of fourth order tensor coefficients can be gained, viz.

$$\boldsymbol{A} = \begin{bmatrix} A_{1111} & A_{1121} & A_{1131} & A_{1112} & \dots & A_{1133} \\ A_{2111} & A_{2121} & \dots & & \dots & A_{2133} \\ \vdots & \vdots & \ddots & & & \vdots \\ & & & & & \\ \vdots & \vdots & & & \ddots & \vdots \\ A_{3311} & A_{3321} & A_{3331} & A_{3312} & \dots & A_{3333} \end{bmatrix} \tag{2.11}$$

or for symmetric coefficients

$$\boldsymbol{A} = \begin{bmatrix} A_{1111} & A_{1122} & A_{1133} & 2\,A_{1112} & 2\,A_{1123} & 2\,A_{1131} \\ A_{2211} & A_{2222} & \dots & & \dots & 2\,A_{2231} \\ \vdots & \vdots & \ddots & & & \vdots \\ & & & & & \\ \vdots & \vdots & & & \ddots & \vdots \\ A_{3311} & A_{3322} & A_{3333} & 2\,A_{3312} & 2\,A_{3323} & 2\,A_{3331} \end{bmatrix}. \tag{2.12}$$

A fourth order tensor might result from a partial derivative of a non-symmetric second order tensor w.r.t. a symmetric second order tensor, or vice versa. In these cases the matrix representations in Eq. (2.11) and Eq. (2.12) are mixed, e.g. the matrix form of the tensor $\mathbb{A} = \dfrac{\partial \mathbf{A}}{\partial \mathbf{B}} = A_{ijkl}\,\boldsymbol{e}_i \otimes \boldsymbol{e}_j \otimes \boldsymbol{e}_k \otimes \boldsymbol{e}_l$, with $\mathbf{B} = \operatorname{sym}(\mathbf{A})$, reads

$$\boldsymbol{A} = \begin{bmatrix} A_{1111} & A_{1122} & A_{1133} & 2\,A_{1112} & 2\,A_{1123} & 2\,A_{1131} \\ A_{2111} & A_{2122} & \dots & & \dots & 2\,A_{2131} \\ \vdots & \vdots & \ddots & & & \vdots \\ & & & & & \\ \vdots & \vdots & & & \ddots & \vdots \\ A_{3311} & A_{3322} & A_{3333} & 2\,A_{3312} & \dots & 2\,A_{3331} \end{bmatrix}. \tag{2.13}$$

Note that all three space dimensions are considered.

2.2 Computational environment

This section summarizes the hardware and software components used for numerical computations in this work. First, three different computing machines are presented. Subsequently, the software tools used for different stages of the simulations are introduced and their interaction is briefly sketched.

2.2.1 Hardware equipment

All simulations in this work have been performed on one of the three machines specified below in Tab. 2.3. All of them are running a 64-bit Linux operating system.

2.2.2 Software components

Numerical implementations of the underlying theories of this thesis have been done in `MATLAB R2019b`. The in-house code accrued within the past years is called `SOAP`, which is an abbreviation for **S**tructural **O**ptimization and **A**nalysis **P**rogram. The main focus of `SOAP` lies on efficient sensitivity analysis of structures with elastoplastic material behavior. The structural analysis is performed utilizing the finite element method, thus, sensitivity relations are discretized in the same manner. Following, three software tools that are

Table 2.3: Computing machines.

Abbreviation	Description
MWS	Dell Precision 7530 Mobile Workstation Intel® Core™ i9-8950HK (hexa-core @ 2.90 GHz) 32 GB DDR4 Memory NVIDIA® Quadro® P3200 Mobile, 6 GB
DWS	Fujitsu Celsius Desktop Workstation 2 × Intel® Xeon® E5-2690 (octa-core @ 2.90 GHz) 64 GB DDR4 Memory NVIDIA® Tesla® C2075, 6 GB
LiDO3	Linux Cluster Dortmund (3rd generation) 4 × Intel® Xeon® E5-2640v4 (deca-core @ 2.40 GHz) up to 1 024 GB DDR4 Memory NVIDIA® Tesla® K40, 12 GB

essential in different stages - that is *preprocessing*, *processing* and *postprocessing* - of the simulations are briefly introduced. Note that for the presentation of `MATLAB` code examples, within this thesis the M-code LaTeX Package [91] is used.

`Gmsh`

`Gmsh`, cf. [64], is an open source three-dimensional finite element mesh generator. It is distributed under the terms of the GNU Public License (GPL). It comes with a built-in CAD engine and offers an intuitive graphical user interface (GUI), which can be used to build up geometries and finite element meshes. Alternatively, `Gmsh` can be run in batch mode by passing an ASCII text file with a `.geo` extension using `Gmsh`'s own scripting language. There also exists an application programming interface (API) that makes it possible to provide code using other programming languages like `C/C++`, `Python` or `Julia`, which is not used within the scope of this thesis. When run in batch mode, `Gmsh` provides the opportunity to provide variables using the `-setnumber` option, which parametrizes the input. This becomes crucial in shape optimization, when the shape defining design parameters are not chosen as nodes of the finite element mesh, but geometrical quantities that parametrize the underlying geometry. In `SOAP`, `Gmsh` is used in the preprocessing stage for mesh generation, as well as for the computation of numerical derivatives of the FE mesh w.r.t. design parameters. More details on this are given in Chap. 6.

MATLAB

MATLAB, cf. [117], distributed by MathWorks®, is a high-level language and interactive environment. It enables to perform computationally intensive tasks and differs from traditionally programming languages, such as C/C++ or Fortran, as it is an *interpreter* that processes source code at runtime. The listed traditional languages need an external *compiler* to convert source code to machine code, which usually leads to much better runtime perfomance of the executable program. However, MATLAB also has the oppertunity to precompile parts of the source code using the MATLAB compiler toolbox. MATLAB's system command is useful to control operations of third party software, e.g. for mesh generation using Gmsh. For structural optimization MATLAB's optimization toolbox also contains powerful functions, such as fmincon or lsqnonlin, that takes complex implementations off the user's hand. By means of the NURBS toolbox, CAGD based geometries can be constructed with Bêzier patches, B-Splines or NURBS. Below, Tab. 2.4 summarizes the mendatory MATLAB toolboxes for the usage of SOAP and replication of the results presented in this thesis.

Table 2.4: MATLAB toolboxes.

Toolbox	Version	Functions / Directives
MATLAB Coder	4.0	codegen
Optimization Toolbox	8.1	fmincon, lsqnonlin
Parallel Computing Toolbox	6.12	parfor
NURBS Toolbox	1.0	

ParaView

The open-source, multi-platform data analysis and visualization application ParaView, cf. [3, 8], allows users to quickly build visualizations to analyse data using qualitative and quantitative techniques. Data exploration can be done interactively or in batch mode. Within the scope of this thesis, ParaView is used to process data like strains or stresses calculated after the simulation using MATLAB within a postprocessing procedure. The data is supplied by means of the .vtk file format that can be processed by ParaView.

ISTRA 4D

Monitoring and evaluation of experimental investigations is done using digital image correlation (DIC) by means of ISTRA 4D. It is a user-friendly software developed by Dantec Dynamics for simple and repeated shearographic measurements and evaluations. It allows multi-camera setups and provides high resolution results with high frame rates. Users can easily define coordinate systems and select measurement points (Gauge points) for the evaluation of the global deformation behavior of the analyzed specimen. Additionally, strain fields are computed and can be visualized at the specimen surfaces. With ISTRA 4D it is also possible to view measurements in real time during the experiment.

Chapter 3

Optimization Strategy

The main goal in this thesis is the optimization of an elastic-plastic structure undergoing large deformation. This chapter gives a brief overview about the solution strategy of the main optimization tasks that represents the frame of the computational procedure within this thesis. The mathematical notation of general optimization problems is introduced and important mathematical algorithms used within the solution strategy are sketched.

Contents

3.1 Introduction

This chapter aims at providing basic information on the optimization techniques used within this thesis to achieve the major goal of the specimen shape optimization and introducing the mathematical notation for general optimization problems.
The field of structural optimization is concerned with fundamental methods and applications of mathematical optimization techniques for computer aided optimal design of structures and mechanical systems in general, cf. e.g. [10, 23, 29, 45, 76, 151]. Within a structural optimization process mathematical and numerical algorithms are employed to detect the best design choice regarding a specific optimization goal. That is, in a mathematical sense, the best choice of a defined set of *design variables* maximizes or minimizes the value of an *objective function*. In the context of structural optimization, design variables parametrize the thermomechanical response of the underlying structure in terms of its topology, geometric shape or constitutive properties. In topology optimization, the densities at discrete elements play the role of design variables, i.e. the optimal material distribution within a fixed design space is detected. This often leads to creation of new or coalescence of initial holes in the structure. Several research groups addressed topics of topology optimization using different approaches not only for solid mechanical problems but also within a multi physical context. More insight can be found e.g. in [1, 24, 86, 136, 156, 157, 183] to name a few. In structural shape optimization, the topology of the analyzed structure is fixed and only the shape of the boundary is desired to change. Design variables are usually lengths, radii or coordinates of geometry controlling points. General and detailed information concerning shape optimization can be found e.g. in [13, 18, 28, 29, 171, 201] that have served as orientation within this thesis. Constitutive properties are concerned with the design of the material's microstructure, which can be differently described depending on the desired resolution. That is, generally a distinction of length scales into macro-, meso- and micro- or even nano-scale is made, cf. e.g. [34, 87, 192]. Within this thesis solely the macro-scale is considered and micromechanical effects are described via macroscopic constitutive laws. Here, the underlying strain energy and dissipation functions and the material dependent constitutive parameters needed for their evaluation completely determine the thermodynamic behavior. Thus, within this thesis the term *constitutive design* is introduced meaning a set of parameters controlling the constitutive material behavior.
Typical optimization goals in solid mechanics are for instance the minimization of weight or the maximization of the stiffness of a given structure. These optimization goals often are not only technologically but also economically relevant. Better performing and light weight structures can save production and shipping costs. However, the choice of the optimal design process is often limited in the sense that the structure has to fulfil specific conditions. These constraints might be of technological nature, like limitation of stresses, manufacturing issues, mass or volume. Also economical aspects often act as constraint in an optimization process. *Constraint functions* can be equality or inequality equations. Additionally, the values of the design variables itself can be limited to lower and upper bounds acting as *box constraints*.
The characteristics of the considered objective and constraint functions affect the choice of the solution strategy. That is, linear programming algorithms (LP) can be used if both, objective and constraint functions linearly depend on the design variables, quadratic

programming (QP) is used for quadratic objective functions and linear constraint functions. Nonlinear programming (NLP) algorithms are used to solve the most general optimization problems in which the objective function, as well as the constraint functions, can be nonlinear. In these cases, usually, the solution has to be determined using an iterative procedure utilizing LP or QP for the solution of a subproblem in each iteration step. Solution methods can be classified into zero order, first order and second order methods. Two famous examples of zero order methods are for instance the simplex method, cf. e.g. [27, 48, 95, 132], or Monte-Carlo simulations, see e.g. [122, 123, 143]. Zero order methods only require the evaluation of the objective and constraint functions, while first order methods require the gradient w.r.t. the design variables to establish a search direction. Prominent examples are for instance the steepest descent method [5, 50, 129] or the method of conjugated gradients [78, 155, 174, 176]. Second order methods require second derivatives, additionally. That is, not only the gradient of the Lagrange function is required, but also the Hessian. In these kinds of methods not a direct increase of the objective function value is aimed but rather the satisfaction of a vanishing gradient indicating a stationary point. The most prominent example of a second order method is most likely Newton's method, which is commonly used in structural mechanics for the solution of nonlinear boundary value problems. The procedure of determining gradient information is called *sensitivity analysis*. Different approaches exist for this purpose that can be classified into analytical and numerical methods. For details on different approaches in sensitivity analysis the interested reader is referred to e.g. [14, 43, 89, 171]. The order of a solution method goes along with numerical efficiency and accuracy of the solutions. However, utilizing higher order methods, only local minima can be detected and the theoretical and in some cases also the numerical effort can be huge. Additionally, often the convexity of the objective function cannot be guaranteed, which might lead to failure of the solution algorithm due to a non-positive definite Hessian. To overcome this, Quasi-Newton methods can be utilized. Here, the Hessian is approximated by means of an update formula that evolves during the iterations and ensures positive definiteness. In this thesis, focus lies of the method of sequential quadratic programming (SQP) that constitutes a Quasi-Newton method utilizing the Broyden-Fletcher-Goldfarb-Shannon (BFGS) update for the Hessian approximation. The SQP method can be seen as state of the art in nonlinear constrained optimization. Details on SQP can be found e.g. in [30, 69, 134, 148, 149] and more information on the BFGS method is given e.g. in [35, 57, 68, 154].
In the following, first the mathematical notation of a general unconstrained optimization problem is introduced. Secondly, basic fundamentals of the SQP method are briefly sketched and the solution strategy for the specimen shape optimization is presented. Here, focus lies on the general approach utilizing the `MATLAB` functions available in the Optimization Toolbox.

3.2 General constrained optimization problem

Let J be an objective function that depends explicitly on the chosen set of design variables $\boldsymbol{s}$, i.e. $J = J(\boldsymbol{s})$. Further, $c_j^{\mathsf{eq}}(\boldsymbol{s},)$ and $c_k^{\mathsf{in}}(\boldsymbol{s})$ constitute the equality and inequality constraints.

The general optimization problem then reads

$$\begin{aligned} \min_{\boldsymbol{s}\in\mathbb{R}^{\mathsf{ndv}}} \quad & J(\boldsymbol{s}), \\ \text{subject to} \quad & c_j^{\mathsf{eq}}(\boldsymbol{s}) = 0, \quad j \in \mathbb{E} := \{1,\ldots,n_{\mathsf{eq}}\}, \\ & c_k^{\mathsf{in}}(\boldsymbol{s}) \leq 0, \quad k \in \mathbb{I} := \{1,\ldots,n_{\mathsf{in}}\}, \\ & s_i^l \leq s_i \leq s_i^u, \quad i = 1,\ldots,\mathsf{ndv}. \end{aligned} \tag{3.1}$$

Note that if both sets of constraints are empty, i.e. if $\mathbb{E} = \mathbb{I} = \emptyset$, the optimization problem simplifies to an unconstrained one. In the general constrained case, most solution algorithms require the reformulation of the constrained problem into an unconstrained problem by means of the *Lagrange formalism*. Therefore, the original objective function is replaced by a manipulated *Lagrange function* $\mathcal{L}$ that additively incorporates the constraint functions using corresponding *Lagrange multipliers* $\boldsymbol{\lambda}$ and $\boldsymbol{\mu}$, viz.

$$\begin{aligned} \mathcal{L}(\boldsymbol{s},\boldsymbol{\lambda},\boldsymbol{\mu}) &:= J(\boldsymbol{s}) + \sum_{j=1}^{n_{\mathsf{eq}}} \lambda_j \, c_j^{\mathsf{eq}}(\boldsymbol{s}) + \sum_{k=1}^{n_{\mathsf{in}}} \mu_k \, c_k^{\mathsf{in}}(\boldsymbol{s}) \\ &= J(\boldsymbol{s}) + \boldsymbol{\lambda}^{\mathsf{T}} \, \boldsymbol{c}^{\mathsf{eq}} + \boldsymbol{\mu}^{\mathsf{T}} \, \boldsymbol{c}^{\mathsf{in}}. \end{aligned} \tag{3.2}$$

The Lagrange multipliers are also known as *adjoint variables*. A solution point is defined by the Karush-Kuhn-Tucker (KKT) optimality criteria

$$\nabla\mathcal{L}(\boldsymbol{s},\boldsymbol{\lambda},\boldsymbol{\mu}) := \begin{bmatrix} \nabla_s\mathcal{L} \\ \nabla_\lambda\mathcal{L} \\ \nabla_\mu\mathcal{L} \end{bmatrix} = \begin{bmatrix} 0 \\ 0 \\ 0 \end{bmatrix}. \tag{3.3}$$

That is, the gradient of the Lagrange function vanishes at a stationary point.

3.3 Solution strategy

The optimization tasks tackled within this thesis are solved by means of `MATLAB` and the available *Optimization Toolbox*. Specially the functions `lsqnonlin` for the solution of non-linear least squares problems and `fmincon` for the solution of general constrained optimization problems are utilized. These `MATLAB` functions provide automatic application of different optimization algorithms chosen by the user. However, the SQP method constitutes the state of the art in nonlinear programming and is therefore used for the specimen shape optimization in this thesis. Its fundamentals are briefly sketched in the following.

3.3.1 Sequential quadratic programming

In the SQP approach, a sequence of quadratic subproblems of the form

$$\min \tilde{J}^k = \frac{1}{2} \, \Delta\boldsymbol{s}^T \, \nabla^2_{ss}\mathcal{L}(\boldsymbol{s}^k,\boldsymbol{\lambda}^k,\boldsymbol{\mu}^k) \, \Delta\boldsymbol{s} + \nabla J(\boldsymbol{s}^k)^T \, \Delta\boldsymbol{s} \tag{3.4}$$

subject to the linearized constraints

$$\begin{aligned} \tilde{\boldsymbol{c}}_k^{\mathsf{eq}} &= \boldsymbol{c}_k^{\mathsf{eq}}(\boldsymbol{s}^k) + \nabla \boldsymbol{c}_k^{\mathsf{eq}}(\boldsymbol{s}^k)^T \, \Delta \boldsymbol{s}^k \quad &= 0, \\ \tilde{\boldsymbol{c}}_k^{\mathsf{in}} &= \boldsymbol{c}_k^{\mathsf{eq}}(\boldsymbol{s}^k) + \nabla \boldsymbol{c}_k^{\mathsf{in}}(\boldsymbol{s}^k)^T \, \Delta \boldsymbol{s}^k \quad &\leq 0, \\ (\boldsymbol{s}^l - \boldsymbol{s}^k) &\leq \Delta \boldsymbol{s} \leq (\boldsymbol{s}^u - \boldsymbol{s}^k), \end{aligned} \tag{3.5}$$

is solved. The solution of the quadratic subproblems in each iteration k can be obtained by means of any QP algorithm and requires the gradient of the objective and constraint functions, as well as the Hessian of the Lagrange function. In the SQP implementation of the `MATLAB` function `fmincon`, an active set strategy is used cf. e.g. [65, 66]. Within the Quasi-Newton procedure, the Hessian of the Lagrange function is approximated using the BFGS update formula as proposed by [75, 140, 149]. The BFGS method ensures positive definiteness of the Hessian and its approximation becomes more accurate with each global SQP iteration. The QP solution forms a new iterate following the update formula

$$\boldsymbol{s}^{k+1} = \boldsymbol{s}^k + \alpha^k \, \Delta \boldsymbol{s}^k, \tag{3.6}$$

where α^k is the step length parameter and $\Delta \boldsymbol{s}^k$ denotes the search direction. The step length parameter can be determined utilizing an appropriate line search procedure to sufficiently decrease a merit function, cf. e.g. [6, 189].
`fmincon` provides the possibility to compute the gradient of the objective and constraint functions automatically by means of the numerical finite difference method. However, this method is numerically costly due to the amount of function evaluations based on the number of design variables. Furthermore, results might be inaccurate depending on the choice of perturbation size. The approach to determine the gradient information pursued within this thesis is the variational sensitivity analysis, in which analytical gradients are derived by means of variational calculus and embedded into the numerical solution framework of the structural analysis problem. Both strategies are briefly explained in the upcoming section.

3.3.2 Determination of gradient information

In this work, two different ways of establishing design sensitivity information, i.e. the computation of gradients of the objective and constraint functions, appear. In the following these two methods are briefly introduced.

Finite difference method. The *finite difference method* (FDM) is a numerical method in which differential quotients (gradients) are approximated by difference quotients at finite equidistant lattice points. That is, the gradient ∇f of a function f is approximated by $\nabla_{\mathsf{FD}} f \approx \nabla f$. Therefore, the value of each design variable is perturbed by a small number ε and the corresponding function values f^{ε} are evaluated. This gives information about the function values in a finite neighbourhood that is used to draw inferences on the gradient of the function in that point. Three variants of the FDM have to be distinguished concerning the direction of perturbation. That is, the *forward, backward* and *central* FDM scheme in which the approximations require the function values regarding positive and

negative perturbations $f^{\varepsilon+}$ and $f^{\varepsilon-}$, as well as the function value at the point itself f. The respective gradient approximations read

$$\begin{aligned} &\text{Forward FDM:} && \nabla^{\mathsf{f}}_{\mathsf{FD}} f := \frac{f^{\varepsilon+} - f}{\varepsilon} \\ &\text{Backward FDM:} && \nabla^{\mathsf{b}}_{\mathsf{FD}} f := \frac{f - f^{\varepsilon-}}{\varepsilon} \\ &\text{Central FDM:} && \nabla^{\mathsf{c}}_{\mathsf{FD}} f := \frac{f^{\varepsilon+} - f^{\varepsilon-}}{2\,\varepsilon} \end{aligned} \tag{3.7}$$

The FDM has the advantage of comparatively simple implementation. However, depending on the complexity of the analyzed function, the FDM might be computationally costly. Furthermore, the accuracy of the results strongly depend on choice of the perturbation size. In theory, the smaller the perturbation size becomes, the better the numerical approximation. In practice, this is connected with the numerical precision of the computing machine. That is, computations of small differences of large numbers or quotients of large and small numbers for instance might not be adequately representable.
`fmincon` offers the possibility of automatic gradient approximation using FDM and several parameters can be adjusted by setting the appropriate options. However, in this work FDM is mainly used purposing the verification of analytically derived gradient information.

Variational design sensitivity analysis. A more reliable approach of computing gradient information is the analytical way. In connection with discrete methods for the solution of the underlying structural mechanical problem, two different approaches that lead the same results have to be distinguished. On the one hand, in the *discrete approach* already discretized model equations are taken as basis for the gradient computations, i.e. discrete quantities are analytically derived. On the other hand, in the *variational approach* the continuous quantities of the underlying structural mechanical problem serve as basis for the gradient derivations. The latter approach is focused within this thesis. The variational design sensitivity analysis (VDSA) requires deep insight into the governing continuum mechanical equations to apply variational tensor analysis for consistent linearizations. The assumption of finite elastoplastic material behavior goes along with highly nonlinear equations and path dependency of the structural response requiring the solution of an initial boundary value problem (IBVP) for the elastoplastic state variables, namely the discrete displacements $\boldsymbol{u} \in \mathbb{R}^{\mathsf{dof}}$ and the set of internal variables connected with dissipative mechanisms $\boldsymbol{h} \in \mathbb{R}^{\mathsf{nhv}}$. Here, dof and nhv represent the number of discrete degrees of freedom and history variables, respectively. Therefore, the functional dependencies have to be identified and the VDSA has to be embedded into the solution procedure of the IBVP, i.e. it has to be consistent with the used discrete time integration scheme. Thus, for any arbitrary physical function f, the total variation takes the form

$$\delta f = \delta_s f + \delta_u f + \delta_{h_n} f = \frac{\partial f}{\partial \boldsymbol{s}}\,\delta \boldsymbol{s} + \frac{\partial f}{\partial \boldsymbol{u}}\,\delta \boldsymbol{u} + \frac{\partial f}{\partial \boldsymbol{h}_n}\,\delta \boldsymbol{h}_n. \tag{3.8}$$

The subscript n indicates that the corresponding set of history variables belong to the prior time step. Obviously, it is necessary to determine the total variations of the structural response $\delta \boldsymbol{u}$ and the history variables $\delta \boldsymbol{h}_n$ representing the elastoplastic state first, before the total variation can be expressed solely in terms of the design variables. The complete derivation of analytical gradient information in connection with finite elastoplasticity is presented in Chap. 5 and the subsequent implementation into the discrete solution procedure is given in Chap. 6. Here, the sensitivity matrix $\boldsymbol{S}$ and the total history design sensitivity matrices are derived and defined as

$$\delta \boldsymbol{u} = \boldsymbol{S}\, \delta \boldsymbol{s} \quad \text{and} \quad \delta \boldsymbol{h}_n = \boldsymbol{Z}_n\, \delta \boldsymbol{s}. \tag{3.9}$$

With this, the total design variation of any physical function can be obtained by

$$\delta f = \left[\frac{\partial f}{\partial \boldsymbol{s}} + \frac{\partial f}{\partial \boldsymbol{u}}\, \boldsymbol{S} + \frac{\partial f}{\partial \boldsymbol{h}_n}\, \boldsymbol{Z}_n \right] \delta \boldsymbol{s} = \nabla f\, \delta \boldsymbol{s}. \tag{3.10}$$

The obtained gradient information can be passed to `fmincon` by setting the appropriate options. With this information `fmincon` can undertake the SQP procedure requiring only one function evaluation in each iteration.

3.3.3 Design parametrization

In structural shape optimization the geometric boundary of the analyzed structure defines its design. Considering the finite element method, the most obvious choice of design variables are the nodal coordinates of the finite element mesh. However, depending on the continuity of the used shape functions and the number of discrete nodes, this approach might result in a high number of design variables ndv and non-smooth boundaries. Thus, it is convenient to parametrize the finite element mesh. Appropriate methods from computer aided geometric design (CAGD) can for instance be used to mathematically describe exact geometric curves, surfaces and volumes with prescribed continuity. Most prominent methods are Bêzier patches, basic splines (B-splines) and non-uniform rational B-splines (NURBS). Here, a prescribed number of control points define the geometry. Based on these geometry descriptions, a finite element mesh can be constructed that is parametrized by the control points. This approach requires a coupling of the geometry description and the finite element mesh, which results in the so-called *design velocity field* consisting of partial derivatives of nodal mesh coordinates w.r.t. the position of the control points. Details are given in Chap. 6.

For the parametrization of complex geometries by means of more accessible and descriptive quantities like e.g. simple lengths or radii, it might also be convenient to utilize third party mesh generation software. In this thesis, for the specimen shape optimization, Gmsh is used, which offers the possibility to parametrize the underlying geometry for mesh generation. The coupling between the geometry description and the corresponding FE mesh, i.e. the corresponding design velocity field, can be determined numerically e.g. by the FDM. This approach requires often remeshing and is not recommended for problems with a huge amount of degrees of freedom, in which the meshing procedure is computationally costly. However, in view of the numerically efficient VDSA and the

considered mesh sizes, within the entire optimization process this overhead is affordable. Within this thesis, not only geometric design sensitivities are considered. The simulations are to be compared to real experiments, which requires the simulation model to fit the constitutive behavior of the analyzed material. In this case the constitutive parameters of the elastoplastic model constitute the design variables. Therefore, geometric shape as well as constitutive design sensitivities have to be derived and computed to be passed to the corresponding mathematical optimizer.

3.3.4 Algorithmic framework

In Fig. 3.1 the schematic framework of solving stated optimization problems followed in this work is illustrated. First, the optimization problem is stated and a start design has to be defined. That is, the structural mechanical problem, the objective and constraint functions, as well as design variables have to be defined. With this, the mechanical response, as well as the response sensitivity are determined within an implicit time integration scheme and the values and gradients of objective and constraint functions can be determined. This means that after the mechanical response in a specific time step is computed using Newton's method, the gradients in the solution point are computed so as to capture the deformation path and its sensitivity. This is repeated for all chosen discrete time steps. After the final time step, the function values of the objective and constraint functions, as well as their gradients w.r.t. the chosen design variables are passed to the mathematical optimizer, which computes a new design until a defined optimality criterion is fulfilled.
The results of the specimen shape optimization considered in this thesis are obtained by means of `fmincon` as mathematical optimizer and are to be validated by comparison with real experiments. Thus, to ensure the constitutive conformity of the numerical model and the analyzed material, a preceding inverse parameter identification is conducted. In this case, a nonlinear objective function of least squares type with only box constraints has to be minimized and the `MATLAB` function `lsqnonlin` is used for the solution, as it is suited to this kind of optimization problems. However, the schematic framework given in Fig. 3.1 is still valid as only the mathematical optimizer is changed.

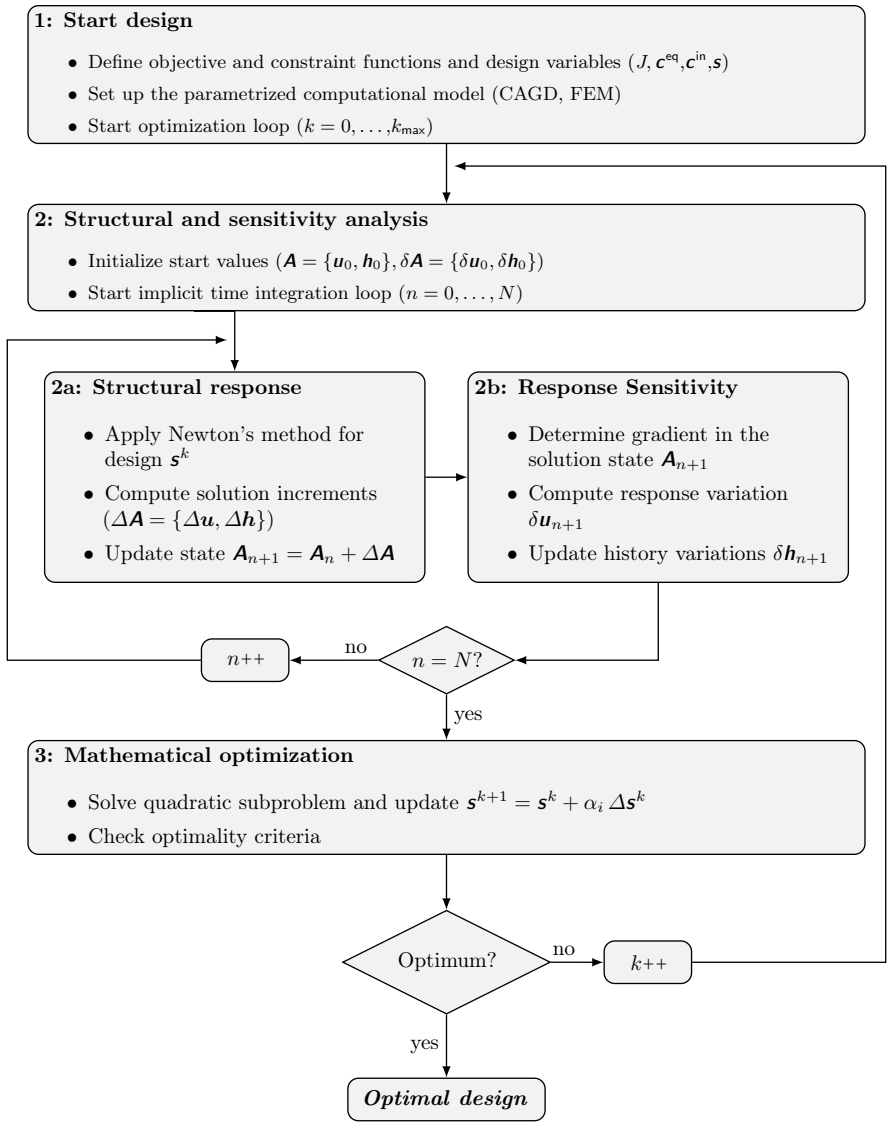

Figure 3.1: General solution procedure of constrained optimization problems utilizing variational sensitivity analysis. The procedure is mostly automated utilizing the `MATLAB` function `fmincon`.

3.4 Summary

This chapter introduces the mathematical notation for general constrained optimization problems. Therefore, the terms *objective and constraint functions* acting as optimization goal and restrictions on the solution are explained. Additionally, *design variables* and possible parametrizations are introduced. Subsequently, the solution strategy followed in this work is illustrated. The optimization solution strategy forms the frame of the computational procedures presented in this work. The sequential quadratic programming (SQP) method is briefly sketched and two different approaches for the determination of gradient information used in this work are introduced. That is, the numerical approach utilizing the finite difference method (FDM), in which differential quotients are approximated by quotients of differences, and the analytical variational approach (VDSA), in which analytical gradients have to be derived based on the underlying governing equations of the structural mechanical problem. The VDSA constitutes a main topic of the work at hand and is explained in detail in subsequent chapters.

Chapter 4

Continuum Mechanics and Finite Element Discretization

The outcome of this chapter represents the solution method for the underlying structural mechanical initial boundary value problem within the scope of the global structural optimization strategy outlined in Chap. 3. The basic framework of continuum mechanics used in this work is outlined. After the description of kinematics, the governing balance equations as well as the laws of thermodynamics are briefly sketched. Based on this, the elastoplastic constitutive model is depicted with its fundamental characteristics. Additionally, as the plastic flow is assumed incompressible in the presented theory, the method of $\overline{F}$ is utilized to prevent volumetric locking within the finite element method. Two simple numerical examples verify the accuracy of the model implementation.

Contents

4.1 Introduction

In continuum mechanics, the physical behavior of a body is assumed to be governed by partial differential equations of continuous media and described by macroscopic models. That is, considering astronomically large or quantumly small scales, the theory of continuum mechanics might lose its validity. In general, three fundamental segments define the theory. The body and its motion and deformation is mathematically described by kinematics. The general balance laws together with a material dependent constitutive law govern the physical response.

This chapter aims at summarizing the general continuum mechanical framework and the chosen constitutive model used within this thesis to describe the elastoplastic material behavior. It can be seen as a necessary preparation in view of the subsequent sensitivity analysis. Thus, in itself, the present chapter does not contain genuinely new results. Although in view of tailoring the equations to the demands of the subsequent sensitivity analysis and in preparation of the prevention of volumetric locking using $\overline{F}$- finite elements, the consistent linearization of the stresses w.r.t. the deformation gradient is derived, which, by the best of the author's knowledge, is not found yet in the relevant literature.

Fundamental basics on general rational thermodynamics can be found in standard works e.g. [181, 182] or in the specific context of plasticity e.g. in [118, 119, 120], where also the concept of modelling irreversible processes by means of internal state variables is reviewed, which goes back to early works like [53, 150]. Continuum mechanics is only sketched to its very basics in this chapter. For more detailed insight into this subject, the interested reader is referred to e.g. [4, 26, 31, 135, 173]. The theory of plasticity is a widespread field of research. Numerous publications dealt with this topic during the past century. At this point some selected works are mentioned. One early pioneering work is e.g. [127], in which the basic formulations of the so called von Mises or J_2 flow theory are presented, which founds on the assumption that the volumetric stress state has negligible influence on the plastic behavior of metals. This fundamental viewpoint of metal plasticity is valid and often applied for a wide class of metals. Standard textbooks like e.g. [42, 110, 159, 172, 190] comprise different approaches of modelling plasticity for small and finite deformations. Additionally, different solution methods are described. The elastoplastic constitutive model used within this thesis is excellently described in [159], which summarizes several works of the authors like e.g. [158, 160, 161, 162, 163, 164, 165, 166, 167, 168, 169, 170]. In several more recent publications, the presented model is used within the scope of isogeometric analysis (IGA), see e.g. [54, 55, 81].

The numerical solution of underlying differential equations of the structural mechanical problem is obtained by means of the finite element method (FEM). Numerous textbooks can be chosen to gain deep insight into the theory of the FEM and advanced topics as e.g. structural dynamics and inelasticity or advanced element technologies. See e.g. [21, 31, 33, 47, 80, 190, 198, 199, 200] to name a few. Within the context of the FEM, it is a commonly known issue that using simple low-order displacement based element formulations, an overstiff structural response is computed for nearly incompressible materials. In [93] different geometrical locking effects in the context of the FEM are summarized and solution approaches are described. As in the J_2 flow theory used in this work, the plastic flow is assumed incompressible, advanced element formulations have to be considered. Due to its simplicity, the method of $\overline{F}$ is chosen as described in e.g. [49, 54, 55, 172].

4.2 Kinematics

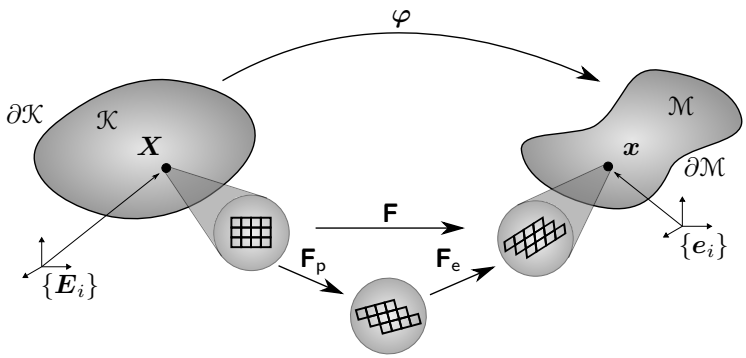

Figure 4.1: Classical kinematics including a local intermediate configuration.

Fig. 4.1 illustrates the classical representation of kinematics in continuum mechanics in connection with multiplicative elastoplasticity. The material body is represented in a fixed and stress free reference configuration $\mathcal{K}$ with basis $\{\boldsymbol{E}_i\}$ and referential points $\boldsymbol{X}$. The deformation mapping

$$\boldsymbol{\varphi} : (\boldsymbol{X},t) \mapsto \boldsymbol{x}(\boldsymbol{X},t), \tag{4.1}$$

maps the referential points to the current deformed configuration $\mathcal{M}$ with basis $\{\boldsymbol{e}_i\}$ and current points $\boldsymbol{x}$. The displacement vector between the points in the current and reference placements is defined as

$$\boldsymbol{u} = \boldsymbol{x} - \boldsymbol{X}; \tag{4.2}$$

The gradient of the deformation mapping w.r.t. the referential points is defined as the deformation gradient

$$\mathbf{F} = \operatorname{Grad} \boldsymbol{\varphi} = \frac{\partial \boldsymbol{x}}{\partial \boldsymbol{X}} = \frac{\partial (\boldsymbol{X} + \boldsymbol{u})}{\partial \boldsymbol{X}} = \mathbf{I} + \operatorname{Grad} \boldsymbol{u} = \frac{\partial x_i}{\partial X_j}\, \boldsymbol{e}_i \otimes \boldsymbol{E}_j. \tag{4.3}$$

It contains a multiaxial stretch and a rigid body rotation, obtained via a polar decomposition

$$\mathbf{F} = \mathbf{R}\mathbf{U} = \mathbf{v}\mathbf{R} \tag{4.4}$$

with the orthogonal rotation tensor $\mathbf{R} \in \mathrm{SO}(3)$ and the right and left stretch tensors $\mathbf{U}$ and $\mathbf{v}$, respectively. Based on the stretch tensors, objective deformation and strain measures can be defined in the reference and the current configuration, e.g. the right and left Cauchy-Green tensors

$$\mathbf{C} = \mathbf{U}^2 = \mathbf{F}^{\mathsf{T}}\mathbf{F} \quad \text{and} \quad \mathbf{b} = \mathbf{v}^2 = \mathbf{F}\mathbf{F}^{\mathsf{T}} \tag{4.5}$$

and the Green-Lagrange and Almansi strain tensors

$$\mathbf{E} = \frac{1}{2}\left(\mathbf{C} - \mathbf{I}\right) \quad \text{and} \quad \mathbf{e} = \frac{1}{2}\left(\mathbf{I} - \mathbf{b}^{-1}\right). \tag{4.6}$$

By means of the deformation gradient, point, area and volume mappings between the reference and the current configurations can be defined, viz.

$$\mathrm{d}\boldsymbol{x} = \mathbf{F}\,\mathrm{d}\boldsymbol{X}, \quad \mathrm{d}\boldsymbol{a} = J\,\mathbf{F}^{-\mathsf{T}}\mathrm{d}\boldsymbol{A}, \quad \mathrm{d}v = J\,\mathrm{d}V, \quad \text{with} \quad J = \det\mathbf{F}. \tag{4.7}$$

For time dependent problems, temporal rates, i.e. derivatives w.r.t. time play an important role. Time differentiation of the displacement field results in a velocity and an acceleration field

$$\dot{\boldsymbol{u}} = \dot{\boldsymbol{x}} = \frac{\partial \boldsymbol{x}}{\partial t} \quad \text{and} \quad \ddot{\boldsymbol{u}} = \ddot{\boldsymbol{x}} = \frac{\partial^2 \boldsymbol{x}}{\partial t^2}. \tag{4.8}$$

The corresponding referential and spatial velocity gradients are defined as

$$\mathrm{Grad}\,\dot{\boldsymbol{x}} = \dot{\mathbf{F}} \quad \text{and} \quad \mathbf{L} := \mathrm{grad}\,\dot{\boldsymbol{x}} = \dot{\mathbf{F}}\,\mathbf{F}^{-1}, \tag{4.9}$$

of which the latter can be decomposed into a symmetric deformation rate $\mathbf{d}$ and a skew symmetric spin $\mathbf{w}$

$$\mathbf{d} = \frac{1}{2}\left(\mathbf{L} + \mathbf{L}^{\mathsf{T}}\right) \quad \text{and} \quad \mathbf{w} = \frac{1}{2}\left(\mathbf{L} - \mathbf{L}^{\mathsf{T}}\right). \tag{4.10}$$

With this, the rate of the right Cauchy-Green tensor can be formulated

$$\dot{\mathbf{C}} = \dot{\mathbf{F}}^{\mathsf{T}}\mathbf{F} + \mathbf{F}^{\mathsf{T}}\dot{\mathbf{F}} = 2\,\mathbf{F}^{\mathsf{T}}\mathbf{d}\,\mathbf{F} = 2\dot{\mathbf{E}}. \tag{4.11}$$

Plastic intermediate configuration

The local plastic intermediate configuration $\mathcal{P}$ is a result of the phenomenological description of elastoplasticity based on a multiplicative split of the deformation gradient

$$\mathbf{F} = \mathbf{F}_{\mathsf{e}}\,\mathbf{F}_{\mathsf{p}}. \tag{4.12}$$

This split is micromechanically motivated as the plastic deformation gradient $\mathbf{F}_{\mathsf{p}}$ is related to lattice dislocation movements connected with the slip of atoms. On the contrary, the elastic deformation gradient represents lattice distortions. Thus, the plastic intermediate configuration can be interpreted as a completely elastic relaxation of the deformed configuration, i.e. $\mathbf{F}_{\mathsf{p}} = \mathbf{F}_{\mathsf{e}}^{-1}\,\mathbf{F}$. Consequently, it is implicitly assumed stress-free. The multiplicative kinematic viewpoint has been considered e.g. in [94, 97, 98, 108, 109, 114, 115, 133, 162]. Based on the multiplicative split in Eq. (4.12), elastic and plastic contributions of the deformation and strain tensors can be obtained in the reference

configuration

$$\mathbf{C}_\mathrm{p} = \mathbf{F}_\mathrm{p}^\mathrm{T}\,\mathbf{F}_\mathrm{p}, \tag{4.13}$$

$$\mathbf{E}_\mathrm{p} = \frac{1}{2}\left(\mathbf{C}_\mathrm{p} - \mathbf{I}\right), \tag{4.14}$$

and in the current configuration

$$\mathbf{b}_\mathrm{e} = \mathbf{F}_\mathrm{e}\,\mathbf{F}_\mathrm{e}^\mathrm{T}, \tag{4.15}$$

$$\mathbf{e}_\mathrm{e} = \frac{1}{2}\left(\mathbf{I} - \mathbf{b}_\mathrm{e}^{-1}\right). \tag{4.16}$$

From Eq. (4.12), Eq. (4.13) and Eq. (4.15) the relationship

$$\mathbf{b}_\mathrm{e} = \mathbf{F}\,\mathbf{C}_\mathrm{p}^{-1}\,\mathbf{F}^\mathrm{T} \quad \Leftrightarrow \quad \mathbf{C}_\mathrm{p}^{-1} = \mathbf{F}^{-1}\,\mathbf{b}_\mathrm{e}\,\mathbf{F}^{-\mathrm{T}} \tag{4.17}$$

can be derived, which identifies the inverse of the plastic right Cauchy-Green tensor as the referential counterpart of the elastic left Cauchy-Green tensor.
Inserting Eq. (4.12) into Eq. (4.9) leads to the definition of the spatial elastic and plastic velocity gradients

$$\mathbf{L} = \dot{\mathbf{F}}_\mathrm{e}\,\mathbf{F}_\mathrm{e}^{-1} + \mathbf{F}_\mathrm{e}\,\dot{\mathbf{F}}_\mathrm{p}\,\mathbf{F}_\mathrm{p}^{-1}\,\mathbf{F}_\mathrm{e}^{-1} = \mathbf{L}_\mathrm{e} + \mathbf{L}_\mathrm{p} \tag{4.18}$$

and consequently, in view of Eq. (4.10), to the additive split of the symmetric deformation rate and skew symmetric spin

$$\mathbf{d} = \mathbf{d}_\mathrm{e} + \mathbf{d}_\mathrm{p} \quad \text{and} \quad \mathbf{w} = \mathbf{w}_\mathrm{e} + \mathbf{w}_\mathrm{p}. \tag{4.19}$$

It should be noted that without any special assumption on the orientation of the plastic intermediate configuration, it is only defined up to a rigid body rotation, see e.g. [153, 159]. Consequently, the plastic deformation gradient $\mathbf{F}_\mathrm{p}$ cannot be chosen as internal variable. This issue is overcome with the assumption of elastic and plastic isotropy, cf. [166, p. 9] or [158], which leads to the identity $\mathbf{F}_\mathrm{e} = \mathbf{v}_\mathrm{e}$, as the elastic rotation tensor is simply given by $\mathbf{R}_\mathrm{e} = \mathbf{I}$. However, in the model used in this thesis, the arbitrariness of the plastic deformation gradient has no effect on the computational procedure, cf. [159]. Here, the authors point to the arbitrariness of the plastic spin in the classical infinitesimal theory of elastoplasticity.
In case that the orientation of the intermediate configuration has to be known even without the assumption of isotropy, the interested reader is referred to e.g. [113], where a so-called isoclinic intermediate configuration is defined.

4.3 Governing equations

In the following, the governing mechanical equations are summarized. Basically, the presented equations represent standard fundamental laws in modern mechanics based on Newton's axioms. Note, as within this thesis only solid mechanical problems are considered, the thermodynamic governing equations are only sketched for the basic needs.

4.3.1 Mass conservation

Within the scope of this thesis, mass is always assumed to be conserved. That is, Newton's first law states the absence of convective mass transfer, such that the mass of a volume element $M = \rho_o \, \mathrm{d}V$ in $\mathcal{K}$ is conserved

$$\dot{M} = \frac{\mathrm{d}}{\mathrm{d}t}(\rho_o \, \mathrm{d}V) = 0 \quad \Rightarrow \quad \rho_o = \text{const.}, \tag{4.20}$$

which leads to a constant density in the reference configuration. Considering the mass of a volume element in the current configuration $m = \rho \, \mathrm{d}v$ and recalling Eq. (4.7), one obtains the local form of the balance of mass

$$\dot{m} = \frac{\mathrm{d}}{\mathrm{d}t}(\rho \, \mathrm{d}v) = \frac{\mathrm{d}}{\mathrm{d}t}(\rho \, J \, \mathrm{d}V) = 0 \quad \Leftrightarrow \quad \dot{\rho} + \rho \, \mathrm{div} \, \dot{\boldsymbol{x}} = 0, \tag{4.21}$$

where $\dot{J} = \rho \, \mathrm{div} \, \dot{\boldsymbol{x}}$ has been used. From the comparison of Eq. (4.20) and Eq. (4.21) it directly follows that

$$J = \frac{\rho_o}{\rho}, \tag{4.22}$$

which means that the density must transform reciprocally to the volume element so as to conserve mass.

4.3.2 Stresses and momentum

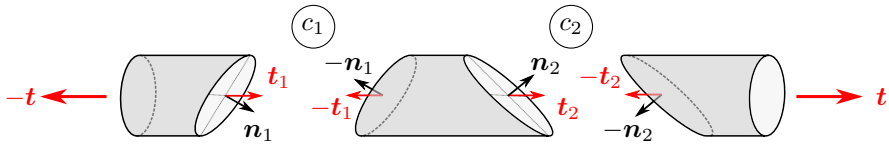

Figure 4.2: 3D rod subjected to traction forces.

Considering two straight cuts (c_1, c_2) through a three dimensional rod subjected to traction forces, as illustrated in Fig. 4.2, Cauchy's fundamental lemma states that the stress vectors acting on opposite sides of the same cut have to be equal in magnitude and opposite in direction. This is equivalent to Newton's third law of motion, viz.

$$-\boldsymbol{t}(\boldsymbol{n}) = \boldsymbol{t}(-\boldsymbol{n}). \tag{4.23}$$

Obviously, the area of the cutting surface changes with the orientation of the cut defined by the normal vector $\boldsymbol{n}$. Consequently, the stress distribution over the cutting surfaces has to change, as the resulting stress vector $\boldsymbol{t}$ has to stay constant to ensure force equilibrium. This leads to *Cauchy's fundamental law* and the definition of the Cauchy stress tensor $\boldsymbol{\sigma}$

$$\boldsymbol{t} = \boldsymbol{\sigma} \, \boldsymbol{n}. \tag{4.24}$$

The Cauchy stress tensor measures forces in the current configuration regarding the deformed infinitesimal area element in the current configuration. Therefore, it is often called *true stress* tensor. Other stress tensors with slight different physical meanings can also be defined. Within the scope of this thesis, the important stress measures are the following. The Kirchhoff stress tensor

$$\boldsymbol{\tau} = J\,\boldsymbol{\sigma} \tag{4.25}$$

weights the Cauchy stress tensor with the determinant of the deformation gradient J. The first Piola-Kirchhoff stress tensor

$$\mathbf{P}^{\mathsf{K}} = J\,\boldsymbol{\sigma}\,\mathbf{F}^{-\mathsf{T}} = \boldsymbol{\tau}\,\mathbf{F}^{-\mathsf{T}} \tag{4.26}$$

is also called engineering stress and measures the forces in the current configuration regarding an infinitesimal undeformed area element in the reference configuration. It is unsymmetric and a two-point tensor, i.e. one of its basis vectors is located in the reference, the other in the current configuration. The basis vectors of the second Piola-Kirchhoff stress tensor are both located in the reference configuration and it measures the forces pulled back to the reference configuration regarding the infinitesimal area element in the reference configuration

$$\mathbf{S} = \mathbf{F}^{-1}\,\mathbf{P}^{\mathsf{K}} = J\,\mathbf{F}^{-1}\,\boldsymbol{\sigma}\,\mathbf{F}^{-\mathsf{T}}. \tag{4.27}$$

The *momentum balance equation* - Newton's second law of motion - states that an object accelerates if the forces acting on it are unbalanced. The local form applied to a volume element in the current configuration is given by

$$\operatorname{div}\boldsymbol{\sigma} + \boldsymbol{b} = \rho\,\ddot{\boldsymbol{x}}, \tag{4.28}$$

with a distributed body force $\boldsymbol{b}$. It can also be expressed in terms of the first Piola-Kirchhoff stress tensor $\mathbf{P}^{\mathsf{K}}$ in the reference configuration and reads

$$\operatorname{Div}\mathbf{P}^{\mathsf{K}} + \boldsymbol{b}_o = \rho_o\,\ddot{\boldsymbol{x}}, \tag{4.29}$$

where $\boldsymbol{b}_o = J\,\boldsymbol{b}$ denotes the body forces in the reference configuration. Assuming static processes, acceleration terms are neglected, thus $\ddot{\boldsymbol{x}} = \mathbf{0}$, which leads to equilibrium of internal and external forces.

The *balance of angular momentum* states that the angular or rotational momentum of a closed system has to remain constant. The sum of external moments, e.g. caused by excentrical forces, have to equal the sum of internal moments. An important result of the angular momentum balance is that the Cauchy stress tensor has to be symmetric

$$\boldsymbol{\sigma} = \boldsymbol{\sigma}^{\mathsf{T}} \tag{4.30}$$

and consequently

$$\boldsymbol{\tau} = \boldsymbol{\tau}^{\mathsf{T}}, \quad \mathbf{P}^{\mathsf{K}}\,\mathbf{F}^{\mathsf{T}} = \mathbf{F}\,(\mathbf{P}^{\mathsf{K}})^{\mathsf{T}}, \quad \mathbf{S} = \mathbf{S}^{\mathsf{T}}. \tag{4.31}$$

4.3.3 Thermodynamic principles

The first principle of thermodynamics - *the conservation of energy* - states that the rate of internal energy per unit volume in the current configuration has to equal the sum of stress power and heat production deducting the divergence of the heat flux, viz.

$$\rho\,\dot{e} = \boldsymbol{\sigma} : \mathbf{d} + \rho\, r - \operatorname{div} \boldsymbol{q}. \tag{4.32}$$

Here, $\dot{e}$ denotes the rate of the specific energy, r represents an internal heat source and $\boldsymbol{q}$ is the heat flux. The product $\boldsymbol{\sigma} : \mathbf{d}$ denotes the stress power per unit volume in the current configuration.
The second principle of thermodynamics - *the entropy inequality* - postulates the irreversibility of entropy production

$$\rho\,\dot{s} + \operatorname{div}\left(\frac{\boldsymbol{q}}{T}\right) - \rho\,\frac{r}{T} \geq 0, \tag{4.33}$$

where $\dot{s}$ denotes the rate of the specific entropy and T is the total temperature. By means of Eq. (4.32) and with the introduction of the Free Helmholtz energy

$$\psi = e - T\,s, \tag{4.34}$$

Eq. (4.33) results in the Clausius-Duhem inequality

$$\boldsymbol{\sigma} : \mathbf{d} - \rho\,(\dot{\psi} + s\,\dot{T}) - \frac{1}{T}\,\boldsymbol{q} \cdot \operatorname{grad} T \geq 0. \tag{4.35}$$

Further, neglecting thermal dissipation and assuming an isothermal process, Eq. (4.35) together with Eq. (4.22) finally simplifies to the dissipation inequality

$$\mathfrak{D}^{\mathrm{p}} = \boldsymbol{\tau} : \mathbf{d} - \rho_o\,\dot{\psi} \geq 0. \tag{4.36}$$

4.3.4 State and internal variables

By means of the internal variable approach in thermodynamics, cf. e.g. [46, 119], dissipative mechanisms are described by a set of internal state variables

$$\boldsymbol{h} = \{h_i\}. \tag{4.37}$$

The entities h_i correspond to scalar or tensorial quantities associated with dissipation. In general, a thermodynamic potential ψ depends on the following set of state variables

$$\psi = \psi(\mathbf{F}, T, \operatorname{grad} T, \boldsymbol{h}) \quad \text{or} \quad \widehat{\psi} = \widehat{\psi}(\mathbf{C}, T, \operatorname{Grad} T, \boldsymbol{h}). \tag{4.38}$$

In the context of this thesis, it is sufficient to assume the thermodynamic process as adiabatic and isothermal, i.e. $\dot{T} = 0$ and $\operatorname{grad} T = \mathbf{0}$. Hence, the thermodynamic state is completely defined by the knowledge of the deformation state and the internal variables,

i.e.

$$\psi = \psi(\mathbf{F},\boldsymbol{h}) \quad \text{or} \quad \widehat{\psi} = \widehat{\psi}(\mathbf{C},\boldsymbol{h}). \tag{4.39}$$

4.4 Elastoplastic constitutive model

Constitutive equations have to fulfil several general thermodynamic axioms. For instance, the *axiom of determinism* states that the current material response at a point is determined by the history of deformation and temperature. Also worth mentioning is the *axiom of objectivity*, which states that the material response is independent of the observing position, i.e. the constitutive equations must be invariant to a rigid body motion with superimposed rotation of the current configuration. Details on these and other axioms of thermodynamics can be found e.g. in [172, 181, 182].
The constitutive model presented in this section is the one described in [159, Chap. 9].

4.4.1 Free energy and elastic stress response

The free energy function is assumed to locally depend on the elastic deformation. Additionally assuming uncoupled hardening mechanisms, leads to the functional form

$$\rho_o\, \psi(\mathbf{F}_\mathrm{e},\boldsymbol{h}) := W(\mathbf{C}_\mathrm{e}) + \phi(\boldsymbol{h}), \tag{4.40}$$

with the elastic strain energy $W(\mathbf{C}_\mathrm{e})$ and the plastic hardening potential $\phi(\boldsymbol{h})$. Forming the time derivative of Eq. (4.40)

$$\dot{\psi} = \frac{\partial \psi}{\partial \mathbf{C}_\mathrm{e}} : \dot{\mathbf{C}}_\mathrm{e} + \frac{\partial \phi}{\partial \boldsymbol{h}}\, \dot{\boldsymbol{h}} \tag{4.41}$$

and using the rate of the elastic right Cauchy-Green tensor

$$\dot{\mathbf{C}}_\mathrm{e} = 2\,\mathbf{F}_\mathrm{e}^\mathsf{T}\, \mathbf{d}_\mathrm{e}\, \mathbf{F}_\mathrm{e}, \tag{4.42}$$

which can be obtained by means of Eq. (4.11) and Eq. (4.19), the dissipation inequality reads

$$\mathfrak{D}^\mathrm{p} = \left(\boldsymbol{\tau} - 2\,\mathbf{F}_\mathrm{e}\, \frac{\partial W}{\partial \mathbf{C}_\mathrm{e}}\, \mathbf{F}_\mathrm{e}^\mathsf{T} \right) : \mathbf{d}_\mathrm{e} + \boldsymbol{\tau} : \mathbf{d}_\mathrm{p} + \frac{\partial \phi}{\partial \boldsymbol{h}}\, \dot{\boldsymbol{h}} \geq 0. \tag{4.43}$$

Using standard arguments from thermodynamics, i.e. assuming that elastic deformations do not produce dissipation, this leads to the constitutive function for the Kirchhoff stress tensor

$$\boldsymbol{\tau} = 2\,\mathbf{F}_\mathrm{e}\, \frac{\partial W}{\partial \mathbf{C}_\mathrm{e}}\, \mathbf{F}_\mathrm{e}^\mathsf{T}. \tag{4.44}$$

The elastic strain energy is further split into uncoupled volumetric and isochoric contributions

$$W = U(J_e) + \widetilde{W}(\widetilde{\mathbf{C}}_\mathsf{e}), \tag{4.45}$$

with

$$U(J_\mathsf{e}) = \frac{1}{2}\,K\,\left[\frac{1}{2}\,(J_\mathsf{e}^2 - 1) - \ln J_\mathsf{e}\right], \quad \widetilde{W}(\widetilde{\mathbf{C}}_\mathsf{e}) = \frac{1}{2}\,G\,\left[\operatorname{tr}\widetilde{\mathbf{C}}_\mathsf{e} - 3\right], \tag{4.46}$$

which directly yields the volumetric and deviatoric stress contributions

$$p = J_\mathsf{e}\,U'(J_\mathsf{e}) \quad \text{and} \quad \boldsymbol{\tau}_{\mathrm{dev}} = 2\,\operatorname{dev}\left[\widetilde{\mathbf{F}}_\mathsf{e}\,\frac{\partial\widetilde{W}}{\partial\widetilde{\mathbf{C}}_\mathsf{e}}\,\widetilde{\mathbf{F}}_\mathsf{e}^{\mathsf{T}}\right] = G\,\operatorname{dev}\widetilde{\mathbf{b}}_\mathsf{e}. \tag{4.47}$$

Here, K and G denote the compression and shear moduli, respectively, and $\widetilde{\mathbf{b}}_\mathsf{e}$ is the elastic isochoric left Cauchy-Green tensor. The uncoupled strain energy function can be found e.g. in [162, 164] and can be interpreted as an extension of the Neo-Hookean model in the compressible range. It has the advantage of poly-convexity and is suitable for large deformations and strains, cf. [162].

4.4.2 Yielding and hardening

Onset of plastic yielding is described by the classical Mises-Huber yielding criterion

$$f(\boldsymbol{\tau}_{\mathrm{dev}},\alpha) = ||\,\boldsymbol{\tau}_{\mathrm{dev}}\,|| - \sqrt{\frac{2}{3}}\,k(\alpha) \leq 0, \tag{4.48}$$

with the internal isotropic hardening variable α, which describes a uniform diameter extension of the von Mises yield cylinder in principal stress space. As it only depends on the Kirchhoff stress deviator $\boldsymbol{\tau}_{\mathrm{dev}}$, it is independent on the hydrostatic stress. The non-linear function

$$k(\alpha) = \sigma_0 + \sigma_\infty\,[1 - \exp(-d\,\alpha)] + H\,\alpha \tag{4.49}$$

describes isotropic hardening during plastic flow. The material parameters σ_0 and σ_∞ denote the initial and limit yield stress, respectively. H is the linear hardening modulus and d is a dimensionless parameter.
As a result of the maximum dissipation principle

$$\max\ \mathfrak{D}^{\mathrm{p}} = \boldsymbol{\tau} : \mathbf{d}_\mathsf{p} + \frac{\partial\phi}{\partial\alpha}\,\dot{\alpha}, \tag{4.50}$$

the plastic potential is chosen as the yield function Eq. (4.48) ($\phi = f$), which together with Eq. (4.40) leads to the associative flow rule in the current configuration

$$\mathcal{L}_v \widetilde{\mathbf{b}}_e = -\frac{2}{3}\gamma \operatorname{tr}\widetilde{\mathbf{b}}_e \mathbf{n}. \tag{4.51}$$

By means of Eq. (4.17), the flow rule can be pulled-back to the reference configuration

$$\frac{\mathrm{d}}{\mathrm{d}t}\widetilde{\mathbf{C}}_p^{-1} = -\frac{2}{3}\gamma \operatorname{tr}\mathbf{b}_e \mathbf{F}^{-1}\mathbf{n}\mathbf{F}^{-\mathsf{T}} =: \dot{\mathbf{c}}_p, \tag{4.52}$$

where $\mathbf{n}$ denotes the flow direction

$$\mathbf{n} = \frac{\boldsymbol{\tau}_{\mathrm{dev}}}{||\boldsymbol{\tau}_{\mathrm{dev}}||}. \tag{4.53}$$

The solution is defined by the Kuhn-Tucker loading/unloading and consistency conditions

$$\gamma \geq 0, \quad f(\boldsymbol{\tau},\alpha) \leq 0, \quad \gamma f(\boldsymbol{\tau},\alpha) = 0 \quad \text{and} \quad \gamma \dot{f}(\boldsymbol{\tau},\alpha) = 0. \tag{4.54}$$

Here, γ denotes the consistency parameter, often called plastic multiplier. The isotropic hardening law describes the evolution of the isotropic hardening variable α

$$\dot{\alpha} = \sqrt{\frac{2}{3}}\gamma. \tag{4.55}$$

Note that in Eq. (4.52) the tensor $\mathbf{c}_p$ is introduced as an abbreviation for the isochoric tensor $\widetilde{\mathbf{C}}_p^{-1}$ for notational convenience.

4.5 Numerical treatment

Following, the continuum constitutive equations are embedded into a computational framework. First, the implicit time integration scheme is introduced in order to solve the rate equations. See e.g. [74] or [142] for more information about numerical solution methods of initial boundary value problems. Subsequently, the classical stress return mapping procedure is sketched. Finally, the continuum equations are spatially discretized using finite elements.

4.5.1 Time integration

The deformation process is assumed quasi-static, i.e. considering time but neglecting inertial effects. Therefore, a discrete pseudo time interval $I_t = [t_0,...,t_N]$ is introduced in order to solve the evolution of the rate equations Eq. (4.52) and Eq. (4.55). An implicit backward Euler time integration scheme is used, in which the actual values at time t_{n+1} are computed from the values of the prior discrete time step t_n, with $n = 0,...,N$. This

results in the discrete evolution equations

$$\widetilde{\mathbf{b}}_{\mathsf{e},n+1} = \widetilde{\mathbf{b}}_{\mathsf{e},n} - \frac{2}{3}\,\Delta\gamma\,\mathrm{tr}\,(\widetilde{\mathbf{b}}_{\mathsf{e},n+1})\,\mathbf{n}_{n+1} \tag{4.56}$$

$$\mathbf{c}_{\mathsf{p},n+1} = \mathbf{c}_{\mathsf{p},n} - \frac{2}{3}\,\Delta\gamma\,\mathrm{tr}\,(\widetilde{\mathbf{b}}_{\mathsf{e},n+1})\,\mathbf{F}_{n+1}^{-1}\,\mathbf{n}_{n+1}\,\mathbf{F}_{n+1}^{-\mathsf{T}} \tag{4.57}$$

and

$$\alpha_{n+1} = \alpha_n + \sqrt{\frac{2}{3}}\Delta\gamma, \tag{4.58}$$

where $\Delta\gamma$ denotes the increment of the plastic multiplier. Within this time integration scheme, the stress state at the end of each time step has to satisfy the discrete version of the Kuhn-Tucker conditions

$$\Delta\gamma \geq 0, \quad f(\boldsymbol{\tau}_{n+1},\alpha_{n+1}) \leq 0, \quad \Delta\gamma\, f(\boldsymbol{\tau}_{n+1},\alpha_{n+1}) = 0. \tag{4.59}$$

Remark 4.1 (Notation) For notational convenience, in the following, quantities evaluated in the prior time step receive the subscript n, whereas the index $n+1$ is omitted for actual values in the actual time step, that is, e.g. $\mathbf{c}_\mathsf{p} := \mathbf{c}_{\mathsf{p},n+1}$ and $\alpha := \alpha_{n+1}$.

4.5.2 Stress return

The local stress response is computed within a two step algorithm called return-mapping-algorithm. First, the deformation state is assumed to be solely elastic and the so-called elastic trial state is computed within the elastic predictor step

$$\alpha^{\mathsf{tr}} = \alpha_n, \tag{4.60}$$

$$\mathbf{c}_\mathsf{p}^{\mathsf{tr}} = \mathbf{c}_{\mathsf{p},n}, \tag{4.61}$$

$$\widetilde{\mathbf{b}}_\mathsf{e}^{\mathsf{tr}} = J^{-\frac{2}{3}}\,\mathbf{F}\,\mathbf{c}_\mathsf{p}^{\mathsf{tr}}\,\mathbf{F}^{\mathsf{T}}, \tag{4.62}$$

$$\boldsymbol{\tau}_{\mathrm{dev}}^{\mathsf{tr}} = G\,\mathrm{dev}\,\widetilde{\mathbf{b}}_\mathsf{e}^{\mathsf{tr}}. \tag{4.63}$$

It is obvious that not only the total deformation gradient $\mathbf{F}$ but also the quantities $\mathbf{c}_{\mathsf{p},n}$ and α_n from the prior pseudo time step have to be known to be able to compute the trial state. Therefore, a history field $\boldsymbol{h} := \{\mathbf{c}_\mathsf{p},\alpha\}$ is introduced, in which the values of $\mathbf{c}_\mathsf{p}$ and α are saved at the end of a converged pseudo time step. The values are initialized with $\mathbf{c}_{\mathsf{p},o} = \mathbf{I}$ and $\alpha_o = 0$ at time t_o, that is, assuming an unplasticized initial configuration.
In view of the Kuhn-Tucker complementary conditions, cf. Eq. (4.59), two cases have to be considered.

Elastic loading/unloading If the yielding condition is fulfilled, i.e. whenever

$$f(\boldsymbol{\tau}^{\mathrm{tr}}_{\mathrm{dev}},\alpha^{\mathrm{tr}}) = ||\,\boldsymbol{\tau}^{\mathrm{tr}}_{\mathrm{dev}}\,|| - \sqrt{\frac{2}{3}}\,k(\alpha^{\mathrm{tr}}) \leq 0, \tag{4.64}$$

with $\Delta\gamma = 0$, the stress state satisfies the Kuhn-Tucker conditions. Then, Eqs. (4.60) - (4.63) are valid and represent the solution point. In this case, no evolution of the history variables appears.

Plastic loading Contrary, if the trial state violates the yielding condition

$$f(\boldsymbol{\tau}^{\mathrm{tr}}_{\mathrm{dev}},\alpha^{\mathrm{tr}}) = ||\,\boldsymbol{\tau}^{\mathrm{tr}}_{\mathrm{dev}}\,|| - \sqrt{\frac{2}{3}}\,k(\alpha^{\mathrm{tr}}) > 0, \tag{4.65}$$

from the discrete Kuhn-Tucker conditions it is obvious that the trial state can not be the solution. Consequently, the history variables evolve following the discrete evolution equations Eq. (4.57) and Eq. (4.58), which implies that $\Delta\gamma > 0$.

Radial return As in the case of plastic loading the increment of the plastic multiplier is non-zero, it directly follows from Eq. (4.59) that

$$f(\boldsymbol{\tau},\alpha) = 0. \tag{4.66}$$

It can be shown that due to the isotropic J_2 theory

$$\mathrm{tr}\,\widetilde{\mathbf{b}}_{\mathrm{e}} = \mathrm{tr}\,\widetilde{\mathbf{b}}^{\mathrm{tr}}_{\mathrm{e}} \quad \text{and} \quad \mathbf{n} = \mathbf{n}^{\mathrm{tr}}, \tag{4.67}$$

which leads to the consistency equation

$$\widehat{f}(\Delta\gamma) := ||\,\boldsymbol{\tau}^{\mathrm{tr}}_{\mathrm{dev}}\,|| - \sqrt{\frac{2}{3}}\,k(\alpha_n + \sqrt{\tfrac{2}{3}}\,\Delta\gamma) - 2\,\overline{\mu}\Delta\gamma = 0, \tag{4.68}$$

where the abbreviation

$$\overline{\mu} = \frac{1}{3}\,G\,\mathrm{tr}\,\widetilde{\mathbf{b}}^{\mathrm{tr}}_{\mathrm{e}} \tag{4.69}$$

has been used, see e.g. [159] for details. Due to the non-linear hardening function, cf. Eq. (4.49), Eq. (4.68) has to be solved for $\Delta\gamma$ within a local Newton-Raphson scheme. The specific update formula reads

$$\Delta\gamma^{(i+1)} = \Delta\gamma^{(i)} - \frac{\widehat{f}(\Delta\gamma^{(i)})}{\widehat{f}'(\Delta\gamma^{(i)})} \tag{4.70}$$

with the explicit derivatives of Eq. (4.68) and Eq. (4.49), respectively

$$\widehat{f}'(\Delta\gamma^{(i)}) = -2\,\overline{\mu} - \frac{2}{3}\,k'(\Delta\gamma^{(i)}) \tag{4.71}$$

$$k'(\Delta\gamma^{(i)}) = d\,\exp\left(-d\,(\alpha_n + \sqrt{\tfrac{2}{3}}\,\Delta\gamma^{(i)})\right)\,\sigma_\infty + H. \tag{4.72}$$

The solution algorithm for the plastic multiplier is given in Alg. 4.4 in pseudo code format. With the increment of the plastic multiplier at hand, the update of the deviatoric stress tensor can be determined

$$\boldsymbol{\tau}_{\mathrm{dev}} = \boldsymbol{\tau}^{\mathsf{tr}}_{\mathrm{dev}} - 2\,\overline{\mu}\,\Delta\gamma\,\mathbf{n}, \quad \mathbf{n} = \frac{\boldsymbol{\tau}^{\mathsf{tr}}_{\mathrm{dev}}}{||\,\boldsymbol{\tau}^{\mathsf{tr}}_{\mathrm{dev}}\,||}, \tag{4.73}$$

Due to the assumption of incompressible plastic flow ($J = J_{\mathsf{e}}$), the hydrostatic pressure can easily be computed to

$$p = p^{\mathsf{tr}} = J\,U'(J) = \frac{1}{2}\,K\,\left(J^2 - 1\right) \tag{4.74}$$

and the total Kirchhoff stress tensor reads

$$\boldsymbol{\tau} = p\,\mathbf{I} + \boldsymbol{\tau}_{\mathrm{dev}}\,. \tag{4.75}$$

Consequently, the first Piola-Kirchhoff stress tensor is given by

$$\mathbf{P}^{\mathsf{K}} = p\,\mathbf{F}^{-\mathsf{T}} + \boldsymbol{\tau}_{\mathrm{dev}}\,\mathbf{F}^{-\mathsf{T}}. \tag{4.76}$$

4.5.3 Weak form and linearization

The non-linear weak form of equilibrium is obtained by taking the weak derivative of the momentum balance Eq. (4.29) obtained by multiplication with a test function $\boldsymbol{v} \in \mathcal{V}$, integrating over the volume and utilizing the divergence theorem in connection with partial integration, which leads to the residual equation regarding the reference configuration

$$\begin{aligned} R(\boldsymbol{u},\boldsymbol{h}_n;\boldsymbol{v}) &= \int_{\mathcal{K}} \mathbf{P}^{\mathsf{K}}(\boldsymbol{u},\boldsymbol{h}_n) : \mathrm{Grad}\,\boldsymbol{v}\,\mathrm{d}V - \lambda\left[\int_{\mathcal{K}} \boldsymbol{b}_0 \cdot \boldsymbol{v}\,\mathrm{d}V + \int_{\partial\mathcal{K}} \boldsymbol{t}_0 \cdot \boldsymbol{v}\,\mathrm{d}\boldsymbol{A}\right] \\ &= R^{\mathsf{int}}(\boldsymbol{u},\boldsymbol{h}_n;\boldsymbol{v}) - \lambda\,R^{\mathsf{ext}}(\boldsymbol{v}) = 0, \end{aligned} \tag{4.77}$$

where $\mathrm{Grad}\,\boldsymbol{v}$ is the gradient of the test function and R^{int} and R^{ext} denote the internal and external part. The parameter λ is introduced as a scaling parameter to represent different load levels at different pseudo time steps witin the implicit time integration scheme. As the primary unknown displacements and the test function are chosen from the same function space, i.e. $\boldsymbol{u},\boldsymbol{v} \in \mathcal{V}$, this procedure is known as the *Bubnov-Galerkin method*. The functional dependencies in Eq. (4.77) indicate that the external forces are assumed deformation and history independent, i.e. $\delta_u \boldsymbol{b}_0 = \delta_u \boldsymbol{t}_0 = \mathbf{0}$. The solution of the nonlinear equilibrium equation is obtained utilizing Newton's method. Therefore, Eq. (4.77) has to

be linearized in direction of the displacement increments $\Delta\boldsymbol{u} \in \mathcal{V}$, viz.

$$R^{\mathsf{int}}(\boldsymbol{u},\boldsymbol{h}_n;\boldsymbol{v}) + \delta_u R^{\mathsf{int}}(\boldsymbol{u},\boldsymbol{h}_n;\boldsymbol{v},\Delta\boldsymbol{u}) = \lambda\, R^{\mathsf{ext}}(\boldsymbol{v}). \tag{4.78}$$

The partial variation of the internal residual is called *tangent stiffness operator* and for a fixed set $\{\widehat{\boldsymbol{u}},\widehat{\boldsymbol{h}}_n\}$ constitutes a bilinear form $k : \mathcal{V} \times \mathcal{V} \to \mathbb{R}$

$$k(\boldsymbol{u},\boldsymbol{h}_n;\boldsymbol{v},\Delta\boldsymbol{u}) = \delta_u R^{\mathsf{int}} = \int_{\mathcal{K}} \delta_u \mathbf{P}^{\mathsf{K}}(\boldsymbol{u},\boldsymbol{h}_n;\Delta\boldsymbol{u}) : \mathrm{Grad}\,\boldsymbol{v}\,\mathrm{d}V. \tag{4.79}$$

With the variation of the first Piola-Kirchhoff stress tensor and the deformation gradient

$$\delta_u \mathbf{P}^{\mathsf{K}}(\boldsymbol{u},\boldsymbol{h}_n;\Delta\boldsymbol{u}) = \frac{\partial \mathbf{P}^{\mathsf{K}}}{\partial \mathbf{F}} : \delta_u \mathbf{F} = \mathbb{A}(\boldsymbol{u},\boldsymbol{h}_n) : \delta_u \mathbf{F}(\Delta\boldsymbol{u}) = \mathbb{A}(\boldsymbol{u},\boldsymbol{h}_n) : \mathrm{Grad}\,\Delta\boldsymbol{u}, \tag{4.80}$$

where the fourth order tensor $\mathbb{A}$ denotes the elastoplastic tangent operator consistent with the algorithm to compute the first Piola-Kirchhoff stress tensor, cf. Eq. (4.76), the tangent stiffness operator can finally be written as

$$k(\boldsymbol{u},\boldsymbol{h}_n;\boldsymbol{v},\Delta\boldsymbol{u}) = \int_{\mathcal{K}} \mathrm{Grad}\,\boldsymbol{v}^{\mathsf{T}} : \mathbb{A}(\boldsymbol{u},\boldsymbol{h}_n) : \mathrm{Grad}\,\Delta\boldsymbol{u}\,\mathrm{d}V. \tag{4.81}$$

Consistent tangent operator

The linearization of the first Piola-Kirchhoff stress tensor $\mathbf{P}^{\mathsf{K}}$ w.r.t. the displacements has to be consistent with the stress return algorithm described earlier. Thus, the implicit update formulae for the volumetric and deviatoric contribution represent the starting point of the derivation, which is performed in App. A.1 in detail. The explicit form of the tangent can be expressed in compact form as

$$\mathbb{A} := \frac{\partial \mathbf{P}^{\mathsf{K}}}{\partial \mathbf{F}} = \left[K\, J^2\, \mathbf{F}^{-\mathsf{T}} \otimes \mathbf{F}^{-\mathsf{T}} - \boldsymbol{\tau}\, \left(\mathbf{F}^{-\mathsf{T}} \otimes \mathbf{F}^{-\mathsf{T}}\right)^{\overset{24}{\mathsf{T}}} + (\mathbb{S} : \mathbb{B}_F) \overset{21}{*} \mathbf{F}^{-\mathsf{T}} \right], \tag{4.82}$$

where the fourth order tensor $\mathbb{S}$ is given by

$$\mathbb{S} := G \left[\beta_0\, \mathbb{I}_{\mathrm{dev}} - \frac{2}{3}\, \Delta\gamma\, \beta_1\, \mathbf{n} \otimes \mathbf{I} + \beta_2\, \mathbf{n} \otimes \mathbf{n} \right], \tag{4.83}$$

with the factors

$$\beta_0 = 1 - 2\,\Delta\gamma\, \frac{\overline{\mu}}{\| \boldsymbol{\tau}^{\mathsf{tr}}_{\mathrm{dev}} \|}, \quad \beta_1 = 1 + 2\,\frac{\overline{\mu}}{f'}, \quad \beta_2 = \beta_1 - \beta_0 \tag{4.84}$$

and the identities

$$\mathbb{B}_F := \left[\mathbb{F} \overset{21}{*} (\mathbf{c}_{\mathsf{p},n}\, \widetilde{\mathbf{F}}^{\mathsf{T}}) + \widetilde{\mathbf{F}}\, \mathbf{c}_{\mathsf{p},n}\, \mathbb{F}^{\overset{12}{\mathsf{T}}} \right], \quad \mathbb{F} := J^{-\frac{1}{3}} \left[(\mathbf{I} \otimes \mathbf{I})^{\overset{23}{\mathsf{T}}} - \frac{1}{3}\, \mathbf{F} \otimes \mathbf{F}^{-\mathsf{T}} \right]. \tag{4.85}$$

Elastoplastic stress projection algorithm

Input: $\{\boldsymbol{m}, \mathbf{F}, \boldsymbol{h}_n\}$

// Elastic predictor

▷ Compute elastic trial stress

1: $J = \det \mathbf{F},\ \widetilde{\mathbf{F}} = J^{-\frac{1}{3}}\,\mathbf{F},\ \widetilde{\mathbf{b}}_{\mathsf{e}}^{\mathsf{tr}} = \widetilde{\mathbf{F}}\,\mathbf{c}_{\mathsf{p},n}\,\widetilde{\mathbf{F}}^{\mathsf{T}},\ \boldsymbol{\tau}_{\mathrm{dev}}^{\mathsf{tr}} = G\,\mathrm{dev}\,\widetilde{\mathbf{b}}_{\mathsf{e}}^{\mathsf{tr}},$

2: $\overline{\mu} = \frac{1}{3}\,G\,\mathrm{tr}\,\widetilde{\mathbf{b}}_{\mathsf{e}}^{\mathsf{tr}},\ \mathbf{n} = \dfrac{\boldsymbol{\tau}_{\mathrm{dev}}^{\mathsf{tr}}}{||\,\boldsymbol{\tau}_{\mathrm{dev}}^{\mathsf{tr}}\,||}$

▷ Check for plastic loading

3: **if** $f^{\mathsf{tr}} = ||\,\boldsymbol{\tau}_{\mathrm{dev}}^{\mathsf{tr}}\,|| - \sqrt{\dfrac{2}{3}}\,k(\alpha_n) \leq 0$ **then**

▷ Elastic state → update $(\cdot) = (\cdot)^{\mathsf{tr}}$

4: **else**

// Stress return mapping (plastic corrector)

▷ Compute $\Delta\gamma$ by solving Eq. (4.68), see Fig. 4.4

5: $\{\Delta\gamma\} \leftarrow$ LocalNewton(α_n,$\boldsymbol{m}$,$\overline{\mu}$)

▷ Update elastoplastic state

6: $\boldsymbol{\tau}_{\mathrm{dev}} = \boldsymbol{\tau}_{\mathrm{dev}}^{\mathsf{tr}} - 2\,\overline{\mu}\,\Delta\gamma\,\mathbf{n}, \qquad \alpha = \alpha_n + \sqrt{\dfrac{2}{3}}\,\Delta\gamma,$

$\widetilde{\mathbf{b}}_{\mathsf{e}} = G^{-1}\,(\boldsymbol{\tau}_{\mathrm{dev}} + \overline{\mu}\,\mathbf{I}), \qquad \mathbf{c}_{\mathsf{p}} = \widetilde{\mathbf{F}}^{-1}\,\widetilde{\mathbf{b}}_{\mathsf{e}}\,\widetilde{\mathbf{F}}^{-\mathsf{T}}$

▷ Update history variables

7: $\boldsymbol{h} = \{\mathbf{c}_{\mathsf{p}}, \alpha\}$

8: **end if**

// Stress response and tangent operator

▷ Stress update

9: $p = \dfrac{K}{2}\,(J^2 - 1),\ \mathbf{P}^{\mathsf{K}} = p\,\mathbf{F}^{-1} + \boldsymbol{\tau}_{\mathrm{dev}}\,\mathbf{F}^{-\mathsf{T}}$

▷ Compute consistent tangent

10: $\mathbb{F} = J^{-\frac{1}{3}}\left[(\mathbf{I}\otimes\mathbf{I})^{\overset{23}{\mathsf{T}}} - \frac{1}{3}\,\mathbf{F}\otimes\mathbf{F}^{-\mathsf{T}}\right],\ \mathbb{B}_F = \left[\mathbb{F}\ \overset{21}{*}\ (\mathbf{c}_{\mathsf{p},n}\,\widetilde{\mathbf{F}}^{\mathsf{T}}) + \widetilde{\mathbf{F}}\,\mathbf{c}_{\mathsf{p},n}\,\mathbb{F}^{\overset{12}{\mathsf{T}}}\right]$

11: $\beta_0 = 1 - 2\,\Delta\gamma\,\dfrac{\overline{\mu}}{||\,\boldsymbol{\tau}_{\mathrm{dev}}^{\mathsf{tr}}\,||},\ \beta_1 = 1 + 2\,\dfrac{\overline{\mu}}{f'},\ \beta_2 = \beta_1 - \beta_0$

12: $\mathbb{S} = G\left[\beta_0\,\mathbb{I}_{\mathrm{dev}} - \dfrac{2}{3}\,\Delta\gamma\,\beta_1\,\mathbf{n}\otimes\mathbf{I} + \beta_2\,\mathbf{n}\otimes\mathbf{n}\right]$

13: $\mathbb{A} = \left[K\,J^2\,\mathbf{F}^{-\mathsf{T}}\otimes\mathbf{F}^{-\mathsf{T}} - \boldsymbol{\tau}\,\left(\mathbf{F}^{-\mathsf{T}}\otimes\mathbf{F}^{-\mathsf{T}}\right)^{\overset{24}{\mathsf{T}}} + (\mathbb{S} : \mathbb{B}_F)\ \overset{21}{*}\ \mathbf{F}^{-\mathsf{T}}\right]$

Figure 4.3: Elastoplastic stress projection algorithm.

Local Newton-Raphson procedure

Input: $\{\alpha_n, \boldsymbol{m}, \overline{\mu}\}$

// Initialize values

▷ Load constitutive parameters

$\{\sigma_0, \sigma_\infty, d, H\} \leftarrow \boldsymbol{m}$

▷ Set start value

$i = 0,\ \Delta\gamma^{(0)} = 0$

// Start iteration loop

while $f(\Delta\gamma^{(i)}) > 0$

$$k(\Delta\gamma^{(i)}) = \sigma_0 + \sigma_\infty \left[1 - \exp\left(-d\,(\alpha_n + \sqrt{\tfrac{2}{3}}\,\Delta\gamma^{(i)})\right)\right] + H\,(\alpha_n + \sqrt{\tfrac{2}{3}}\,\Delta\gamma^{(i)})$$

$$f(\Delta\gamma^{(i)}) = \| \boldsymbol{\tau}^{\mathsf{tr}}_{\mathrm{dev}} \| - \sqrt{\frac{2}{3}}\, k(\Delta\gamma^{(i)}) - 2\,\overline{\mu}\,\Delta\gamma^{(i)}$$

$$k'(\Delta\gamma^{(i)}) = d\,\exp\left(-d\,(\alpha_n + \sqrt{\tfrac{2}{3}}\,\Delta\gamma^{(i)})\right)\,\sigma_\infty + H$$

$$f'(\Delta\gamma^{(i)}) = -2\,\overline{\mu} - \frac{2}{3}\,k'(\Delta\gamma^{(i)})$$

$$\Delta\gamma^{(i+1)} = \Delta\gamma^{(i)} - \frac{f(\Delta\gamma^{(i)})}{f'(\Delta\gamma^{(i)})}$$

$$i = i + 1$$

end while

Figure 4.4: Local Newton-Raphson procedure.

The entire computational procedure is summarized in Fig. 4.3 in pseudo code format. The complete derivation of the algorithmic tangent can be found in App. A.1.

4.5.4 Finite element equations

The spatial continuum equations are discretized by means of isoparametric finite elements. Note that for notational convenience, in the following approximations only linear arguments are given. Recalling the definitions mentioned in Sec. 2.1.2 and utilizing standard relations from the finite element method, sketched in App. B.1, the discrete element matrix forms of the weak equilibrium and the tangent stiffness operator are approximated by, respectively,

$$\begin{aligned} R^h(\boldsymbol{v}^h) &= \bigcup_e \boldsymbol{v}_e^T \left(\int_{\Omega_e} \boldsymbol{G}^T\, \boldsymbol{P}^K \,\mathrm{d}V - \lambda \left[\int_{\Omega_e} \boldsymbol{N}^T\, \boldsymbol{b}_0 \,\mathrm{d}V + \int_{\partial\Omega_e} \boldsymbol{N}^T\, \boldsymbol{t}_0 \,\mathrm{d}\boldsymbol{A} \right] \right) \\ &= \bigcup_e \boldsymbol{v}_e^T\, (\boldsymbol{R}_e^{\mathsf{int}} - \lambda\, \boldsymbol{R}_e^{\mathsf{ext}}) = \bigcup_e \boldsymbol{v}_e^T\, \boldsymbol{R}_e = \boldsymbol{v}^T\, \boldsymbol{R} \end{aligned} \tag{4.86}$$

and

$$\begin{aligned} k^h(\boldsymbol{v}^h,\Delta\boldsymbol{u}^h) &= \bigcup_e \boldsymbol{v}_e^T \int_{\Omega_e} \boldsymbol{G}^T \boldsymbol{A}\boldsymbol{G}\,\mathrm{d}V\,\Delta\boldsymbol{u}_e \\ &= \bigcup_e \boldsymbol{v}_e^{\mathsf{T}}\,\boldsymbol{K}_e\,\Delta\boldsymbol{u}_e = \boldsymbol{v}^T\,\boldsymbol{K}\,\Delta\boldsymbol{u}. \end{aligned} \tag{4.87}$$

The resulting linear equation system that has to be solved within each Newton iteration reads

$$R^h(\boldsymbol{v}^h) + k(\boldsymbol{v}^h,\Delta\boldsymbol{u}^h) = \boldsymbol{v}^T\,(\boldsymbol{R} + \boldsymbol{K}\,\Delta\boldsymbol{u}) = 0, \tag{4.88}$$

which, excluding the trivial solution ($\boldsymbol{v} = \boldsymbol{0}$), implies

$$\boldsymbol{K}\,\Delta\boldsymbol{u} = -\boldsymbol{R} = -(\boldsymbol{R}^{\mathsf{int}} + \lambda\,\boldsymbol{R}^{\mathsf{ext}}). \tag{4.89}$$

Here, the scaling factor λ represents different load levels within the implicit time integration procedure. To ensure positive definiteness of the tangent stiffness matrix $\boldsymbol{K}$, the applied Dirichlet boundary conditions have to be incorporated by partitioning the equation system as follows

$$\begin{bmatrix} \boldsymbol{K}_{aa} & \boldsymbol{K}_{ab} \\ \boldsymbol{K}_{ba} & \boldsymbol{K}_{bb} \end{bmatrix} \begin{bmatrix} \Delta\boldsymbol{u}_a \\ \Delta\boldsymbol{u}_b \end{bmatrix} = - \begin{bmatrix} \boldsymbol{R}_a \\ \boldsymbol{R}_b \end{bmatrix}. \tag{4.90}$$

Here, the indices a and b correspond to the unknown and prescribed degrees of freedom, respectively. The reduced tangent stiffness matrix $\boldsymbol{K}_{aa}$ is positive definite and the linearized equation system can be solved for the unknown displacement increment within each Newton iteration

$$\Delta\boldsymbol{u}_a = -\boldsymbol{K}_{aa}^{-1}\,(\boldsymbol{R}_a + \boldsymbol{K}_{ab}\,\Delta\boldsymbol{u}_b). \tag{4.91}$$

4.6 Volumetric locking and advanced finite elements

It is commonly known that within the solution procedure of the finite element method, volumetric locking effects occur in the case of incompressible material behavior, especially using low order displacement elements. As in the described J_2 flow theory, plastic yielding is assumed to be incompressible, it is convenient to use advanced finite elements that prevent those locking effects and are therefore more efficient as reasonable results are obtained with comparatively coarser meshes. There are many approaches to overcome different locking effects in finite elements. Often, these are based on multi-field functionals like e.g. the *Hellinger-Reissner* or *Hu-Washizu* functionals. A good overview of different element technologies can be found, e.g. in [93]. Most approaches to prevent volumetric locking have in common that the volumetric part of the deformation is somehow under-integrated resulting in constant volumetric stress response throughout an element, if linear shape functions are used.

4.6.1 Method of modified deformation gradient

Within this thesis, the so-called $\overline{\mathbf{F}}$ method is used because of its simple implementation and efficiency. An additional advantage is that the approach is independent on the choice of the constitutive model. The formulation presented is oriented towards [49, 172] that share the basic ideas with [54, 55].
The main idea is to evaluate the volumetric contribution of the deformation gradient at the element centroid, which leads to the modified deformation gradient $\overline{\mathbf{F}}$

$$\overline{\mathbf{F}} = \left(\frac{J_0}{J}\right)^{\frac{1}{3}} \mathbf{F}. \tag{4.92}$$

Here, $J_0 = \det \mathbf{F}_0$ denotes the determinant of the deformation gradient evaluated at the element centroid and thus is constant throughout the element. Evaluating all constitutive equations presented in this chapter for $\mathbf{F} = \overline{\mathbf{F}}$, that is, $\mathbf{P}^{\mathsf{K}}(\overline{\mathbf{F}})$, $\boldsymbol{h}(\overline{\mathbf{F}})$ prevents volumetric locking in the stress response of the finite element. Consequently, the consistent tangent in Eq. (4.82) has to be evaluated at $\mathbf{F} = \overline{\mathbf{F}}$. Consistent linearization leads to the necessity to compute the derivatives of $\overline{\mathbf{F}}$ w.r.t. $\mathbf{F}$ and $\mathbf{F}_0$, which are straight forward and read

$$\begin{aligned} \delta\overline{\mathbf{F}} =& \frac{\partial \overline{\mathbf{F}}}{\partial \mathbf{F}} : \delta\mathbf{F} + \frac{\partial \overline{\mathbf{F}}}{\partial \mathbf{F}_0} : \delta\mathbf{F}_0 = \left[3\ (\mathbf{I}\otimes\mathbf{I})^{\overset{23}{\mathsf{T}}} - \mathbf{F}\otimes\mathbf{F}^{-\mathsf{T}}\right] : \delta\mathbf{F} + \left[\mathbf{F}\otimes\mathbf{F}_0^{-\mathsf{T}}\right] : \delta\mathbf{F}_0 \\ =& \mathbb{D} : \delta\mathbf{F} + \mathbb{D}_0 : \delta\mathbf{F}_0. \end{aligned} \tag{4.93}$$

Following the convention in Chap. 2 for general unsymmetric matrix representations of fourth order tensors, the modified gradient operator for the $\overline{F}$ element can be written as

$$\overline{\boldsymbol{G}}_i = \boldsymbol{D}\,\boldsymbol{G}_i + \boldsymbol{D}_0\,\boldsymbol{G}_{0,i}, \tag{4.94}$$

for each integration point i. Consequently, the element contributions of the residual inner force vector and the stiffness matrix are given by

$$\boldsymbol{R}_e = \int_{\Omega_e} \boldsymbol{G}^{\mathsf{T}}\,\overline{\boldsymbol{P}}^{\mathsf{K}}\,\mathrm{d}V \quad \text{and} \quad \boldsymbol{K}_e = \int_{\Omega_e} \boldsymbol{G}^{\mathsf{T}}\,\overline{\boldsymbol{A}}\,\overline{\boldsymbol{G}}\,\mathrm{d}V, \tag{4.95}$$

where the overlining of $\overline{\boldsymbol{P}}^{\mathsf{K}}$ and $\overline{\boldsymbol{A}}$ indicate that these quantities are evaluated for the modified tensor $\overline{\mathbf{F}}$ rather than $\mathbf{F}$.

4.6.2 Verifications

To verify the accuracy of the model implementation and the corresponding novelly derived tangent operator, two prevalent examples from literature are chosen. First, the Cook's membrane problem is analyzed in plane strain conditions. Secondly, the necking of a circular bar in 3D is simulated. The material properties used for both model problems are summarized in Tab. 4.1.

Table 4.1: Material properties for finite deformation plasticity.

K	G	σ_0	σ_∞	d	H
164.21 GPa	80.193 8 GPa	450 MPa	715 MPa	16.93	129.24 MPa

Plane strain Cook's membrane

A tapered panel is clamped on the left and subjected to a shearing load on the right end. This plane strain problem constitutes a standard test for bending dominated structural response. The load $F = 5\,\text{kN}$ is applied within 10 linear steps and equally distributed on the right edge nodes. Fig. 4.5(a) shows the initial mesh consisting of 144 $\overline{F}$-elements and the corresponding boundary conditions. The deformed structure is plotted in Fig. 4.5(b), where also the volumetric stress distribution is pictured. No volumetric locking effect is noticeable. Neither the stress distribution shows localizations, nor the top displacement is underestimated. For comparison, in Fig. 4.6(a) the results using linear displacement elements are displayed. Obviously, the structural deformation is underestimated, which can be explained by examining the volumetric stress distribution. At the upper left corner the volumetric stress localizes due to the over stiff volumetric response. Fig. 4.6(b) displays the top displacement monitored over increasing mesh sizes, starting from 2×2 and ending with 128×128, for the pure displacement formulation and the $\overline{F}$-formulation. It can clearly be seen that the $\overline{F}$-formulation shows better results than the displacement element for coarse meshes, although both formulations seem to converge to the same solution.
Reviewing the relevant literature, cf. e.g. [67, 141, 158, 172], the computed simulation results concur with the results documented in literature. See also [54, 55] for simulations within an isogeometric framework.

Necking of cylindrical bar

A full 3D analysis of the necking of a cylindrical bar is conducted. This example is well documented in literature and constitutes one of the most common benchmarks for finite strain plasticity, see e.g. [152, 159, 163, 165, 172]. The bar has a length of 53.334 mm and a radius of 6.413 mm. To trigger the necking, a geometric imperfection in form of a small linear tapering of 0.982 % of the radius in the centre of the bar is provided. Due to symmetry, only one octant of the bar is modelled. The mesh consisting of 960 $\overline{F}$ elements and the corresponding symmetric boundary conditions are pictured in Fig. 4.7(a). In this simulation a top displacement of 7 mm is applied within 2 main steps, each consisting of 10 substeps. Firstly, a top displacement of 5.6 mm is applied within 10 linear steps, secondly the top displacement is increased to 7 mm also within 10 linear steps. The deformed structure as well as the von Mises stress response and the plastic strain distribution are illustrated in Fig. 4.7(b). The necking behavior can clearly be observed. In the load-displacement diagram, cf. Fig. 4.8(a), the beginning of the phenomenon appears in form of a decreasing reaction force at about 3 mm top displacement. The normalized central radius is plotted against the top displacements in Fig. 4.8(b), which emphasizes this and clearly shows the necking effect. In contrast, using pure displacement finite elements, the necking phenomenon can not be captured adequately.

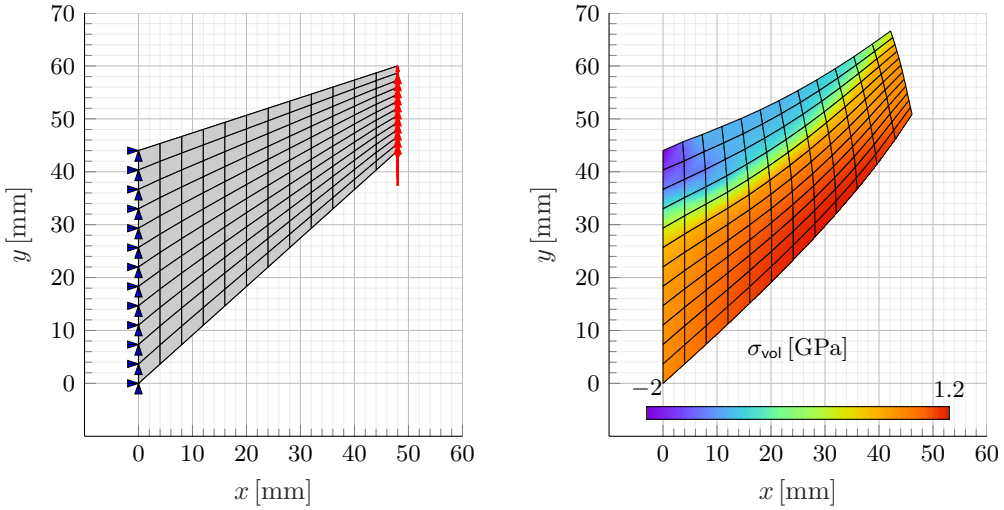

Figure 4.5: Cook's membrane example: (a) initial mesh 12×12, (b) deformed configuration and volumetric stress distribution ($\overline{F}$ formulation.)

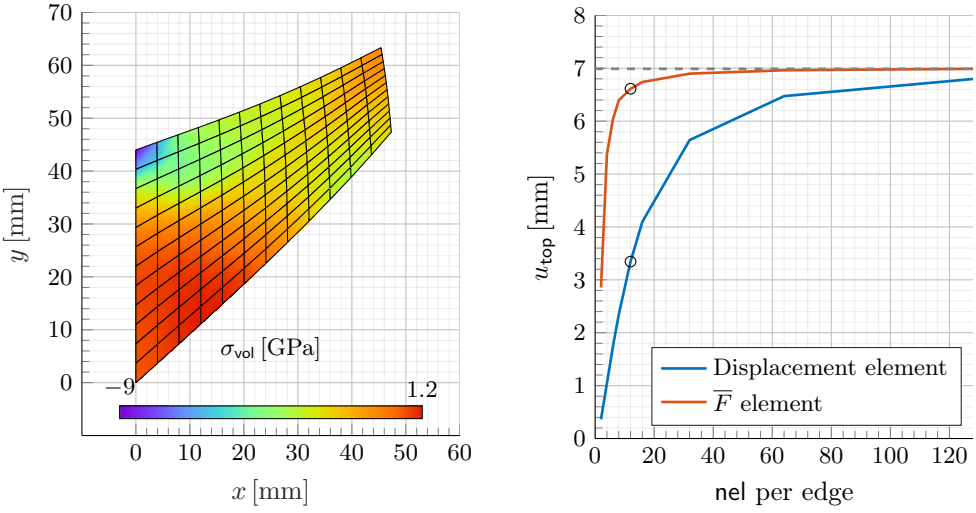

Figure 4.6: Cook's membrane example: (a) deformed configuration and volumetric stress distribution (std. displacement formulation), (b) top displacement for different mesh sizes.

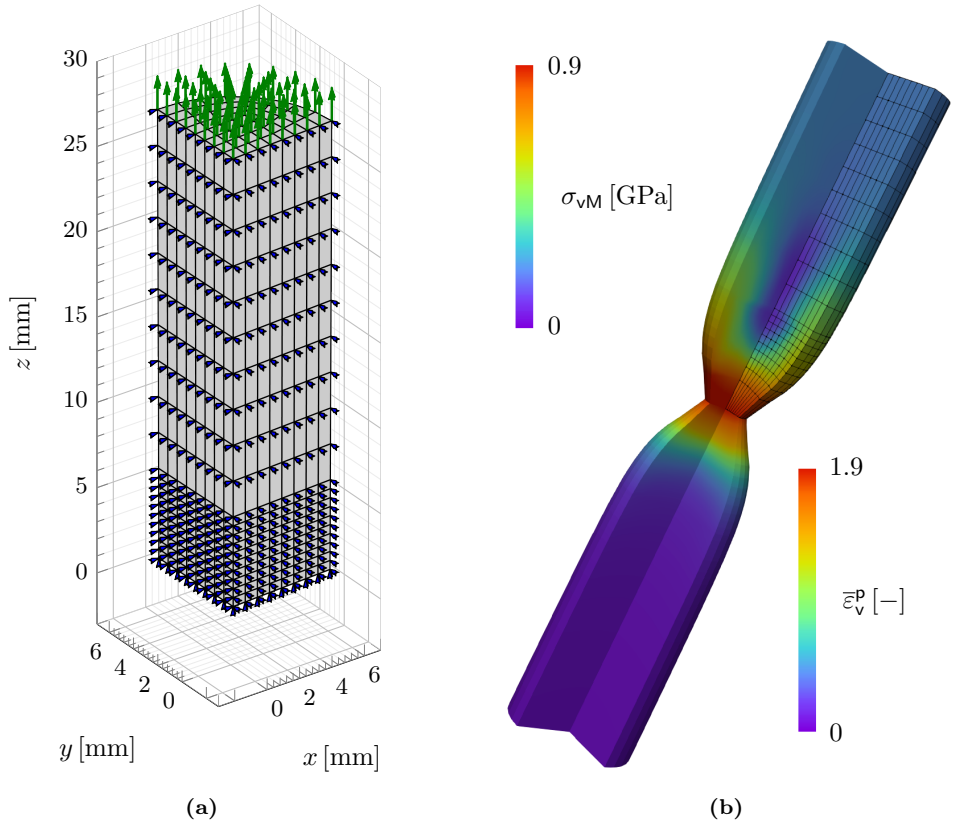

Figure 4.7: Necking of cylindrical bar example: (a) initial mesh and symm. boundary conditions, (b) final deformation, von Mises stress (top) and equiv. plast. strain (bottom).

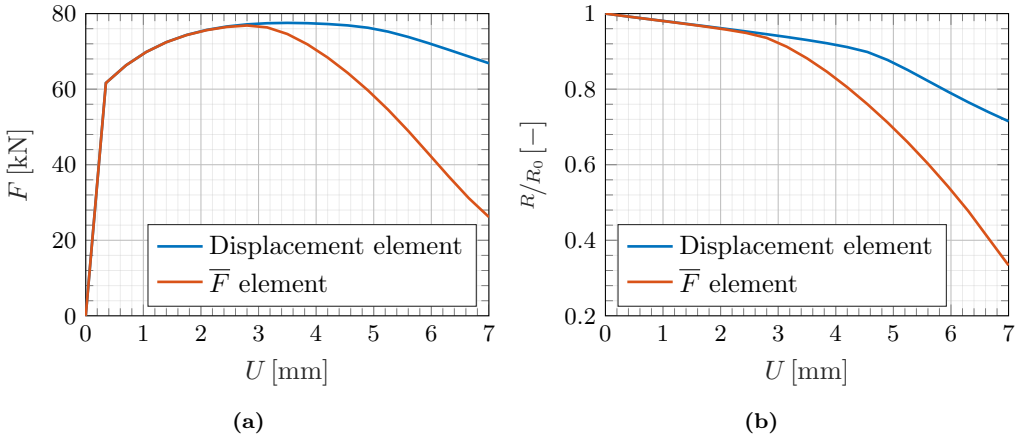

Figure 4.8: Necking of cylindrical bar example: (a) load vs. displacements, (b) normalized central radius vs. displacements.

4.7 Summary

This chapter provides a compact summary of the general continuum mechanical framework needed for the solution of the elastoplastic structural mechanical problem. Beginning with the introduction of kinematics that is based on a multiplicative decomposition of elastic and plastic contributions of the deformation gradient, $\mathbf{F} = \mathbf{F}_e \mathbf{F}_p$, the governing balance equations and fundamental thermodynamic laws are sketched. The most important characteristics of the chosen elastoplastic constitutive model are depicted and the solution method, i.e. the implicit stress return-mapping-algorithm, for the resulting initial value problem is described. Consistent linearization of the first Piola-Kirchoff stress tensor is stated. Note that a complete derivation is given in App. A.1. Although the presented model does not contain genuine novelties, it is worth mentioning that the formulation in this work slightly differs from the original, cf. [159], where the authors indicate the formulation regarding the reference configuration, which has been done in this work. Formulations of the model regarding the reference configuration have already been presented in [103, 104] and also [81]. After standard finite element discretization of the global model equations, the method of $\overline{F}$, used to prevent volumetric locking in connection with low order finite elements and the incompressible J_2 flow theory, is briefly described and all necessary linearizations are given. Finally, two well documented benchmark problems verify the accuracy of the model. The plane strain Cook's membrane problem represents a standard test for bending dominated structural response. The second example, the necking of a cylindrical bar problem, is one of the most common benchmark problems in 3D finite strain plasticity. The simulations of both examples provide reasonable results compared with results in literature.

Chapter 5

Variational Design Sensitivities

The most challenging and main task of this research is the sensitivity analysis of the elastoplastic material model introduced in Chap. 4. This includes the analytical derivations presented in this chapter, as well as the numerical implementation, discussed in the subsequent Chap. 6. The variational approach described in the following is based on an enhanced viewpoint of kinematics. Briefly, a third configuration is added that parametrizes the design of the reference configuration in a continuum mechanical framework. All structural and physical sensitivities are derived consistent with the computational algorithm. Special focus lies on the deformation history captured by the internal history variables as their variations have to be considered for all total design variations.

Contents

5.1 Introduction

Utilizing gradient based methods for the solution of a structural optimization problem, it is necessary to determine the gradient of the objective and constraint functions. In fact, these gradients answer the question how the considered function values change by variations of model inputs that include the geometrical shape, topology or thermodynamic properties of the underlying structural analysis problem. Obviously, the more complex the model description becomes, the more input variables exist, of which not all are desired to change. Thus, usually a selection is defined and called *design variables*. The entirety of all design variables then parametrize the *design* of the considered problem.
The determination procedure of the mentioned gradients w.r.t. the defined design variables is called *design sensitivity analysis* (DSA). Different approaches have come up in the past decades, cf. e.g. [12, 14, 32, 43, 77, 89, 125, 138, 171, 180, 201]. It is important to distinguish between *local* and *global* approaches, cf. e.g. [32]. While local DSA approaches in a mathematical sense focus on the sensitivity of a design around a certain point of interest, global approaches are to analyze uncertainties of model inputs and their effect on the outputs. Clearly, local methods are used in the case of deterministic models, whereas global methods are needed in a probabilistic setting. The authors in [147] complain that the term sensitivity analysis is often misused in literature, as it is frequently used although no analysis in a mathematical sense has been performed. Further, local methods - for instance *one at a time* (OAT) methods - are utilized for obtaining sensitivities of probabilistic models, where a global method should be consulted.
Global methods are not part of discussion in this work. Reviewing Chap. 4, it is obvious that the class of tackled structural analysis problems is all through deterministic. For more details about global sensitivity analysis methods, see e.g. [32, 83, 147] and references therein.
Focussing on local DSA methods, further distinctions have to be processed. Methods can either be analytical, numerical or semi-analytical. All of these classes can further be split into continuum and discrete formulations. While continuum approaches take the continuum equations of the underlying structural analysis problem as basis, discrete approaches build up on already discretized equations. A prominent example of a numerical DSA method is the *finite differences method* (FDM), in which continuous derivatives, i.e. differential quotients, are replaced by difference quotients. This method is somewhat simple and constitutes an OAT method, as the gradient w.r.t. each design variable is computed individually, while fixing all the others. Depending on the model complexity and the effective number of design variables, the FDM can become computationally expensive.

In this thesis, attention is drawn to a continuous, analytical approach utilizing variational calculus. Based on an advanced viewpoint of kinematics formulated in [13, 18], sensitivity formulations can naturally be embedded into the continuum mechanical framework. The kinematic viewpoint is gained by taking one step back from the usual observation frame of a thermodynamic process in a space-time continuum. This step offers a new dimension of the event horizon leading to a *design-space-time continuum* illustrated in Fig. 5.1. Here, two observation frames, i.e. thermodynamic space-time-continua, are illustrated at two different designs. In each observation frame ($\mathfrak{F}_0 = \mathfrak{F}(s_0)$ and $\mathfrak{F}_s = \mathfrak{F}(s)$) the usual continuum mechanical framework as described in Chap. 4 holds. Thus, the deformation

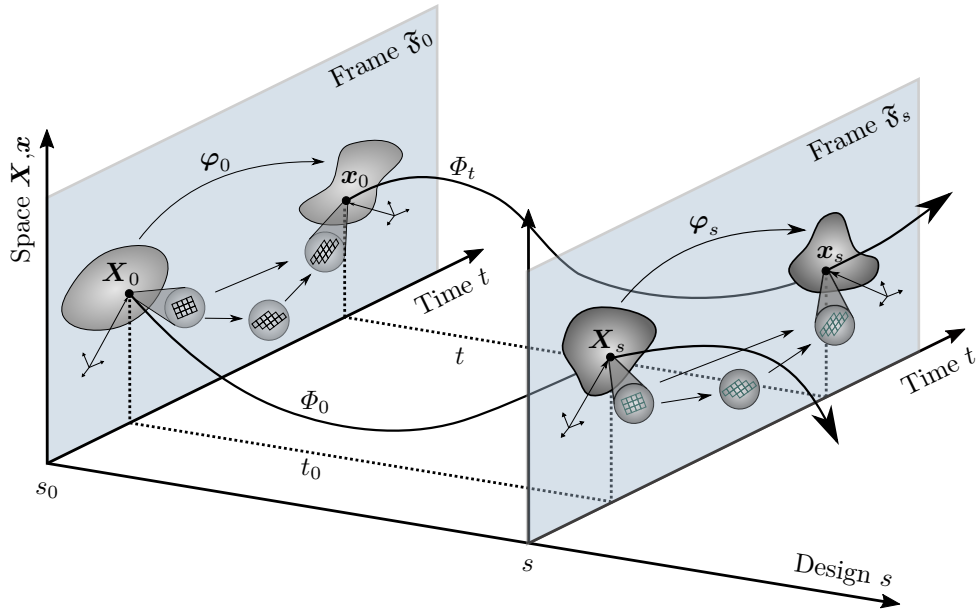

Figure 5.1: Design-space-time continuum. Rework of original illustration in [18, p. 21].

mappings $\boldsymbol{\varphi}_0 = \boldsymbol{\varphi}(s_0,t)$ and $\boldsymbol{\varphi}_s = \boldsymbol{\varphi}(s,t)$ describe the motion of the material points from the reference to the current position of the respective design. The two design trajectories describe continuous design changes at a fixed time, i.e. $\Phi_0 = \Phi(s,t_0)$ and $\Phi_t = \Phi(s,t)$. Understanding the configurations of a material body as a differentiable manifold, enables the possibility to introduce a design independent local configuration, see [12, 13, 16, 18] for details. Herewith, it is possible to separate geometrical and physical quantities so as to avoid the occurrence of implicit dependencies while performing analytical derivations. In the original work, this kinematic concept is called *local-convective*. In the following, it will be termed *enhanced kinematics*.

The presented variational approach has been successfully applied in different fields of computational solid mechanics. For instance in [87] the approach is applied in the context of multi-scale problems, or in [63] in the context of buckling of hyperelastic shells. The article [14] gives an excellent overview on the approach in the context of linear and nonlinear elasticity, see also [116]. Dynamic problems have been tackled in e.g. [124]. In [175] variational sensitivities are derived in the context of the theory of porous media. Isotropic damage is tackled in [19] and growth phenomena are discussed in [17].

Elastoplastic design sensitivities are addressed in the pioneering contributions [20, 185, 186, 187] that constitute the basis of the approach presented in this thesis, although it differs in the choice of the mechanical material model and in computational details. Clearly, the work at hand shares the basic concepts, i.e. the variational approach based on the enhanced kinematic viewpoint and the treatment of internal variables and their variations, with the mentioned preparatory works. However, in this work a more modern constitutive model that includes non-linear isotropic hardening is considered. As it is not based on a logarithmic strain measure, no complicated isotropic tensor functions like

the tensor logarithm, or the tensor exponential function appears, which avoids expensive spectral decompositions for linearizations. Moreover, sensitivities are not only derived w.r.t. geometric design variables, but also w.r.t. constitutive parameters. This widens the field of applications and structural design. General continuous derivations of physical design variations are given and computational details will be addressed in the subsequent Chap. 6.
The proposed approach is distinct from other variational techniques but shares ideas and therefore can be linked to prominent methods such as the *Material Derivative Approach* - also called *speed method* -, cf. e.g. [201] and the *Domain Parametrization Approach*, cf. e.g. [138]. Numerous investigations address theoretical and computational details that are linked to pioneering contributions such as [125]. More information about design sensitivity analysis and different methods can be found e.g. in [43, 77, 89, 171, 202] and references therein. Important aspects and equations of the variational method at hand have already been published by the author, cf. [100, 101, 102, 103, 104], and are derived here in more detail.
Recalling Fig. 5.1 and considering the structural analysis problem in each frame to be path dependent - as in the present case of elastoplasticity -, the sensitivity analysis has to follow that path, too. Thus, in each time step, the gradient of the desired functions that are somehow described by the design trajectories has to be computed. Note that within a structural optimization problem the design of a material body describes its topology, shape and thermodynamic properties, which is indicated in Fig. 5.1 by the different shape and microstructure colours.

5.2 Design parametrization

Structural design is a quite far reaching term. In the context of structural optimization it often stands for the geometrical layout of a structure, i.e. size, topology or shape. Within this work, two different kinds of design layout are presented. These are the geometrical shape and the constitutive parameters of the underlying mechanical model. The topology of all analyzed structures is assumed to remain unchanged. Topology optimization is therefore not tackled within this thesis.
In the following, the different design parametrizations used in this work are explained. Note that it is even possible to choose all design parametrizations simultaneously, which results in an equation system with different kinds of unknowns. However, the issues arising are that the design variables and gradients might have to be scaled due to numerical difficulties computing very large and very small values. Additionally, the optimization problem should be well stated to be able to identify a unique optimum. This will be further discussed in Chap. 6.

5.2.1 Geometry

Within a continuum mechanical framework, geometric shape sensitivities can be obtained variationally by choosing the referential coordinates $\boldsymbol{X}$ as design variables. Geometric design variations are therefore denoted by $\delta\boldsymbol{X}$. As any physical response of the mechanical system depends on its geometry, implicit dependencies arise and the total variations of the

quantities of interest are demanded. Due to the enhanced kinematic viewpoint explained in Sec. 5.3, elegant formulations can be found that avoid these implicit dependencies.

Remark 5.1 (Geometry, mesh and CAGD) In context of the finite element method, geometric sensitivities can be determined regarding the nodal coordinates of the finite element mesh. If nodal coordinates are the chosen design variables, updating the mesh within the structural optimization procedure might cause non-smooth boundaries. Additionally, based on the refinement of the finite element mesh, the number of design variables might be huge. Therefore, for efficient computations, it is convenient to parametrize the FE mesh, e.g. by means of CAGD, where the control points of the curves, surfaces and volumes can be chosen as design variables. On element level, geometric shape sensitivities are still computed regarding the nodal coordinates but can be easily mapped to the CAGD control points by means of the so called design velocity field, which in fact represents the partial derivative of the FE mesh coordinates w.r.t. the control point coordinates and thus describes the change of the mesh coordinates by variations of the control point coordinates. These topics will be part of discussion in Chap. 6.

5.2.2 Constitutive properties

By choosing the constitutive parameters as design variables, sensitivities of quantities of interest w.r.t. material properties can be obtained. These parameters are defined by the underlying mechanical material model. For the present model, the elastic material behavior is described via the bulk and shear moduli K and G. In the plastic regime, the material behavior is described by four additional parameters, namely the initial yield stress σ_0, the limit yield stress σ_∞, the linear hardening modulus H and a dimensionless parameter d. All these plastic constitutive parameters control the exponential hardening curve $k(\alpha)$, cf. Eq. (4.49). Thus, it is convenient to introduce the constitutive design vector $\boldsymbol{m}$ and its variation $\delta\boldsymbol{m}$ of the form

$$\boldsymbol{m} = \begin{bmatrix} K & G & k \end{bmatrix} \quad \text{and} \quad \delta\boldsymbol{m} = \begin{bmatrix} \delta K & \delta G & \delta k \end{bmatrix}. \tag{5.1}$$

Remark 5.2 (Notation) In the following, variations and derivatives w.r.t. general design parameters are indicated by the vector $\delta\boldsymbol{s}$. Depending on the choice of design parametrization, at the respective passages the design vector is replaced by the specific chosen design vector, i.e.

$$\delta\boldsymbol{s} := \delta\boldsymbol{X} \text{ (geometry)} \quad \text{or} \quad \delta\boldsymbol{s} := \delta\boldsymbol{m} \text{ (const. parameters)}. \tag{5.2}$$

With the choice of design parametrization, functional dependencies change, which is mentioned separately at the relevant points.

5.3 Enhanced kinematics

In the context of structural optimization, the material body is not considered with a fixed reference configuration. Thus, it is convenient to work with an enhanced kinematic concept. Therefore, in the lower part of Fig. 4.1 another configuration is added. This configuration

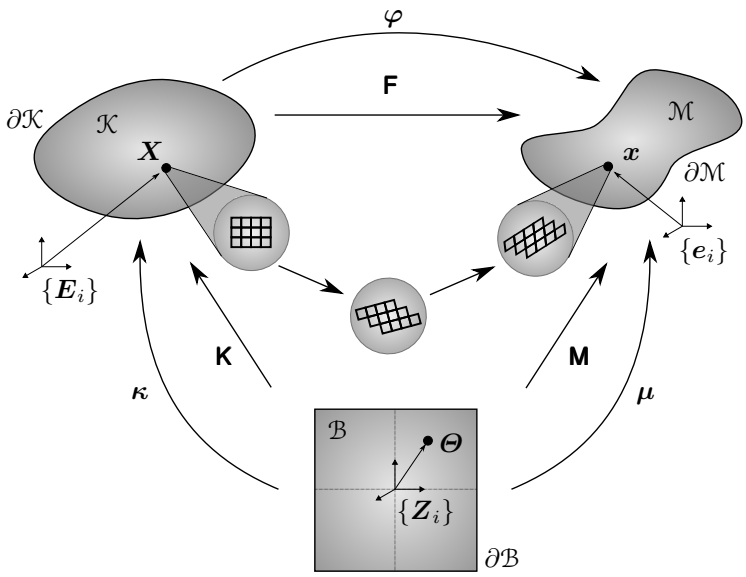

Figure 5.2: Enhanced kinematics.

parametrizes the reference configuration in terms of arbitrary design parameters s_i and represents a fixed parameter space $\mathcal{B}$ with Cartesian basis $\{\boldsymbol{Z}_i\}$ and local coordinates $\boldsymbol{\Theta}$. This improved viewpoint on the material body is motivated by arguments from differential geometry and goes back to the works [18, 26, 135]. By means of the parameter space, it is possible to rigorously separate physical and geometrical quantities. Consequently, the classical deformation mapping in Eq. (4.1) can be decomposed into two independent mappings, i.e. the design dependent geometry mapping $\boldsymbol{\kappa}(\boldsymbol{\Theta},s)$ and the time dependent motion mapping $\boldsymbol{\mu}(\boldsymbol{\Theta},t)$

$$\boldsymbol{\kappa} : (\boldsymbol{\Theta},s) \mapsto \boldsymbol{X}(\boldsymbol{\Theta},s) \text{ and } \boldsymbol{\mu} : (\boldsymbol{\Theta},t) \mapsto \boldsymbol{x}(\boldsymbol{\Theta},t). \tag{5.3}$$

With the corresponding tangent mappings

$$\mathbf{K} = \operatorname{GRAD} \boldsymbol{\kappa} = \frac{\partial X_i}{\partial \Theta_j}\, \boldsymbol{E}_i \otimes \boldsymbol{Z}_j \text{ and } \mathbf{M} = \operatorname{GRAD} \boldsymbol{\mu} = \frac{\partial x_i}{\partial \Theta_j}\, \boldsymbol{e}_i \otimes \boldsymbol{Z}_j, \tag{5.4}$$

not only the deformation mapping but also the deformation gradient can be decomposed and written as

$$\boldsymbol{\varphi} = \boldsymbol{\mu} \circ \boldsymbol{\kappa}^{-1} \text{ and } \mathbf{F} = \mathbf{M}\mathbf{K}^{-1} = \frac{\partial \boldsymbol{x}}{\partial \boldsymbol{\Theta}} \left(\frac{\partial \boldsymbol{X}}{\partial \boldsymbol{\Theta}} \right)^{-1} = \frac{\partial x_i}{\partial \Theta_k} \left(\frac{\partial X_j}{\partial \Theta_k} \right)^{-1} \boldsymbol{e}_i \otimes \boldsymbol{E}_j. \tag{5.5}$$

Mappings of infinitesimal line elements are therefore defined as

$$\mathrm{d}\boldsymbol{x} = \mathbf{F}\, \mathrm{d}\boldsymbol{X} = \mathbf{M}\mathbf{K}^{-1}\, \mathrm{d}\boldsymbol{X} = \mathbf{M}\, \mathrm{d}\boldsymbol{\Theta} \tag{5.6}$$

and infinitesimal area elements can be transformed using the relations

$$\mathrm{d}\boldsymbol{a} = J\,\mathbf{F}^{-\mathsf{T}}\,\mathrm{d}\boldsymbol{A} = J\,J_{\mathsf{K}}\,\mathbf{F}^{-\mathsf{T}}\,\mathbf{K}^{-\mathsf{T}}\,\mathrm{d}\boldsymbol{A}_{\Theta} = J_{\mathsf{M}}\,\mathbf{M}^{-\mathsf{T}}\,\mathrm{d}\boldsymbol{A}_{\Theta}. \tag{5.7}$$

Consequently, volumes can be mapped using the determinants of the tangent mappings

$$\mathrm{d}v = J\,\mathrm{d}V = J\,J_{\mathsf{K}}\,\mathrm{d}V_{\Theta} = J_{\mathsf{M}}\,\mathrm{d}V_{\Theta}, \tag{5.8}$$

with

$$J = \det\mathbf{F}, \quad J_{\mathsf{K}} = \det\mathbf{K}, \quad J_{\mathsf{M}} = \det\mathbf{M}. \tag{5.9}$$

Remark 5.3 (Local intermediate configuration and parameter space) Note that in general it is possible to define a mapping between the parameter space and the plastic intermediate configuration, presuming that the tensors $\mathbf{F}_{\mathsf{e}}$ and $\mathbf{F}_{\mathsf{p}}$ are uniquely defined. As within the computational procedure explained in Chap. 4, all essential quantities are either defined in the reference or the current configuration, there is no need to define such a mapping and is therefore neglected within this thesis.

5.4 Elastoplastic response sensitivity

Usually, the objective function and often also constraint functions depend on the mechanical response of the investigated structure. Thus, the elastoplastic response sensitivities are desired. It can be obtained utilizing variational principles at continuous level.

5.4.1 Weak equilibrium requirement

The solution of Eq. (4.77) represents a global equilibrium point $(\widehat{\boldsymbol{s}},\boldsymbol{u}^*,\boldsymbol{h}^*)$ for a fixed design $\widehat{\boldsymbol{s}}$. At such a point, response sensitivities are obtained variationally at continuous level, i.e. continuous in space, as the computational algorithm has to be consistent with the time discretization used to solve the mechanical behavior in structural analysis. As Eq. (4.77) has to hold for any design change $\delta\boldsymbol{s}$, its total variation has to vanish, cf. [18, 102, 185], which yields

$$\delta R = \delta_u R + \delta_s R + \delta_{h_n} R = k(\boldsymbol{v},\delta\boldsymbol{u}) + p(\boldsymbol{v},\delta\boldsymbol{s}) + h(\boldsymbol{v},\delta\boldsymbol{h}_n) = 0, \tag{5.10}$$

where the bilinear form $k : \mathcal{V}\times\mathcal{V}\to\mathbb{R}$ is the tangent stiffness operator already known from structural analysis. The tangent pseudoload operator $p : \mathcal{V}\times\mathcal{S}\to\mathbb{R}$ represents the partial variation of the weak equilibrium w.r.t. design and also is a bilinear form. The third bilinear form $h : \mathcal{V}\times\mathcal{G}\to\mathbb{R}$ corresponds to the deformation history represented by the internal variables that has to be captured and considered for all total variations, cf. [100, 101, 102, 103, 104, 185], and is called history sensitivity operator. Note that the operators introduced above are generally semi-bilinear. However, as the sensitivities are derived in a solution point of a fixed design, they become bilinear forms.
In the following, the general equations for the mentioned tangent operators are given and

explicit formulas considering the constitutive model described in Chap. 4 are presented. At some points, a distinction of the choice of design variable type has to be made.

5.4.2 Tangent pseudoload

The tangent pseudoload operator represents the partial variation of the global weak equilibrium w.r.t. to the chosen design parametrization. Independent on the choice of design variables, the general form of this partial variation regarding the parameter space $\mathcal{B}$ reads

$$\begin{aligned}\delta_s R = &\int_{\partial\mathcal{B}} \delta_s \mathbf{P}^{\mathsf{K}} : \operatorname{Grad} \boldsymbol{v}\, J_{\mathsf{K}}\, \mathrm{d}V_\Theta \\ &+ \int_{\partial\mathcal{B}} \mathbf{P}^{\mathsf{K}} : \delta_s \operatorname{Grad} \boldsymbol{v}\, J_{\mathsf{K}}\, \mathrm{d}V_\Theta \\ &+ \int_{\partial\mathcal{B}} \mathbf{P}^{\mathsf{K}} : \operatorname{Grad} \boldsymbol{v}\, \delta_s J_{\mathsf{K}}\, \mathrm{d}V_\Theta.\end{aligned} \tag{5.11}$$

The arising functional dependencies differ with the choice of design variables. In the following the specific pseudoload operators regarding the three mentioned design parametrizations are derived.

Geometric shape design. Geometric shape sensitivities are derived by choosing the vector of referential coordinates as design vector $\boldsymbol{s} := \boldsymbol{X}$. The three partial variations of Eq. (5.11) depend on the geometric shape, which leads to

$$\begin{aligned}\delta_X R = &\int_{\partial\mathcal{B}} \delta_X \mathbf{P}^{\mathsf{K}} : \operatorname{Grad} \boldsymbol{v}\, J_{\mathsf{K}}\, \mathrm{d}V_\Theta \\ &+ \int_{\partial\mathcal{B}} \mathbf{P}^{\mathsf{K}} : \delta_X \operatorname{Grad} \boldsymbol{v}\, J_{\mathsf{K}}\, \mathrm{d}V_\Theta \\ &+ \int_{\partial\mathcal{B}} \mathbf{P}^{\mathsf{K}} : \operatorname{Grad} \boldsymbol{v}\, \delta_X J_{\mathsf{K}}\, \mathrm{d}V_\Theta.\end{aligned} \tag{5.12}$$

The partial variation of the gradient of the test function can easily be identified to

$$\delta_X \operatorname{Grad} \boldsymbol{v} = -\operatorname{Grad} \boldsymbol{v}\, \operatorname{Grad} \delta\boldsymbol{X}, \tag{5.13}$$

cf. e.g. [18, 116], where also the partial variation of the determinant of the geometry gradient is derived to

$$\delta_X J_{\mathsf{K}} = J_{\mathsf{K}}\, \operatorname{Div} \delta\boldsymbol{X}. \tag{5.14}$$

The partial variation of the first Piola-Kirchhoff stress tensor w.r.t. geometric shape design is already partially known from structural analysis. Recalling Eq. (4.80), the

consistent tangent operator, which is derived in the appendix, cf. A.1, represents the partial derivative of the first Piola-Kirchhoff stress tensor w.r.t. the deformation gradient $\mathbf{F}$. Thus, the partial variation w.r.t. the geometric coordinates can simply be written as

$$\delta_X \mathbf{P}^{\mathsf{K}} = \frac{\partial \mathbf{P}^{\mathsf{K}}}{\partial \mathbf{F}} : \delta_X \mathbf{F} = \mathbb{A} : \delta_X \mathbf{F}, \tag{5.15}$$

where

$$\delta_X \mathbf{F} = -\operatorname{Grad} \boldsymbol{u} \operatorname{Grad} \delta \boldsymbol{X}, \tag{5.16}$$

which can be easily derived by means of the enhanced kinematic viewpoint, cf. e.g. [18, 87, 116]. Finally, the pseudoload operator for geometric shape design reads

$$\begin{aligned} \delta_X R = &- \int_{\partial \mathcal{K}} [\mathbb{A} : (\operatorname{Grad} \boldsymbol{u} \operatorname{Grad} \delta \boldsymbol{X})] : \operatorname{Grad} \boldsymbol{v} \, \mathrm{d}V \\ &- \int_{\partial \mathcal{K}} \mathbf{P}^{\mathsf{K}} : \operatorname{Grad} \boldsymbol{v} \operatorname{Grad} \delta \boldsymbol{X} \, \mathrm{d}V \\ &+ \int_{\partial \mathcal{K}} \mathbf{P}^{\mathsf{K}} : \operatorname{Grad} \boldsymbol{v} \operatorname{Div} \delta \boldsymbol{X} \, \mathrm{d}V, \end{aligned} \tag{5.17}$$

where the identity $\mathrm{d}V = J_{\mathsf{K}} \, \mathrm{d}V_\Theta$ has been used to express the term regarding the reference configuration $\mathcal{K}$.

Constitutive design. For the sensitivity regarding material parameters, the design vector is chosen as the vector containing the material parameters $\boldsymbol{s} := \boldsymbol{m}$. In this case, only the stress tensor depends on the chosen design parametrization, thus

$$\delta_m R = \int_{\mathcal{K}} \delta_m \mathbf{P}^{\mathsf{K}} \operatorname{Grad} \boldsymbol{v}^{\mathsf{T}} \, \mathrm{d}V \quad \text{and} \quad \delta_m \operatorname{Grad} \boldsymbol{v} = \mathbf{0}, \quad \delta_m J_{\mathsf{K}} = 0. \tag{5.18}$$

The partial variation of the first Piola-Kirchhoff stress tensor w.r.t. the constitutive parameters can be expressed as

$$\begin{aligned} \delta_m \mathbf{P}^{\mathsf{K}} &= \frac{\partial \mathbf{P}^{\mathsf{K}}}{\partial \boldsymbol{m}} \, \delta \boldsymbol{m} = \frac{\partial \mathbf{P}^{\mathsf{K}}}{\partial K} \, \delta K + \frac{\partial \mathbf{P}^{\mathsf{K}}}{\partial G} \, \delta G + \frac{\partial \mathbf{P}^{\mathsf{K}}}{\partial k} \, \delta k \\ &= \frac{J^2 - 1}{2} \, \mathbf{F}^{-\mathsf{T}} \, \delta K + \mathbf{H}_{\mathsf{m}} \, \mathbf{F}^{-\mathsf{T}} \, \delta G - 2 \sqrt{\frac{2}{3}} \, \overline{\mu} \, \mathbf{n} \, \mathbf{F}^{-\mathsf{T}} \, \delta k =: \underline{\mathbf{M}} \, \delta \boldsymbol{m}, \end{aligned} \tag{5.19}$$

with the second order tensor

$$\mathbf{H}_{\mathsf{m}} = (\beta_0 \mathbb{I}_{\mathrm{dev}} + \beta_2 \mathbf{n} \otimes \mathbf{n}) : \operatorname{dev} (\widetilde{\mathbf{b}}_{\mathsf{e}}^{\mathsf{tr}}) - 2 \Delta\gamma \frac{\overline{\mu}}{G} \beta_1 \mathbf{n}, \tag{5.20}$$

which is derived in detail in App. A.2. Consequently, the constitutive pseudoload operator

is given by

$$\delta_m R = \int_{\mathcal{K}} \left(\frac{J^2-1}{2} \mathbf{F}^{-\mathsf{T}} \, \delta K + \mathbf{H}_{\mathsf{m}} \mathbf{F}^{-\mathsf{T}} \, \delta G - 2\sqrt{\frac{2}{3}} \, \overline{\mu} \, \mathbf{n} \mathbf{F}^{-\mathsf{T}} \, \delta k \right) : \operatorname{Grad} \boldsymbol{v} \, \mathrm{d}V. \tag{5.21}$$

5.4.3 History sensitivity

In the present model of elastoplasticity, dissipation processes are captured by the evolution of internal variables. Within the implicit time integration scheme, the actual mechanical response at time t_{n+1} depends on the values of the internal variables stored at the end of the prior discrete time step t_n. Algorithmically consistent design linearization necessitates the computation of the influence of the internal variables on the structural response, as well as the influence of the chosen design concerning the evolution of the internal variables. The history sensitivity operator denotes the partial variation of the global weak equilibrium w.r.t. the internal history variables of the prior pseudo-time step $\boldsymbol{h}_n$ and reads

$$\delta_{h_n} R = \int_{\partial\mathcal{K}} \delta_{h_n} \mathbf{P}^{\mathsf{K}} : \operatorname{Grad} \boldsymbol{v} \, \mathrm{d}V \tag{5.22}$$

as only the first Piola-Kirchhoff stress tensor depends on the history variables, i.e. $\delta_{h_n} \operatorname{Grad} \boldsymbol{v} = \mathbf{0}$ and $\delta_{h_n} J_{\mathsf{K}} = 0$. Recalling the set of internal history variables $\boldsymbol{h} = \{\mathbf{c}_{\mathsf{p}}, \alpha\}$, the partial variation of the first Piola-Kirchhoff stress tensor w.r.t. the history variables reads

$$\delta_{h_n} \mathbf{P}^{\mathsf{K}} = \frac{\partial \mathbf{P}^{\mathsf{K}}}{\partial \boldsymbol{h}_n} \, \delta \boldsymbol{h}_n = \frac{\partial \mathbf{P}^{\mathsf{K}}}{\partial \mathbf{c}_{\mathsf{p},n}} : \delta \mathbf{c}_{\mathsf{p},n} + \frac{\partial \mathbf{P}^{\mathsf{K}}}{\partial \alpha_n} \, \delta \alpha_n. \tag{5.23}$$

The partial variations are derived in detail in App. A.3.1 and respectively read

$$\mathbb{q}_{\mathsf{c}} := \frac{\partial \mathbf{P}^{\mathsf{K}}}{\partial \mathbf{c}_{\mathsf{p},n}} = (\mathbb{S} : \mathbb{B}_C) \overset{21}{*} \mathbf{F}^{-\mathsf{T}} \quad \text{and} \quad \mathbf{q}_\alpha := \frac{\partial \mathbf{P}^{\mathsf{K}}}{\partial \alpha_n} = \sqrt{\frac{2}{3}} \, k' \, (1-\beta_1) \, \mathbf{n} \mathbf{F}^{-\mathsf{T}}, \tag{5.24}$$

with the identity

$$\mathbb{B}_C := \widetilde{\mathbf{F}} \, \mathbb{I}_s \overset{21}{*} \widetilde{\mathbf{F}}^{\mathsf{T}} \tag{5.25}$$

and the tensor $\mathbb{S}$ from Eq. (4.83). The first derivative of the scalar hardening function, cf. Eq. (4.49), is straight forward and reads

$$k' = \sigma_\infty \, d \, \exp(-d\,\alpha) + H. \tag{5.26}$$

Hence, the history sensitivity operator finally reads

$$\delta_{h_n} R = \int_{\partial\mathcal{K}} \left[\mathbb{q}_{\mathsf{c}} : \delta \mathbf{c}_{\mathsf{p},n} + \mathbf{q}_\alpha \, \delta \alpha_n \right] : \operatorname{Grad} \boldsymbol{v} \, \mathrm{d}V. \tag{5.27}$$

The total variations of the history variables of the prior time step t_n have to be known to be able to compute the variation Eq. (5.23). Thus, it is essential to update these total variations at the end of a converged time step.

5.4.4 Update of history variations

As the internal variables evolve within a solution step, their variations do likewise. Thus, at the end of a time step that has caused plastic yielding, the variations of the history variables have to be updated and stored for the subsequent step. The general update formula for the total variations stored in the vector $\delta\boldsymbol{h} = \{\delta\mathbf{c}_\mathsf{p}, \delta\alpha\}$ reads

$$\delta\boldsymbol{h} = \delta_u\boldsymbol{h} + \delta_s\boldsymbol{h} + \delta_{h_n}\boldsymbol{h} = \frac{\partial\boldsymbol{h}}{\partial\boldsymbol{u}}\,\delta\boldsymbol{u} + \frac{\partial\boldsymbol{h}}{\partial\boldsymbol{s}}\,\delta\boldsymbol{s} + \frac{\partial\boldsymbol{h}}{\partial\boldsymbol{h}_n}\,\delta\boldsymbol{h}_n. \tag{5.28}$$

Just as for the derivation of the different pseudo load operators for different design parametrizations, the functional dependencies in Eq. (5.28) change with the choice of design variables. Therefore, a distinction is necessary at this point.

Geometric shape design. For geometric design, i.e. $\boldsymbol{s} := \boldsymbol{X}$, Eq. (5.28) takes the form

$$\delta\boldsymbol{h} = \frac{\partial\boldsymbol{h}}{\partial\mathbf{F}} : (\delta_u\mathbf{F} + \delta_X\mathbf{F}) + \frac{\partial\boldsymbol{h}}{\partial\boldsymbol{h}_n}\delta\boldsymbol{h}_n, \tag{5.29}$$

where the partial variations $\delta_u\mathbf{F}$ and $\delta_X\mathbf{F}$ are already known , cf. Eq. (4.80) and Eq. (5.16). The partial derivatives of the internal history variables w.r.t. the deformation gradient are derived in App. A.3.2. For the internal history variable $\mathbf{c}_\mathsf{p}$ one obtains

$$\begin{aligned}\frac{\partial\mathbf{c}_\mathsf{p}}{\partial\mathbf{F}} &= \widetilde{\mathbf{F}}^{-1}\,\mathbb{C} \overset{21}{*} \widetilde{\mathbf{F}}^{-\mathsf{T}} - \left[\left(\widetilde{\mathbf{F}}^{-1}\otimes\widetilde{\mathbf{F}}^{-\mathsf{T}}\right)^{\overset{23}{\mathsf{T}}} \overset{21}{*} \left(\widetilde{\mathbf{b}}_\mathsf{e}\,\widetilde{\mathbf{F}}^{-\mathsf{T}}\right) + \widetilde{\mathbf{F}}^{-1}\widetilde{\mathbf{b}}_\mathsf{e}\left(\widetilde{\mathbf{F}}^{-\mathsf{T}}\otimes\widetilde{\mathbf{F}}^{-\mathsf{T}}\right)^{\overset{24}{\mathsf{T}}}\right] : \mathbb{F} \\ &=: \mathbb{A}_c,\end{aligned} \tag{5.30}$$

where the tensor $\mathbb{F}$ is defined in Eq. (4.85) and the tensor $\mathbb{C}$ represents the partial derivative of the isochoric elastic left Cauchy-Green deformation tensor $\widetilde{\mathbf{b}}_\mathsf{e}$ w.r.t. the deformation gradient and is given by

$$\mathbb{C} := \frac{\partial\widetilde{\mathbf{b}}_\mathsf{e}}{\partial\mathbf{F}} = \left(\frac{1}{G}\,\mathbb{S} + \frac{1}{3}\,\mathbf{I}\otimes\mathbf{I}\right) : \mathbb{B}_F, \tag{5.31}$$

see App. A.3.2 for a detailed derivation. The partial derivative of the isochoric hardening variable can be written as

$$\frac{\partial\alpha}{\partial\mathbf{F}} = \sqrt{\frac{2}{3}}\,\frac{G}{f'}\left(\frac{2}{3}\,\Delta\gamma\,\mathbf{I} - \mathbf{n}\right) : \mathbb{B}_F =: \mathbf{A}_\alpha, \tag{5.32}$$

with the already known tensor $\mathbb{B}_F$, cf. Eq. (4.85).

Constitutive design. Choosing the constitutive parameters as design variables, i.e. $\boldsymbol{s} := \boldsymbol{m}$, Eq. (5.28) takes the form

$$\delta \boldsymbol{h} = \frac{\partial \boldsymbol{h}}{\partial \mathbf{F}} : \delta_u \mathbf{F} + \frac{\partial \boldsymbol{h}}{\partial \boldsymbol{m}}\, \delta \boldsymbol{m} + \frac{\partial \boldsymbol{h}}{\partial \boldsymbol{h}_n}\, \delta \boldsymbol{h}_n. \tag{5.33}$$

The partial derivatives of the internal history variables w.r.t. the material parameters can be identified to

$$\delta_m \mathbf{c}_\mathsf{p} = \frac{1}{G^2}\, \mathbb{B}_C^{-1} : \left[(G\, \mathbf{H}_\mathsf{m} - \boldsymbol{\tau}_{\mathrm{dev}})\, \delta G - \sqrt{\frac{2}{3}}\, G\, (1-\beta_1)\, \mathbf{n}\, \delta k \right] \tag{5.34}$$

for the internal variable $\mathbf{c}_\mathsf{p}$, where the second order tensor $\mathbf{H}_\mathsf{m}$ has been used, cf. Eq. (5.20). For the isochoric hardening variable α the partial variation reads

$$\delta_m \alpha = \sqrt{\frac{2}{3}} \left[\frac{\Delta\gamma}{G}\, (\beta_1 - 1) - \frac{1}{f'} \mathbf{n} : \operatorname{dev} \widetilde{\mathbf{b}}_\mathsf{e}^{\mathsf{tr}} \right] \delta G + \frac{2}{3\, f'}\, \delta k. \tag{5.35}$$

A complete derivation of Eq. (5.34) and Eq. (5.35) can be found in App. A.3.2.

Independent on the choice of design variables, in all cases, the partial variations of the internal variables w.r.t. their counterparts from the previous pseudo-time step are needed and read

$$\begin{aligned} \delta_{h_n} \mathbf{c}_\mathsf{p} &= \frac{1}{G}\, \mathbb{B}_C^{-1} : \left(\mathbb{S} + \frac{1}{3}\, \mathbf{I} \otimes \mathbf{I} \right) : \mathbb{B}_C : \delta \mathbf{c}_{\mathsf{p},n} + \sqrt{\frac{2}{3}}\, k' \, (1-\beta_1)\, \mathbb{B}_C^{-1} : \mathbf{n}\, \delta \alpha_n \\ &= \mathbb{C}_\mathsf{c} : \delta \mathbf{c}_{\mathsf{p},n} + \mathbf{C}_\alpha\, \delta \alpha_n, \end{aligned} \tag{5.36}$$

and

$$\begin{aligned} \delta_{h_n} \alpha &= \sqrt{\frac{2}{3}}\, \frac{G}{f'} \left(\frac{2}{3}\, \Delta\gamma\, \mathbf{I} - \mathbf{n} \right) : \mathbb{B}_C : \delta \mathbf{c}_{\mathsf{p},n} + \left(1 + \frac{2}{3}\, \frac{k'}{f'} \right) \delta \alpha_n \\ &= \mathbf{T}_\mathsf{c} : \delta \mathbf{c}_{\mathsf{p},n} + T_\alpha\, \delta \alpha_n, \end{aligned} \tag{5.37}$$

for the internal history variables $\mathbf{c}_\mathsf{p}$ and α, respectively, with the identity

$$\mathbb{B}_C^{-1} := \widetilde{\mathbf{F}}^{-1}\, \mathbb{I}_s\, {}^{21}_{*}\, \widetilde{\mathbf{F}}^{-\mathsf{T}} \tag{5.38}$$

and the fourth order tensor $\mathbb{B}_C$ from Eq. (5.25). Detailed derivations of Eq. (5.36) and Eq. (5.37) can also be found in App. A.3.2.

5.5 Physical sensitivities

Usually, a structural optimization problem depends on the physical behavior of the analyzed structure. The physical state of a given design is defined by the set $(\boldsymbol{u}, \boldsymbol{h}_n)$. Physical quantities not only depend on the geometry of the structural analysis problem, but also

on the deformation and constitutive response, e.g strains or stresses, and can either be the objective that is to be minimized or play the role of constraints. Following, the general steps to compute sensitivities of physical quantities are presented and applied to two exemplary scalar stress measures, i.e. the von Mises equivalent stress and the mean stress.

5.5.1 General variational form

Considering an arbitrary nonlinear physical functional $f(\boldsymbol{s},\boldsymbol{u},\boldsymbol{h}_n)$, its total variation is given by

$$\delta f = \delta_s f + \delta_u f + \delta_{h_n} f = a(\boldsymbol{s},\boldsymbol{u},\boldsymbol{h}_n;\delta\boldsymbol{s}) + b(\boldsymbol{s},\boldsymbol{u},\boldsymbol{h}_n;\delta\boldsymbol{u}) + c(\boldsymbol{s},\boldsymbol{u},\boldsymbol{h}_n;\delta\boldsymbol{h}_n). \tag{5.39}$$

The operators a,b and c have to be evaluated at a global solution point $(\widehat{\boldsymbol{s}},\boldsymbol{u}^*,\boldsymbol{h}_n^*)$ with fixed design $\widehat{\boldsymbol{s}}$ and hence are linear forms $a : \mathbb{S} \to \mathbb{R}$, $b : \mathcal{V} \to \mathbb{R}$ and $c : \mathcal{H} \to \mathbb{R}$ and read

$$\delta f = \delta_s f + \delta_u f + \delta_{h_n} f = \frac{\partial f}{\partial \boldsymbol{s}}\,\delta\boldsymbol{s} + \frac{\partial f}{\partial \boldsymbol{u}}\,\delta\boldsymbol{u} + \frac{\partial f}{\partial \boldsymbol{h}_n}\,\delta\boldsymbol{h}_n. \tag{5.40}$$

The computation of the partial derivatives of f w.r.t. $\boldsymbol{s}$, $\boldsymbol{u}$ and $\boldsymbol{h}_n$ is usually straight forward and not further focussed on in this paragraph. However, the total variations of the displacements and the history variables are examined more closely.
Assuming that Eq. (4.78) has a real solution implies that also a solution can be found for $\delta\boldsymbol{u}$ from Eq. (5.10). With the definition of the implicit sensitivity operator, cf. [87],

$$\delta\boldsymbol{u} =: S(\widehat{\boldsymbol{s}},\boldsymbol{u}^*,\boldsymbol{h}_n^*;\delta\boldsymbol{s}), \tag{5.41}$$

further thoughts can be made on the total history variations. Recalling Eq. (5.28) and considering Eq. (5.41) one obtains

$$\delta\boldsymbol{h} = \frac{\partial \boldsymbol{h}}{\partial \boldsymbol{s}}\delta\boldsymbol{s} + \frac{\partial \boldsymbol{h}}{\partial \boldsymbol{u}} \circ S + \frac{\partial \boldsymbol{h}}{\partial \boldsymbol{h}_n}\,\delta\boldsymbol{h}_n =: Z(\widehat{\boldsymbol{s}},\boldsymbol{u}^*,\boldsymbol{h}_n^*;\delta\boldsymbol{s}), \tag{5.42}$$

where the implicit history design sensitivity operator Z is defined. Note that as a consequence of Eq. (5.42), $\delta\boldsymbol{h}_n = Z_n(\widehat{\boldsymbol{s}},\boldsymbol{u}_n^*,\boldsymbol{h}_{n-1};\delta\boldsymbol{s})$. Now it is possible to express the total variation of a physical quantity solely w.r.t. the design $\boldsymbol{s}$, which leads to the total design variation of the history variables

$$\delta\boldsymbol{h} = \frac{\partial \boldsymbol{h}}{\partial \boldsymbol{s}}\,\delta\boldsymbol{s} + \frac{\partial \boldsymbol{h}}{\partial \boldsymbol{u}} \circ S + \frac{\partial \boldsymbol{h}}{\partial \boldsymbol{h}_n} \circ Z_n. \tag{5.43}$$

Finally, Eq. (5.40) takes the form

$$\delta f = \frac{\partial f}{\partial \boldsymbol{s}}\,\delta\boldsymbol{s} + \frac{\partial f}{\partial \boldsymbol{u}} \circ S + \frac{\partial f}{\partial \boldsymbol{h}_n} \circ Z_n. \tag{5.44}$$

Note that $\delta \boldsymbol{h}_n = Z_n(\widehat{\boldsymbol{s}},\boldsymbol{u}_n^*,\boldsymbol{h}_{n-1}^*;\delta \boldsymbol{s})$ and by assuming $\delta \boldsymbol{h}_0 = \boldsymbol{0}$ at time t_0, the update formula Eq. (5.43) simplifies to

$$\delta \boldsymbol{h} = \frac{\partial \boldsymbol{h}}{\partial \boldsymbol{u}} \circ S + \frac{\partial \boldsymbol{h}}{\partial \boldsymbol{s}}\, \delta \boldsymbol{s} \tag{5.45}$$

in the very first pseudo-time step. Consequently, the influence of the history variables on the design variation of any physical quantity only appears subsequent to a plastic step. Thus, it is important to update the history variations at the end of each pseudo time step. Depending on the type of chosen design variables, the implicit operators are denoted with the superscript ^{X} for geometric and ^{m} for constitutive design, i.e. e.g. $S^X = S(\widehat{\boldsymbol{s}},\boldsymbol{u},\boldsymbol{h}_n;\delta \boldsymbol{X})$ or $Z_n^m = Z_n(\widehat{\boldsymbol{s}},\boldsymbol{u},\boldsymbol{h}_n;\delta \boldsymbol{m})$.

Remark 5.4 (Implicit operators) The implicit operators S and Z can be explicitly determined after reformulation of the continuum equations into a discrete matrix form. The resulting matrices are essential for the presented approach and contain important information on the structural and physical behavior of the analyzed problem. Details on the computation of these explicit matrices are given in Sec. 6.3.3.

5.5.2 Stress variations

The general variational form of a total design variation of a physical quantity is applied to two stress measures, namely the equivalent von Mises stress σ_{eq} and the mean stress σ_{m}, which are respectively given by

$$\sigma_{\mathsf{eq}} = \sqrt{3\, J_2(\boldsymbol{\tau}_{\mathrm{dev}})} \quad \text{and} \quad \sigma_{\mathsf{m}} = \frac{1}{3}\, I_1(\boldsymbol{\tau}), \tag{5.46}$$

with $I_1(\boldsymbol{\tau}) = \mathrm{tr}\,(\boldsymbol{\tau})$ and $J_2(\boldsymbol{\tau}_{\mathrm{dev}}) = \frac{1}{2}\,\boldsymbol{\tau}_{\mathrm{dev}} : \boldsymbol{\tau}_{\mathrm{dev}}$ denoting the first and second invariants of the Kirchhoff stress tensor and its deviatoric contribution, respectively. Their total variations $\delta\sigma_{\mathsf{m}}$ and $\delta\sigma_{\mathsf{eq}}$ can be expressed as

$$\delta\sigma_{\mathsf{m}} = \frac{\partial \sigma_{\mathsf{m}}}{\partial \boldsymbol{\tau}} : \delta\boldsymbol{\tau} = \frac{1}{3}\,\mathbf{I} : \delta\boldsymbol{\tau} \quad \text{and} \quad \delta\sigma_{\mathsf{eq}} = \frac{\partial \sigma_{\mathsf{eq}}}{\partial \boldsymbol{\tau}} : \delta\boldsymbol{\tau} = \frac{3}{2\,\sigma_{\mathsf{eq}}}\,\boldsymbol{\tau}_{\mathrm{dev}} : \delta\boldsymbol{\tau}, \tag{5.47}$$

respectively. For both, the physical variation of interest is the total design variation of the Kirchhoff stres stensor $\delta\boldsymbol{\tau}$, which in its general form reads

$$\delta\boldsymbol{\tau} = \delta_s\boldsymbol{\tau} + \delta_u\boldsymbol{\tau} + \delta_{h_n}\boldsymbol{\tau} = \frac{\partial \boldsymbol{\tau}}{\partial \boldsymbol{s}}\,\delta\boldsymbol{s} + \frac{\partial \boldsymbol{\tau}}{\partial \boldsymbol{u}} \circ S + \frac{\partial \boldsymbol{\tau}}{\partial \boldsymbol{h_n}} \circ Z_n. \tag{5.48}$$

At this point a distinction on the choice of design parametrization has to be made.

Geometric shape design. For geometric design ($\boldsymbol{s} := \boldsymbol{X}$), the Kirchhoff stress tensor depends on the geometric design as well as on the displacements via the deformation

gradient. Thus, Eq. (5.48) can be written as

$$\delta\boldsymbol{\tau} = \frac{\partial\boldsymbol{\tau}}{\partial\mathbf{F}} : (\delta_X\mathbf{F} + \delta_u\mathbf{F}\circ S^X) + \frac{\partial\boldsymbol{\tau}}{\partial\boldsymbol{h_n}}\circ Z_n^X. \tag{5.49}$$

Constitutive design. For constitutive design, the Kirchhoff stress tensor explicitly depends on the design variables. Therefore, Eq. (5.48) takes the form

$$\delta\boldsymbol{\tau} = \frac{\partial\boldsymbol{\tau}}{\partial\boldsymbol{m}}\,\delta\boldsymbol{m} + \frac{\partial\boldsymbol{\tau}}{\partial\mathbf{F}} : \delta_u\mathbf{F}\circ S^m + \frac{\partial\boldsymbol{\tau}}{\partial\boldsymbol{h_n}}\circ Z_n^m. \tag{5.50}$$

Here, the partial variation of the Kirchhoff stress tensor w.r.t. the constitutive parameters can be obtained considering Eq. (5.19) and Eq. (4.26). One obtains

$$\delta_m\boldsymbol{\tau} = \delta_m\mathbf{P}^{\mathsf{K}}\,\mathbf{F}^{\mathsf{T}} = \frac{J^2-1}{2}\,\mathbf{I}\,\delta K + \mathbf{H}_{\mathsf{m}}\,\delta G - 2\sqrt{\frac{2}{3}}\,\overline{\mu}\,\mathbf{n}\,\delta k =: \underline{\mathbf{M}}_{\tau}\,\delta\boldsymbol{h}_n. \tag{5.51}$$

By means of Eq. (4.83) and Eq. (A.3), the partial derivative of the Kirchhoff stress tensor w.r.t. the deformation gradient for the presented model can be revealed as

$$\mathbb{o} := \frac{\partial\boldsymbol{\tau}}{\partial\mathbf{F}} = K\,J^2\,\mathbf{I}\otimes\mathbf{F}^{-\mathsf{T}} + \mathbb{S}. \tag{5.52}$$

The partial derivatives of the Kirchhoff stress tensor w.r.t. the internal variables are given in App. A.3.1 and read

$$\frac{\partial\boldsymbol{\tau}}{\partial\mathbf{c}_{\mathsf{p},n}} = \mathbb{S} : \mathbb{B}_C =: \mathbb{D}_{\mathsf{c}} \quad \text{and} \quad \frac{\partial\boldsymbol{\tau}}{\partial\alpha_n} = \sqrt{\frac{2}{3}}\,(1-\beta_1)\,\mathbf{n} =: \mathbf{D}_{\alpha}. \tag{5.53}$$

5.6 Summary and concluding remarks

This chapter presents a complete derivation of design sensitivities utilizing a variational approach. The term design is explained to parametrize the geometrical and thermodynamic properties of the material body. Within the scope of this thesis, thermodynamic properties are described by the constitutive parameters $\boldsymbol{m}$ governing the elastic and plastic response behavior, whereas the referential coordinates $\boldsymbol{X}$ define the geometry. Based on the enhanced viewpoint of kinematics, it is possible to separate geometrical from physical quantities, which avoids complicated implicit dependencies, if geometrical sensitivities are required, and additionally allows a compact representation of total design variations of any physical quantity.
The essential equation $\delta R = 0$, cf. Eq. (5.10), restricts a design variation to constitute an equilibrium point and is therefore used to identify the total design sensitivity of the structural response. The arising tangent operators are given with all corresponding variations. Special attention has to be drawn on the deformation history that is captured by the internal history variables. Their influence on the structural response must not be disregarded. Thus, total design variations of the history variables have to be determined. Within the implicit time integration scheme, all linearizations are performed consistent

with the stress projection algorithm presented in Sec. 4.5.2. As the design variations of the history variables of the prior pseudo-time step are required in most of the arising design variations, it is important to update those at the end of the current pseudo-time step and save them for the subsequent.
The fact that the variation of the structural response has to be known for the computation of physical sensitivities, including the update of the variations of internal history variables, gives rise to a staggered scheme for the computations. The computational treatment including discretization and embedding of the appearing matrix forms into the finite element framework is presented in Chap. 6. Here, additionally the possibility of a semi-analytical approach is described that is generally valid for the choice of any constitutive model with dissipative mechanisms described via local internal history variables within an implicit time integration procedure.

Chapter 6

Computation of Design Sensitivities

This chapter aims at embedding the continuously derived design sensitivities in Chap. 5 into the computational framework of the finite element method, sketched briefly in Chap. 4. Therefore, it constitutes the second main part in this thesis, i.e. efficient design sensitivity computations. The continuum equations are discretized utilizing finite element approximations analogously to the discretization of the structural analysis problem. The essential matrix representations of sensitivity operators are derived and the computation algorithms are presented. Additionally, a semi-analytical way of computing the demanded sensitivities is sketched. Finally, some benchmark examples compare the efficiency and quality of the obtained gradient information with the numerical method of finite differences.

Contents

6.1 Introduction

In Chap. 5, the sensitivity relations of the structural response and arbitrary physical functions have been derived analytically by means of a variational approach. For the numerical implementation, the resulting equations have to be embedded into the computational framework, that is, the finite element method (FEM). For details on the numerical approximations, the interested reader is referred to the relevant standard literature e.g. [21, 31, 80, 172, 190, 199] to name a few. Most relevant aspects and notations for the work at hand can also be found in App. B.1.
The approximations of the sensitivity relations follow the same concepts mentioned above, see for example [14, 63, 88, 116]. However, within the finite element method, the underlying *real* geometry of the considered structure is not directly available. This means that in the case of optimal shape design, only the nodal coordinates of the discrete mesh nodes can be adapted. Depending on the degree of the interpolating shape functions, this might result in non-smooth boundaries and additionally, depending on the discretization density, a high number of design variables might occur. Therefore, it is convenient to parametrize the underlying geometry from which the FE mesh is constructed. In this context, approaches used in computer aided geometric design (CAGD), e.g. Bézier splines, basis splines (B-splines) or non-uniform rational B-Splines (NURBS) have been proven to constitute good alternatives, cf. e.g. [63, 87, 116]. However, as the computational results are obtained by means of the FEM, a coupling between CAGD and FEM has to be established. This leads to the so-called design velocity field that couples continuous CAGD geometry descriptions and discrete FE approximations.
This chapter aims at the discrete formulation of the sensitivity relations regarding the finite element approximations, as well as the projection to continuous geometry descriptions by means of design velocity fields. Further, computational and algorithmic details are given and corresponding pseudo code is provided. Finally, the possibility of semi-analytical computations of design sensitivity information in the context of implicit path dependent material behavior is presented. Some numerical benchmarks are performed in order to emphasize the accuracy and applicability of the presented approach.

6.2 Discrete design parametrization

In the following, the different discrete design parametrizations are introduced. For the case of geometric design, the concept of the so-called design velocity field is explained. For constitutive design, the discrete design vector $\boldsymbol{m}$ including all elastic and plastic parameters of the material model explained in Chap. 4 is introduced.

6.2.1 Geometry and FE mesh

Mathematical exact geometry descriptions can be obtained by means of computer aided geometric design (CAGD). Curves, surfaces and volumes can for instance be described by Bézier splines, basis splines (B-Splines) or, more general, non-uniform rational B-Splines (NURBS). All of these have in common that the displayed curves and surfaces are controlled by a set of control points. Choosing these control points as design variables in shape optimization has two main advantages. First, continuity of boundaries can be

controlled and thus can be ensured smooth. Secondly, the number of design variables can be decreased drastically as a few control points can be used to describe complex geometries for which plenty FE nodes must be used to gain a reasonable approximation.
NURBS represent the most general and most versatile geometry description, as additional factors are used to weight control points, which results in higher or lower attraction of the respective knot on the curve compared to B-Splines. However, in shape optimization these additional weighting factors constitute additional unknowns and the uniqueness of the description is not guaranteed. Therefore, within the work at hand B-Spline geometry descriptions are used.
As the finite element method is used to solve the physical initial boundary value problem and to compute the sensitivities in a solution point, the obtained gradients have to be transformed to control point coordinates of the geometry description. This can be gained by taking the partial derivative of the nodal FE coordinates $\boldsymbol{X}$ w.r.t. the control points of the mesh controlling geometry description $\boldsymbol{p}$. The resulting matrix is called design velocity matrix and reads

$$\boldsymbol{D}^{\mathrm{v}} := \left[\frac{\partial \boldsymbol{X}}{\partial \boldsymbol{p}}\right]. \tag{6.1}$$

The NURBS toolbox [137] can be used in Matlab to construct NURBS and B-Spline geometries and additionally offers functions that evaluate partial derivatives. Solely the coordinates of the control points and the corresponding knot vectors for each spatial direction are needed to invoke the function `nrbmak`, which produces a Matlab `struct` that can be used to construct a visualization mesh by means of the function `nrbeval`. The constructed mesh can also be used for the FE discretization. Finally, the design velocity matrix can be computed by means of the function `nrbeval_der_p`, which computes the partial derivatives of the NURBS geometry evaluated at the mesh nodes w.r.t. the coordinates of the control points. An example of constructing a NURBS geometry and the corresponding FE mesh utilizing the NURBS toolbox is given in Fig. B.1 in App. B.2.

6.2.2 Discrete constitutive design

The constitutive parameters that can be chosen as design variables are prescribed by the underlying constitutive model. In the present elastoplastic model, the two elastic parameters (K,G), as well as the four plastic parameters (σ_0, σ_∞, H, d), describe the material behavior. All of these parameters are chosen as design variables, thus the discrete vectors of constitutive design variables and their variations read

$$\begin{aligned} \boldsymbol{m} &= \begin{bmatrix} K & G & \sigma_0 & \sigma_\infty & H & d \end{bmatrix}, \\ \delta\boldsymbol{m} &= \begin{bmatrix} \delta K & \delta G & \delta\sigma_0 & \delta\sigma_\infty & \delta H & \delta d \end{bmatrix}. \end{aligned} \tag{6.2}$$

With these, the variations of the bulk modulus and the shear modulus, as well as the hardening function, see Eq. (5.1), can in a discrete setting be expressed by

$$\begin{aligned}
\delta K &:= \frac{\partial K}{\partial \boldsymbol{m}}\,\delta \boldsymbol{m} = \begin{bmatrix} 1 & 0 & 0 & 0 & 0 & 0 \end{bmatrix}\,\delta \boldsymbol{m},\\
\delta G &:= \frac{\partial G}{\partial \boldsymbol{m}}\,\delta \boldsymbol{m} = \begin{bmatrix} 0 & 1 & 0 & 0 & 0 & 0 \end{bmatrix}\,\delta \boldsymbol{m},\\
\delta k &:= \frac{\partial k}{\partial \boldsymbol{m}}\,\delta \boldsymbol{m} = \begin{bmatrix} 0 & 0 & 1 & (1-\exp(-d\,\alpha)) & \alpha & \sigma_\infty \exp(-d\,\alpha) \end{bmatrix}\,\delta \boldsymbol{m}.
\end{aligned} \tag{6.3}$$

6.3 Discrete sensitivities

In App. B.1, the standard finite element discretization is sketched and the approximations of the geometry, displacements and test functions are given. Following the same concepts, the following approximations of the geometry and displacement variations can be defined

$$\delta \boldsymbol{X}^h = \sum_{i=1}^{\text{nnode}} N_i\,\delta \boldsymbol{X}_i \quad \text{and} \quad \delta \boldsymbol{u}^h = \sum_{i=1}^{\text{nnode}} N_i\,\delta \boldsymbol{u}_i, \tag{6.4}$$

as well as their referential gradients and divergences

$$\operatorname{Grad} \delta \boldsymbol{X}^h = \sum_{i=1}^{\text{nnode}} \delta \boldsymbol{X}_i\,\boldsymbol{L}_i^T, \qquad \operatorname{Div} \delta \boldsymbol{X}^h = \sum_{i=1}^{\text{nnode}} \boldsymbol{L}_i^T\,\delta \boldsymbol{X}_i \qquad \text{and} \tag{6.5}$$

$$\operatorname{Grad} \delta \boldsymbol{u}^h = \sum_{i=1}^{\text{nnode}} \delta \boldsymbol{u}_i\,\boldsymbol{L}_i^T, \qquad \operatorname{Div} \delta \boldsymbol{u}^h = \sum_{i=1}^{\text{nnode}} \boldsymbol{L}_i^T\,\delta \boldsymbol{u}_i, \tag{6.6}$$

respectively. Based on these approximations, discrete matrix forms of the continuously derived sensitivities for the different design parametrizations can be constructed. Note that for the partial variation of the deformation gradient w.r.t. geometric design, cf. Eq. (5.16), the discrete version of the form

$$\delta_X \boldsymbol{F} = -\sum_i \boldsymbol{G}_i\,\operatorname{Grad} \boldsymbol{u}^h\,\delta \boldsymbol{X}_i = -\sum_i \boldsymbol{G}_i^X\,\delta \boldsymbol{X}_i = -\boldsymbol{G}^X\,\delta \boldsymbol{X} \tag{6.7}$$

can be defined. Choosing control point coordinates as design variables, Eq. (6.8) can be transformed to

$$\delta_p \boldsymbol{F} = -\sum_i \boldsymbol{G}_i^X\,\boldsymbol{D}_i^{\text{v}}\,\delta \boldsymbol{p} = -\boldsymbol{G}^p\,\delta \boldsymbol{p}. \tag{6.8}$$

In connection with the $\overline{F}$ method the consistent discrete gradient operators then read

$$\delta_X \overline{\boldsymbol{F}} = -\sum_i \overline{\boldsymbol{G}}_i \operatorname{Grad} \boldsymbol{u}^h \, \delta \boldsymbol{X}_i = -\sum_i \overline{\boldsymbol{G}}_i^X \, \delta \boldsymbol{X}_i = -\overline{\boldsymbol{G}}^X \, \delta \boldsymbol{X}, \tag{6.9}$$

$$\delta_p \overline{\boldsymbol{F}} = -\sum_i \overline{\boldsymbol{G}}_i^X \, \boldsymbol{D}_i^{\mathsf{v}} \, \delta \boldsymbol{p} = -\overline{\boldsymbol{G}}^p \, \delta \boldsymbol{p}, \tag{6.10}$$

see also Eq. (4.94).

6.3.1 Discrete pseudoload

By means of the discrete approximations in Eqs. (6.4), (6.5) and (6.6), the discrete matrix forms of the geometric and constitutive pseudoload operators can be composed. At this point, again a distinction of the chosen design parametrizations has to be made.

Geometric shape design. The continuous geometric pseudoload operator has been derived in Sec. 5.4.2 and is given in Eq. (5.17). Considering the discrete gradient and divergence operators, the discrete geometric pseudoload operator reads

$$\begin{aligned} p_X^h(\boldsymbol{v}^h, \delta \boldsymbol{X}^h) &= \bigcup_e \sum_i \sum_j \boldsymbol{v}_i^T \left[\int_{\Omega_e} -\boldsymbol{G}_i^{\mathsf{T}} \, \overline{\boldsymbol{A}} \, \overline{\boldsymbol{G}}_j^X - \overline{\mathbf{P}}^{\mathsf{K}} \left(\boldsymbol{L}_j \, \boldsymbol{L}_i^{\mathsf{T}} - \boldsymbol{L}_i \, \boldsymbol{L}_j^{\mathsf{T}} \right) \mathrm{d}V \right] \delta \boldsymbol{X}_j^h \\ &= \bigcup_e \boldsymbol{v}_e^T \, \overline{\boldsymbol{P}}_e^{\mathsf{X}} \, \delta \boldsymbol{X}_e^h = \boldsymbol{v}^T \, \overline{\boldsymbol{P}}^{\mathsf{X}} \, \delta \boldsymbol{X}^h, \end{aligned} \tag{6.11}$$

with the nodal based discrete geometric pseudoload matrix $\overline{\boldsymbol{P}}^{\mathsf{X}} \in \mathbb{R}^{\mathsf{ndof} \times \mathsf{ndof}}$. Choosing mesh controlling geometric parameters, i.e. e.g. the control points $\boldsymbol{p}$ of the underlying geometry description, as design variables and utilizing the design velocity matrix on element level, leads to the discrete geometric pseudoload operator

$$p_p^h(\boldsymbol{v}^h, \delta \boldsymbol{p}) = \bigcup_e \boldsymbol{v}_e^T \, \overline{\boldsymbol{P}}_e^{\mathsf{X}} \, \boldsymbol{D}_e^{\mathsf{v}} \, \delta \boldsymbol{p} = \bigcup_e \boldsymbol{v}_e^T \, \overline{\boldsymbol{P}}_e^{\mathsf{p}} \, \delta \boldsymbol{p} = \boldsymbol{v}^T \, \overline{\boldsymbol{P}}^{\mathsf{p}} \, \delta \boldsymbol{p}, \tag{6.12}$$

with the control point based discrete geometric pseudoload matrix $\overline{\boldsymbol{P}}^{\mathsf{p}} \in \mathbb{R}^{\mathsf{ndof} \times \mathsf{ndv}}$.

Constitutive design. In the discrete setting, the constitutive sensitivity operator from Eq. (5.21) can be approximated by

$$p_m^h(\boldsymbol{v}^h, \delta \boldsymbol{m}) = \bigcup_e \sum_i \boldsymbol{v}_i^T \left[\int_{\Omega_e} \boldsymbol{G}_i^{\mathsf{T}} \, \overline{\boldsymbol{M}} \, \mathrm{d}V \right] \delta \boldsymbol{m} = \bigcup_e \boldsymbol{v}_e^{\mathsf{T}} \, \overline{\boldsymbol{P}}_e^{\mathsf{m}} \, \delta \boldsymbol{m} = \boldsymbol{v}^T \, \overline{\boldsymbol{P}}^{\mathsf{m}} \, \delta \boldsymbol{m}, \tag{6.13}$$

where the matrix form $\boldsymbol{M}$ of the partial derivative of the first Piola Kirchhoff stress tensor w.r.t. constitutive parameters is given in Eq. (A.38).

6.3.2 Discrete history sensitivity

At each integration point the discrete vector of internal variables is defined as

$$\boldsymbol{h} := \begin{bmatrix} \boldsymbol{c}_{\mathsf{p}}^T & \alpha \end{bmatrix}^T = \begin{bmatrix} c_{11}^{\mathsf{p}} & c_{22}^{\mathsf{p}} & \dots & 2\,c_{31}^{\mathsf{p}} & \alpha \end{bmatrix}^T, \tag{6.14}$$

with the symmetric components c_{ij}^{p} of the matrix form of the internal variable $\mathbf{c}_{\mathsf{p}}$ that are sorted corresponding to Eq. (2.9) and the isochoric hardening variable α. Analogously, the vector of variations of internal history variables is introduced, viz.

$$\delta\boldsymbol{h} := \begin{bmatrix} \delta\boldsymbol{c}_{\mathsf{p}}^T & \delta\alpha \end{bmatrix}^T = \begin{bmatrix} \delta c_{11}^{\mathsf{p}} & \delta c_{22}^{\mathsf{p}} & \dots & 2\,\delta c_{31}^{\mathsf{p}} & \delta\alpha \end{bmatrix}^T. \tag{6.15}$$

The discrete version of the history sensitivity operator, cf. Eq. (5.27), is then given by

$$h(\boldsymbol{v},\delta\boldsymbol{h}_n) = \bigcup_e \sum_i \boldsymbol{v}_i^T \left[\int_{\Omega_e} \boldsymbol{G}_i^T \left[\frac{\partial \overline{\boldsymbol{P}}^{\mathsf{K}}}{\partial \boldsymbol{h}_n} \right] \mathrm{d}V \right] \delta\boldsymbol{h}_n = \bigcup_e \boldsymbol{v}_e^T \, \boldsymbol{H}_e \, \delta\boldsymbol{h}_n, \tag{6.16}$$

where the partial variations of the first Piola-Kirchhoff stress tensor w.r.t. the internal history variables are given by the matrix forms of the tensors $\mathbf{q}_{\mathsf{c}}$ and $\mathbf{q}_\alpha$ from Eq. (5.24), corresponding to the conventions in Sec. 2.1.2, viz.

$$\boldsymbol{q}_{\mathsf{c}} := \left[\frac{\partial \overline{\boldsymbol{P}}^{\mathsf{K}}}{\partial \boldsymbol{c}_{\mathsf{p},n}} \right] \in \mathbb{R}^{9\times 6}, \quad \boldsymbol{q}_\alpha := \left[\frac{\partial \overline{\boldsymbol{P}}^{\mathsf{K}}}{\partial \alpha_n} \right] \in \mathbb{R}^{9\times 1}. \tag{6.17}$$

Note that the vector of variations of internal history variables can be expressed in terms of design changes, considering that it is evaluated in a solution point of the structural analysis problem with fixed design. Recalling Eq. (5.42), its discrete version becomes

$$\delta\boldsymbol{h} = \left[\frac{\partial \boldsymbol{h}}{\partial \boldsymbol{u}} \boldsymbol{S} + \frac{\partial \boldsymbol{h}}{\partial \boldsymbol{h}_n} \boldsymbol{Z}_n + \frac{\partial \boldsymbol{h}}{\partial \boldsymbol{s}} \right] \delta\boldsymbol{s} = \boldsymbol{Z}\,\delta\boldsymbol{s}, \tag{6.18}$$

regardless of whether geometric shape or constitutive design is chosen. Here, the matrix $\boldsymbol{Z}$ has the structure

$$\boldsymbol{Z} := \begin{bmatrix} \boldsymbol{Z}^{\mathsf{c}} \\ \boldsymbol{Z}^{\alpha} \end{bmatrix} \in \mathbb{R}^{7\times \mathsf{ndv}} \quad \text{with} \quad \boldsymbol{Z}^{\mathsf{c}} = \left[\frac{\mathrm{d}\boldsymbol{c}_{\mathsf{p}}}{\mathrm{d}\boldsymbol{s}} \right] \in \mathbb{R}^{6\times \mathsf{ndv}} \quad \text{and} \quad \boldsymbol{Z}^{\alpha} = \left[\frac{\mathrm{d}\alpha}{\mathrm{d}\boldsymbol{s}} \right] \in \mathbb{R}^{1\times \mathsf{ndv}} \tag{6.19}$$

and contains the values that have to be saved in each integration point of each finite element in every pseudo-time step for the subsequent step. On element level the entries of the matrix $\boldsymbol{Z}$ are loaded and Eq. (6.16) can be transformed to

$$h(\boldsymbol{v},\delta\boldsymbol{s}) = \bigcup_e \boldsymbol{v}_e^T \, \boldsymbol{H}_e \, \boldsymbol{Z}_n \, \delta\boldsymbol{s} = \bigcup_e \boldsymbol{v}_e^T \, \boldsymbol{Q}_e \, \delta\boldsymbol{s} = \boldsymbol{v}^T \, \boldsymbol{Q} \, \delta\boldsymbol{s}. \tag{6.20}$$

Here, the matrix $\boldsymbol{Q} \in \mathbb{R}^{\mathsf{ndof} \times \mathsf{ndv}}$ directly connects the structural response with respect to design changes that effect the deformation history and on element level reads

$$\boldsymbol{Q}_e = \int_{\Omega_e} \boldsymbol{G}^T \left(\boldsymbol{q}_{\mathsf{c}} \, \boldsymbol{Z}_n^{\mathsf{c}} + \boldsymbol{q}_\alpha \, \boldsymbol{Z}_n^\alpha \right) \mathrm{d}V = \int_{\Omega_e} \boldsymbol{G}^T \, \boldsymbol{q} \, \boldsymbol{Z}_n \, \mathrm{d}V, \tag{6.21}$$

with $\boldsymbol{q} = \begin{bmatrix} \boldsymbol{q}_{\mathsf{c}} & \boldsymbol{q}_\alpha \end{bmatrix} \in \mathbb{R}^{9 \times 7}$. The matrices $\boldsymbol{S}$ and $\boldsymbol{Z}$ are further declared in the following.

6.3.3 Total sensitivity matrix

From the matrix form of Eq. (5.10)

$$\begin{aligned} \delta \boldsymbol{R} &= \left[\frac{\partial \boldsymbol{R}}{\partial \boldsymbol{u}} \right] \delta \boldsymbol{u} + \left[\frac{\partial \boldsymbol{R}}{\partial \boldsymbol{s}} \right] \delta \boldsymbol{s} + \left[\frac{\partial \boldsymbol{R}}{\partial \boldsymbol{h}_n} \right] \delta \boldsymbol{h}_n = \boldsymbol{0} \\ &= \boldsymbol{K} \, \delta \boldsymbol{u} + \boldsymbol{P} \, \delta \boldsymbol{s} + \boldsymbol{H} \, \delta \boldsymbol{h}_n, \end{aligned} \tag{6.22}$$

where $\boldsymbol{R} \in \mathbb{R}^{\mathsf{ndof}}$, the total sensitivity matrix $\boldsymbol{S} \in \mathbb{R}^{\mathsf{ndof} \times \mathsf{ndv}}$ can be derived, that connects the total variation of the structural response $\delta \boldsymbol{u}$ with design variations $\delta \boldsymbol{s}$

$$\begin{aligned} \delta \boldsymbol{u} &= -\boldsymbol{K}^{-1} \left[\boldsymbol{P} \, \delta \boldsymbol{s} + \boldsymbol{H} \, \delta \boldsymbol{h}_n \right] \\ &= -\boldsymbol{K}^{-1} \left[\boldsymbol{P} + \boldsymbol{Q} \right] \delta \boldsymbol{s} = \boldsymbol{S} \, \delta \boldsymbol{s}. \end{aligned} \tag{6.23}$$

Here, the matrix $\boldsymbol{K} \in \mathbb{R}^{\mathsf{ndof} \times \mathsf{ndof}}$ denotes the tangent stiffness matrix, cf. Eq. (4.87), $\boldsymbol{H} \in \mathbb{R}^{\mathsf{ndof} \times \mathsf{nhv}}$ is the history sensitivity matrix and $\boldsymbol{P} \in \mathbb{R}^{\mathsf{ndof} \times \mathsf{ndv}}$ constitutes the pseudoload matrix. Note that all equations in this subsection are valid regardless of the chosen design parametrization. Hence, $\boldsymbol{P}$ can either be the geometric or the constitutive pseudo load matrix, or even a combination of both. The matrix $\boldsymbol{Z}_n \in \mathbb{R}^{\mathsf{nhv} \times \mathsf{ndv}}$ is the total design derivative of the history variables and is obtained utilizing the discrete update formula in Eq. (6.18). In the algorithmic manner, by assuming $\boldsymbol{h}_0 = \boldsymbol{0}$ and $\boldsymbol{Z}_0 = \boldsymbol{0}$ at time $t = t_0$, from Eq. (6.23) one obtains

$$\boldsymbol{S}_1 = -\boldsymbol{K}_1^{-1} \left(\boldsymbol{P}_1 + \boldsymbol{Q}_1 \right) = -\boldsymbol{K}_1^{-1} \, \boldsymbol{P}_1, \tag{6.24}$$

as also $\boldsymbol{Q}_1 = \boldsymbol{0}$, and therefore

$$\delta \boldsymbol{h}_1 = \left[\frac{\partial \boldsymbol{h}_1}{\partial \boldsymbol{u}} \, \boldsymbol{S}_1 + \frac{\partial \boldsymbol{h}_1}{\partial \boldsymbol{s}} \right] \delta \boldsymbol{s} = \boldsymbol{Z}_1 \, \delta \boldsymbol{s}, \tag{6.25}$$

for the first pseudo-time step, i.e. $t = t_1$. The sensitivities corresponding to the deformation history have to be evaluated at the end of each time step that causes plastic yielding and saved for the subsequent step.

6.3.4 Discrete history sensitivity update

At the end of each pseudo time step that causes plastic yielding, the discrete values of sensitivities of the internal variables have to be updated and saved following Eq. (6.18).

The partial derivatives needed are derived in Sec. 5.4.4. The update formulae for the variations of the internal history variables $\boldsymbol{c}_\mathsf{p}$ and α respectively read

$$\delta\boldsymbol{c}_\mathsf{p} = \delta_u\boldsymbol{c}_\mathsf{p} + \delta_s\boldsymbol{c}_\mathsf{p} + \delta_{h_n}\boldsymbol{c}_\mathsf{p} \quad \text{and} \quad \delta\alpha = \delta_u\alpha + \delta_s\alpha + \delta_{h_n}\alpha. \tag{6.26}$$

Before a distinction of the chosen design description has to be made, the discrete partial variations of the internal history variables w.r.t. their counterparts of the prior load step are given, as these are demanded regardless of the choice of design parametrization. Recalling Eq. (5.36) and Eq. (5.37), their discrete versions read

$$\delta_{h_n}\boldsymbol{c}_\mathsf{p} = \boldsymbol{C}_\mathsf{c}\,\delta\boldsymbol{c}_{\mathsf{p},n} + \boldsymbol{C}_\alpha\,\delta\alpha_n = (\boldsymbol{C}_\mathsf{c}\,\boldsymbol{Z}_n^\mathsf{c} + \boldsymbol{C}_\alpha\,\boldsymbol{Z}_n^\alpha)\,\delta\boldsymbol{s} = \boldsymbol{C}\,\boldsymbol{Z}_n\,\delta\boldsymbol{s} \tag{6.27}$$

and

$$\delta_{h_n}\alpha = \boldsymbol{T}_\mathsf{c}\,\delta\boldsymbol{c}_{\mathsf{p},n} + T_\alpha\,\delta\alpha_n = (\boldsymbol{T}_\mathsf{c}\,\boldsymbol{Z}_n^\mathsf{c} + T_\alpha\,\boldsymbol{Z}_n^\alpha)\,\delta\boldsymbol{s} = \boldsymbol{T}\,\boldsymbol{Z}_n\,\delta\boldsymbol{s}, \tag{6.28}$$

with $\boldsymbol{C} = \begin{bmatrix}\boldsymbol{C}_\mathsf{c} & \boldsymbol{C}_\alpha\end{bmatrix} \in \mathbb{R}^{6\times 7}$ and $\boldsymbol{T} = \begin{bmatrix}\boldsymbol{T}_\mathsf{c} & T_\alpha\end{bmatrix} \in \mathbb{R}^{1\times 7}$, respectively, where $\boldsymbol{C}_\mathsf{c}$, $\boldsymbol{C}_\alpha$ and $\boldsymbol{T}_\mathsf{c}$, T_α are matrix forms of the tensors in Eq. (5.36) and Eq. (5.37) corresponding to the conventions mentioned in Chap. 2.

Remark 6.1 Note that $\boldsymbol{Z}_n \in \mathbb{R}^{7\times\mathsf{ndv}}$ automatically inherits the correct size depending on the design parametrization. That is, by assuming $\boldsymbol{h}_n = \boldsymbol{0}$ in the current time step t_{n+1}, only the partial variations w.r.t. displacements and design come into action. Therefore, the size of $\boldsymbol{Z}_n$ is prescribed by the size of the sensitivity matrix $\boldsymbol{S} \in \mathbb{R}^{\mathsf{ndof}\times\mathsf{ndv}}$. Depending on the choice of design variables, the corresponding sensitivity matrix is indicated with subscripts as follows. For geometric design $\boldsymbol{S}_X$ and $\boldsymbol{S}_p$ are used, while $\boldsymbol{S}_m$ is used in the case of constitutive design. Such a distinction is not made for the matrix $\boldsymbol{Z}_n$, as its size and meaning is obvious by context.

Geometric shape design. In the case of geometric design, the design variables can either be chosen as the nodal coordinates of the FE nodes, or mesh controlling control point coordinates based on a CAGD geometry description. The discrete versions of the update formulae for the variations of the internal variables $\boldsymbol{c}_\mathsf{p}$ and α, are respectively given by

$$\begin{aligned}\delta\boldsymbol{c}_\mathsf{p} &= \delta_u\boldsymbol{c}_\mathsf{p} + \delta_X\boldsymbol{c}_\mathsf{p} + \delta_{h_n}\boldsymbol{c}_\mathsf{p} = \overline{\boldsymbol{A}}_\mathsf{c}\,(\delta_u\boldsymbol{F} + \delta_X\overline{\boldsymbol{F}}) + \boldsymbol{C}\,\boldsymbol{Z}_n\,\delta\boldsymbol{X} \\ &= [\overline{\boldsymbol{A}}_\mathsf{c}\,(\overline{\boldsymbol{G}}\,\boldsymbol{S}_X - \overline{\boldsymbol{G}}^X) + \boldsymbol{C}\,\boldsymbol{Z}_n]\,\delta\boldsymbol{X}\end{aligned} \tag{6.29}$$

and

$$\begin{aligned}\delta\alpha &= \delta_u\alpha + \delta_X\alpha + \delta_{h_n}\alpha = \boldsymbol{A}_\alpha\,(\delta_u\boldsymbol{F} + \delta_X\boldsymbol{F}) + \boldsymbol{T}\,\boldsymbol{Z}_n\,\delta\boldsymbol{X} \\ &= [\overline{\boldsymbol{A}}_\alpha\,(\overline{\boldsymbol{G}}\,\boldsymbol{S}_X - \overline{\boldsymbol{G}}^X) + \boldsymbol{T}\,\boldsymbol{Z}_n]\,\delta\boldsymbol{X}.\end{aligned} \tag{6.30}$$

regarding the nodal mesh coordinates, or by

$$\begin{aligned}\delta\boldsymbol{c}_\mathsf{p} &= \delta_u\boldsymbol{c}_\mathsf{p} + \delta_p\boldsymbol{c}_\mathsf{p} + \delta_{h_n}\boldsymbol{c}_\mathsf{p} = \overline{\boldsymbol{A}}_\mathsf{c}\,(\delta_u\overline{\boldsymbol{F}} + \delta_p\overline{\boldsymbol{F}}) + \delta_{h_n}\boldsymbol{c}_\mathsf{p} \\ &= [\overline{\boldsymbol{A}}_\mathsf{c}\,(\overline{\boldsymbol{G}}\,\boldsymbol{S}_p - \overline{\boldsymbol{G}}^p) + \boldsymbol{C}\,\boldsymbol{Z}_n]\,\delta\boldsymbol{p}\end{aligned} \tag{6.31}$$

and

$$\begin{aligned}\delta\alpha &= \delta_u\alpha + \delta_p\alpha + \delta_{h_n}\alpha = \overline{\boldsymbol{A}}_\alpha\,(\delta_u\overline{\boldsymbol{F}} + \delta_p\overline{\boldsymbol{F}}) + \delta_{h_n}\alpha \\ &= [\overline{\boldsymbol{A}}_\alpha\,(\overline{\boldsymbol{G}}\,\boldsymbol{S}_p - \overline{\boldsymbol{G}}^p) + \boldsymbol{T}\,\boldsymbol{Z}_n]\,\delta\boldsymbol{p},\end{aligned} \tag{6.32}$$

where the gradient information w.r.t. the nodal coordinates are already transformed to the control point coordinates using the design velocity matrix. Here, $\overline{\boldsymbol{A}}_\mathsf{c}$ and $\overline{\boldsymbol{A}}_\alpha$ are matrix forms of the tensors in Eq. (5.30) and Eq. (5.32) evaluated for $\overline{\boldsymbol{F}}$, respectively. By definition of the matrices

$$\boldsymbol{A}_\mathsf{h} = \left[\frac{\partial \boldsymbol{h}}{\partial \boldsymbol{F}}\right] = \begin{bmatrix}\boldsymbol{A}_\mathsf{c} \\ \boldsymbol{A}_\alpha\end{bmatrix} \in \mathbb{R}^{7\times 9} \quad \text{and} \quad \boldsymbol{C}_\mathsf{h} = \left[\frac{\partial \boldsymbol{h}}{\partial \boldsymbol{h}_n}\right] = \begin{bmatrix}\boldsymbol{C} \\ \boldsymbol{T}\end{bmatrix} \in \mathbb{R}^{7\times 7}, \tag{6.33}$$

the update formulae can be written in compact form for the discrete vector of variations of history variables, cf. Eq. (6.15), and reads

$$\delta\boldsymbol{h} = \delta_u\boldsymbol{h} + \delta_X\boldsymbol{h} + \delta_{h_n}\boldsymbol{h} = [\overline{\boldsymbol{A}}_\mathsf{h}\,(\overline{\boldsymbol{G}}\,\boldsymbol{S}_X - \overline{\boldsymbol{G}}^X) + \boldsymbol{C}_\mathsf{h}\,\boldsymbol{Z}_n]\,\delta\boldsymbol{X} \tag{6.34}$$

or

$$\delta\boldsymbol{h} = \delta_u\boldsymbol{h} + \delta_p\boldsymbol{h} + \delta_{h_n}\boldsymbol{h} = [\overline{\boldsymbol{A}}_\mathsf{h}\,(\overline{\boldsymbol{G}}\,\boldsymbol{S}_p - \overline{\boldsymbol{G}}^p) + \boldsymbol{C}_\mathsf{h}\,\boldsymbol{Z}_n]\,\delta\boldsymbol{p} \tag{6.35}$$

depending on the chosen geometric design parametrization.

Constitutive design. The algorithmic update formulae in the case of constitutive design are given in Eq. (5.34) and Eq. (5.35) and in a discrete setting can be expressed by

$$\begin{aligned}\delta\boldsymbol{c}_\mathsf{p} &= \delta_u\boldsymbol{c}_\mathsf{p} + \delta_m\boldsymbol{c}_\mathsf{p} + \delta_{h_n}\boldsymbol{c}_\mathsf{p} = \overline{\boldsymbol{A}}_\mathsf{c}\,\delta_u\boldsymbol{F} + \overline{\boldsymbol{m}}_\mathsf{c}\,\delta\boldsymbol{m} + \boldsymbol{C}\,\boldsymbol{Z}_n\,\delta\boldsymbol{m} \\ &= \left[\overline{\boldsymbol{A}}_\mathsf{c}\,\overline{\boldsymbol{G}}\,\boldsymbol{S}_m + \overline{\boldsymbol{m}}_\mathsf{c} + \boldsymbol{C}\,\boldsymbol{Z}_n\right]\,\delta\boldsymbol{m}\end{aligned} \tag{6.36}$$

and

$$\begin{aligned}\delta\alpha &= \delta_u\alpha + \delta_m\alpha + \delta_{h_n}\alpha = \overline{\boldsymbol{A}}_\alpha\,\delta_u\boldsymbol{F} + \overline{\boldsymbol{m}}_\alpha\,\delta\boldsymbol{m} + \boldsymbol{T}\,\boldsymbol{Z}_n\,\delta\boldsymbol{m} \\ &= \left[\overline{\boldsymbol{A}}_\alpha\,\boldsymbol{G}\,\boldsymbol{S}_m + \overline{\boldsymbol{m}}_\alpha + \boldsymbol{T}\,\boldsymbol{Z}_n\right]\,\delta\boldsymbol{m},\end{aligned} \tag{6.37}$$

see also App. A.3.2 for details on the matrices $\overline{\boldsymbol{m}}_\mathsf{c}$ and $\overline{\boldsymbol{m}}_\alpha$. Note that the overlining notation is used here to indicate that these quantities have to be evaluated for $\overline{\boldsymbol{F}}$ for the present case that the $\overline{F}$-method is utilized to prevent volumetric locking. Analogously to the update formula in the geometric shape design case, with the definition of the matrix

$$\boldsymbol{m}_\mathsf{h} = \left[\frac{\partial \boldsymbol{h}}{\partial \boldsymbol{m}}\right] = \begin{bmatrix}\boldsymbol{m}_\mathsf{c} \\ \boldsymbol{m}_\alpha\end{bmatrix} \in \mathbb{R}^{7\times 6} \tag{6.38}$$

it is possible to formulate the compact form

$$\delta\boldsymbol{h} = \delta_u\boldsymbol{h} + \delta_m\boldsymbol{h} + \delta_{h_n}\boldsymbol{h} = \left[\overline{\boldsymbol{A}}_\mathsf{h}\,\boldsymbol{G}\,\boldsymbol{S}_m + \overline{\boldsymbol{m}}_\mathsf{h} + \boldsymbol{C}_\mathsf{h}\,\boldsymbol{Z}_n\right]\,\delta\boldsymbol{m}. \tag{6.39}$$

6.4 Discrete objective and constraint function sensitivity

The general variational form of any arbitrary physical function has been derived in Sec. 5.5. In the following the discrete counterparts are given and demonstrated on the two stress measures analogously to Sec. 5.5.2.

6.4.1 General discrete form

Recalling the general variational form of a physical functional, cf. Eq. (5.40), the implicit operators S and Z_n can be explicitly determined in the discrete setting. That is, as explained in Sec. 6.3.3, the sensitivity matrix $\boldsymbol{S}$ and the total design derivative matrix of the internal history variables $\boldsymbol{Z}_n$ are their discrete counterparts. Thus, the relations

$$\delta \boldsymbol{u} = \boldsymbol{S}\, \delta \boldsymbol{s} \quad \text{and} \quad \delta \boldsymbol{h}_n = \boldsymbol{Z}_n \delta \boldsymbol{s} \tag{6.40}$$

apply and the general discrete form of the total design variation of any physical quantity can be written as

$$\delta f = \frac{\partial f}{\partial \boldsymbol{s}}\, \delta \boldsymbol{s} + \frac{\partial f}{\partial \boldsymbol{u}}\, \delta \boldsymbol{u} + \frac{\partial f}{\partial \boldsymbol{h}_n}\, \delta \boldsymbol{h}_n = \left(\frac{\partial f}{\partial \boldsymbol{s}} + \frac{\partial f}{\partial \boldsymbol{u}}\, \boldsymbol{S} + \frac{\partial f}{\partial \boldsymbol{h}_n}\, \boldsymbol{Z}_n \right) \delta \boldsymbol{s}. \tag{6.41}$$

6.4.2 Discrete stress variations

As an example for the sensitivity computation of a physical quantity, the two stress measures already introduced in Sec. 5.5.2, i.e. the mean stress σ_{m} and the von Mises equivalent stress σ_{eq}, are considered. Recalling the continuous variations in Eq. (5.47), their discrete counterparts read

$$\delta \sigma_{\mathsf{m}} = \frac{1}{3}\, \boldsymbol{I}^T\, \delta \boldsymbol{\tau} \quad \text{and} \quad \delta \sigma_{\mathsf{eq}} = \frac{2}{3\, \sigma_{\mathsf{eq}}}\, \operatorname{dev} \boldsymbol{\tau}^T\, \delta \boldsymbol{\tau}, \tag{6.42}$$

where

$$\boldsymbol{I} = \begin{bmatrix} 1 & 1 & 1 & 0 & 0 & 0 \end{bmatrix}^{\mathsf{T}} \tag{6.43}$$

and

$$\operatorname{dev} \boldsymbol{\tau} = \begin{bmatrix} \operatorname{dev} \tau_{11} & \operatorname{dev} \tau_{22} & \operatorname{dev} \tau_{33} & \operatorname{dev} \tau_{12} & \operatorname{dev} \tau_{23} & \operatorname{dev} \tau_{31} \end{bmatrix}^T \tag{6.44}$$

are the column matrix forms of the identity tensor and the deviatoric Kirchhoff stress tensor, respectively. As already mentioned in Sec. 5.5.2, for both stress measures, the total variation of the Kirchhoff stresses is demanded. Its total variation in the discrete framework is given by

$$\delta \boldsymbol{\tau} = \delta_u \boldsymbol{\tau} + \delta_s \boldsymbol{\tau} + \delta_{h_n} \boldsymbol{\tau}. \tag{6.45}$$

Regardless of the choice of design parametrization, the partial variations of the Kirchhoff stress tensor w.r.t. the internal history variables have to be computed. The discrete

equation reads

$$\delta_{h_n} \boldsymbol{\tau} = \boldsymbol{D}_{\mathsf{c}}\, \delta \boldsymbol{c}_n^{\mathsf{p}} + \boldsymbol{D}_{\alpha}\, \delta \alpha_n = \boldsymbol{D}_{\mathsf{h}}\, \delta \boldsymbol{h}_n, \tag{6.46}$$

where $\boldsymbol{D}_{\mathsf{h}} = \begin{bmatrix} \boldsymbol{D}_{\mathsf{c}} & \boldsymbol{D}_{\alpha} \end{bmatrix} \in \mathbb{R}^{6\times 7}$ is a hypervector containing the matrix forms $\boldsymbol{D}_{\mathsf{c}} \in \mathbb{R}^{6\times 6}$ and $\boldsymbol{D}_{\alpha} \in \mathbb{R}^{6\times 1}$ of the tensors $\mathbb{D}_{\mathsf{c}}$ and $\mathbf{D}_{\alpha}$ from Eq. (5.53).
For the computations of the partial variations w.r.t. displacements and design, a distinction between the different design parametrizations has to be made.

Geometric shape design. In the case of geometric shape design, the discrete counterpart of the total variation in Eq. (5.49) is given by

$$\begin{aligned} \delta \boldsymbol{\tau} &= \overline{\boldsymbol{a}}\, (\delta_u \overline{\boldsymbol{F}} + \delta_X \overline{\boldsymbol{F}}) + \boldsymbol{D}\, \boldsymbol{Z}_n\, \delta \boldsymbol{X} \\ &= [\overline{\boldsymbol{a}}\, (\overline{\boldsymbol{G}}\, \boldsymbol{S}_X - \overline{\boldsymbol{G}}^{X}) + \boldsymbol{D}\, \boldsymbol{Z}_n]\, \delta \boldsymbol{X}, \end{aligned} \tag{6.47}$$

or by means of a mesh controlling geometry description

$$\begin{aligned} \delta \boldsymbol{\tau} &= \overline{\boldsymbol{a}}\, (\delta_u \overline{\boldsymbol{F}} + \delta_p \overline{\boldsymbol{F}}) + \boldsymbol{D}\, \boldsymbol{Z}_n\, \delta \boldsymbol{p} \\ &= [\overline{\boldsymbol{a}}\, (\overline{\boldsymbol{G}}\, \boldsymbol{S}_p - \overline{\boldsymbol{G}}^{p}) + \boldsymbol{D}\, \boldsymbol{Z}_n]\, \delta \boldsymbol{p}, \end{aligned} \tag{6.48}$$

with the discrete vector of control point coordinates $\boldsymbol{p}$. Here,

$$\overline{\boldsymbol{a}} := \left[\frac{\partial \overline{\boldsymbol{\tau}}}{\partial \overline{\boldsymbol{F}}} \right] \tag{6.49}$$

represents the matrix form of the tensor $\mathbf{a}$ in Eq. (5.52) evaluated at $\overline{\boldsymbol{F}}$.

Constitutive design. In the case of constitutive design, the discrete counterpart of the total variation in Eq. (5.50) reads

$$\begin{aligned} \delta \boldsymbol{\tau} &= \overline{\boldsymbol{a}}\, \delta_u \overline{\boldsymbol{F}} + \delta_m \boldsymbol{\tau} + \boldsymbol{D}\, \boldsymbol{Z}_n\, \delta \boldsymbol{p} \\ &= [\overline{\boldsymbol{a}}\, \overline{\boldsymbol{G}}\, \boldsymbol{S}_p + \overline{\boldsymbol{M}}_{\tau} + \boldsymbol{D}\, \boldsymbol{Z}_n]\, \delta \boldsymbol{m}, \end{aligned} \tag{6.50}$$

where $\overline{\boldsymbol{M}}_{\tau}$ is the matrix form of the tensor $\underline{\mathbf{M}}_{\tau}$ in Eq. (5.51) evaluated at $\overline{\boldsymbol{F}}$ and has the same structure as the matrix $\boldsymbol{M}$ in Eq. (A.38) with the only difference that $\boldsymbol{\tau}$ is symmetric and therefore its rows are sorted in the symmetric way, cf. Sec. 2.1.2.

6.5 Numerical implementation

In the following, some fundamental details on the numerical implementation are presented. First, the global staggered procedure to compute the demanded global sensitivities is explained. Further, the necessary computations on finite element level are briefly summarized. Subsequently, the necessary augmentation of the stress projection algorithm for the consistent local sensitivity computations are sketched. Finally, a semi-analytical method

is presented that preserves the overall framework but replaces some complex analytical derivatives by numerical difference quotients by means of the finite difference method.

6.5.1 Staggered computation procedure

Reviewing previous sections in this chapter, it becomes clear that the sensitivity information of the global structural response has to be known to be able to compute the sensitivity information of any physical quantity that might act as objective or constraint function within an optimization task. This motivates the staggered computation procedure. That is, firstly, the element contributions of the pseudoload and history sensitivity matrices are assembled to their global counterparts. Secondly, the global response sensitivity matrix is calculated by solving Eq. (6.23). Finally, the element contributions of any arbitrary physical function sensitivity can be computed and assembled to the global quantity. Note that it is important to update the history variables as well as their sensitivity information afterwards and not before any of the mentioned steps. Fig. 6.1 summarizes the necessary steps in pseudocode format. Note that for the different tasks on finite element level, task switches (`tsw`) are introduced. That is, the task switches distinguish between computing response sensitivities (`'res_sens'`), update history sensitivities (`'upd_hist'`), or compute objective or constraint sensitivities (`'obj_constr'`).

Remark 6.2 (Element design velocity matrix) For the case of geometric shape design, it is convenient to evaluate the global design velocity matrix for each finite element and project sensitivity information from nodal FE coordinates to the chosen geometry description. This reduces respective matrix sizes of all geometric sensitivities and therefore saves memory as the sensitivity information of the internal variables has to be saved at the end of each pseudo time step. This does not hold true if the number of design variables is higher than the number of degrees of freedom in the finite element model ($\mathsf{ndv} > \mathsf{dof}$).

6.5.2 Computation of element contributions

On finite element level, the element contributions of the pseudoload and history sensitivity matrices have to be computed, as well as the physical function sensitivity and the updates of the internal variable sensitivity, depending on the corresponding task that is identified by means of the value of the task switch (`tsw`), cf. Sec 6.5.1. In Fig. 6.2 the respective computations are presented in pseudocode format. Note that an additional sensitivity switch (`ssw`) is introduced to distinguish between geometric (`'geo'`) and constitutive (`'mat'`) design variables.

6.5.3 Augmentation of the stress projection algorithm

In the context of the presented approach, it is necessary to enhance the return mapping algorithm, cf. Fig. 4.3, to additionally compute the demanded gradients in the context of design sensitivity analysis. That is, besides the stress projection and the consistent tangent, the algorithm has to compute additional partial variations depending on the respective task switch (`tsw`).

Computation of global design sensitivities

Input: $\{\texttt{ssw}, \boldsymbol{X}, \boldsymbol{m}, \boldsymbol{K}, \boldsymbol{u}, \mathcal{H}_n, \boldsymbol{D}^{\mathsf{v}}\}$

// Assemble pseudo load and history sensitivity matrices
▷ Element loop
1: **for** $ie = 1 : \mathsf{nel}$
2: **Set** `tsw = 'res_sens'`
▷ Call to element routine
3: $\{\boldsymbol{P}_{ie}, \boldsymbol{Q}_{ie}\} \leftarrow \text{ELEMENT}(\texttt{tsw}, \texttt{ssw}, \boldsymbol{m}, \boldsymbol{u}[ie], \mathcal{H}_n[ie], \boldsymbol{D}^{\mathsf{v}}[ie], [\,])$
▷ Assemble $\boldsymbol{P}$ and $\boldsymbol{Q}$
4: $\boldsymbol{P}[ie] \leftarrow \boldsymbol{P}[ie] + \boldsymbol{P}_{ie}$
5: $\boldsymbol{Q}[ie] \leftarrow \boldsymbol{Q}[ie] + \boldsymbol{Q}_{ie}$
6: **end for**

// Solve global response sensitivity
▷ Global sensitivity matrix
7: $\boldsymbol{S} = -\boldsymbol{K}^{-1}(\boldsymbol{P} + \boldsymbol{Q})$

// Assemble physical function and sensitivity and update history field
▷ Element loop
8: **for** $ie = 1 : \mathsf{nel}$
9: **Set** `tsw = 'obj_constr'`
▷ Call to element routine
10: $\{\boldsymbol{f}_{ie}, \nabla \boldsymbol{f}_{ie}\} \leftarrow \text{ELEMENT}(\texttt{tsw}, \texttt{ssw}, \boldsymbol{m}, \boldsymbol{u}[ie], \mathcal{H}_n[ie], \boldsymbol{D}^{\mathsf{v}}[ie], \boldsymbol{S}[ie])$
▷ Assemble physical function and gradient
11: $\boldsymbol{f}[ie] \leftarrow \boldsymbol{f}[ie] + \boldsymbol{f}_{ie}$
12: $\nabla \boldsymbol{f}[ie] \leftarrow \nabla \boldsymbol{f}[ie] + \nabla \boldsymbol{f}_{ie}$
13: **Set** `tsw = 'upd_hist'`
▷ Call to element routine
14: $\{\boldsymbol{h}_{ie}, \boldsymbol{Z}_{ie}\} \leftarrow \text{ELEMENT}(\texttt{tsw}, \texttt{ssw}, \boldsymbol{m}, \boldsymbol{u}[ie], \mathcal{H}_n[ie], \boldsymbol{D}^{\mathsf{v}}[ie], \boldsymbol{S}[ie])$
▷ Assemble history field
15: $\mathcal{H}[ie] \leftarrow \{\boldsymbol{h}_{ie}, \boldsymbol{Z}_{ie}\}$
16: **end for**

Output: $\{\boldsymbol{f}, \nabla \boldsymbol{f}, \boldsymbol{S}, \mathcal{H}\}$

Figure 6.1: Staggered global design sensitivity computation procedure.

Computation of element design sensitivities

function ELEMENT(tsw,ssw$\boldsymbol{X}_{ie}$,$\boldsymbol{m}$,$\boldsymbol{u}_{ie}$,$\mathcal{H}_{n,ie}$)

  Load $\{\boldsymbol{h}_n,\boldsymbol{Z}_n\} \leftarrow \mathcal{H}_{n,ie}$
  ▷ Compute isoparametric shape functions and gradient operators
  $\{\boldsymbol{G},\boldsymbol{L},\det J\} \leftarrow (\boldsymbol{X})$
  ▷ Compute modified deformation gradient and gradient operators
  $\{\overline{\boldsymbol{F}},\overline{\boldsymbol{G}},\overline{\boldsymbol{G}}^X\} \leftarrow (\boldsymbol{u}_{ie},\boldsymbol{G})$
  ▷ Integration loop
  for $ip = 1 :$ ngp
  ▷ Volume element
    $\mathrm{d}V = \det J\, w_{ip}$
    switch tsw
      case 'res_sens'
        $\{\overline{\boldsymbol{P}}^{\mathsf{K}},\overline{\boldsymbol{A}},\overline{\boldsymbol{q}},\overline{\boldsymbol{M}}\} \leftarrow$ STRESS_PROJ_SENS(tsw,$\boldsymbol{m}$,$\overline{\boldsymbol{F}}$,$\boldsymbol{h}_n[ip]$)
        switch ssw
          case 'geo'
            $\boldsymbol{P}_{ie} = \boldsymbol{P}_{ie} - \boldsymbol{G}^T\,\boldsymbol{A}\,\overline{\boldsymbol{G}}^X - \overline{\mathbf{P}}^{\mathsf{K}}(\sum_i \sum_j \boldsymbol{L}_j \boldsymbol{L}_i^T - \boldsymbol{L}_i\,\boldsymbol{L}_j^T)\,\mathrm{d}V$
          case 'mat'
            $\boldsymbol{P}_{ie} = \boldsymbol{P}_{ie} + \boldsymbol{G}^T\,\overline{\boldsymbol{M}}\,\mathrm{d}V$
        end switch ▷ ssw
        $\boldsymbol{Q}_{ie} = \boldsymbol{Q}_{ie} + \boldsymbol{G}^T\,\boldsymbol{q}\,\boldsymbol{Z}_n[ip]\,\mathrm{d}V$
      case 'upd_hist'
        $\{\overline{\boldsymbol{A}}_{\mathsf{h}},\overline{\boldsymbol{m}}_{\mathsf{h}},\overline{\boldsymbol{C}}_{\mathsf{h}},\boldsymbol{h}[ip]\} \leftarrow$ STRESS_PROJ_SENS(tsw,$\boldsymbol{m}$,$\overline{\boldsymbol{F}}$,$\boldsymbol{h}_n[ip]$)
        switch ssw
          case 'geo'
            $\boldsymbol{Z}_{ie}[ip] = \overline{\boldsymbol{A}}_{\mathsf{h}}\,(\overline{\boldsymbol{G}}\,\boldsymbol{S}_{ie} - \overline{\boldsymbol{G}}^X) + \overline{\boldsymbol{C}}_{\mathsf{h}}\,\boldsymbol{Z}_n[ip]$
          case 'mat'
            $\boldsymbol{Z}_{ie}[ip] = \overline{\boldsymbol{A}}_{\mathsf{h}}\,\overline{\boldsymbol{G}}\,\boldsymbol{S}_{ie} + \overline{\boldsymbol{m}}_{\mathsf{h}} + \overline{\boldsymbol{C}}_{\mathsf{h}}\,\boldsymbol{Z}_n[ip]$
        end switch ▷ ssw
      case 'obj_constr'
        $\{\overline{\boldsymbol{\tau}},\overline{\boldsymbol{a}},\overline{\boldsymbol{M}}_\tau,\boldsymbol{D}\} \leftarrow$ STRESS_PROJ_SENS(tsw,$\boldsymbol{m}$,$\boldsymbol{F}$,$\boldsymbol{h}_n[ip]$)
        $\sigma_{\mathsf{eq}}[ip] = \sqrt{\frac{3}{2}\,\mathrm{dev}\,\boldsymbol{\tau}^T \mathrm{dev}\,\boldsymbol{\tau}}$
        switch ssw
          case 'geo'
            $\nabla\sigma_{\mathsf{eq}}[ip] = \frac{3}{2\,\sigma_{\mathsf{eq}}}\,\mathrm{dev}\,\boldsymbol{\tau}^T\,(\overline{\boldsymbol{a}}\,(\overline{\boldsymbol{G}}\,\boldsymbol{S} - \overline{\boldsymbol{G}}^X) + \boldsymbol{D}\,\boldsymbol{Z}_n[ip])$
          case 'mat'
            $\nabla\sigma_{\mathsf{eq}}[ip] = \frac{3}{2\,\sigma_{\mathsf{eq}}}\,\mathrm{dev}\,\boldsymbol{\tau}^T\,(\overline{\boldsymbol{a}}\,\overline{\boldsymbol{G}}\,\boldsymbol{S} + \overline{\boldsymbol{M}}_\tau + \boldsymbol{D}\,\boldsymbol{Z}_n[ip])$
        end switch ▷ ssw
    end switch ▷ tsw
  end for

  return $(\boldsymbol{R}_{ie},\boldsymbol{K}_{ie},\boldsymbol{P}_{ie},\boldsymbol{Q}_{ie},\mathcal{H}_{ie},\boldsymbol{\tau},\nabla\boldsymbol{\tau})$

Figure 6.2: Essential design sensitivity computations on finite element level.

Computation of stress projection design sensitivities

Input: $\{\texttt{tsw}, \boldsymbol{m}, \boldsymbol{F}, \boldsymbol{h}_n^{ip}\}$

// Apply standard stress projection algorithm, cf. Fig. 4.3

$\{\boldsymbol{P}^{\mathsf{K}}, \boldsymbol{A}, \boldsymbol{h}^{ip}\} \leftarrow \text{STRESS\_PROJECTION}(\boldsymbol{m}, \boldsymbol{F}, \boldsymbol{h}_n^{ip})$

// Compute additional sensitivity information

switch `tsw`

  case `'res_sensi'`

  ▷ Additional matrix forms for response sensitivity

    $\boldsymbol{q} = \left[\dfrac{\partial \boldsymbol{P}^{\mathsf{K}}}{\partial \boldsymbol{h}_n^{ip}}\right]$, see Eq. (6.17)

    switch `ssw`

      case `'mat'`

        $\boldsymbol{M} = \left[\dfrac{\partial \boldsymbol{P}^{\mathsf{K}}}{\partial \boldsymbol{m}}\right]$, see Eq. (A.38)

    end switch

  case `'upd_hist'`

  ▷ Additional matrix forms for history sensitivity update

    $\boldsymbol{A}_{\mathsf{h}} = \left[\dfrac{\partial \boldsymbol{h}^{ip}}{\partial \boldsymbol{F}}\right]$ and $\boldsymbol{C}_{\mathsf{h}} = \left[\dfrac{\partial \boldsymbol{h}^{ip}}{\partial \boldsymbol{h}_n^{ip}}\right]$ see Eq. (6.33)

    switch `ssw`

      case `'mat'`

        $\boldsymbol{m}_{\mathsf{h}} = \left[\dfrac{\partial \boldsymbol{h}^{ip}}{\partial \boldsymbol{m}}\right]$, see Eq. (6.38)

    end switch

  case `'obj_constr'`

  ▷ Additional matrix forms for obj/constr sensitivity

    $\boldsymbol{a} = \left[\dfrac{\partial \boldsymbol{\tau}}{\partial \boldsymbol{F}}\right]$ and $\boldsymbol{D}_{\mathsf{h}} = \left[\dfrac{\partial \boldsymbol{\tau}}{\partial \boldsymbol{h}_n^{ip}}\right]$, see Eq. (6.49) and Eq. (6.46)

    switch `ssw`

      case `'mat'`

        $\boldsymbol{M}_{\tau} = \left[\dfrac{\partial \boldsymbol{\tau}}{\partial \boldsymbol{m}}\right]$, see Eq. (6.50)

    end switch

end switch

Output: $\{\boldsymbol{P}^{\mathsf{K}}, \boldsymbol{A}, \boldsymbol{q}, \boldsymbol{M}, \boldsymbol{A}_{\mathsf{h}}, \boldsymbol{m}_{\mathsf{h}}, \boldsymbol{C}_{\mathsf{h}}, \boldsymbol{\tau}, \boldsymbol{a}, \boldsymbol{M}_{\tau}, \boldsymbol{D}\}$

Figure 6.3: Design sensitivity augmentations on stress projection level.

6.5.4 Semi-analytical computations

In this section a semi-analytical approach is discussed in which parts of the necessary sensitivity information is computed numerically by means of the finite difference method. Strictly speaking, only parts of the matrix forms that represent partial design and history derivatives on stress projection level are numerically determined. Therefore, the overall framework for the computation of sensitivity information as explained previously on element and global level still keeps its structure. For reasons of brevity, the presented semi-analytical approach focuses only on geometric design parametrizations. However, it can easily be adapted to any type of design parametrization. Although basically any quantity that is an outcome of the stress projection algorithm can be derived numerically, in this approach it is assumed that the consistent analytical tangent stiffness operator is known, which also implies the knowledge of the partial derivatives of the internal history variables w.r.t. the deformation, e.g. in form of the deformation gradient. Thus, the explicit matrix forms representing the demanded partial derivatives that are numerically obtained are $\boldsymbol{q}$ and $\boldsymbol{C}_{\mathsf{h}}$. Additionally, considering a stress measure depending on the Kirchhoff stress tensor as objective or constraint function, the matrix $\boldsymbol{D}_{\mathsf{h}}$ can be obtained numerically. Instead of computing the analytically derived matrix forms as shown in line 9 of Fig. 6.2, a local finite difference scheme is deployed for the numerical determination of the demanded derivatives. In Fig. 6.4, the specific changes of the algorithm to incorporate the semi-analytical approach are highlighted. Note that of course the computations of the sensitivity information regarding the internal variables as shown in Fig. 6.3 in the semi-analytical case becomes redundant. That is, the part of the algorithm on finite element level sketched in Fig. 6.4 replaces lines `9,18` and `26` in Fig. 6.2. Note that only the standard stress projection algorithm, cf. Fig. 4.3, has to be conducted.
The major advantages of the semi-analytical approach are on the one hand its implementation simplicity and on the other hand it offers the possibility to consider different constitutive laws that describe micromechanical phenomena by means of local internal variables, as in the elastoplasic model deployed in this work. However, it comes with additional computational cost, as many evaluations on the lowest algorithmic level have to be performed. At the end of the following section the analytical and the semi-analytical approaches are compared in terms of accuracy and performance considering the elastoplastic constitutive model explained in Chap. 4.

6.6 Benchmarks

This section aims at verifying the accuracy of the presented variational approach of the computation of elastoplastic design sensitivity information. For this, firstly the analytical partial derivatives on stress projection level are compared with the solution of the numerical finite difference method. Secondly, a benchmark example is chosen so as to verify the analytical global response sensitivity accuracy. Finally, a constrained shape optimization problem is conducted.

Computation of element design sensitivities (semi-analytical)

```
1:  function ELEMENT(tsw,sswX_ie,m,u_ie,H_{n,ie})
2:      Load {h_n,Z_n} ← H_{n,ie}
  ...
9:      {P^K,A,h^ip} ← STRESS_PROJECTION(m,F,h_n^ip)
9.1:    for i_h = 1 : nhv
9.2:        h_n^ip+[i_h] = h_n^ip[i_h] + ε
9.3:        switch tsw
9.4:            case 'res_sensi'
9.5:                {P̄^K+} ← STRESS_PROJECTION(m,F,h_n^ip+)
9.6:                q̄[i_h] = (P̄^K+ − P̄^K) /ε
9.7:            case 'update_history'
9.8:                {h^ip+} ← STRESS_PROJECTION(m,F,h_n^ip+)
9.9:                C_h[i_h] = (h^ip+ − h̄^ip) /ε
9.10:           case 'obj_constr'
9.11:               {τ^ip+} ← STRESS_PROJECTION(m,F,h_n^ip+)
9.12:               D_h[i_h] = (τ^ip+ − τ̄^ip) /ε
9.13:       end switch
9.14:   end for
  ...
```

Figure 6.4: Algorithmic changes on finite element level for semi-analytical approach.

Stress projection level

To test the derived partial design derivatives on stress projection level, a randomly chosen deformation gradient that leads to an elastoplastic stress update is prescribed

$$F_{\text{test}} = \begin{bmatrix} 0.991 & -0.019 & 0.000 \\ 0.026 & 1.084 & 0.000 \\ 0.400 & -0.100 & 1.000 \end{bmatrix}. \tag{6.51}$$

The values of the internal history variables are initialized to

$$\boldsymbol{c}^{\text{p}} = \begin{bmatrix} 1.028 & 0.642 & 1.117 & -0.043 & 0.032 & -0.106 \end{bmatrix}^T \quad \text{and} \quad \alpha = 0.142 \tag{6.52}$$

and the constitutive parameters are the same as in the examples in Chap. 4. The method of finite differences is used to verify the accuracy of the analytically derived design sensitivities of the stress tensors $\boldsymbol{P}^{\text{K}}$ and $\boldsymbol{\tau}$, as well as the internal history variables $\boldsymbol{h} = \{\boldsymbol{c}^{\text{p}}, \alpha\}$. Therefore, the demanded partial derivatives of the mentioned quantities w.r.t. the deformation gradient $\boldsymbol{F}$, the internal history variables of the prior load step and the constitutive parameters are numerically approximated. These quantities correspond to the matrices $\boldsymbol{A}$, $\boldsymbol{A}_{\text{h}}$, $\boldsymbol{a}$ and $\boldsymbol{q}$, $\boldsymbol{C}_{\text{h}}$, $\boldsymbol{D}_{\text{h}}$, as well as $\boldsymbol{M}$, $\boldsymbol{m}_{\text{h}}$, $\boldsymbol{M}_{\tau}$ in Fig. 6.3, respectively. Fig. 6.5

shows the relative error

$$e_{\boldsymbol{x}}^{\mathsf{rel}} = \frac{\|\boldsymbol{x}_{\mathsf{an}} - \boldsymbol{x}_{\mathsf{num}}\|}{\|\boldsymbol{x}_{\mathsf{num}}\|} \tag{6.53}$$

between the analytical solution matrix $\boldsymbol{x}_{\mathsf{an}}$ and the corresponding numerical solution matrix $\boldsymbol{x}_{\mathsf{num}}$ obtained by a central finite difference scheme, for different perturbation values ranging from $\varepsilon \in [1 \times 10^{-14}, \dots, 1 \times 10^{-1}]$. By examining each sub-figure individually, it can clearly be observed that the smallest relative errors for all three quantities correspond to almost the same perturbation value. That is, for the partial derivatives w.r.t. the deformation gradient and the internal history variables, the best numerical results are obtained for perturbation values between $\varepsilon \approx 1 \times 10^{-6}$ and $\varepsilon \approx 1 \times 10^{-4}$, while for the partial derivatives w.r.t. the constitutive parameters best results correspond to perturbation values between $\varepsilon \approx 1 \times 10^{-4}$ and $\varepsilon \approx 1 \times 10^{-5}$. Below and above these values, the relative errors increase and the numerical results become inaccurate. Note that the optimal perturbation size might change with the variation of any model parameter, i.e. in most cases they are not known in advance. This emphasizes the convenience of the proposed variational approach for the analytical derivation, as the results are independent of the choice of numerical parameters.

Global and element level

The accuracy of the global and element matrices representing different design sensitivities is verified by means of the comparison with numerical results obtained utilizing a central finite difference scheme. In this case, a benchmark example of a flat uniaxial tensile test specimen is conducted and the partial derivatives w.r.t. geometric shape and constitutive design are examined. The 200 mm long specimen has a width of 50 mm and a thickness of 2 mm and has a central hole with a 10 mm diameter. Due to symmetry, only one octant of the geometry has to be modelled. In Fig. 6.6 the specimen B-Spline geometry model and the finite element mesh with indicated symmetric boundary conditions are illustrated. In total, 20 control points (CP) define the geometry, of which the $\mathsf{ndv} = 17$ indicated by the red circles are chosen as design variables, see also Tab. 6.1. Corresponding `MATLAB` code for the construction of the geometry description and the finite element mesh, as well as the corresponding design velocity matrix utilizing the NURBS Toolbox, is given in Fig. B.1 in App. B.1. In this benchmark example, a displacement of 3 mm is applied at the outer edge of the specimen within 20 linear increasing steps. Subsequently, 60 % of the applied displacement is released also within 20 linear steps, so as to construct a loading/unloading scenario. The chosen initial constitutive parameters are $K = 54.17\,\mathrm{GPa}$, $G = 25\,\mathrm{GPa}$, $\sigma_0 = 340\,\mathrm{MPa}$, $\sigma_\infty = 480\,\mathrm{MPa}$, $d = 25.5$, $H = 650\,\mathrm{MPa}$. The global quantities that are tested are the global pseudoload and history sensitivity matrices $\boldsymbol{P}$ and $\boldsymbol{Q}$, the global sensitivity matrix $\boldsymbol{S}$, as well as the gradient of the von Mises stresses $\nabla\sigma_{\mathsf{eq}}$ representing a physical function. Note that it is not possible to directly test the history sensitivity matrix within a finite difference scheme. Therefore, its values are indirectly computed by means of Eq. (6.23). Rearranging this equation and inserting the finite difference approximations of the pseudoload matrix and the sensitivity matrix, as well as the analytical stiffness

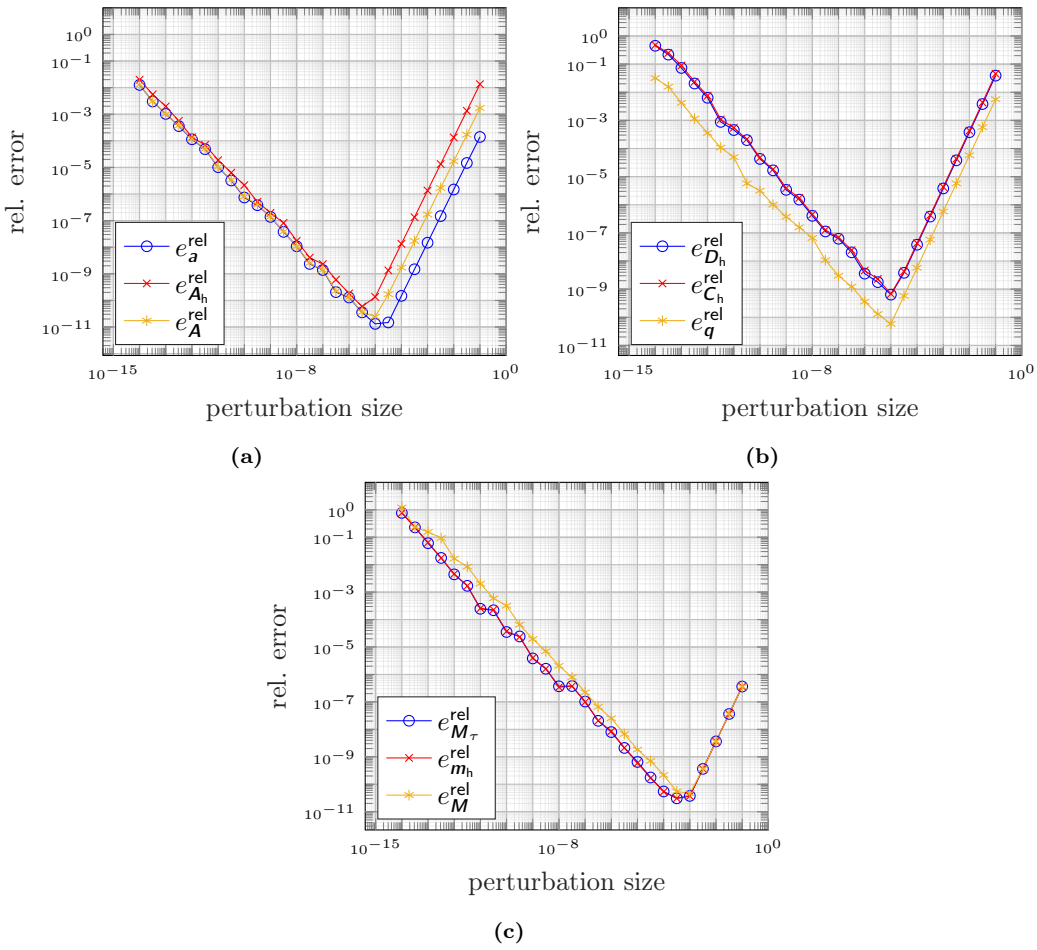

Figure 6.5: Sensitivity verifications: Relative error on stress projection level. Partial derivatives, (a) w.r.t. deformation gradient [$\boldsymbol{A}$, $\boldsymbol{A}_\mathrm{h}$ and $\boldsymbol{a}$], (b) w.r.t. prior internal history variables [$\boldsymbol{q}$, $\boldsymbol{C}_\mathrm{h}$ and $\boldsymbol{D}_\mathrm{h}$], (c) w.r.t. constitutive parameters [$\boldsymbol{M}$, $\boldsymbol{m}_\mathrm{h}$, $\boldsymbol{M}_\tau$].

matrix leads to the following approximation of the history sensitivity matrix

$$\boldsymbol{Q}_\mathrm{fd} = \boldsymbol{K}\,\boldsymbol{S}_\mathrm{fd} - \boldsymbol{P}_\mathrm{fd}. \tag{6.54}$$

A central finite difference scheme is used and the respective relative errors are computed following Eq. (6.53) and are plotted over the total 40 linear load steps in Fig. 6.7. It can clearly be seen that the error increases drastically at load step 16. At this point the necking phenomenon elevates and large plastic deformations occur. The clearly recognizable increased error can be explained by the fact that the method of finite differences no longer delivers adequate results in this region, since very small design changes have very large

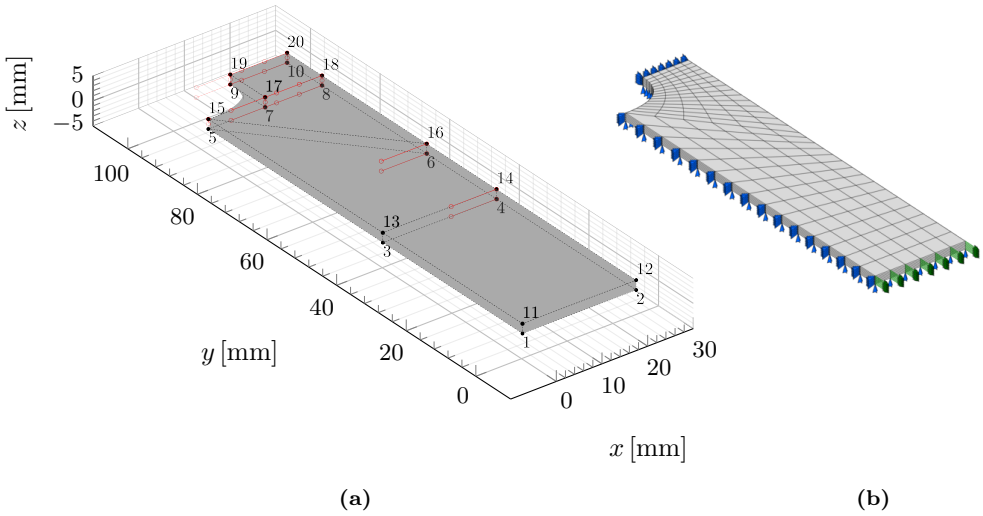

Figure 6.6: Uniaxial tensile test specimen: Initial design, (a) geometry model, (b) FE mesh and boundary conditions.

effects on the structural behavior. Contrary, the accuracy of the analytical variational approach is not to be doubted, as the error decreases after load step 16 and the sensitivity information provided depends on the values of the prior load steps within the implicit time integration scheme. That is, an error in the analytical approach would have increased over time. Therefore, this emphasizes the superiority of the analytical variational approach as it is numerically more efficient and delivers much more accurate and reliable sensitivity information independent from the choice of numerical parameters.

Constrained shape optimization

In this section the shape of the uniaxial tensile test specimen represented by a B-Spline geometry description, cf. Fig. 6.6, is optimized. The aim of the optimization is to increase plastic strain localization in the central zone of the specimen, while limiting the stress intensity in the end zone of the specimen. Therefore, the accumulative plastic strain values in the central area of the specimen are collected into a vector $\boldsymbol{\alpha}^{\mathsf{c}}$ and its length is maximized. The central specimen zone is defined by all FE nodes located at $y \geq 85\,\mathrm{mm}$. Additionally, inequality constraints on the values of the equivalent von Mises stress are chosen to eliminate any plastic deformations in the end zone, which contrary to the central zone is defined by all FE nodes located at $y < 85\,\mathrm{mm}$. Furthermore, the central specimen cross section area A^{cs} must not be less than $10\,\mathrm{mm}^2$ and shall remain a regular rectangle. For the structural analysis problem, in this case no unloading is considered and the number of load steps is increased to 200 ensuring stability of the implicit structural mechanical solution algorithm, as considerably higher plastic deformations can be expected. The

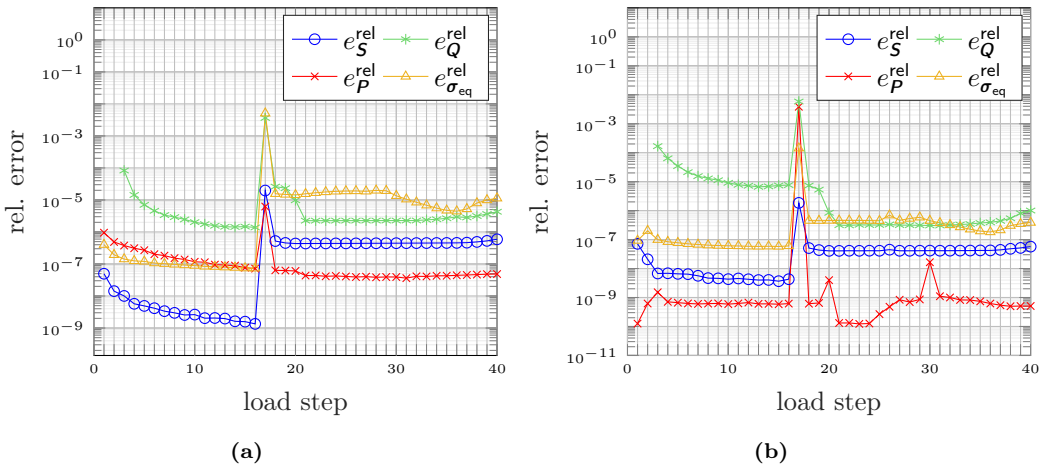

Figure 6.7: Sensitivity verifications: Relative error on global level, (a) geometric shape design, (b) constitutive design.

optimization problem reads

$$\begin{aligned} \max \quad & J(\boldsymbol{s}) = \|\boldsymbol{\alpha}^{\mathsf{c}}(\boldsymbol{s})\|_2^2 \\ \text{s.t.} \quad & \sigma_{\mathsf{eq}}^k \leq 340\,\mathrm{MPa}, \quad k = 1,\ldots,n_k \\ & A^{\mathsf{cs}} \geq 10\,\mathrm{mm}^2, \qquad \boldsymbol{A}^{\mathsf{lin}}\,\boldsymbol{s} = \boldsymbol{0}, \quad \boldsymbol{s}^l \leq \boldsymbol{s} \leq \boldsymbol{s}^u, \end{aligned} \tag{6.55}$$

with appropriate lower and upper bounds on the chosen design variables, given in Tab. 6.1. The matrix $\boldsymbol{A}^{\mathsf{lin}}$ represents a set of linear equality constraints to ensure the rectangular cross section shape, i.e. to ensure $9x = 19x$, $10x = 20x$, $19z = 20z$. The solution of the problem is obtained utilizing the SQP algorithm provided by the `MATLAB` function `fmincon`. The two solution methods developed in this work, i.e. the analytical and the semi-analytical approach, are employed and the results are compared in terms of accuracy and computational efficiency. Note that for the semi-analytical approach a central finite difference scheme with a perturbation size of 1×10^{-6} is used. The resulting optimal geometry and the corresponding FE mesh are illustrated in Fig. 6.8. The history of the objective function values are plotted in Fig. 6.9(a). Note that the objective function values are plotted negatively as the maximization problem is transformed to a minimization problem by inverting the sign of the scalar objective function. Providing gradient information based on the semi-analytical approach obviously results in less accuracy, which becomes clear by comparing the number of iterations needed to find the optimum. Using the semi-analytical approach, 25 iterations are necessary to finally reach convergence, while in the analytical approach only 9 iterations are necessary. In total, the analytical approach has been ~ 2.5 times faster in terms of measured CPU time. Thus, it is obvious that the analytical approach is numerically much more efficient than the semi-analytical approach and additionally provides most accurate results. However, the semi-analytical

approach does not require deep knowledge on the underlying mechanical model and can easily be implemented. It also delivers reliable results, whereby particular attention must be paid to the perturbation size and the type of finite difference scheme. In some cases, the forward and backward FDM might not be accurate enough and the optimization might fail. The central finite difference scheme used in this benchmark example constitutes the most accurate but also most time consuming FDM scheme. Furthermore, a good choice for the perturbation size is generally not known in advance. Therefore, some studies are necessary in advance.

In Tab. 6.1, the optimal values of the chosen design variables are shown. Additionally, in Fig. 6.9(b), the full initial and optimal geometries are plotted, as well as the accumulative plastic strain contribution and the equivalent von Mises stress contribution. The optimal design is characterized by a smooth notch in thickness direction and a tapered central zone leading to a decreased cross section area. Both results in triggering localization in the central zone of the specimen, which has been the goal of the shape optimization. Additionally, it can be seen that the von Mises stress distribution in the end zone of the optimized specimen has been drastically decreased compared to the initial design of the specimen. The value of the objective function could be increased from $J^{\mathsf{init}} = 4.5184$ to $J^{\mathsf{opt}} = 9.04$, which is a relative change of $\sim 100\,\%$. Additionally, the cross section area has a value of $A^{\mathsf{cs}} = 10\,\mathrm{mm}$, which intuitively makes sense from an engineering point of view, as the highest stresses can be expected for the lowest possible area. The chosen stress constraints on the von Mises stresses at the FE nodes in the end zone of the specimen have entirely been fulfilled and the constraint violation value could be decreased from 20 to 0.

Table 6.1: Uniaxial specimen optimization: Design variables.

DV No.	CP No.	Direction	s^l	s^u	s^{init}	s^{opt}
1	4	x	15	25	25	25
2	6	x	15	25	25	25
3	7	x	5	20	12.5	10
4	8	x	15	25	25	15
5	9	x	5	20	12.5	10
6	10	x	15	25	25	15
7	14	x	15	25	25	25
8	16	x	15	25	25	25
9	17	x	5	20	12.5	10
10	18	x	15	25	25	15
11	19	x	5	20	12.5	10
12	20	x	15	25	25	15
13	15	z	1	2	2	2
14	17	z	1	2	2	1
15	18	z	1	2	2	1
16	19	z	1	2	2	1
17	20	z	1	2	2	1

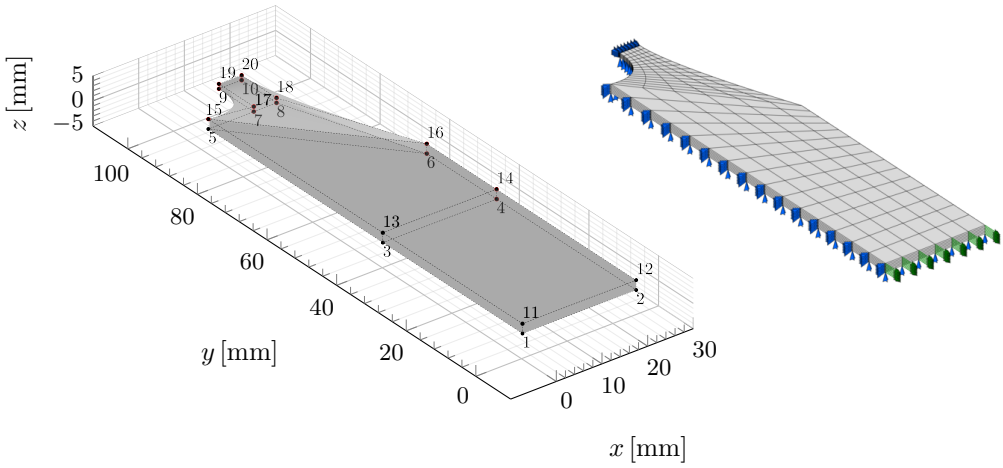

(a) **(b)**

Figure 6.8: Uniaxial specimen optimization: Optimal design, (a) geometry model, (b) FE mesh and boundary conditions.

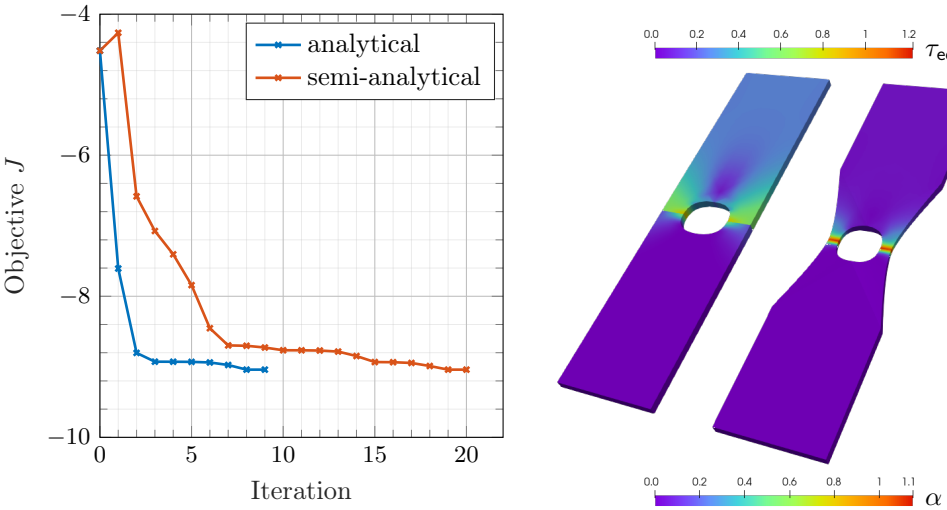

(a) **(b)**

Figure 6.9: Uniaxial specimen optimization: Results, (a) history of objective function value, (b) initial (left) and optimized design (right), accumulative plastic strain (bottom) and von Mises stress (top).

6.7 Summary

The continuously derived design sensitivity information is embedded into the finite element framework in this chapter. Therefore, the discrete design parametrization used within this thesis is introduced and discrete design approximations are presented. From the important equilibrium constraint in Eq. (6.23), the total response sensitivity matrix can be derived that depends on the pseudoload and history sensitivity matrices constituting the discrete versions of the pseudoload and history sensitivity operators. Specific matrix forms of all demanded quantities are explicitly stated. Furthermore, the developed algorithm for the computations of design sensitivity information consistent with the finite element method is presented and pseudocode is provided at three levels, i.e. global, element and integration point level. Firstly, the stress projection algorithm presented in Chap. 4 is augmented for the computations of the demanded partial derivatives of stresses and history variables at each integration point. Secondly, the computations of the element contributions of the pseudoload and history sensitivity matrices are presented, as well as the computations needed for the update of the history sensitivity information on finite element level. Finally, the staggered computation procedure is shown consisting of the assemblage of the element contributions and the computation of the total sensitivity matrix that is then used for the evaluation of design sensitivities of any physical function, as well as the update of the history sensitivities. All of the presented parts of the overall algorithm are verified by comparison of the analytically obtained results with numerically obtained results within specific benchmark examples.
Further, a semi-analytical approach is presented, in which the demanded partial derivatives w.r.t. the internal history variables are gained numerically by means of the FDM. The advantage of the semi-analytical approach is that it is valid for the computations of design sensitivities for any constitutive law that uses local internal variables to capture dissipative mechanisms within an implicit time integration scheme.
An academic benchmark example of a volume minimization of a uniaxial tensile test specimen is presented and the solution using the analytical and semi-analytical approach are compared in terms of accuracy and numerical cost. The results emphasize the advantages of the variational design sensitivity approach for which comparatively high theoretical effort is needed, which is paid back by highest accuracy and low computational cost. Furthermore, the method does not rely on the adequate choice of numerical parameters that might affect the results drastically.

Chapter 7

Optimal Specimen Design

In this chapter the presented gradient based optimization strategy is used to improve the shape of the cruciform X0-specimen for biaxial experiments. Before the shape optimization is conducted, the presented approach is used to identify the constitutive parameters of the mechanical model to accurately describe the behavior of the aluminium alloy $AlMgSi_1$ (EN AW 6082-T6) that is used for the experiments. This demands the solution of a first inverse problem, that is, a parameter identification in which the elastoplastic constitutive parameters are chosen as design variables and the global numerically determined deformation response of a uniaxial tensile test is fitted to experimental data. Thereafter, the geometric shape optimization is performed considering two different biaxial loading scenarios. Numerical results of the optimization are presented and compared to experimental results of the initial and optimized specimen shapes. The experiments have been monitored by means of digital image correlation (DIC) for the visualization of displacement and strain fields. Subsequently, a scanning electron microscope (SEM) has been used to examine the fracture surfaces in detail.

Contents

7.1 Introduction

For the macroscopic description of the onset and evolution of damage in the material behavior of ductile metals, adequate damage models have to be developed and calibrated by means of experimental investigations. For instance, in the damage function in [36] that is used to describe the onset of damage - similar to the yielding condition indicating onset of plastic flow in elastoplasticity - two damage mode parameters α^{da} and β^{da} capture the stress state dependence of the ductile damage behavior, viz.

$$f^{\mathsf{da}}(\boldsymbol{\tau}) = \alpha^{\mathsf{da}}\, I_1 + \beta^{\mathsf{da}}\, \sqrt{J_2} - \sigma_0^{\mathsf{da}}. \tag{7.1}$$

Here, σ_0^{da} is the initial damage threshold and I_1 and J_2 denote the first invariant and the second deviatoric invariant of the Kirchhoff stress tensor, respectively. The damage mode parameters are connected with damage mechanisms occurring on micro scale level, cf. e.g. [36, 38, 39]. Additionally, the evolution of damage is described by means of material and stress state dependent parameters $\overline{\alpha}^{\mathsf{da}}$, $\overline{\beta}^{\mathsf{da}}$ and $\overline{\gamma}^{\mathsf{da}}$

$$\dot{\mathbf{H}}^{\mathsf{da}} = \dot{\mu} \left(\frac{\overline{\alpha}^{\mathsf{da}}}{\sqrt{3}}\, \mathbf{I} + \overline{\beta}^{\mathsf{da}}\, \mathbf{N}^{\mathsf{da}} + \overline{\gamma}^{\mathsf{da}}\, \mathbf{M}^{\mathsf{da}} \right). \tag{7.2}$$

Here, μ is the equivalent damage variable indicating the amount of damage and $\mathbf{N}^{\mathsf{da}}$ and $\mathbf{M}^{\mathsf{da}}$ are normalized stress tensors. All these stress state dependent parameters are related to the examined material and characterize its damage behavior. Due to the dependency of the examined material, these parameters have to be identified by experiments.
In Fig. 7.1, a selection of widely used test specimen is shown that have been designed for different purposes. The pictured uniaxial specimens have for instance been designed for the characterization of elastoplastic deformation behavior at high stress states or for the examination of shear stress states. The pictured biaxial specimens can be used in different loading scenarios that can also be non-proportional. Conducting experiments with differently designed specimen, specific material dependent parameters can be identified that characterize the material behavior. The cruciform shaped X0-specimen developed in [59] is made for biaxial testing and tailored for damage characterization. That is, the experimental identification of the stress state dependent damage parameters mentioned earlier. One mentionable advantage of the X0-specimen is that it can be applied to different loading scenarios resulting in a wide range of different stress states. This is crucial for the isolation of different damage mechanisms and for the identification of the connected damage parameters, see also [62].
The goal of the shape optimization is to further improve the X0-specimen shape for two different load cases producing tension and shear dominated stress states, respectively, so as to obtain more distinct and preferably homogeneous stress states. The tension dominated stress state, i.e. load case 1/1, is produced by equal tension loads at both in plane axis of the specimen. The shear dominated stress state, i.e. load case -1/1, is produced by inverting the loading direction of one axis. In a first attempt in this thesis, focus lies on the stress triaxiality for which a high correlation to damage mechanisms can be observed. The stress triaxiality is defined as the ratio of the mean stress σ_{m} and the von Mises

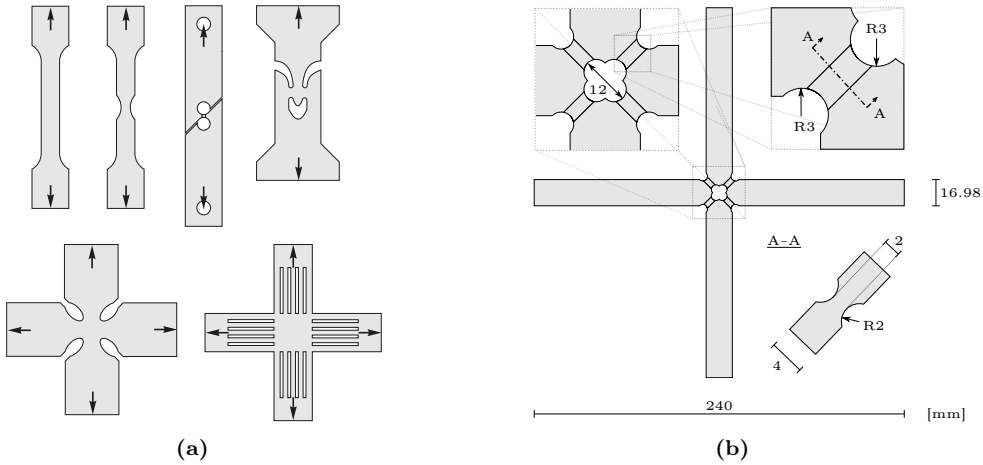

Figure 7.1: Standard and X0-specimen geometries: (a) standard uniaxial (top) and biaxial (bottom) specimen geometries [62], (b) X0-specimen geometry [61].

equivalent stress σ_{eq}, viz.

$$\eta = \frac{\sigma_{\mathsf{m}}}{\sigma_{\mathsf{eq}}} = \frac{I_1}{3\sqrt{3\,J_2}}. \tag{7.3}$$

With this definition, a posivive stress triaxiality means that the stress state is tension dominated, while a negative stress triaxiality indicates a compression stress state. Shear stress dominance correlates to a stress triaxiality around $\eta \approx 0$. It can be observed that for high stress triaxialities the leading damage mechanism is nucleation, growth and coalescence of voids. In contrast, for low or even negative stress triaxialities, formation and evolution of micro-shear cracks trigger damage as leading mechanism, cf. Fig. 7.2 in which schematic impressions on the local damage behavior and different micromechanical damage mechanisms occurring at different stress triaxiality levels are sketched. With increasing strains plastic deformations follow primarily elastic deformations, which at further stress levels leads to onset and evolution of damage until final failure. Hereby, the stress state and intensity triggers the leading damage mechanism. By maximization or minimization of the stress triaxiality as the objective of the optimization problem, the stress states and therefore the leading damage mechanisms can be isolated and experimentally evaluated. After the solution of the optimization problems, experiments with the initial and the two optimized X0-specimen geometries are conducted. Results obtained by digital image correlation (DIC) during the experiment, as well as scanning electron microscopy (SEM) of the fracture surfaces are compared to the simulation results. Note that for the accurate simulation of real world experiments, it is important to calibrate the parameters of the underlying constitutive model. To achieve this, in advance to the geometric shape optimization of the X0-specimen, the elastoplastic constitutive parameters are identified by solving an inverse curve fitting problem. That is, the global deformation behavior of the simulation of a uniaxial tensile test is fitted to experimental data. The examined

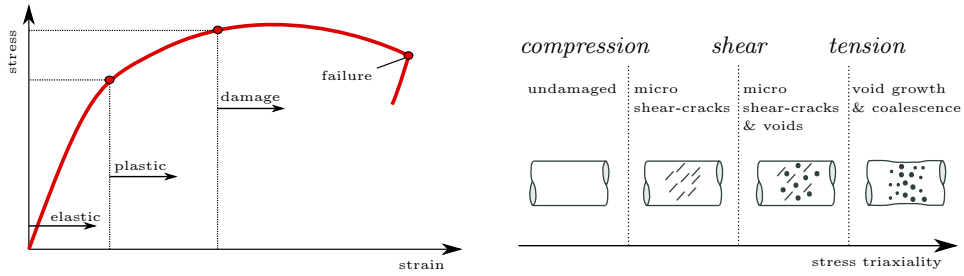

Figure 7.2: Local damage mechanisms: (a) local material behavior at different stress-strain levels, (b) micromechanical damage mechanisms at different stress triaxiality levels [59].

material used is the aluminium alloy $AlMgSi_1$ (EN AW 6082-T6).
Parts of the results of the shape optimization of the X0-specimen have already been published in the authors contributions [103, 104].

7.2 Identification of constitutive parameters

For the studies with the X0-specimen, the aluminium alloy $AlMgSi_1$ (EN AW 6082-T6) is used. To ensure reasonable results of the simulation data within the optimization process, the constitutive parameters that control the material behavior of the mechanical model have to be calibrated. Therefore, a standard uniaxial tensile test of a flat specimen is considered, cf. Fig. 7.3(a). Experimental data, in form of load-displacement curves measured at specific Gauge points utilizing a DIC system, are taken as a reference to fit the material behavior.

7.2.1 Structural analysis problem

The corresponding discrete FE model is pictured in Fig. 7.3(b). Here, also the location of the Gauge point that is used for the displacement measurements is indicated. Note that due to reasons of symmetry, only one octant of the specimen has to be modelled incorporating symmetric boundary conditions. Thus, the displacement of the chosen Gauge point Δu_{ref} has to be doubled for the comparison with the experimental data. The FE mesh consists of 1 539 hexahedral $\overline{F}$ elements and thus, the discrete FE problem counts 4 872 degrees of freedom. An initial guess of the constitutive parameters for the examined aluminium alloy is taken from [59], in which parameters have been identified for a similar alloy and a similar constitutive law. The parameters are summarized in Tab. 7.1. A maximum displacement of 3.8 mm is prescribed at the edge within 200 linear steps. This time discretization implies that the number of data points that are compared with the experimental measurements is $n_{\mathsf{dp}} = 200$.

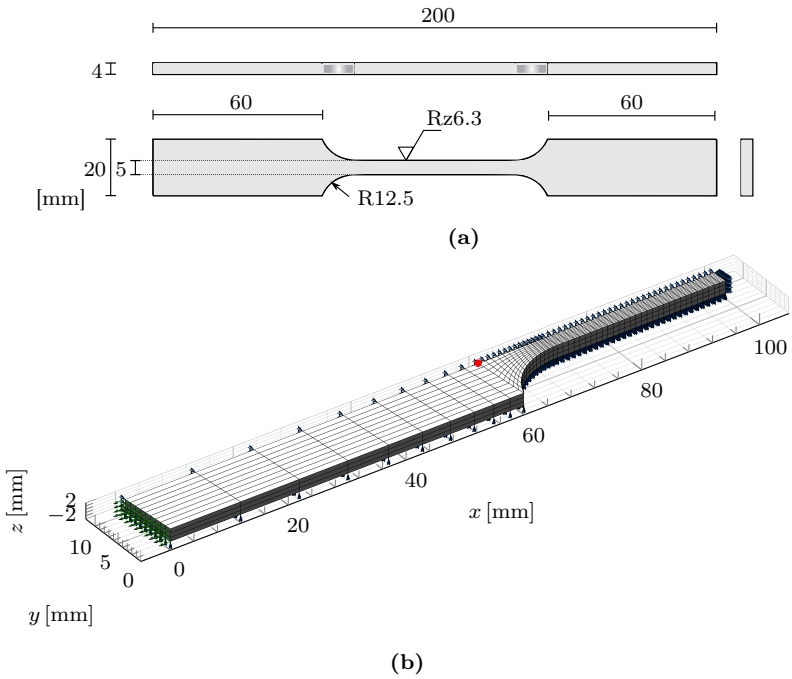

Figure 7.3: Parameter identification: Uniaxial specimen, (a) technical drawing, (b) FE mesh and symmetric boundary conditions ($\frac{1}{8}$th geometry).

Table 7.1: Initial set of constitutive parameters.

$\boldsymbol{K}$	$\boldsymbol{G}$	$\boldsymbol{\sigma_0}$	$\boldsymbol{\sigma_\infty}$	$\boldsymbol{d}$	$\boldsymbol{H}$
57.5 GPa	26.54 GPa	320 MPa	420 MPa	30	650 MPa

7.2.2 Inverse problem

The optimization problem is to minimize the error between the experimentally measured and numerically simulated data. That is, the measured and simulated load-displacement curves are fitted by adjusting the constitutive parameters. Thus, the inverse parameter identification problem is defined as

$$\min_{m} \quad J(\boldsymbol{m}) = ||\boldsymbol{f}^{\mathsf{R}}(\boldsymbol{m}) - \boldsymbol{F}^{\mathsf{R}}||_2^2, \quad \text{s.t.} \qquad m_l^i \leq m^i \leq m_u^i, \tag{7.4}$$

with the vectors $\boldsymbol{F}^{\mathsf{R}}$ containing the measured reaction forces and $\boldsymbol{f}^{\mathsf{R}}(\boldsymbol{m})$ containing the simulated reaction forces in longitudinal direction that depend on the set of constitutive parameters. For a gradient based solution of this inverse problem, the sensitivity information of the reaction forces w.r.t. constitutive parameters $\boldsymbol{m} = \begin{bmatrix} K & G & \sigma_0 & \sigma_\infty & d & H \end{bmatrix}$ are demanded. Details on this can be found in [87]. Briefly, concerning to Eq. (4.90) the partitioning of the total residual and its variation can be split into an internal and an

external part, viz.

$$\boldsymbol{R} = \begin{bmatrix} \boldsymbol{R}_a^{\text{int}} \\ \boldsymbol{R}_b^{\text{int}} \end{bmatrix} - \lambda \begin{bmatrix} \boldsymbol{R}_a^{\text{ext}} \\ \boldsymbol{R}_b^{\text{ext}} \end{bmatrix} \quad \text{and} \quad \delta\boldsymbol{R} = \begin{bmatrix} \delta\boldsymbol{R}_a^{\text{int}} \\ \delta\boldsymbol{R}_b^{\text{int}} \end{bmatrix} - \lambda \begin{bmatrix} \delta\boldsymbol{R}_a^{\text{ext}} \\ \delta\boldsymbol{R}_b^{\text{ext}} \end{bmatrix}, \tag{7.5}$$

for the corresponding load level represented by the scaling factor λ. The demanded reaction forces are stored in the external residual part corresponding to the known degrees of freedom $\boldsymbol{R}_b^{\text{ext}}$, which is indicated by the index b. Considering an equilibrium point, i.e. $\boldsymbol{R}(\boldsymbol{u},\boldsymbol{h}_n) = \boldsymbol{0}$, it is obvious that $\boldsymbol{R}_b^{\text{int}} = \lambda\,\boldsymbol{R}_b^{\text{ext}}$. Recalling Eq. (6.23) and Eq. (6.22) and taking into account that $\delta\boldsymbol{u}_b = \boldsymbol{0}$, finally leads to the conditional equation

$$\delta\boldsymbol{R}_b^{\text{ext}} = [\boldsymbol{K}_{ba}\,\boldsymbol{S}_a + \boldsymbol{P}_b + \boldsymbol{Q}_b]\;\delta\boldsymbol{m}. \tag{7.6}$$

The solution of the inverse parameter identification problem is obtained by means of the MATLAB solver `lsqnonlin` and the built-in trust-region-reflective algorithm. Details on selected options and usage of `lsqnonlin` are given Fig. 7.4 in MATLAB code format, where also the chosen values of the box constraints for the design variables are declared. The function `@Obj` is a separate MATLAB routine that evaluates the objective function J in Eq. (7.4), as well as its gradient for the actual set of constitutive parameters.

```
% Set initial point
K = 57.5;     % [GPa]
G = 26.54;    % [GPa]
sig0 = 0.32; % [GPa]
sig8 = 0.1;  % [GPa]
d = 30;       % [-]
H = 0.65;     % [GPa]

m0 = [ K  G  sig0  sigd  d  H ];
% Set box constraints
%      K   G     sig0  H     sig8  d
Lb = [ 40  0.1   0.2   0.10  0.05  10.0 ];
Ub = [ 70  0.49  0.5   100   0.2   50.0 ];

% Set options for lsqnonlin
options = optimoptions('lsqnonlin',...
                       'Algorithm','trust-region-reflective',...
                       'FunctionTolerance',1e-6,...
                       'OptimalityTolerance',1e-6,...
                       'SpecifyObjectiveGradient',true,...
                       'TypicalX',x0);
% Invoke lsqnonlin
[m,normr,r,exit,out,lambda,jac] = lsqnonlin(@Obj,x0,Lb,Ub,options);
```

Figure 7.4: MATLAB code example: Call to `lsqnonlin`.

7.2.3 Curve fitting results

The curve fitting process reached convergence after 22 iterations, i.e. the chosen tolerance on the relative change of the value of the objective function compared to the prior iteration has reached the chosen tolerance of $tol = 1 \times 10^{-6}$, cf. Fig. 7.4. The history of the objective function value over the 22 iterations is plotted in Fig. 7.5(a). The rapid decrease of the function value emphasizes the accuracy of the supplied gradient information. In Fig. 7.5(b) the load-displacement curves are displayed for the initial guess, the first iteration and the converged iteration. The constitutive parameters identified in the final converged iteration are summarized in Tab. 7.2. The value of the objective function could be decreased from 534.6 to 2.329 8, which is a relative improvement of $\sim 99.6\,\%$. With the identified constitutive parameters at hand, the main shape optimization of the X0-specimen can be conducted.

Table 7.2: Identified set of constitutive parameters.

K	G	σ_0	σ_∞	d	H
61.4 GPa	26.7 GPa	277 MPa	64.3 MPa	23.7	292 MPa

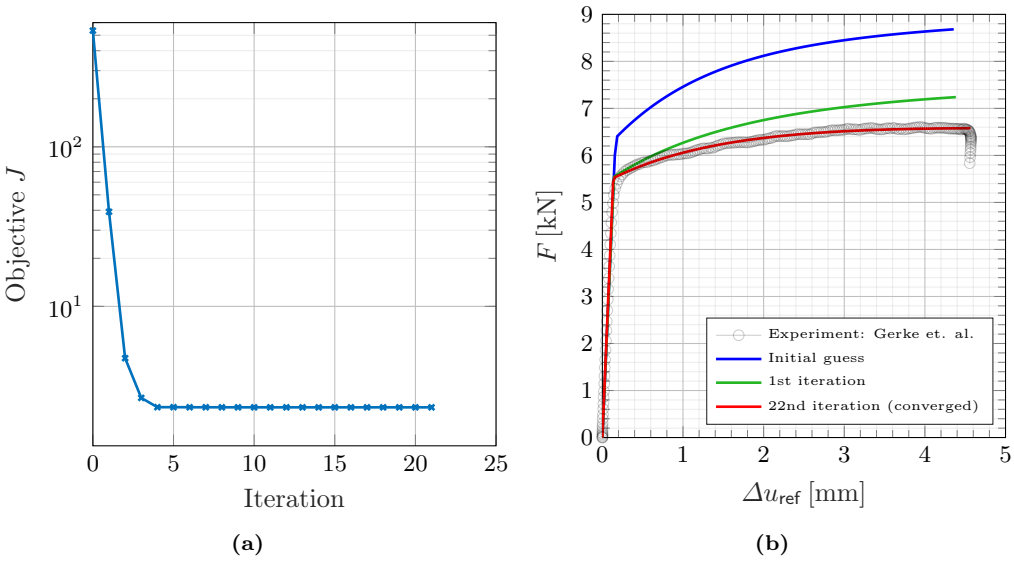

Figure 7.5: Parameter identification: Results, (a) history of the objective function value, (b) load-displacement diagrams in different iterations.

7.3 Shape optimization of the X0-specimen

The main task in this section is the application of the presented gradient based optimization strategy to the shape improvement of the X0-specimen. In Sec. 7.2 the constitutive parameters for the $AlMgSi_1$ (EN AW 6082-T6) aluminium alloy have been identified within a

preceding inverse curve fitting procedure. In the current section the geometric shape of the X0-specimen is optimized considering two different loading scenarios. Firstly, the loading conditions of both axes are equal 1/1, which leads to a tension dominated stress state in the notched area of the specimen. In this case, the shape is optimized so as to maximize the tension dominance, i.e. to increase the stress triaxiality in the controlled cross section area. Secondly, the loading conditions of both axes are contrary -1/1, which leads to a shear dominated stress state in the notched specimen area. In this case, optimizing the specimen shape is to maximize the shear dominance, i.e. to decrease the stress triaxiality. After presenting the structural analysis problems, the corresponding inverse shape optimization problems are stated and the solution strategy is explained. Subsequently, the resulting optimal specimen shapes are experimentally examined and measurement data is compared to the simulation data.

7.3.1 Structural analysis problem

Fig. 7.6 illustrates the FE model, where symmetries in longitudinal, lateral and thickness direction are exploited, i.e. one octant of the geometry is modelled. Thus, symmetric boundary conditions are exploited at the symmetry planes. The FE mesh consists of $\mathsf{nel} = 5\,376$ $\overline{F}$-finite elements and the total number of degrees of freedom is $\mathsf{ndof} = 21\,375$. Predefined displacements are applied at nodes on the top and the right edges of the mesh. The maximum values are $\overline{u}^{\mathsf{max}}_{1/1} = 0.15\,\mathrm{mm}$ and $\overline{u}^{\mathsf{max}}_{\text{-}1/1} = \pm\,0.625\,\mathrm{mm}$ for the corresponding load case, respectively. The mesh is constructed utilizing `Gmsh` and the solution is processed by means of `MATLAB`. The solution of the discrete boundary value problem $\boldsymbol{u}$ is used in a post processing step to evaluate the stress triaxiality, cf Eq. (7.3).

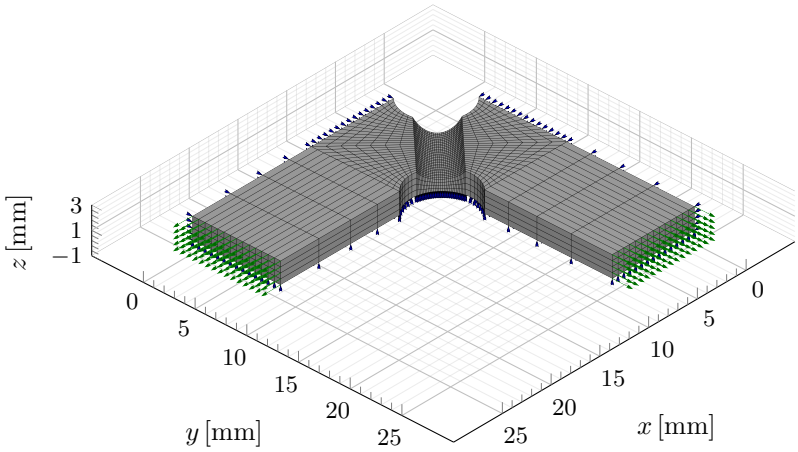

Figure 7.6: X0-specimen: FE mesh and boundary conditions.

7.3.2 Inverse problems

The goal of the shape optimization is to gain a distinct and preferably homogeneous stress triaxiality distribution in the notched specimen area, where it is assumed to fail.

To achieve this, the stress triaxiality is to be maximized or minimized depending on the respective load case (1/1 or -1/1), while keeping the cross section area constant. The changes of the geometric shape have to fulfil certain producibility constraints at reasonable costs, i.e. the fabrication process constrains the choice and limits of design variables. On that account, the design variables are chosen as the inner (R_i) and outer (R_o) in plane radii, as well as the radius of the notch in thickness direction (R_t) and the penetration depth (D), cf. Fig 7.7. Thus, the discrete vector of design variables reads

$$\boldsymbol{p} := \begin{bmatrix} R_i & R_o & R_t & D \end{bmatrix}, \tag{7.7}$$

that is, the number of design variables is $\mathsf{ndv} = 4$. As two different load scenarios are considered, as already mentioned, two inverse shape optimization problems are stated.

Load case 1/1. In this load case, both axis are equally loaded, which leads to tension dominance and a comparatively high stress triaxiality in the notched specimen area. Thus, the optimization goal is the maximization of the stress triaxiality in this area. The corresponding optimization problem reads

$$\begin{aligned} \max_{\boldsymbol{p}} \quad & J\left(\boldsymbol{u}(\boldsymbol{p})\right) = || \, \boldsymbol{\eta}_{\mathsf{cs}}\left(\boldsymbol{u}(\boldsymbol{p})\right) \, || \\ \text{s.t.} \quad & c_{\mathsf{eq}}(\boldsymbol{p}) = 0, \\ & c_{\mathsf{in}}(\boldsymbol{p}) \leq 0, \\ & p_{\mathsf{l}}^i \leq p^i \leq p_{\mathsf{u}}^i, \quad i = 1, \dots \mathsf{ndv}, \end{aligned} \tag{7.8}$$

with the box constraints

$$\boldsymbol{p}_{\mathsf{l}} = \begin{bmatrix} 1.0 & 1.0 & 1.0 & 1.0 \end{bmatrix}, \quad \boldsymbol{p}_{\mathsf{u}} = \begin{bmatrix} 4.0 & 4.0 & 3.0 & 1.5 \end{bmatrix}. \tag{7.9}$$

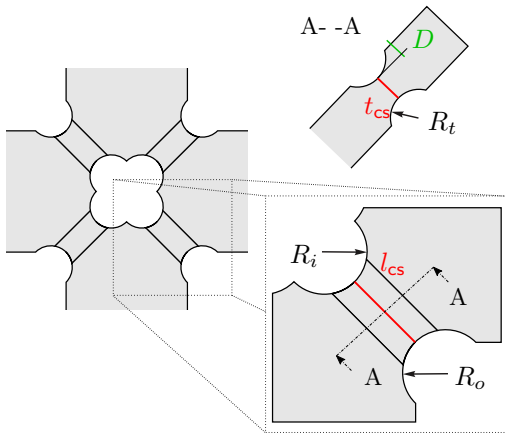

Figure 7.7: Design variables in the notched area.

Load case -1/1. In contrast to the former load case, inverting the direction of the loading of one axis, the stress state in the notched specimen area is shear dominated. In this case, the stress triaxiality is near zero. Hence, the goal of the shape optimization is a minimization of the stress triaxiality in the notched specimen area, which leads to the following optimization problem

$$\begin{aligned} \min_{\boldsymbol{p}} \quad & J(\boldsymbol{u}(\boldsymbol{p})) = || \, \boldsymbol{\eta}_{\mathsf{cs}}(\boldsymbol{u}(\boldsymbol{p})) \, || \\ \text{s.t.} \quad & c_{\mathsf{eq}}(\boldsymbol{p}) = 0, \\ & c_{\mathsf{in}}(\boldsymbol{p}) \leq 0, \\ & p_{\mathsf{l}}^i \leq p^i \leq p_{\mathsf{u}}^i, \quad i = 1, \dots \mathsf{ndv}, \end{aligned} \tag{7.10}$$

with the box constraints

$$\boldsymbol{p}_{\mathsf{l}} = \begin{bmatrix} 1.0 & 1.0 & 1.0 & 0.5 \end{bmatrix}, \quad \boldsymbol{p}_{\mathsf{u}} = \begin{bmatrix} 5.5 & 5.5 & 4.0 & 1.5 \end{bmatrix}. \tag{7.11}$$

In both optimization problems, the objective function that is to be maximized or minimized is chosen as the Euclidean norm of the vector $\boldsymbol{\eta}^{\mathsf{cs}}$ that collects the values of the stress triaxiality at the FE nodes located at the cross section in the notched specimen area. The equality and inequality constraints for both problems are identical. A constant cross section area is ensured by the equality constraint

$$c_{\mathsf{eq}} = l_{\mathsf{cs}} \cdot t_{\mathsf{cs}} - 12 \, \mathrm{mm}^2 = 0. \tag{7.12}$$

Further, three inequality constraints are chosen for producibility reasons, as well as to prevent destruction of the geometry and FE mesh during the optimization process. Therefore, the inner and outer in plane radii are said to be greater than the radius in thickness direction and the penetration depth shall remain smaller than the radius in thickness direction. This leads to the three inequality constraints

$$\boldsymbol{c}_{\mathsf{in}} = \begin{bmatrix} R_t - R_i \\ R_t - R_o \\ D - R_t \end{bmatrix} \leq \boldsymbol{0}. \tag{7.13}$$

For the gradient based solution of the two above shape optimization problems, the gradient of the objective function has to be provided, which includes the computation of the design velocity matrix connecting the chosen design variables with the FE mesh. As the FE mesh is constructed by means of `Gmsh`, the design velocity matrix has to be computed numerically. For this purpose, the finite difference method is conducted as it is simple to implement and sufficiently accurate in this context. The `MATLAB` implementation utilizing the built in `system` command that allows communication with third party software - presuming the correct system setup - is illustrated in Fig. B.2 for the FE mesh of the X0-specimen and the chosen design variables. Recalling Eq. (6.42) and Eq. (6.48), the

```
%% Make sure gmsh is on PATH
a = system('gmsh --version');
switch a
    case 0
        fprintf('gmsh found \n')
    otherwise
        error('gmsh not found!')
    end
%% Mesh geometry parameterized by design vector p
system(['gmsh '...
        ' -setnumber Ri ',num2str(p(1),10),...
        ' -setnumber Ro ',num2str(p(2),10),...
        ' -setnumber Rt ',num2str(p(3),10),...
        ' -setnumber D  ',num2str(p(4),10),...
        ' -format m -3 -o X0.m X0.geo']);
% Nodes stored in array POS
run('X0.m');
% Number degrees of freedom
ndof = size(POS,1)*size(POS,2);
% Store nodal coordinates in vector  X
X = reshape(POS,ndof,1);

%%  Compute design velocity matrix using forward finite differences
% Initialize Q
Q = zeros(ndof,length(p));

% Set perturbation value
e = sqrt(eps);
for i=1:length(p)
    pp = x;
    % perturb parameters
    pp(i) = pp(i)+e;
    system(['gmsh '...
            ' -setnumber Ri ',num2str(pp(1),10),...
            ' -setnumber Ro ',num2str(pp(2),10),...
            ' -setnumber Rt ',num2str(pp(3),10),...
            ' -setnumber d  ',num2str(pp(4),10),...
            ' -format m -3 -o X0p.m X0.geo']);
    run(X0p.m)
    Xp = reshape(POS,ndof,1);

    Q(:,i) = (Xp-X)/e;
end
```

Figure 7.8: MATLAB code example: Numerical design velocity matrix.

gradient of the stress triaxiality is straight forward and reads

$$\begin{aligned}\delta\eta &= \frac{1}{3\,\sigma_{\mathsf{eq}}}\left(\boldsymbol{I}^T - \frac{2\,\eta}{\sigma_{\mathsf{eq}}}\,\mathrm{dev}\,\boldsymbol{\tau}^T\right)\,\delta\boldsymbol{\tau} \\ &= \frac{1}{3\,\sigma_{\mathsf{eq}}}\left(\boldsymbol{I}^T - \frac{2\,\eta}{\sigma_{\mathsf{eq}}}\,\mathrm{dev}\,\boldsymbol{\tau}^T\right)\,[\overline{\boldsymbol{a}}\,(\overline{\boldsymbol{G}}\,\boldsymbol{S}_p - \overline{\boldsymbol{G}}^p) + \boldsymbol{D}\,\boldsymbol{Z}_n]\,\delta\boldsymbol{p}.\end{aligned} \tag{7.14}$$

This, together with the partial derivative of the Euclidean vector norm finally leads to the gradient of the objective function, viz.

$$\delta J = \frac{1}{||\,\boldsymbol{\eta}_{\mathsf{cs}}\,||}\,\boldsymbol{\eta}_{\mathsf{cs}}^{\mathsf{T}}\,\delta\boldsymbol{\eta}_{\mathsf{cs}}, \tag{7.15}$$

with Eq. (7.14) constituting the entries of the vector $\delta\boldsymbol{\eta}_{\mathsf{cs}}$ at each of the chosen FE nodes located at the cross section area. The gradient based solutions of both shape optimization problems is obtained utilizing the `MATLAB` function `fmincon` and the built-in SQP solution algorithm available through the Optimization Toolbox. However, for comparison, the optimizations have also been conducted utilizing the built-in 'interior-point' algorithm. In both cases, the gradient information is provided utilizing the methods described in earlier chapters. Note that for the solution of the maximization problem in Eq. (7.8), the problem is transformed into a minimization problem by changing the sign of the objective function. This results in

$$\min_{\boldsymbol{p}} \quad J\,(\boldsymbol{u}(\boldsymbol{p})) = -||\,\boldsymbol{\eta}_{\mathsf{cs}}\,(\boldsymbol{u}(\boldsymbol{p}))\,|| \tag{7.16}$$

subject to the same constraints as in Eq. (7.9).

7.3.3 Optimization results

The solutions of the above stated shape optimization problems, cf. Eq. (7.8) and Eq. (7.10) are given in Tab. 7.3. Both algorithms, the SQP and the interior-point algorithm converged to almost the same optimal solutions. However, the SQP algorithm has been more efficient in terms of function evaluations and overall computation time. The variants of optimal shapes with round off values are illustrated in Fig. 7.10 for the respective maximization and minimization problem. On this basis, the specimen geometries have been fabricated. Corresponding to load case 1/1, the optimized geometry is denoted by V_{11} and analogously, $\mathrm{V}_{\text{-}11}$ denotes the optimized geometry for load case -1/1.

Load case 1/1. V_{11} is characterized by a smaller notch radius in thickness direction $R_t = 1.0\,\mathrm{mm}$, whereas the penetration depth remains constant at $D = 1.0\,\mathrm{mm}$. The outer in plane radius has been reduced to $R_o = 1.0\,\mathrm{mm}$ and the inner in plane radius remains constant at $R_i = 3.0\,\mathrm{mm}$. A more elevated stress triaxiality under 1/1-loading and a more reduced zone with increased strains can be expected for V_{11} due to the reduced notch radii, which indicates more brittle fracture behavior.

```
% Set initial point
R1 = 3.0; R2 = 3.0; R3 = 2.0; d = 1.0;
p0 = [ R1 R2 R3 d ]';

% Box constraints
%      R1     R2     R3     d
Lb = [ 1.0    1.0    0.5    0.5 ];
Ub = [ 5.5    5.5    4.0    1.5 ];

% Options for fmincon
options = optimoptions('fmincon',...
                       'Algorithm','sqp',... % or 'interior-point'
                       'OptimalityTolerance',1e-6,...
                       'ConstraintTolerance',1e-6,...
                       'SpecifyObjectiveGradient',true,...
                       'SpecifyConstraintGradient',true,...
                       'StepTolerance',1e-6);
% Invoke fmincon
[p,fval,exit,out,lambda,grad,hess] = fmincon(@Obj,p0,[],[],[],[], ...
                                             Lb,Ub,@Constr,options);
%% Simultaneous computation of objective and constraint functions
% Initialize shared variables
xLast = []; obj_it = []; gobj_it = [];
c_it = []; gc_it = []; ceq_it = []; gceq_it = [];
function [y,dy] = Obj(x)
  % Evaluate objective function at iteration it
  if ~isequal(x,xLast) % Check if computation is necessary
     [obj_it,gobj_it,c_it,gc_it,ceq_it,gceq_it] = cmp_objconstr(x);
     xLast = x;
  end
% Set output for objective function and gradient
  y = obj_it;
  dy = gobj_it;
end

function [c,ceq,gc,gceq] = Constr(x)
  % Evaluate constraint functions at iteration it
  if ~isequal(x,xLast) % Check if computation is necessary
    [obj_it,gobj_it,c_it,gc_it,ceq_it,gceq_it] = cmp_objconstr(x);
    xLast = x;
  end
% Set output for constraint functions and gradients
  c = c_it;
  gc = gc_it;
  ceq = ceq_it;
  gceq = gceq_it;
end
```

Figure 7.9: MATLAB code example: Call to `fmincon`.

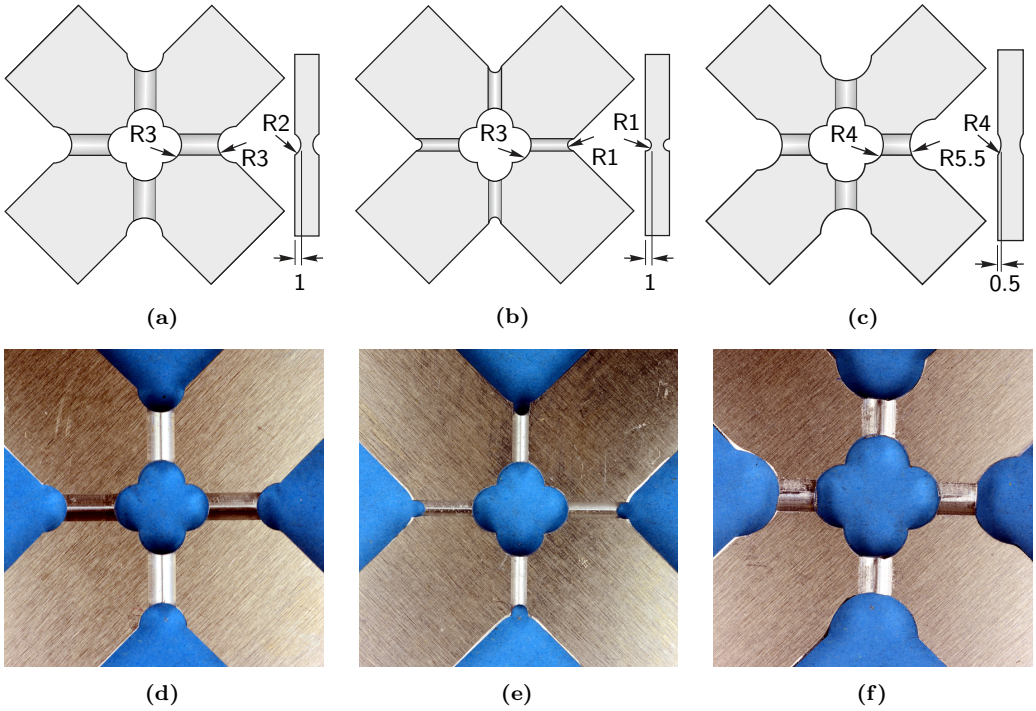

Figure 7.10: Initial and optimized X0-specimen geometries: (a) initial geometry, (b) optimized geometry V_{11} , (c) optimized geometry $V_{\text{-}11}$,(d) initial X0-specimen photography, (e) V_{11} photography, (d) $V_{\text{-}11}$ photography.

Load case -1/1. In contrast, $V_{\text{-}11}$ is characterized by a reduced penetration depth of $D = 0.5\,\text{mm}$, which leads to a smaller width of the notched area of 4.0 mm based on the constant cross section of $12.0\,\text{mm}^2$, see Eq. (7.12). Additionally, the notch radius in thickness direction $R_t = 3.0\,\text{mm}$ and the outer in plane radius $R_o = 4.0\,\text{mm}$ have been enlarged, whereas the inner in plane radius remains constant at $R_i = 3.0\,\text{mm}$. Hence, it can be expected that for $V_{\text{-}11}$ zones with elevated strain increase, i.e. it is likely to observe more ductile behavior. Consequently, under 1/1-loading a reduced stress triaxiality can be expected for $V_{\text{-}11}$.

In Tab. 7.3, the relative change of the objective function is given as

$$c_{\text{rel}} = \frac{|\, J^{\text{init}} - J^{\text{opt}} \,|}{|\, J^{\text{init}} \,|} = \frac{\Delta J}{|\, J_{\text{init}} \,|}. \tag{7.17}$$

Here, J^* denotes the value of the objective function in the converged solution point. Fig. 7.11 illustrates the history of the value of the objective function during the two optimization processes. In both cases, the optimization procedure stopped after reaching the relative step tolerance of $tol = 1 \times 10^{-6}$. Details on stopping criteria can be found e.g. in [134].

Table 7.3: Initial and optimal values of the design variables.

	R_i [mm]	R_o [mm]	R_t [mm]	D [mm]	c_{rel} [%]
Initial	3.000	3.000	2.000	1.000	-
SQP					
V_{11}	3.108	1.000	1.000	0.964	25.15
V_{-11}	4.003	5.500	4.000	0.500	16.67
IP					
V_{11}	3.049	1.000	1.000	0.985	24.95
V_{-11}	4.003	5.499	3.999	0.500	16.67

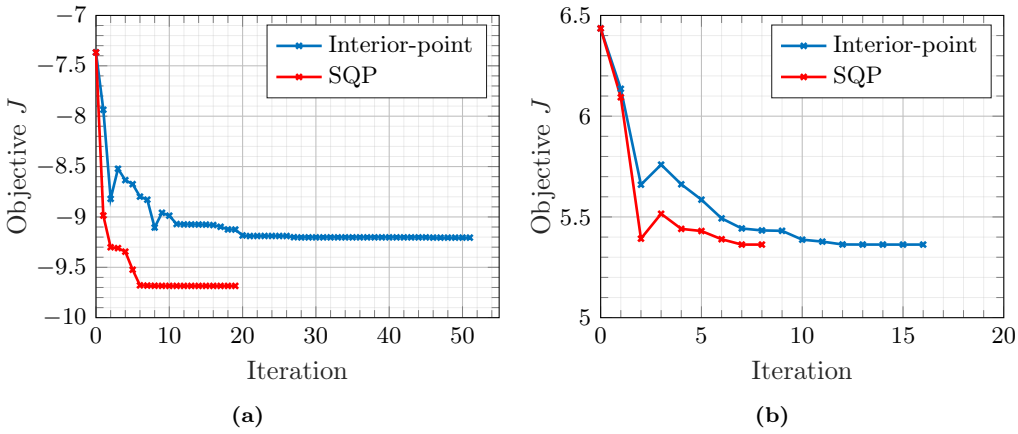

Figure 7.11: Objective function value history: (a) load case 1/1, (b) load case -1/1.

The stress triaxiality distributions at the cross section of the notched specimen area are displayed in Fig. 7.12 at the end of the simulations for all three geometries and both load cases, respectively. Note that consequently in Fig. 7.12(b) and Fig. 7.12(e) the objective quantity η on the optimized geometry corresponding to the respective load case are shown; further results serve as reference.

The optimized geometry V_{11}, cf. Fig. 7.12(b) for 1/1-loading indicates stress triaxialities up to $\eta \approx 1.12$ at the centre of the cross section, whereas the initial geometry in Fig. 7.12(a) indicates values up to $\eta \approx 0.8$. Hence, the geometry changes, i.e. primarily the sharp notch in thickness direction, lead to substantially higher tension dominated stress triaxialities. In contrast, V_{-11} shown in Fig. 7.12(c) that has been optimized for -1/1-loading only reaches values up to $\eta \approx 0.68$. Hence, the effect of the optimization process can be clearly seen for load case 1/1.

As opposed to this, for $-1/1$ loading, see Fig. 7.12(c) to 7.12(e), the influence of the optimization process is less obvious. Here, all three geometries show values ranging from $\eta \approx 0.04$ to 0.2 in a similar distribution throughout the cross section characterizing a shear dominated stress state.

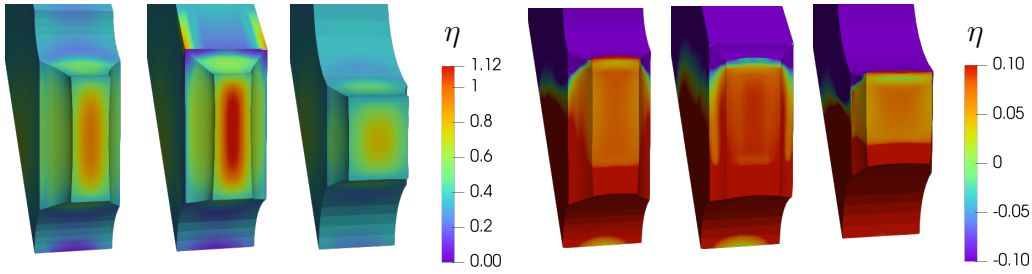

(a) Basis **(b)** V_{11} **(c)** $V_{\text{-}11}$ **(c)** Basis **(d)** V_{11} **(e)** $V_{\text{-}11}$

Figure 7.12: Stress triaxiality distribution at the cross section area: (a)-(c) load case 1/1, (d)-(f) load case -1/1.

For reference, in Fig. 7.13, also the values of the lode parameter ω, which is defined by

$$\omega = \frac{2\,\tau_2 - \tau_1 - \tau_3}{\tau_1 - \tau_3}, \quad \text{with} \quad \tau_1 \leq \tau_2 \leq \tau_3, \tag{7.18}$$

where τ_i represent the principal Kirchhoff stress components, are illustrated at the cross section area for all three geometries and both load cases, although it has not been involved into the optimization process. However, besides the stress triaxiality it also characterizes the stress state. That is, a value of $\omega = 0$ indicates a shear dominated stress state, whereas values of $\omega = -1$ and $\omega = 1$ indicate biaxial tension or compression, respectively. For 1/1-loading, the influence of shape optimization can clearly be noted, see Fig. 7.13(a) to 7.13(c). Both, the initial geometry and V_{11} with a cross sectional area of 6.0 mm by 2.0 mm, show values between $\omega \approx -0.2$ and $\omega \approx -1.0$, whereas $V_{\text{-}11}$ in Fig. 7.13 (c) with a cross-sectional area of 4.0 mm by 3.0 mm shows values close to $\omega \approx -1$. Again, under $-1/1$-loading the influence of the shape optimization is less significant and a homogeneous distribution with mainly values around $\omega \approx 0$ can be observed for all three geometries.

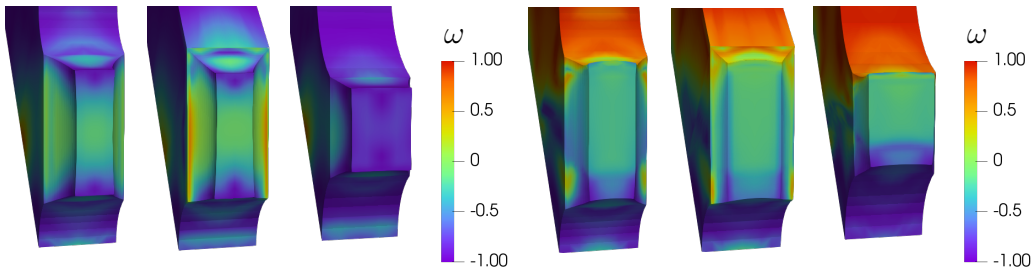

(a) Basis **(b)** V_{11} **(c)** $V_{\text{-}11}$ **(c)** Basis **(d)** V_{11} **(e)** $V_{\text{-}11}$

Figure 7.13: Lode parameter distribution at the cross section area: (a)-(c) load case 1/1, (d)-(f) load case -1/1.

7.4 Experimental investigations

For verification of the simulation results, the initial as well as the two optimized X0-specimen geometries have been fabricated and examined experimentally. Each geometry

has been tested three times for each load step. Hence, in total, 18 biaxial experiments haven been performed. In the following, after introducing the experimental equipment, the experimentally measured and simulated results are compared and discussed.

7.4.1 Experimental setup

The experiments have been performed with the biaxial test machine LFM-BIAX 20 kN produced by Walter+Bai, Switzerland. The specimens are clamped in the four cylinder heads and the machine reports the cylinder displacements and applied forces. For avoidance of non-symmetric behavior during the experimental process, a stable displacement driven procedure has been used as described in [59]. The relative nominal displacements $\Delta u_{\mathrm{ref}.i} = u_{i.1} - u_{i.2}$ are introduced, with the nominal displacements $u_{i.j}$ of the Gauge points indicated by red dots in Fig. 7.14, as well as the averaged forces $F_i = 0.5\,(F_{i.1} + F_{i.2})$, that serve as adequate displacement and force measures.

The displacement fields have been monitored at the specimen surfaces during the experiments by means of a Q-400 digital image correlation (DIC) system provided by Limess/Dantec. Therefore, four cameras have been used from the upside and two additional cameras monitoring displacement fields from the downside of the specimen. The cameras are equipped with 6.0 Mpx and 75 mm lenses, respectively and monitor the movement of randomly distributed small discrete points that have been applied to the specimen surfaces before the experiments in form of a *speckle pattern*. Forces $F_{i.j}$ and machine displacements $u^{\mathrm{M}}_{i.j}$ have been transmitted to the DIC system and stored within the corresponding data sets. Subsequently, by post processing the DIC data using `ISTRA 4D`, the nominal displacements have been extracted.

After the biaxial experiments, macro photographs have been taken of the fractured specimen and furthermore, the fracture surface has been examined in detail by means of scanning electron microscopy (SEM). Therefore, the scanning electron microscope Zeiss EVO LS15, located at the laboratory of the Institut für Werkstoffe des Bauwesens at the Universität der Bundeswehr München has been used. The electrons used by SEM have a wave length of approximately 0.008 nm compared to visible light with a wave length between approximately 400-800 nm in a light microscope. This allows magnifications of

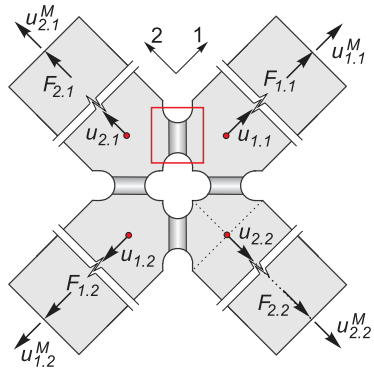

Figure 7.14: Notation of experimental technique [61].

surfaces up to 1 000 000 x. Further details on the experimental techniques can be found in [61]. Visual impressions of the experimental equipment are given in Fig. 7.15.

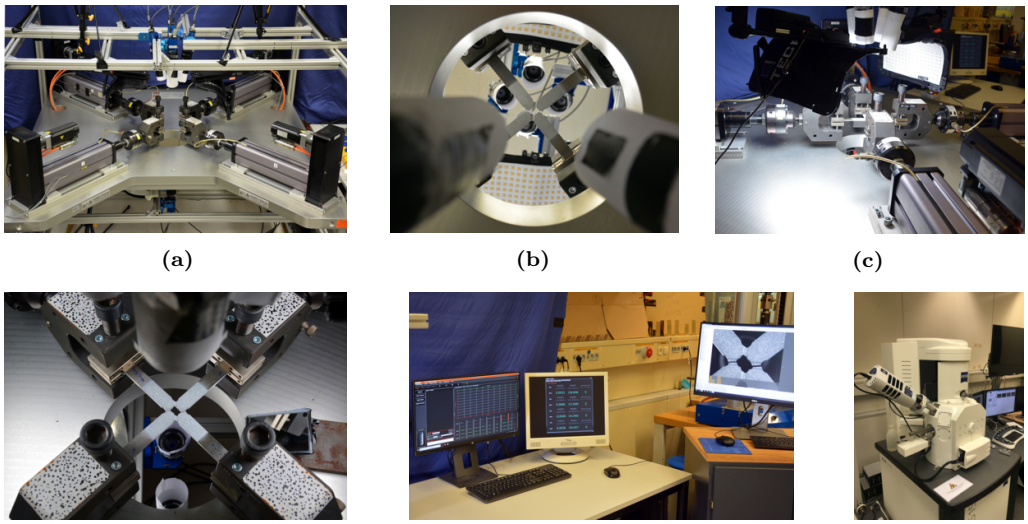

Figure 7.15: Experimental equipment: (a) biaxial testing machine, (b) clamped specimen (bottom view), (c) camera positioning, (d) clamped specimen (top view), (e) DIC system, (f) Scanning Electron Microscope.

7.4.2 Results and comparison

Next, the experimental results are presented and compared with the results of the simulations with focus on the global force-displacement response, as well as on the local deformation and fracture behavior.

Forces and displacements

In Fig. 7.16 the numerically (sim) and experimentally (exp) obtained force-displacement curves for 1/1-loading (a) and -1/1-loading (b) are displayed. Note that the relative nominal displacements of the numerical simulations have been extracted at the corresponding nodes of the FE mesh matching the Gauge points of the experimental measurements and simply doubled due to symmetry.
Within the elastic region the influence of the geometry changes can clearly be observed in both loading scenarios. V_{11} shows the stiffest response due to the sharper notch radius in thickness direction with $R_t = 1.0\,\text{mm}$ that causes a relatively small region of elevated elastic deformations. Contrary, $V_{\text{-}11}$ shows the softest response caused by a radius in thickness direction of $R_t = 1.0\,\text{mm}$ and a reduced penetration depth of $D = 0.5\,\text{mm}$. As expected, the response of the initial geometry is located in between the two optimized geometries. This effect is obvious for 1/1-loading and also present for -1/1-loading, although less pronounced. Overall, a good agreement can be observed of the simulated and the

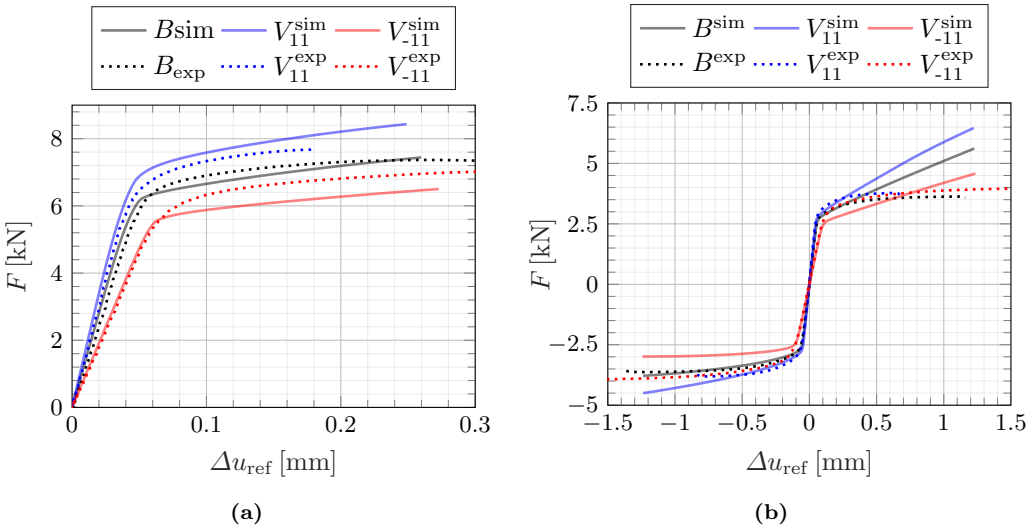

Figure 7.16: X0-specimen: Load vs. displacements, (a) load case 1/1, (b) load case -1/1.

experimentally measured forces and displacements in the elastic region.
In the inelastic region, the behavior is reasonably predicted, considering the fact that the constitutive parameters have been identified by fitting the global load-displacement curves of a uniaxial tension test and keeping in mind that elastic-plastic material behavior based on the von Mises yield criterion and isochoric inelastic deformations have been considered in the simulations. Hence, material degradation due to damage has not been included in the numerical model. For 1/1-loading it can be observed that the simulations of the initial geometry and V_{-11} underestimate the load, whereas in the simulation of V_{11} the load is overestimated. This can be seen as related to the increased stress triaxiality of V_{11} under 1/1-loading, see Fig. 7.12. In the -1/1 load case more elevated relative displacements $\Delta u_{\mathrm{ref}.i}$ occur, see Fig. 7.16(b). For both, the tension as well as the compression axis, the elastic behavior is estimated in good accordance. The inelastic behavior is estimated in a reasonable way, while for the tension axis the loads are overestimated starting from a relative displacement at about $\Delta u_{\mathrm{ref}.2} \approx 0.4\,\mathrm{mm}$, see Fig. 7.16(b).

Deformation and fracture behavior

In the photos of the resulting fractured specimens shown in Fig. 7.17, a good impression on the overall deformation behavior in the central specimen part can be gained. Here, a hierarchy with respect to the macroscopic deformation behavior can clearly be observed. That is, regardless of the load case, V_{-11} behaves most ductile and V_{11} behaves most brittle. Note that the fracture occurs in different parallel notch pairs at the vertical or the horizontal symmetry axis. This is due to natural material and experimental imperfections and does not have any effect on the evaluations. By means of the DIC system, the deformation behavior of the specimen surfaces can be monitored during the experiment.

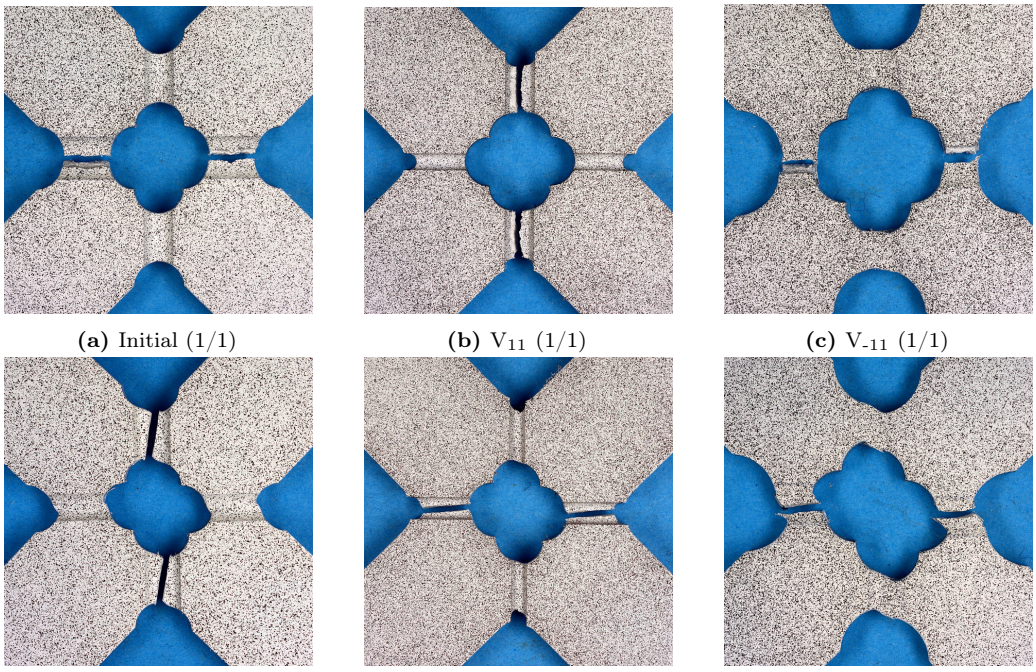

(a) Initial (1/1) **(b)** V_{11} (1/1) **(c)** $V_{\text{-}11}$ (1/1)

(d) Initial (-1/1) **(e)** V_{11} (-1/1) **(f)** $V_{\text{-}11}$ (-1/1)

Figure 7.17: Fractured specimens: All three geometries for the different load cases: (a)-(c) load case 1/1, (d)-(e) load case -1/1.

In Fig. 7.18 the first principal strains for the three different geometries and both load cases are displayed that have been reported by the DIC system just before fracture occurrence. Significant influence of the geometry on the deformation and fracture behavior can be observed. Especially, for V_{11} the sharp notch in thickness direction causes a reduced area of elevated strains and consequently less overall deformation before fracture. That is, the fracture behavior is more brittle. For comparison in Fig. 7.19 the corresponding first principal strains obtained from the FE simulations are shown. The qualitative and quantitative conformity can clearly be observed, especially for the 1/1 load case for all three geometries. In the load case -1/1, the simulations of the initial geometry and V_{11} overestimate the strains at the notch surfaces compared to the measured DIC data.

After completing the experiments, the fracture surfaces have been analyzed by SEM. The fracture surfaces have been examined at different positions at the boundary and the centre of the fracture surface with three magnification factors, namely 500 x, 2 000 x and 10 000 x. Representative pictures are given in Fig. 7.20 and Fig. 7.21 for 1/1-loading and -1/1-loading, respectively. Here, in the upper row (a-c) a representative area at the centre of the fracture surface is represented and the lower row reflects a representative area towards the outer radius R_o.
For 1/1-loading the texture of all fracture surfaces point to nucleation, growth and coalescence of voids. This relates to the indicated tension dominated stress state, that is, a high

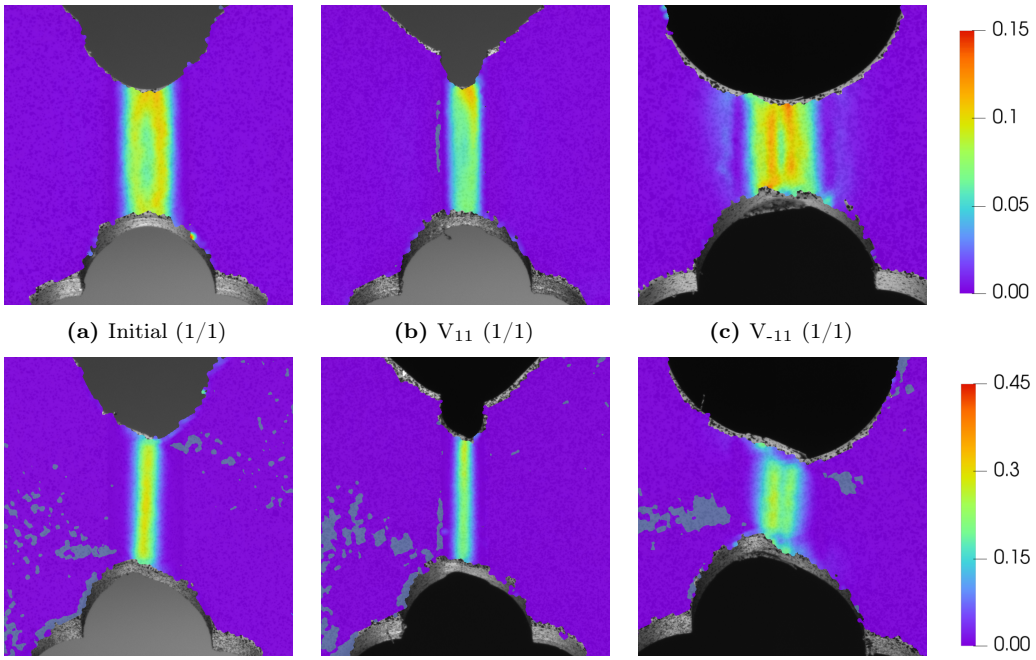

(a) Initial (1/1) **(b)** V_{11} (1/1) **(c)** $V_{\text{-}11}$ (1/1)

(d) Initial (-1/1) **(e)** V_{11} (-1/1) **(f)** $V_{\text{-}11}$ (-1/1)

Figure 7.18: First principal strains reported by digital image correlation (DIC). All three geometries for the different load cases: (a)-(c) load case 1/1, (d)-(e) load case -1/1.

stress triaxiality, cf. Fig. 7.12(a) to 7.12(c) and low Lode parameter, cf. Fig. 7.13(a) to 7.13(c). For V_{11} that has been optimized for the 1/1-load case, significantly higher stress triaxialities have been predicted, which is reflected by the failure behavior, as Fig. 7.20(b) indicates remarkably larger voids and a more brittle behavior compared to the initial geometry, cf. Fig. 7.20(a), and $V_{\text{-}11}$, see Fig. 7.20(c). For all three geometries similar stress triaxiality values of approximately $\eta = 0.4$ have been predicted towards the outer radius. The SEM images in Fig. 7.20(d) to 7.20(f) indicate the corresponding material failure characterized by smaller voids. No significant differences between the different geometries occur in this region. Further SEM images of the fracture surfaces are presented in App. C.

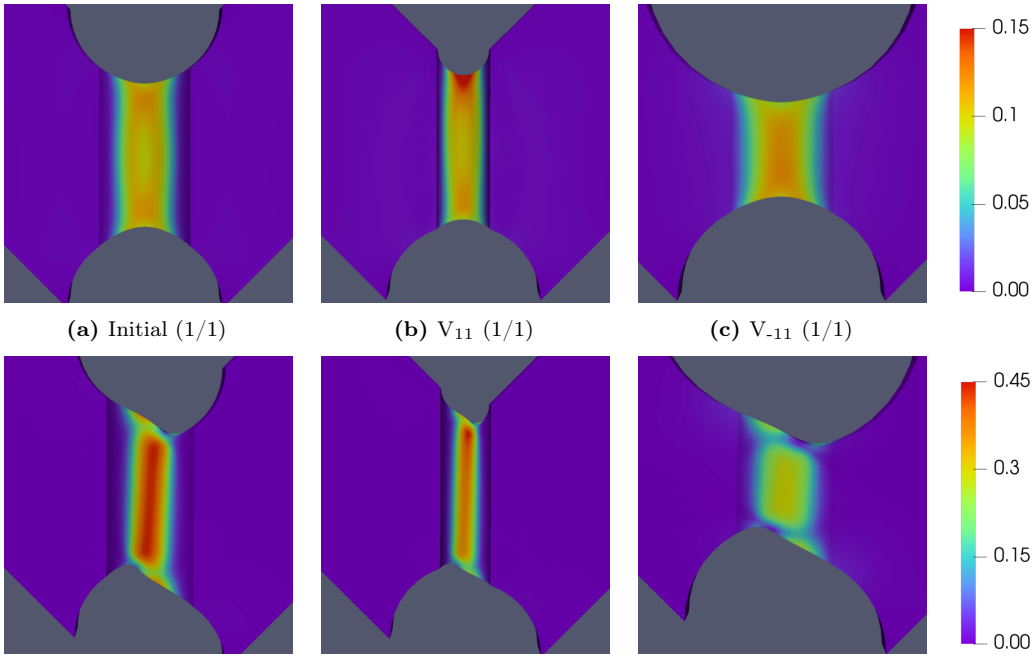

(a) Initial (1/1) **(b)** V_{11} (1/1) **(c)** $V_{\text{-}11}$ (1/1)

(d) Initial (-1/1) **(e)** V_{11} (-1/1) **(f)** $V_{\text{-}11}$ (-1/1)

Figure 7.19: First principal strains calculated numerically. All three geometries for the different load cases: (a)-(c) load case 1/1, (d)-(e) load case -1/1.

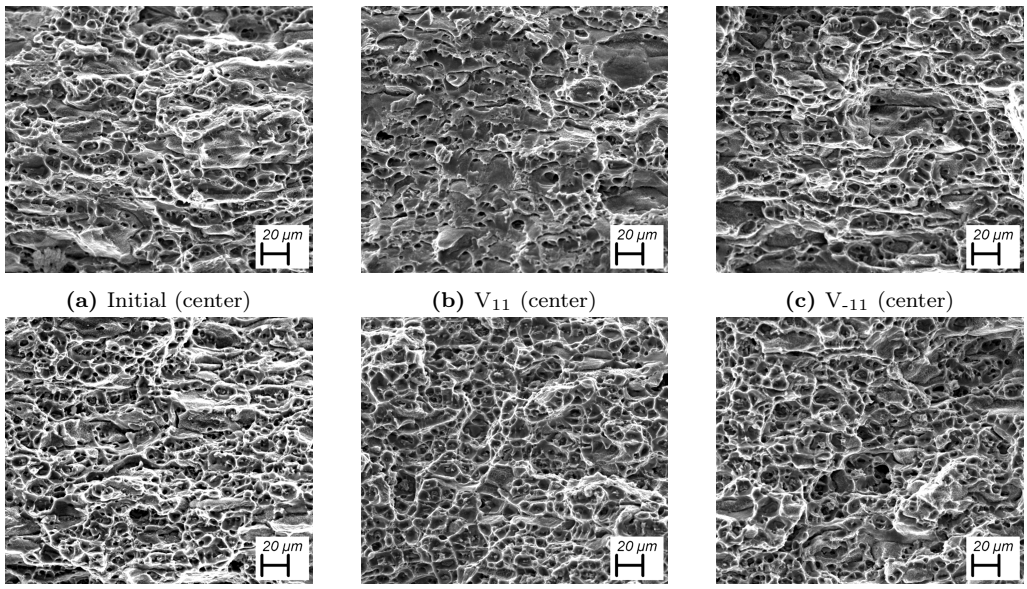

(a) Initial (center) **(b)** V_{11} (center) **(c)** $V_{\text{-}11}$ (center)

(d) Initial (boundary) **(e)** V_{11} (boundary) **(f)** $V_{\text{-}11}$ (boundary)

Figure 7.20: Scanning electron microscopy images: Load case 1/1, (a) initial geometry, central; (b) V_{11} geometry, central; (c) $V_{\text{-}11}$ geometry, central; (d) initial geometry, boundary; (e) $V_{\text{-}11}$ geometry, boundary; (f) $V_{\text{-}11}$ geometry, boundary.

Under -1/1-loading the numerical simulations have predicted stress triaxialities of approximately $\eta = 0.05$, cf. Fig. 7.12(c) to 7.12(e) and values of the Lode parameter mainly around $\omega = 0$, cf. Fig. 7.13(c) to 7.13(e). This reflects a shear dominated stress state, which corresponds to the SEM images of the fracture surfaces that indicate fracture behavior initiated by micro shear cracks. However, the SEM images look rather homogeneous and no significant differences can be observed between the three different geometries in all three evaluation positions, cf. Fig. 7.21.

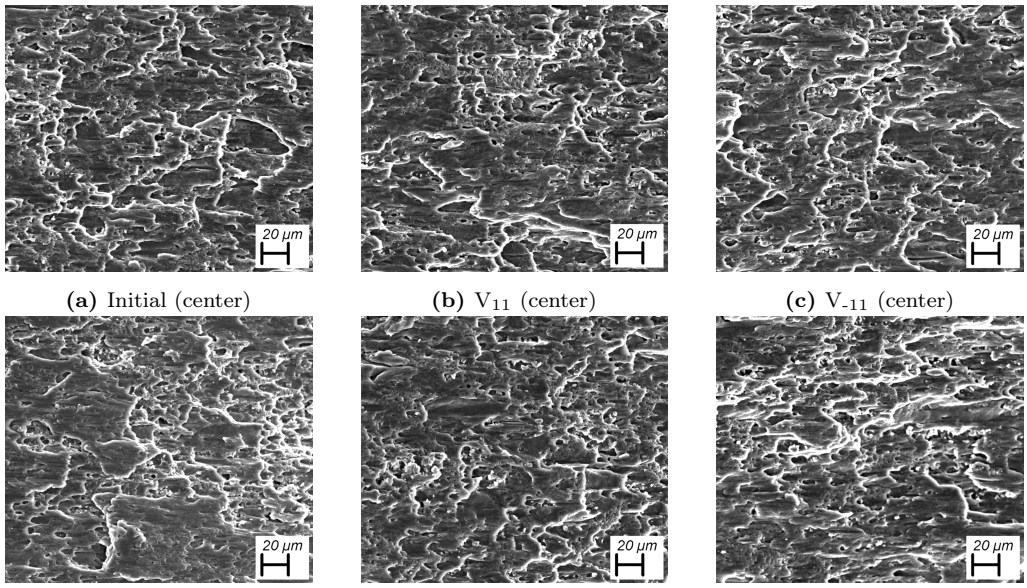

(a) Initial (center) **(b)** V_{11} (center) **(c)** $V_{\text{-}11}$ (center)

(d) Initial (boundary) **(e)** V_{11} (boundary) **(f)** $V_{\text{-}11}$ (boundary)

Figure 7.21: Scanning electron microscopy images: Load case -1/1, (a) initial geometry, central; (b) V_{11} geometry, central; (c) $V_{\text{-}11}$ geometry, central; (d) initial geometry, boundary; (e) V_{11} geometry, boundary; (f) $V_{\text{-}11}$ geometry, boundary.

7.5 Summary

This chapter discusses the shape optimization of the biaxially loaded X0-specimen with the objective of distinct and preferably homogeneous stress states for two different load cases so as to isolate corresponding damage mechanisms acting on the micro level. Under 1/1-loading both axis are under traction, which leads to a tension dominated stress state and high stress triaxialites in the notched specimen area. In this case the leading damage mechanism is nucleation, growth and coalescence of voids. Contrary, for -1/1-loading one axis is under traction and the other under compression. This leads to a shear dominated stress state and stress triaxialities around $\eta \approx 0$. In shear dominated stress states the leading damage mechanism is evolution of micro shear cracks.
The shape optimization focuses on the maximization and minimization of the stress triaxiality in the cross section of the specimen notches corresponding to the respective load case. That is, for 1/1-loading the stress triaxiality has been maximized and for -1/1-loading

it has been minimized. Therefore, the geometry is parametrized by three radii and one penetration depth. The cross section is kept constant during the optimization process to maintain preferably homogeneous stress states. The solutions of the optimization problems have been obtained by means of gradient based methods utilizing the `Matlab` function `fmincon`. Elastoplastic constitutive parameters are identified in advance by fitting the global force-displacement curve of a uniaxial tensile test made of the aluminium alloy $AlMgSi_1$ (EN AW 6082-T6) used for the studies of the X0-specimen. The desired values and gradients of objective and constraint functions for both, the shape optimization and the parameter identification, are provided by the FEM based elastoplastic structural and corresponding design sensitivity analysis explained in Chap. 4, 5 and 6. The objective values of the shape optimization tasks could be improved by $\sim 25\,\%$ for 1/1-loading and $\sim 17\,\%$ for -1/1-loading. Due to the variational approach for the sensitivity analysis, the optimization problems modelling the mechanical intention of distinct and preferably homogeneous stress ensured limited numerical cost and reasonable computation times and only a small number of iterations to convergence of the algorithms are needed. This emphasizes the practicability and convenience of the chosen computational approach that generates quantitative results that are not available by engineering intuition.
Furthermore, experiments with the initial X0-specimen geometry, as well as the two load case dependent optimal geometries, V_{11} and $V_{\text{-}11}$, are conducted and evaluated. By means of a DIC system, the global deformation behavior is tracked during the experiment. Further, the fracture surfaces are examined by SEM. Simulation and experimental results are compared and discussed. Overall, the experiments confirmed the numerically predicted results. The geometry optimized for the 1/1 load case V_{11} shows the most brittle deformation behavior in both load cases, while $V_{\text{-}11}$ that is optimized for the -1/1 load case shows the most ductile deformation behavior. The SEM pictures of the fracture surfaces especially indicate the increased stress triaxiality of V_{11} under 1/1-loading. However, the effect of the optimization on the fracture behavior is less obvious for the -1/1 load case.

Chapter 8

Concluding Summary and Outlook

This final chapter aims at summarizing the developments and findings acquired within this thesis and drawing conclusions. All tackled topics are briefly reviewed and the obtained results are highlighted. A concluding outlook gives hints and inspirations for future research investigations.

Within this thesis, a complete structural optimization strategy based on variational design sensitivity analysis considering finite elestoplastic deformations for geometric shape and macroscopic constitutive design has been developed. In order to maintain the main goal of this thesis, i.e. the shape optimization of the X0-specimen, the solution framework of a general constrained optimization problem has been presented in Chap. 3. The choice of the SQP algorithm in combination with the BFGS Hessian approximation constitutes a state-of-the-art method and requires the computation of objective and constraint function values, as well as their gradient information regarding the chosen design parametrization. The theoretical and computational tasks consisting of the structural analysis and variational design sensitivity analysis (VDSA) have been clearly designated.
For preparation, in Chap. 4 the continuum thermomechanical framework has been sketched. The deployed elastoplastic constitutive model suited for finite deformations has been explained and the solution of the structural mechanical problem utilizing the finite element method has been outlined. Due to the assumption of plastic incompressibility and the known locking effects occurring at utilizing low order finite elements, the so-called $\overline{F}$-method has been chosen for remedy. Complete consistent linearizations have been provided and the numerical model has been undertaken selected standard benchmarks.
Based on these preparations, the main topic, i.e. the VDSA of the elastoplastic model has been focused in Chap. 5. Here, the fundamental idea of the variational approach based on an enhanced viewpoint of kinematics has been sketched. The fundamental principles have been applied to the spatially continuous model equations of the elastoplastic structural analysis problem. The enhanced kinematic viewpoint allows for strict separation of geometrical and physical properties within the natural framework of continuum mechanics. This makes complex derivations significantly easier, as implicit dependencies can be elegantly circumvented. The approach has first been used to derive the sensitivity information of the elastoplastic structural response. Based on this, the approach to determine demanded physical function sensitivities like stress measures has been presented. The VDSA requires deep knowledge of the underlying governing equations, as well as numerical implementation techniques, especially due to the non-linear elastoplastic material behavior.
The continuous sensitivity relations derived in Chap. 5 had to be implemented into

the general finite element framework for the solution of the structural analysis problem. Therefore, in Chap. 6, discrete design parametrizations based on CAGD-FEM coupling have been introduced and the discrete approximations for the design variations have been stated. Consistent with the $\overline{F}$-method, all necessary design sensitivity quantities have been derived and formulated in a compact matrix notation. The computational algorithms needed for embedding the additional sensitivity information into the finite element framework have been explained and pseudo code examples were provided for each algorithmic level. Additionally to the analytical approach, the possibility of computing semi-analytical sensitivity information has been presented. Here, parts of the sensitivity information corresponding to the deformation history can be obtained numerically by means of the finite difference method. Both approaches are validated and compared by means of numerical benchmarks.
In Chap. 7 the main shape optimization of the X0-specimen has been performed. Based on the general structural optimization framework prepared in the previous chapters, two different kinds of inverse design problems were tackled. Before the actual shape optimization, the constitutive parameters controlling the elastoplastic structural response had to be fitted to the material used for the experiments. Therefore, an inverse parameter identification fitting the global force-displacement response of a uniaxial tension test had to be solved in advance. The main shape optimization with the aim to obtain distinct and preferably homogeneous stress states in terms of the stress triaxiality has successfully been realized subsequently. For the two different loading scenarios, i.e. 1/1-loading producing tensile stress states and high stress triaxialities and -1/1-loading producing shear stress states and low stress triaxialities, two different optimization problems have been stated. For the 1/1-load case the stress triaxiality in the notched specimen area was maximized, contrary, for the -1/1-load case the stress triaxiality in that area was minimized. The two respective optimal solutions V_{11} and $V_{\text{-}11}$ that have been optimized for the corresponding load case show improvements of $\sim 25\,\%$ and $\sim 17\,\%$ regarding the value of the objective functions compared to the initial geometry. The accuracy of the numerically obtained optima have been experimentally validated. The experiments with all three geometries for both loading scenarios have been monitored by digital image correlation (DIC) and furthermore the fracture surfaces have been examined by means of scanning electron microscopy (SEM) for examination of the deformation and fracture behavior. Overall, the experimental results lined up well with the numerical predictions. For V_{11} in both loading scenarios the most brittle fracture behavior could be observed numerically and experimentally, while $V_{\text{-}11}$ showed the most ductile response. However, in the -1/1 load case the numerical model overestimates the stress response especially for the tension axis. Additionally, the comparison of the principle strains obtained numerically and measured by the DIC shows better similarities in the 1/1-load case. This is also reflected by the examination of the fracture surfaces. For V_{11} , the SEM images show significantly larger and well-pronounced voids in the 1/1-load case indicating the increased stress triaxiality due to the shape optimization.

In the context of optimal specimen shape design, the work at hand has proposed a computationally efficient method for the solution of optimal geometric design considering finite elastoplastic deformations. The obtained optimal geometries can be used to further develop and calibrate complex constitutive models covering micromechanical effects coupled to specific stress states. The developed method can also be used for parameter

identification purposes and shape optimization of any elastoplastic structure. That is, it is not limited to the special case of optimal specimen design. Linking to other structural mechanical topics in the context of VDSA is very conceivable and could open a variety of applications. For instance in [63] hyperelastic solid shell finite elements are used and the idea of design exploration is formulated. Here, singular value decomposition is utilized to explore the inner structure of the structural response sensitivity. This can be used to identify major and minor influencing design parameters and could therefore be used to calibrate the resolution of the optimization problem. In [88] the basic VDSA ideas are applied to multiscale design. That is, the structural analysis problem considers the geometric design of the microstructure. It could be shown that the VDSA could successfully be applied within the FE^2 method. Combination with topology optimization approaches as e.g. proposed in e.g. [15, 145, 188] have also proven to be promising. Here, the basic idea of the extended finite element method (XFEM) is extended to the so-called modified extended finite element method (YFEM). Utilizing topological derivatives, it is possible that additionally to changing the shape, also voids or inclusions can occur based on the values of defined level-set functions. That is, simultaneous topology and shape changes can be considered. The class of materials is limited in this thesis to elastoplastic metals. Extensions of the constitutive model can be challenging in view of the consistent VDSA, however in [71, 73] a gradient-enhanced non-local damage model could successfully be used within a similar structural optimization setup in the context of metal forming. Due to the modular formulation of the algorithms in the VDSA framework, adaption of new and established developments is uncomplicated. For instance, in [72, 100, 102], external load scaling parameters have been chosen as design variables. However, modern technologies offer ways of developing better methods in all of the tackled research fields. The presented geometric shape parametrization based on an computer aided geometry description is used for the optimization in this work. Calculations, i.e. the structural and sensitivity analysis are performed based on a geometry approximation within the finite element method. In the recent decade, the method of isogeometric analysis (IGA) has gained popularity. Here, the underlying CAGD geometry is directly used for the computational analysis as the underlying basis spline interpolation functions represent the solution space of the underlying boundary value problem. Isogeometric sensitivity analysis of elastoplastic structures based on VDSA could have the advantage of even more efficiency and flexibility of the computational model as even with lower degrees of freedom complex geometries are exactly represented. Re-meshing and the necessity to determine a design velocity field within the iterative optimization procedure omits completely. Modern manufacturers are able to directly process the CAGD data for production in high resolution.

In the sense of optimal specimen design this might lead to novel designing techniques and explorations of innovative specimen and experimental design in general.

Bibliography

[1] Aage, N., E. Andreassen, B. Lazarov, and O. Sigmund: 'Giga-voxel computational morphogenesis for structural design'. *Nature* (Oct. 2017), vol. 550: pp. 84–86. doi: 10.1038/nature23911 (cit. on pp. 5, 18).

[2] Abdelhay, A., O. Dawood, A. Bassiuny, E. Elhalawany, and M. Mustafa: 'A Newly Developed Cruciform Specimens Geometry for Biaxial Stress Evaluation Using NDE'. May 2009 (cit. on p. 6).

[3] Ahrens, J., B. Geveci, and C. Law: *ParaView: An End-User Tool for Large Data Visualization*. Visualization Handbook, Elsevier, 2005. url: https://www.paraview.org/ (cit. on p. 15).

[4] Altenbach, H.: *Kontinuumsmechanik: Einführung in die materialunabhängigen und materialabhängigen Gleichungen*. Springer DE, 2012. doi: 10.1007/978-3-662-47070-1 (cit. on p. 28).

[5] Arfken, G. B., H. J. Weber, and F. E. Harris: 'Further Topics in Analysis'. *Mathematical Methods for Physicists (Seventh Edition)*. Ed. by Arfken, G. B., H. J. Weber, and F. E. Harris. Seventh Edition. Boston: Academic Press, 2013. Chap. 12: pp. 551–598. doi: 10.1016/B978-0-12-384654-9.00012-8 (cit. on p. 19).

[6] Armijo, L.: 'Minimization of functions having Lipschitz continuous first partial derivatives.' *Pacific Journal of Mathematics* (1966), vol. 16(1): pp. 1–3. doi: pjm/1102995080 (cit. on p. 21).

[7] Audi: *Inspiration aus der Natur: Mit diesem Wissen konstruierte Audi das Gerüst des ASF, das aus Strangpressprofilen und Druckgussteilen besteht.* [Online; accessed April 28, 2021]. Sept. 2013. url: https://www.krafthand.de/artikel/20-jahre-karosserie-leichtbau-bei-audi-pemiere-des-neuen-a-8-bei-iaa-13097/ (cit. on p. 3).

[8] Ayachit, U.: *The ParaView Guide: A Parallel Visualization Application*. Kitware, 2015 (cit. on p. 15).

[9] Bai, Y. and T. Wierzbicki: 'A new model of metal plasticity and fracture with pressure and Lode dependence'. *International Journal of Plasticity* (2008), vol. 24(6): pp. 1071–1096. doi: 10.1016/j.ijplas.2007.09.004 (cit. on p. 2).

[10] Baier, H., C. Sesselberg, and B. Specht: *Optimierung in der Strukturmechanik*. Vieweg+Teubner Verlag, 1994. doi: 10.1007/978-3-322-90700-4 (cit. on pp. 5, 18).

[11] Baptista, R., R. Cláudio, L. Reis, J. Madeira, and M. Freitas: 'Optimal Cruciform Specimen Design Using the Direct Multi-search Method and Design Variable Influence Study'. *Procedia Structural Integrity* (Dec. 2017), vol. 5: pp. 659–666. doi: 10.1016/j.prostr.2017.07.037 (cit. on p. 6).

[12] Barthold, F.-J.: 'Remarks on variational shape sensitivity analysis based on local coordinates'. *Engineering Analysis with Boundary Elements* (2008), vol. 32(11). Special Issue on Shape and Topology Sensitivity Analysis: Theory and Applications (Guest Editors: R.A. Feijoo and E. Taroco): pp. 971–985. doi: 10.1016/j.enganabound.2007.09.007 (cit. on pp. 6, 52, 53).

[13] Barthold, F.-J.: 'Theorie und Numerik zur Berechnung und Optimierung von Strukturen aus isotropen, hyperelastischen Materialien'. PhD thesis. Universität Hannover, 1993. doi: 10.17877/DE290R-7352 (cit. on pp. 6, 18, 52, 53).

[14] Barthold, F.-J., N. Gerzen, W. Kijanski, and D. Materna: 'Efficient Variational Design Sensitivity Analysis'. *Mathematical Modeling and Optimization of Complex Structures*. Ed. by Neittaanmäki, P., S. Repin, and T. Tuovinen. Vol. 40. Computational Methods in Applied Sciences. Switzerland: Springer International Publishing, 2016. doi: 10.1007/978-3-319-23564-6_14 (cit. on pp. 6, 19, 52, 53, 68).

[15] Barthold, F.-J. and D. Materna: 'A modified extended finite element method approach for design sensitivity analysis'. *International Journal for Numerical Methods in Engineering* (2015), vol. 104(3): pp. 209–234. doi: 10.1002/nme.4930 (cit. on p. 117).

[16] Barthold, F.-J. and E. Stein: 'A continuum mechanical based formulation of the variational sensitivity analysis in structural optimization. Part I: Analysis'. *Structural Optimization* (1996), vol. 11(1/2): pp. 29–42. doi: 10.1007/BF01279652 (cit. on p. 53).

[17] Barthold, F.-J.: 'A structural optimization viewpoint on growth phenomena'. *Bulletin of the Polish Academy of Sciences, Technical Sciences* (Apr. 2011), vol. 60. doi: 10.2478/v10175-012-0033-6 (cit. on p. 53).

[18] Barthold, F.-J.: 'Zur Kontinuumsmechanik inverser Geometrieprobleme'. Habilitation. Braunschweiger Schriften zur Mechanik 44-2002, TU Braunschweig, 2004. doi: 10.17877/DE290R-13502 (cit. on pp. 6, 18, 52, 53, 56–59).

[19] Barthold, F.-J. and M. Firuziaan: 'Optimization of hyperelastic materials with isotropic damage'. *Structural and Multidisciplinary Optimization* (Jan. 2000), vol. 20: pp. 12–21. doi: 10.1007/s001580050131 (cit. on p. 53).

[20] Barthold, F.-J. and K. Wiechmann: 'A Comparison of Displacement and Mixed Finite Element Formulations for Variational Design Sensitivity Analysis'. *III European Conference on Computational Mechanics*. Ed. by Motasoares, C. A., J. A. C. Martins, H. C. Rodrigues, J. A. C. Ambrósio, C. A. B. Pina, C. M. Motasoares, E. B. R. Pereira, and J. Folgado. Dordrecht: Springer Netherlands, 2006: pp. 645–645. doi: 10.1007/1-4020-5370-3_645 (cit. on p. 53).

[21] Bathe, K.-J.: *Finite - Elemente - Methoden*. Berichtigter Nachdr. Berlin: Springer-Verlag GmbH, 1990 (cit. on pp. 5, 28, 68, 155).

[22] Bauer, J., K. Priesnitz, M. Schemmann, B. Brylka, and T. Böhlke: 'Parametric shape optimization of biaxial tensile specimen'. *PAMM* (2016), vol. 16(1): pp. 159–160. doi: 10.1002/pamm.201610068 (cit. on p. 6).

[23] Bendsøe, M.: *Optimization of Structural Topology, Shape, and Material*. Springer Berlin Heidelberg, 1995 (cit. on pp. 5, 18).

[24] Bendsøe, M. P. and O. Sigmund: *Topology Optimization*. 2nd ed. Springer, Berlin, Heidelberg, 2004. doi: 10.1007/978-3-662-05086-6 (cit. on pp. 5, 18).

[25] Benzerga, A. A. and J.-B. Leblond: 'Ductile Fracture by Void Growth to Coalescence'. *Advances in Applied Mechanics*. Ed. by Aref, H. and E. van der Giessen. Vol. 44. Advances in Applied Mechanics. Elsevier, 2010: pp. 169–305. doi: 10.1016/S0065-2156(10)44003-X (cit. on pp. 2, 5).

[26] Bertram, A.: *Axiomatische Einführung in die Kontinuumsmechanik*. Mannheim [u.a.]: BI-Wiss.-Verl., 1989: 287 S. (Cit. on pp. 28, 56).

[27] Bixby, R.: 'Implementing the Simplex Method: The Initial Basis'. *INFORMS Journal on Computing* (1992), vol. 4: pp. 267–284. doi: 10.1287/ijoc.4.3.267 (cit. on p. 19).

[28] Bletzinger, K.-U.: 'Formoptimierung von Flächentragwerken'. PhD thesis. Institut für Baustatik, Universität Stuttgart, 1990 (cit. on pp. 6, 18).

[29] Bletzinger, K.-U., M. Firl, J. Linhard, and R. Wüchner: 'Optimal shapes of mechanically motivated surfaces'. *Computer Methods in Applied Mechanics and Engineering* (Jan. 2010), vol. 199: pp. 324–333. doi: 10.1016/j.cma.2008.09.009 (cit. on pp. 5, 6, 18).

[30] Boggs, P. and J. Tolle: 'Sequential Quadratic Programming'. *Acta Numerica* (Jan. 1995), vol. 4: pp. 1–51. doi: 10.1017/S0962492900002518 (cit. on p. 19).

[31] Bonet, J. and R. Wood: *Nonlinear Continuum Mechanics for Finite Element Analysis*. Cambridge University Press, 1997. doi: 10.1017/CBO9780511755446 (cit. on pp. 5, 28, 68, 155).

[32] Borgonovo, E. and E. Plischke: 'Sensitivity analysis: A review of recent advances'. *European Journal of Operational Research* (2016), vol. 248(3): pp. 869–887. doi: 10.1016/j.ejor.2015.06.032 (cit. on pp. 6, 52).

[33] Borst, R., M. Crisfield, J. Remmers, and C. Verhoosel: *Non-linear Finite Element Analysis of Solids and Structures, Volume 1*. July 2012. doi: 10.1002/9781118375938 (cit. on pp. 5, 28).

[34] Brcic, M., M. Canadija, and J. Brnic: 'Multiscale Modeling of Nanocomposite Structures with Defects'. *Advances in Fracture and Damage Mechanics XII*. Vol. 577. Key Engineering Materials. Trans Tech Publications Ltd, Jan. 2014: pp. 141–144. doi: 10.4028/www.scientific.net/KEM.577-578.141 (cit. on p. 18).

[35] Broyden, C.: 'The Convergence of a Class of Double-rank Minimization Algorithms 1. General Considerations'. *Ima Journal of Applied Mathematics* (1970), vol. 6: pp. 76–90. doi: 10.1093/imamat/6.1.76 (cit. on p. 19).

[36] Brünig, M.: 'An anisotropic ductile damage model based on irreversible thermodynamics'. *International Journal of Plasticity* (2003), vol. 19(10): pp. 1679–1713. doi: https://doi.org/10.1016/S0749-6419(02)00114-6 (cit. on pp. 2, 5, 92).

[37] Brünig, M., D. Brenner, and S. Gerke: 'Stress state dependence of ductile damage and fracture behavior: Experiments and numerical simulations'. *Engineering Fracture Mechanics* (2015), vol. 141: pp. 152–169. doi: 10.1016/j.engfracmech.2015.05.022 (cit. on p. 3).

[38] Brünig, M., O. Chyra, D. Albrecht, L. Driemeier, and M. Alves: 'A ductile damage criterion at various stress triaxialities'. *International Journal of Plasticity* (2008), vol. 24(10): pp. 1731–1755. doi: 10.1016/j.ijplas.2007.12.001 (cit. on pp. 2, 92).

[39] Brünig, M., S. Gerke, and V. Hagenbrock: 'Stress-state-dependence of damage strain rate tensors caused by growth and coalescence of micro-defects'. *International Journal of Plasticity* (2014), vol. 63: pp. 49–63. doi: 10.1016/j.ijplas.2014.04.007 (cit. on p. 92).

[40] Brünig, M., S. Gerke, and M. Zistl: 'Experiments and numerical simulations with the H-specimen on damage and fracture of ductile metals under non-proportional loading paths'. *Engineering Fracture Mechanics* (2019), vol. 217: p. 106531. doi: 10.1016/j.engfracmech.2019.106531 (cit. on p. 3).

[41] Chaboche, J. L.: 'Continuum Damage Mechanics: Part I—General Concepts'. *Journal of Applied Mechanics* (Mar. 1988), vol. 55(1): pp. 59–64. doi: 10.1115/1.3173661 (cit. on p. 2).

[42] Chen, W. and D. Han: *Plasticity for Structural Engineers*. J. Ross Publishing Classics. J. Ross Pub., 2007 (cit. on pp. 5, 28).

[43] Choi, K. and N. Kim: *Structural Sensitivity Analysis and Optimization I: Linear Systems*. Vol. 1. Nov. 2004. doi: 10.1007/b138709 (cit. on pp. 6, 12, 19, 52, 54).

[44] Chowdhury, N., J. Wang, and W. Chiu: 'Design of a Flat Plate Specimen Suitable for Biaxial Tensile Tests on Polymer Materials'. *Polymers and Polymer Composites* (Nov. 2015), vol. 23: pp. 627–638. doi: 10.1177/096739111502300905 (cit. on p. 6).

[45] Christensen, P. and A. Klarbring: *An Introduction to Structural Optimization*. Springer Netherlands, 2009. doi: 10.1007/978-1-4020-8666-3 (cit. on pp. 5, 18).

[46] Coleman, B. D. and M. E. Gurtin: 'Thermodynamics with Internal State Variables'. *The Journal of Chemical Physics* (1967), vol. 47: pp. 597–613. doi: 10.1063/1.1711937 (cit. on p. 34).

[47] Crisfield, M.: *Non-linear Finite Element Analysis of Solids and Structures: Advanced topics*. Non-linear Finite Element Analysis of Solids and Structures. Wiley, 1991 (cit. on pp. 5, 28).

[48] Dantzig, G. B., A. Orden, and P. Wolfe: 'The generalized simplex method for minimizing a linear form under linear inequality restraints.' *Pacific Journal of Mathematics* (1955), vol. 5(2): pp. 183–195. doi: pjm/1103044531 (cit. on p. 19).

[49] de Souza Neto, E., D. Perić, M. Dutko, and D. Owen: 'Design of simple low order finite elements for large strain analysis of nearly incompressible solids'. *International Journal of Solids and Structures* (1996), vol. 33(20): pp. 3277–3296. doi: 10.1016/0020-7683(95)00259-6 (cit. on pp. 5, 28, 45).

[50] Debye, P.: *Näherungsformeln für die Zylinderfunktionen für große Werte des Arguments und unbeschränkt veränderliche Werte des Index*. Dec. 1909. doi: 10.1007/bf01450097. url: 10.1007/bf01450097 (cit. on p. 19).

[51] Demmerle, S. and J. Boehler: 'Optimal design of biaxial tensile cruciform specimens'. *Journal of the Mechanics and Physics of Solids* (1993), vol. 41(1): pp. 143–181. doi: 10.1016/0022-5096(93)90067-P (cit. on p. 6).

[52] Dobbin, D.: 'MEX-files and MATLAB Compiler'. *MATLAB Central File Exchange. Retrieved May 5* (2021), vol. URL: www.mathworks.com/matlabcentral/fileexchange/4008-mex-files-and-matlab-compiler (cit. on p. 158).

[53] Duhem, P.: 'Traité D'Énergétique ou de Thermodynamique Générale'. *Monatshefte für Mathematik und Physik* (Dec. 1913), vol. 24: A3. DOI: 10.1007/BF01708141 (cit. on p. 28).

[54] Elguedj, T. and T. Hughes: 'Isogeometric analysis of nearly incompressible large strain plasticity'. *Comput. Methods Appl. Mech. Engng.* (2014), vol. 268: pp. 388–416. DOI: 10.1016/j.cma.2013.09.024 (cit. on pp. 28, 45, 46).

[55] Elguedj, T., Y. Bazilevs, V. Calo, and T. Hughes: 'B-bar an F-bar projection methods for nearly incompressible linear and non linear elasticity and plasticity using higher order NURBS element'. *Comput. Method Appl. Mech. Engrg.* (Feb. 2008), vol. 197: pp. 2732–2762 (cit. on pp. 5, 28, 45, 46).

[56] Etling, T. and R. Herzog: 'Optimum Experimental Design by Shape Optimization of Specimens in Linear Elasticity'. *SIAM Journal on Applied Mathematics* (Jan. 2018), vol. 78: pp. 1553–1576. DOI: 10.1137/17M1147743 (cit. on p. 6).

[57] Fletcher, R.: 'A New Approach to Variable Metric Algorithms'. *Comput. J.* (1970), vol. 13: pp. 317–322 (cit. on p. 19).

[58] Gao, X., G. Zhang, and C. Roe: 'A Study on the Effect of the Stress State on Ductile Fracture'. *International Journal of Damage Mechanics* (2010), vol. 19(1): pp. 75–94. DOI: 10.1177/1056789509101917 (cit. on p. 2).

[59] Gerke, S., P. Adulyasak, and M. Brünig: 'New biaxially loaded specimens for the analysis of damage and fracture in sheet metals'. *International Journal of Solids and Structures* (2017), vol. 110-111: pp. 209–218. DOI: 10.1016/j.ijsolstr.2017.01.027 (cit. on pp. 3, 7, 92, 94, 107).

[60] Gerke, S., M. Schmidt, M. Dirian, and M. Brünig: 'Damage and Fracture of Ductile Sheet Metals: Experiments and Numerical Simulations with New Biaxial Specimens'. *Advances in Mechanics of Materials and Structural Analysis*. Ed. by Altenbach, H., F. Jablonski, W. H. Müller, K. Naumenko, and P. Schneider. Vol. 80. Cham: Springer International Publishing, 2018: pp. 99–116. DOI: 10.1007/978-3-319-70563-7{\textunderscore}5 (cit. on pp. 3, 7).

[61] Gerke, S., M. Zistl, A. Bhardwaj, and M. Brünig: 'Experiments with the X0-specimen on the effect of non-proportional loading paths on damage and fracture mechanisms in aluminum alloys'. *International Journal of Solids and Structures* (May 2019), vol. 163: pp. 157–169. DOI: 10.1016/j.ijsolstr.2019.01.007 (cit. on pp. 3, 7, 93, 107, 108).

[62] Gerke, S., M. Zistl, and M. Brünig: 'Experiments and numerical simulation of damage and fracture of the X0-specimen under non-proportional loading paths'. *Engineering Fracture Mechanics* (Feb. 2020), vol. 224: p. 106795. doi: 10.1016/j.engfracmech.2019.106795 (cit. on pp. 3, 7, 92, 93).

[63] Gerzen, N.: 'Analysis and Applications of Variational Sensitivity Information in Structural Optimisation'. Dissertation. TU Dortmund, 2014. doi: 10.17877/DE290R-919 (cit. on pp. 6, 53, 68, 117).

[64] Geuzaine, C. and J.-F. Remacle: 'Gmsh: a three-dimensional finite element mesh generator with built-in pre- and post-processing facilities'. *International Journal for Numerical Methods in Engineering* (2009), vol. 79(11): pp. 1309–1331 (cit. on p. 14).

[65] Gill, P., W. Murray, M. Saunders, and M. Wright: *Numerical Linear Algebra And Optimization*. Avalon Publishing, 1991 (cit. on p. 21).

[66] Gill, P. E., W. Murray, M. A. Saunders, and M. H. Wright: 'Procedures for Optimization Problems with a Mixture of Bounds and General Linear Constraints'. *ACM Trans. Math. Softw.* (Aug. 1984), vol. 10(3): pp. 282–298. doi: 10.1145/1271.1276 (cit. on p. 21).

[67] Glaser, S. and F. Armero: 'On the formulation of enhanced strain finite elements in finite deformations'. *Engineering Computations* (1997), vol. 14(7): pp. 759–791. doi: 10.1108/02644409710188664 (cit. on p. 46).

[68] Goldfarb, D.: 'A family of variable-metric methods derived by variational means'. *Mathematics of Computation* (1970), vol. 24: pp. 23–26 (cit. on p. 19).

[69] Gould, N., D. Orban, and P. Toint: 'Numerical methods for large-scale non-linear optimization'. *Acta Numerica* (2005), vol. 14: pp. 299–361. doi: 10.1017/S0962492904000248 (cit. on p. 19).

[70] Gruben, G., O. S. Hopperstad, and T. Børvik: 'Evaluation of uncoupled ductile fracture criteria for the dual-phase steel Docol 600DL'. *International Journal of Mechanical Sciences* (2012), vol. 62(1): pp. 133–146. doi: 10.1016/j.ijmecsci.2012.06.009 (cit. on p. 2).

[71] Guhr, F., F.-J. Barthold, A. Menzel, L. Sprave, and J. Liedmann: 'Sensitivity analysis of a non-local, gradient enhanced damage model'. *PAMM* (2018), vol. 18(1): e201800147. doi: 10.1002/pamm.201800147 (cit. on p. 117).

[72] Guhr, F., F.-J. Barthold, R. Meya, and A. Tekkaya: 'Load Optimisation for Air Bending in the Context of Damage Reduction'. *PAMM* (Nov. 2019), vol. 19. doi: 10.1002/pamm.201900179 (cit. on p. 117).

[73] Guhr, F., L. Sprave, F.-J. Barthold, and A. Menzel: 'A Computational shape optimisation for a gradient-enhanced continuum damage model'. *Computational Mechanics* (2020), vol.: pp. 1105–1124. doi: 10.1007/s00466-019-01810-3 (cit. on p. 117).

[74] Hairer, E., S. Norsett, and G. Wanner: *Solving Ordinary Differential Equations I: Nonstiff Problems*. Vol. 8. Jan. 1993. doi: 10.1007/978-3-540-78862-1 (cit. on p. 37).

[75] Han, S.-P.: 'A globally convergent method for nonlinear programming'. *Journal of Optimization Theory and Applications* (1975), vol. 22: pp. 297–309. doi: 10.1007/BF00932858 (cit. on p. 21).

[76] Harzheim, L.: *Strukturoptimierung: Grundlagen und Anwendungen*. Edition Harry Deutsch. Verlag Europa-Lehrmittel Nourney, Vollmer, 2014 (cit. on pp. 5, 18).

[77] Haug, E., K. Choi, and V. Komkov: *Design Sensitivity Analysis of Structural Systems*. Jan. 1986 (cit. on pp. 6, 12, 52, 54).

[78] Hestenes, M. R. and E. Stiefel: 'Methods of conjugate gradients for solving linear systems'. *Journal of research of the National Bureau of Standards* (1952), vol. 49: pp. 409–435. doi: 10.6028/JRES.049.044 (cit. on p. 19).

[79] Hiyoshi, N., T. Itoh, M. Sakane, T. Tsurui, M. Tsurui, and C. Hisaka: 'Development of miniature cruciform specimen and testing machine for multiaxial creep investigation'. *Theoretical and Applied Fracture Mechanics* (2020), vol. 108: p. 102582. doi: 10.1016/j.tafmec.2020.102582 (cit. on p. 6).

[80] Hughes, T. J. R.: *The Finite Element Method: Linear Static and Dynamic Finite Element Analysis*. Dover Civil and Mechanical Engineering. Dover Publications, 2012 (cit. on pp. 5, 28, 68, 155).

[81] Huynh, G., X. Zhuang, H. Bui, G. Meschke, and H. Nguyen-Xuan: 'Elasto-plastic large deformation analysis of multi-patch thin shells by isogeometric approach'. *Finite Elements in Analysis and Design* (June 2020), vol. 173: p. 103389. doi: 10.1016/j.finel.2020.103389 (cit. on pp. 28, 49).

[82] Imtiaz, H., Y. Fang, J. Du, and B. Liu: 'Fundamental problem in optimizing the biaxial testing specimen'. *Science China Technological Sciences* (Mar. 2019), vol. 62. doi: 10.1007/s11431-018-9459-7 (cit. on p. 6).

[83] Iooss, B. and P. Lemaítre: 'Uncertainty Management in Simulation-Optimization of Complex Systems'. Ed. by G., D. and M. C. Operations Research/Computer Science Interfaces Series, vol 59. Springer, Boston, 2015. Chap. A Review on Global Sensitivity Analysis Methods: pp. 101–122. doi: 10.1007/978-1-4899-7547-8_5 (cit. on p. 52).

[84] Item 149279 of Seattle Municipal Archives: *Flickr: Boeing 767 over Mount Rainier circa 1980s*. [Online; accessed April 28, 2021]. URL: https://www.flickr.com/photos/seattlemunicipalarchives/11803255264 (cit. on p. 3).

[85] Itskov, M.: 'Tensor Algebra and Tensor Analysis for Engineers: With Applications to Continuum Mechanics'. *Mathematical Engineering*. Springer, 2009. DOI: 10.1007/978-3-642-30879-6 (cit. on p. 143).

[86] Junker, P. and K. Hackl: 'A variational growth approach to topology optimization'. *Structural and Multidisciplinary Optimization* (Aug. 2015), vol. 52: pp. 1–12. DOI: 10.1007/s00158-015-1241-0 (cit. on pp. 5, 18).

[87] Kijanski, W.: 'Optimal material design based on variational sensitivity analysis'. Dissertation. TU Dortmund, 2018. DOI: 10.17877/DE290R-19865 (cit. on pp. 6, 18, 53, 59, 63, 68, 95).

[88] Kijanski, W. and F.-J. Barthold: 'Two-scale shape optimisation based on numerical homogenisation techniques and variational sensitivity analysis'. *Computational Mechanics* (Apr. 2021), vol. 67: pp. 1–20. DOI: 10.1007/s00466-020-01955-6 (cit. on pp. 6, 68, 117).

[89] Kim, N. and K. Choi: *Structural Sensitivity Analysis and Optimization II: Nonlinear Systems and Applications*. Oct. 2004. DOI: 10.1007/b138895 (cit. on pp. 6, 12, 19, 52, 54).

[90] Klemensø, T., E. Lund, and B. Sørensen: 'Optimal Shape of Thin Tensile Test Specimen'. *Journal of the American Ceramic Society* (2007), vol. 90(6): pp. 1827–1835. DOI: 10.1111/j.1551-2916.2007.01538.x (cit. on p. 6).

[91] Knorn, F.: 'M-code LaTeX Package'. *MATLAB Central File Exchange. Retrieved May 6* (2021), vol. URL: https://www.mathworks.com/matlabcentral/fileexchange/8015-m-code-latex-package (cit. on p. 14).

[92] koala-al.com: *Ship Aluminium*. [Online; accessed April 28, 2021]. URL: http://www.koala-al.com/d/pic/marine-market/ (cit. on p. 3).

[93] Koschnick, F.: 'Geometrische Locking-Effekte bei Finiten Elementen und ein allgemeines Konzept zu ihrer Vermeidung'. Dissertation. München: Technische Universität München, 2004 (cit. on pp. 5, 28, 44).

[94] Kroner, E. and C. Teodosiu: 'Lattice defect approach to plasticity and viscoplasticity'. Jan. 1974: pp. 45–70. DOI: 10.1007/978-94-010-2311-5_3 (cit. on p. 30).

[95] Lagarias, J., J. Reeds, M. Wright, and P. Wright: 'Convergence Properties of the Nelder–Mead Simplex Method in Low Dimensions'. *SIAM Journal on Opti-*

mization (Dec. 1998), vol. 9: pp. 112–147. DOI: 10.1137/S1052623496303470 (cit. on p. 19).

[96] LAMKANFI, E., W. VAN PAEPEGEM, and J. DEGRIECK: 'Shape optimization of a cruciform geometry for biaxial testing of polymers'. *Polymer Testing* (Jan. 2014), vol. 41. DOI: 10.1016/j.polymertesting.2014.09.016 (cit. on p. 6).

[97] LEE, E. H. and D. T. LIU: 'Finite-Strain Elastic-Plastic Theory with Application to Plane-Wave Analysis'. *Journal of Applied Physics* (1967), vol. 38(1): pp. 19–27. DOI: 10.1063/1.1708953 (cit. on p. 30).

[98] LEE, E.: *Elastic-plastic Deformation at Finite Strains*. Ed. by AMERICAN SOCIETY OF MECHANICAL ENGINEERS AND STANFORD UNIVERSITY CALIF DEPT. OF APPLIED MECHANICS. American Society of Mechanical Engineers. Defense Technical Information Center, 1968. DOI: 10.1115/1.3564580 (cit. on p. 30).

[99] LEMAITRE, J.: 'A Continuous Damage Mechanics Model for Ductile Fracture'. *Journal of Engineering Materials and Technology-transactions of The Asme* (1985), vol. 107: pp. 83–89. DOI: 10.1115/1.3225775 (cit. on p. 2).

[100] LIEDMANN, J. and F.-J. BARTHOLD: 'Sensitivity Analysis of Elastoplastic Structural Response regarding Geometry and External Loads'. *Proc. 6th ECCM and 7th ECFD* (2018), vol. (cit. on pp. 54, 57, 117).

[101] LIEDMANN, J. and F.-J. BARTHOLD: 'Variational Sensitivity Analysis of Elastoplastic Structures Applied to Optimal Shape of Specimens'. *Proceedings of the 13th World Congress of Structural and Multidisciplinary Optimization (WCSMO13)* (2019), vol. 13 (cit. on pp. 54, 57).

[102] LIEDMANN, J. and F.-J. BARTHOLD: 'Sensitivity Analysis of Nonlinear Structural Response regarding Geometry and External Loads'. *PAMM* (2018), vol. 18(1): e201800135. DOI: 10.1002/pamm.201800135 (cit. on pp. 54, 57, 117).

[103] LIEDMANN, J. and F.-J. BARTHOLD: 'Variational Sensitivity Analysis of Elastoplastic Structures Applied to Optimal Shape of Specimens'. *Structural and Multidisciplinary Optimization* (Apr. 2020), vol. 61(6): pp. 2237–2251. DOI: 10.1007/s00158-020-02492-9 (cit. on pp. 6, 10, 49, 54, 57, 94).

[104] LIEDMANN, J., S. GERKE, F.-J. BARTHOLD, and M. BRÜNIG: 'Shape optimization of the X0-specimen: theory, numerical simulation and experimental verification'. *Computational Mechanics* (2020), vol. DOI: 10.1007/s00466-020-01900-7 (cit. on pp. 6, 49, 54, 57, 94).

[105] LIPPMANN, H. and J. LEMAITRE: *A Course on Damage Mechanics*. Springer Berlin Heidelberg, 2013. URL: https://books.google.de/books?id=m7X0CAAAQBAJ (cit. on pp. 2, 5).

[106] LodecJinshu.com: *Aluminium innovation in high-speed trains*. [Online; accessed April 28, 2021]. URL: http://lodecjinshu.com/en/innovation-aluminium-trains/ (cit. on p. 3).

[107] Lu, Z., J.-Y. Zhao, C.-Y. Zhou, and X.-H. He: 'Optimization Design of a Small-Sized Cruciform Specimen for Biaxial Fatigue Testing'. *Metals* (2020), vol. 10(9). DOI: 10.3390/met10091148 (cit. on p. 6).

[108] Lubliner, J.: 'A maximum-dissipation principle in generalized plasticity'. *Acta Mechanica* (1984), vol. 52: pp. 225–237. DOI: 10.1007/BF01179618 (cit. on p. 30).

[109] Lubliner, J.: 'Normality rules in large-deformation plasticity'. *Mechanics of Materials* (1986), vol. 5(1): pp. 29–34. DOI: 10.1016/0167-6636(86)90013-X (cit. on p. 30).

[110] Lubliner, J.: *Plasticity Theory*. Dover books on engineering. Dover Publications, 2008 (cit. on pp. 5, 28).

[111] Lyadova, K. A., V. V. Shadrin, L. V. Kovtanyuk, and A. S. Ustinova: 'Shape Optimization of a biaxially loaded specimen'. *Proceedings of XLI International Summer School–Conference APM 2013*. 2013 (cit. on p. 6).

[112] Makris, A., T. Vandenbergh, C. Ramault, D. V. Hemelrijck, E. Lamkanfi, and W. V. Paepegem: 'Shape optimisation of a biaxially loaded cruciform specimen'. *Polymer Testing* (2010), vol. 29(2): pp. 216–223. DOI: 10.1016/j.polymertesting.2009.11.004 (cit. on p. 6).

[113] Mandel, J.: 'Equations constitutives et directeurs dans les milieux plastiques et viscoplastiques'. *International Journal of Solids and Structures* (1973), vol. 9(6): pp. 725–740. DOI: 10.1016/0020-7683(73)90120-0 (cit. on p. 31).

[114] Mandel, J.: 'Foundations of Continuum Mechanics'. *Foundations of Continuum Thermodynamics*. Ed. by Domingos, J. J. D., M. N. R. Nina, and J. H. Whitelaw. London: Macmillan Education UK, 1973. Chap. Thermodynamics and Plasticity: pp. 283–304. DOI: 10.1007/978-1-349-02235-9_15 (cit. on p. 30).

[115] Mandel, J.: 'Generalisation de la theorie de plasticite de W. T. Koiter'. *International Journal of Solids and Structures* (1965), vol. 1(3): pp. 273–295. DOI: 10.1016/0020-7683(65)90034-X (cit. on p. 30).

[116] Materna, D.: 'Structural and Sensitivity Analysis for the Primal and Dual Problems in the Physical and Material Spaces'. Dissertation. TU Dortmund, 2009. DOI: 10.17877/DE290R-474 (cit. on pp. 6, 53, 58, 59, 68).

[117] MATLAB: *9.7.0.1190202 (R2019b)*. Natick, Massachusetts: The Mathworks Inc., 2018. URL: https://www.mathworks.com/products/matlab.html (cit. on p. 15).

[118] Maugin, G. A.: *The Thermomechanics of Plasticity and Fracture*. Cambridge Texts in Applied Mathematics. Cambridge University Press, 1992. DOI: 10.1017/CBO9781139172400 (cit. on pp. 5, 28).

[119] Maugin, G. A. and W. Muschik: 'Thermodynamics with Internal Variables. Part I. General Concepts'. *Journal of Non-Equilibrium Thermodynamics* (1994), vol. 19(3). DOI: 10.1515/jnet.1994.19.3.217 (cit. on pp. 28, 34).

[120] Maugin, G. A. and W. Muschik: 'Thermodynamics with Internal Variables. Part II. Applications'. *Journal of Non-Equilibrium Thermodynamics* (1994), vol. 19(3). DOI: 10.1515/jnet.1994.19.3.250 (cit. on p. 28).

[121] Mazzolani, F.: 'Structural Applications of Aluminium in Civil Engineering'. *Structural Engineering International* (Nov. 2006), vol. 16: pp. 280–285. DOI: 10.2749/101686606778995128 (cit. on p. 2).

[122] Metropolis, N.: 'The Beginning of the Monte Carlo Method'. 1987 (cit. on p. 19).

[123] Metropolis, N., A. W. Rosenbluth, M. N. Rosenbluth, A. H. Teller, and E. Teller: 'Equation of State Calculations by Fast Computing Machines'. *The Journal of Chemical Physics* (1953), vol. 21(6): pp. 1087–1092. DOI: 10.1063/1.1699114 (cit. on p. 19).

[124] Meyer, L.: 'Formoptimierung in der Strukturdynamik'. Dissertation. Universität Hannover, 1997 (cit. on pp. 6, 53).

[125] Michaleris, P., D. Tortorelli, and C. Vidal: 'Tangent operators and design sensitivity formulations for transient non-linear coupled problems with applications to elastoplasticity'. *Int. J. Numer. Methods Engng.* (1994), vol. 37: pp. 2471–2499. DOI: 10.1002/nme.1620371408 (cit. on pp. 6, 52, 54).

[126] Miehe, C.: 'Numerical computation of algorithmic (consistent) tangent moduli in large-strain computational inelasticity'. *Computational Methods in Applied Mechanics and Engineering* (1995), vol. 134: pp. 223–240. DOI: 10.1016/0045-7825(96)01019-5 (cit. on p. 5).

[127] Mises, R. von: 'Mechanik der festen Körper im plastisch-deformablen Zustand'. *Nachrichten von der Gesellschaft der Wissenschaften zu Göttingen, Mathematisch-Physikalische Klasse* (1913), vol. 1913: pp. 582–592 (cit. on pp. 5, 28).

[128] Mohr, D. and S. Henn: 'Calibration of Stress-triaxiality Dependent Crack Formation Criteria: A New Hybrid Experimental–Numerical Method'. *Experimental*

Mechanics (2007), vol. 47(6): pp. 805–820. DOI: 10.1007/s11340-007-9039-7 (cit. on p. 3).

[129] MORSE, P. and H. FESHBACH: *Methods of Theoretical Physics*. International series in pure and applied physics. McGraw-Hill, 1953 (cit. on p. 19).

[130] MULAY, A. and V. BAGUL: 'Design optimisation of cruciform specimen in biaxial test using MADM methods'. *Australian Journal of Mechanical Engineering* (Apr. 2020), vol.: pp. 1–11. DOI: 10.1080/14484846.2020.1752883 (cit. on p. 6).

[131] NASA (CREW OF SKYLAB): *Skylab*. [Online; accessed April 28, 2021]. Feb. 1974. URL: https://flic.kr/p/RUN8h (cit. on p. 3).

[132] NELDER, J. and R. MEAD: 'A Simplex Method for Function Minimization'. *Comput. J.* (1965), vol. 7: pp. 308–313. DOI: 10.1093/COMJNL/7.4.308 (cit. on p. 19).

[133] NEMAT-NASSER, S.: 'On Finite Deformation Elasto-Plasticity'. *International Journal of Solids and Structures* (1982), vol. 18(10): pp. 857–872 (cit. on pp. 5, 30).

[134] NOCEDAL, J. and S. WRIGHT: *Numerical Optimization*. Springer Series in Operations Research and Financial Engineering. Springer New York, 2006. DOI: 10.1007/978-0-387-40065-5 (cit. on pp. 19, 104).

[135] NOLL, W.: 'A New Mathematical Theory of Simple Materials'. *Archive for Rational Mechanics and Analysis* (1972), vol. DOI: 10.1007/978-3-642-65817-4_15 (cit. on pp. 28, 56).

[136] OLE SIGMUND, K. M.: 'Topology optimzation approaches'. *Structural and Multidisciplinary Optimization* (2013), vol. 48: pp. 1031–1055. DOI: 10.1007/s00158-013-0978-6 (cit. on pp. 5, 18).

[137] PENGUIAN: 'NURBS Toolbox by D.M. Spnik'. *MATLAB Central File Exchange* (2020), vol. Retrieved December 14, 2020. URL: https://www.mathworks.com/matlabcentral/fileexchange/26390-nurbs-toolbox-by-d-m-spink (cit. on pp. 69, 158).

[138] PHELAN, D. and R. HABER: 'Sensitivity analysis of linear elastic systems using domain parametrization and mixed mutual energy principle'. *Comput. Methods Appl. Mech. Engng.* (1989), vol. 77: pp. 31–59. DOI: 10.1016/0045-7825(89)90127-8 (cit. on pp. 6, 52, 54).

[139] POWELL, M. J. D.: 'An efficient method for finding the minimum of a function of several variables without calculating derivatives'. *The Computer Journal* (Jan. 1964), vol. 7(2): pp. 155–162. DOI: 10.1093/comjnl/7.2.155 (cit. on p. 6).

[140] POWELL, M.: *A Fast Algorithm for Nonlinearly Constrained Optimization Calculations*. Ed. by WATSON, G. Vol. 630. Springer, Berlin, Heidelberg, 1978. Chap. Nu-

merical Analysis. Lecture Notes in Mathematics, DOI: 10.1007/BFb0067703 (cit. on p. 21).

[141] RAMESH, B. and A. MANIATTY: 'Stabilized finite element formulation for elastic–plastic finite deformations'. *Computer Methods in Applied Mechanics and Engineering* (Feb. 2005), vol. 194: pp. 775–800. DOI: 10.1016/j.cma.2004.06.025 (cit. on p. 46).

[142] REINHARDT, H.: *Numerik gewöhnlicher Differentialgleichungen: Anfangs- und Randwertprobleme*. De Gruyter Lehrbuch. De Gruyter, 2008 (cit. on p. 37).

[143] ROSENBLUTH, M.: 'Genesis of the Monte Carlo Algorithm for Statistical Mechanics'. (Nov. 2003), vol. 690. DOI: 10.1063/1.1632112 (cit. on p. 19).

[144] ROTH, C. C. and D. MOHR: 'Ductile fracture experiments with locally proportional loading histories'. *International Journal of Plasticity* (2016), vol. 79: pp. 328–354. DOI: 10.1016/j.ijplas.2015.08.004 (cit. on pp. 2, 6).

[145] ROTTHAUS, M. and F.-J. BARTHOLD: 'Aspects of sensitivity analysis using the level-set method in structural optimization'. *Pamm* (Dec. 2007), vol. 7: pp. 4040041–4040042. DOI: 10.1002/pamm.200700793 (cit. on p. 117).

[146] ROUSSELIER, G.: 'Ductile fracture models and their potential in local approach of fracture'. *Nuclear Engineering and Design* (1987), vol. 105(1): pp. 97–111. DOI: 10.1016/0029-5493(87)90234-2 (cit. on p. 2).

[147] SALTELLI, A., K. A. KALININA, W. BECKER, P. FENNELL, F. FERRETTI, N. HOLST, S. LI, and Q. WU: 'Why so many published sensitivity analyses are false: A systematic review of sensitivity analysis practices'. *Environ. Model. Softw.* (2019), vol. 114: pp. 29–39. DOI: 10.1016/j.envsoft.2019.01.012 (cit. on p. 52).

[148] SCHITTKOWSKI, K.: 'NLPQL: A fortran subroutine solving constrained nonlinear programming problems'. *Annals of Operations Research* (June 1986), vol. (5): pp. 485–500. DOI: 10.1007/BF02022087 (cit. on p. 19).

[149] SCHITTKOWSKI, K.: 'On the convergence of a sequential quadratic programming method with an augmented lagrangian line search function'. *Mathematische Operationsforschung und Statistik. Series Optimization* (1983), vol. 14(2): pp. 197–216. DOI: 10.1080/02331938308842847 (cit. on pp. 19, 21).

[150] SCHRÖDINGER, E.: 'Die Wandlungen der Mechanik und die mechanische Naturerklärung'. *Monatshefte für Mathematik und Physik* (Dec. 1913), vol. 24: A25–A27. DOI: 10.1007/BF01708178 (cit. on p. 28).

[151] SCHUMACHER, A.: *Optimierung mechanischer Strukturen*. Springer-Verlag Berlin Heidelberg, 2005. DOI: 10.1007/b138046 (cit. on pp. 5, 18).

[152] Seitz, A.: 'Computational Methods for Thermo-Elasto-Plastic Contact'. PhD thesis. Technische Universität München, 2019 (cit. on p. 46).

[153] Seitz, A., W. A. Wall, and A. Popp: 'A computational approach for thermo-elasto-plastic frictional contact based on a monolithic formulation using non-smooth nonlinear complementarity functions'. *Advanced Modeling and Simulation in Engineering Sciences* (Mar. 2018), vol. 5(1). doi: 10.1186/s40323-018-0098-3 (cit. on p. 31).

[154] Shanno, D.: 'Conditioning of Quasi-Newton Methods for Function Minimization'. *Mathematics of Computation* (1970), vol. 24: pp. 647–656. doi: 10.2307/2004840 (cit. on p. 19).

[155] Shewchuk, J. R.: *An Introduction to the Conjugate Gradient Method Without the Agonizing Pain*. Tech. rep. USA, 1994 (cit. on p. 19).

[156] Sigmund, O.: 'A 99 Line Topology Optimization Code Written in MATLAB. Structural and Multidisciplinary Optimization 21, 120-127'. *Structural and Multidisciplinary Optimization* (Apr. 2001), vol. 21: pp. 120–127. doi: 10.1007/s001580050176 (cit. on pp. 5, 18).

[157] Sigmund, O. and J. Petersson: 'Numerical instabilities in topology optimization: A survey on procedures dealing with checkerboards, mesh-dependencies and local minima'. *Structural Optimization* (Aug. 1998), vol. 16: pp. 68–75. doi: 10.1007/BF01214002 (cit. on pp. 5, 18).

[158] Simo, J. C. and F. Armero: 'Geometrically non-linear enhanced strain mixed methods and the method of incompatible modes'. *International Journal for Numerical Methods in Engineering* (1992), vol. 33(7): pp. 1413–1449. doi: 10.1002/nme.1620330705 (cit. on pp. 28, 31, 46).

[159] Simo, J. C. and T. J. R. Hughes: *Computational Inelasticity (Interdisciplinary Applied Mathematics)*. Springer, July 2000. doi: 10.1007/b98904 (cit. on pp. 5, 28, 31, 35, 39, 46, 49).

[160] Simo, J. C. and J. W. Ju: 'On continuum damage-elastoplasticity at finite strains'. *Computational Mechanics* (1989), vol. 5: pp. 375–400. doi: 10.1007/BF01047053 (cit. on pp. 5, 28).

[161] Simo, J. C. and K. S. Pister: 'Remarks on Rate Constitutive Equations for Finite Deformation Problems: Computational Implications'. *Computer Methods in Applied Mechanics and Engineering* (1984), vol. 46: pp. 201–215. doi: 10.1016/0045-7825(84)90062-8 (cit. on p. 28).

[162] Simo, J.: 'A framework for finite strain elastoplasticity based on maximum plastic dissipation and the multiplicative decomposition: Part I. Continuum formulation'.

Comput. Methods Appl. Mech. Engng. (1988), vol. 66(2): pp. 199–219. DOI: 10.1016/0045-7825(88)90076-X (cit. on pp. 28, 30, 36).

[163] Simo, J.: 'A framework for finite strain elastoplasticity based on maximum plastic dissipation and the multiplicative decomposition. Part II: Computational aspects'. *Computer Methods in Applied Mechanics and Engineering* (1988), vol. 68(1): pp. 1–31. DOI: 10.1016/0045-7825(88)90104-1 (cit. on pp. 28, 46).

[164] Simo, J.: 'A J2-flow theory exhibiting a corner-like effect and suitable for large-scale computation'. *Computer Methods in Applied Mechanics and Engineering* (1987), vol. 62(2): pp. 169–194. DOI: 10.1016/0045-7825(87)90022-3 (cit. on pp. 28, 36).

[165] Simo, J.: 'Algorithms for static and dynamic multiplicative plasticity that preserve the classical return mapping schemes of the infinitesimal theory'. *Computer Methods in Applied Mechanics and Engineering* (1992), vol. 99(1): pp. 61–112. DOI: 10.1016/0045-7825(92)90123-2 (cit. on pp. 28, 46).

[166] Simo, J.: 'On the computational significance of the intermediate configuration and hyperelastic stress relations in finite deformation elastoplasticity'. *Mechanics of Materials* (1985), vol. 4(3): pp. 439–451. DOI: 10.1016/0167-6636(85)90039-0 (cit. on pp. 28, 31).

[167] Simo, J. and M. Ortiz: 'A unified approach to finite deformation elastoplastic analysis based on the use of hyperelastic constitutive equations'. *Computer Methods in Applied Mechanics and Engineering* (1985), vol. 49(2): pp. 221–245. DOI: 10.1016/0045-7825(85)90061-1 (cit. on p. 28).

[168] Simo, J. and R. Taylor: 'Consistent tangent operators for rate-independent elastoplasticity'. *Computer Methods in Applied Mechanics and Engineering* (1985), vol. 48(1): pp. 101–118. DOI: 10.1016/0045-7825(85)90070-2 (cit. on p. 28).

[169] Simo, J., R. Taylor, and K. Pister: 'Variational and projection methods for the volume constraint in finite deformation elasto-plasticity'. *Computer Methods in Applied Mechanics and Engineering* (1985), vol. 51(1): pp. 177–208. DOI: 10.1016/0045-7825(85)90033-7 (cit. on p. 28).

[170] Simo, J. and R. Taylor: 'A return mapping algorithm for plane stress elastoplasticity'. *International Journal for Numerical Methods in Engineering* (1986), vol. 22(3): pp. 649–670 (cit. on p. 28).

[171] Sokołowski, J. and J. Zolésio: *Introduction to shape optimization: shape sensitivity analysis*. Springer series in computational mathematics. Springer-Verlag, 1992. DOI: 10.1007/978-3-642-58106-9 (cit. on pp. 6, 12, 18, 19, 52, 54).

[172] Souza Neto, E. A. de, D. Perić, and D. R. J. Owen: *Computational Methods for Plasticity: Theory and Applications*. 1st ed. Wiley, Jan. 2009. doi: 10.1002/9780470694626 (cit. on pp. 5, 28, 35, 45, 46, 68, 155).

[173] Stein, E. and F. Barthold: 'Werkstoffe: Elastizitätstheorie'. *Der Ingenieurbau: Grundwissen*. Ed. by Mehlhorn, G. Ernst & Sohn, 1997 (cit. on p. 28).

[174] Stiefel, E.: 'Über einige Methoden der Relaxationsrechnung'. *Zeitschrift für angewandte Mathematik und Physik ZAMP* (1952), vol. 3(1): pp. 1–33. doi: 10.1007/BF02080981 (cit. on p. 19).

[175] Stieghan, J.: 'Variationelle Sensitivitätsanalyse in der Theorie poröser Medien'. PhD thesis. Technische Universität Braunschweig, 2008 (cit. on pp. 6, 53).

[176] Stoer, J., R. Bartels, W. Gautschi, R. Bulirsch, and C. Witzgall: *Introduction to Numerical Analysis*. Texts in Applied Mathematics. Springer New York, 2002. doi: 10.1007/978-1-4757-2272-7 (cit. on p. 19).

[177] TAG Farnborough Airport / 3DReid Architects: *Farnborough Airport*. [Online; accessed April 28, 2021]. Sept. 2011. url: https://www.archdaily.com/172247/tag-farnborough-airport-3d-reid-architects (cit. on p. 3).

[178] The Mathworks, Inc.: *Cell Arrays*. Natick, Massachusetts, United States, 2021. url: https://de.mathworks.com/help/matlab/cell-arrays/ (cit. on p. 158).

[179] The Mathworks, Inc.: *Parallel Computing Toolbox*. Natick, Massachusetts, United States, 2021. url: https://de.mathworks.com/help/parallel-computing/ (cit. on p. 158).

[180] Tortorelli, D. A. and P. Michaleris: 'Design sensitivity analysis: Overview and review'. *Inverse Problems in Engineering* (1994), vol. 1(1): pp. 71–105. doi: 10.1080/174159794088027573 (cit. on pp. 6, 52).

[181] Truesdell, C. and W. Noll: *The Non-Linear Field Theories of Mechanics*. Ed. by Antman, S. S. Springer, 2004. doi: 10.1007/978-3-662-10388-3 (cit. on pp. 28, 35).

[182] Truesdell, C.: *Rational Thermodynamics*. MacGraw-Hill series in modern applied mathematics. MacGraw-Hill, 1969. doi: 10.1007/978-1-4612-5206-1 (cit. on pp. 28, 35).

[183] Vogel, A. and P. Junker: 'Adaptive thermodynamic topology optimization'. *Structural and Multidisciplinary Optimization* (Jan. 2021), vol. 63: pp. 1–25. doi: 10.1007/s00158-020-02667-4 (cit. on pp. 5, 18).

[184] Voyiadjis, G. Z. and P. I. Kattan: 'A plasticity-damage theory for large deformation of solids—I. Theoretical formulation'. *International Journal of Engineering Science* (1992), vol. 30(9): pp. 1089–1108. doi: 10.1016/0020-7225(92)90059-P (cit. on p. 2).

[185] Wiechmann, K.: 'Theorie und Numerik zur Berechnung und Optimierung von Strukturen mit elastoplastischen Deformationen'. Dissertation. Institut für Baumechanik und Numerische Mechanik, Universität Hannover, 2000 (cit. on pp. 6, 53, 57).

[186] Wiechmann, K. and F.-J. Barthold: 'Remarks on variational design sensitivity analysis of structures with large elasto-plastic deformations'. Sept. 1998. doi: 10.2514/6.1998-4752 (cit. on pp. 6, 53).

[187] Wiechmann, K. and E. Stein: 'Shape optimization for elasto-plastic deformation'. *International Journal of Solids and Structures* (Nov. 2006), vol. 43: pp. 7145–7165. doi: 10.1016/j.ijsolstr.2006.03.025 (cit. on pp. 6, 53).

[188] Wohlgemuth, F. and F.-J. Barthold: 'Controlling Physical Properties on Interfaces Using Parametrised Level Set Methods and Extended Finite Element Method'. *PAMM* (Nov. 2019), vol. 19. doi: 10.1002/pamm.201900455 (cit. on p. 117).

[189] Wolfe, P.: 'Convergence Conditions for Ascent Methods'. *SIAM Review* (1969), vol. 11(2): pp. 226–235. doi: 10.1137/1011036 (cit. on p. 21).

[190] Wriggers, P.: 'Finite Elemente in der Baustatik'. Vieweg, 2008. Chap. Nichtlineare Finite-Elemente-Methode. doi: 10.1007/978-3-8348-9447-2_6 (cit. on pp. 5, 28, 68, 155).

[191] Wriggers, P.: *Nichtlineare Finite-Element-Methoden*. Springer DE, 2001. doi: 10.1007/978-3-642-56865-7 (cit. on p. 5).

[192] Wriggers, P. and M. Hain: 'Micro-Meso-Macro Modelling of Composite Materials'. *Computational Plasticity*. Ed. by Oñate, E. and R. Owen. Dordrecht: Springer Netherlands, 2007: pp. 105–122. doi: 10.1007/978-1-4020-6577-4_7 (cit. on p. 18).

[193] Zhao, K., L. Chen, R. Xiao, Z. Ding, and L. Zhou: 'Design of a biaxial tensile testing device and cruciform specimens for large plastic deformation in the central zone'. *Journal of Materials Science* (May 2019), vol. 54(9): pp. 7231–7245. doi: 10.1007/s10853-019-03358-2 (cit. on p. 6).

[194] Zhao, X., Z. Berwick, J. Krieger, H. Chen, S. Chambers, and G. Kassab: 'Novel Design of Cruciform Specimens for Planar Biaxial Testing of Soft Materials'. *Experimental Mechanics* (Mar. 2013), vol. 54: pp. 343–356. doi: 10.1007/s11340-013-9808-4 (cit. on p. 6).

[195] Zheng, K., D. J. Politis, L. Wang, and J. Lin: 'A review on forming techniques for manufacturing lightweight complex—shaped aluminium panel components'. *International Journal of Lightweight Materials and Manufacture* (June 2018), vol. 1(2): pp. 55–80. doi: 10.1016/j.ijlmm.2018.03.006 (cit. on p. 2).

[196] Zhu, Z., Z. Lu, P. Zhang, W. Fu, C. Zhou, and X. He: 'Optimal Design of a Miniaturized Cruciform Specimen for Biaxial Testing of TA2 Alloys'. *Metals* (July 2019), vol. 9: p. 823. doi: 10.3390/met9080823 (cit. on p. 6).

[197] Zidane, I., C. Zhang, D. Guines, L. Leotoing, and E. Ragneau: 'Optimization of Biaxial Tensile Specimen Shape from Numerical Investigations'. Vol. 45. Sept. 2008 (cit. on p. 6).

[198] Zienkiewicz, O. C. and R. L. Taylor: *Finite Element Method - Volume 2: Solid Mechanics*. Butterworth Heinemann, 2000 (cit. on pp. 5, 28).

[199] Zienkiewicz, O. C. and R. L. Taylor: *The Finite Element Method Volume 1: The Basis*. Butterworth-Heinemann, 2000 (cit. on pp. 5, 28, 68, 155).

[200] Zienkiewicz, O., R. Taylor, and D. Fox: *The Finite Element Method for Solid and Structural Mechanics*. Jan. 2005: pp. 85617–85634 (cit. on pp. 5, 28).

[201] Zolésio, J.: 'The material derivative (or speed) method for shape optimization'. *Optimization of Distributed Parameter Structures*. Ed. by Haug, E. and J. Céa. Alphen aan den Rijn, The Netherlands: Sijthoff and Noordhoff, 1981: pp. 1049–1151. doi: 10.1007/978-94-009-8606-0_12 (cit. on pp. 6, 18, 52, 54).

[202] Zupan, N. and J. Korelc: 'Sensitivity analysis based multi-scale methods of coupled path-dependent problems'. *Computational Mechanics* (Sept. 2019), vol. 65(1): pp. 229–248. doi: 10.1007/s00466-019-01762-8 (cit. on p. 54).

List of Figures

List of Tables

Appendix A

Detailed Derivations and Important Variations

A.1 Consistent tangent operator

In this section, the linearization of the First Piola-Kirchhoff stress tensor is derived, consistent with the implicit stress integration scheme described in Chap. 4. Due to the type of strain energy function, cf. Eq. (4.46), the first Piola Kirchhoff stress tensor can easily be split in to a volumetric and a deviatoric contribution

$$\mathbf{P}^{\mathsf{K}} = \mathbf{P}^{\mathsf{K}}_{\mathrm{vol}} + \mathbf{P}^{\mathsf{K}}_{\mathrm{dev}} = J\,p\,\mathbf{F}^{-\mathsf{T}} + \mathbf{s}\,\mathbf{F}^{-\mathsf{T}} = p\,\overset{+}{\mathbf{F}} + \mathbf{s}\,\mathbf{F}^{-\mathsf{T}}, \tag{A.1}$$

with the cofactor of the deformation gradient $\overset{+}{\mathbf{F}} = J\,\mathbf{F}^{-\mathsf{T}}$. The linearization w.r.t. displacements is then performed on each contribution separately. The volumetric part is independent of the internal variables, due to the isochosric plastic flow. Thus, the partial variation of the volumetric part reads

$$\delta_u \mathbf{P}^{\mathsf{K}}_{\mathrm{vol}} = \delta_u p\ \overset{+}{\mathbf{F}} + p\,\delta_u\ \overset{+}{\mathbf{F}}\,. \tag{A.2}$$

The partial variation of the hydrostatic pressure $p = U'(J)$ is straight forward and reads

$$\delta_u p = U''(J)\,\frac{\partial J}{\partial \mathbf{F}} : \delta_u \mathbf{F} = \frac{K}{2\,J}\,\left(J^2+1\right)\,\mathbf{F}^{-\mathsf{T}} : \delta_u \mathbf{F}. \tag{A.3}$$

The partial derivative of the cofactor of a tensor w.r.t. the tensor itself can be found e.g. in [85] and its partial variation reads

$$\delta_u\ \overset{+}{\mathbf{F}} = J\,\left[\left(\mathbf{F}^{-\mathsf{T}}\otimes\mathbf{F}^{-\mathsf{T}}\right) + \left(\mathbf{F}^{-\mathsf{T}}\otimes\mathbf{F}^{-\mathsf{T}}\right)^{\overset{24}{\mathsf{T}}}\right] : \delta_u \mathbf{F}. \tag{A.4}$$

Inserting Eq. (A.3) and Eq. (A.4) into Eq. (A.2), finally leads to

$$\begin{aligned}\delta_u \mathbf{P}^{\mathsf{K}}_{\mathrm{vol}} &= \left[K\,J^2\,\left(\mathbf{F}^{-\mathsf{T}}\otimes\mathbf{F}^{-\mathsf{T}}\right) - J\,p\,\left(1-J^2\right)\,\left(\mathbf{F}^{-\mathsf{T}}\otimes\mathbf{F}^{-\mathsf{T}}\right)^{\overset{24}{\mathsf{T}}}\right] : \delta_u \mathbf{F} \\ &= \mathbb{A}_{\mathrm{vol}} : \delta_u \mathbf{F}.\end{aligned} \tag{A.5}$$

For the linearization of the deviatoric part, the evolution of the internal variables have to be considered, i.e. the dependencies of the deviatoric stress w.r.t. the elastic trial state has to be elaborated carefully. The partial variation of the deviatoric First Piola-Kirchhoff

stress tensor reads

$$\delta_u \mathbf{P}^{\mathsf{K}}_{\mathrm{dev}} = \delta_u \mathbf{s}\, \mathbf{F}^{-\mathsf{T}} + \mathbf{s}\, \delta_u \mathbf{F}^{-\mathsf{T}}. \tag{A.6}$$

Here, the partial variation of the inverser transpose deformation gradient is given by

$$\delta_u \mathbf{F}^{-\mathsf{T}} = \frac{\partial \mathbf{F}^{-\mathsf{T}}}{\partial \mathbf{F}} : \delta_u \mathbf{F} = -\left(\mathbf{F}^{-\mathsf{T}} \otimes \mathbf{F}^{-\mathsf{T}}\right)^{\overset{24}{\mathsf{T}}} : \delta_u \mathbf{F}. \tag{A.7}$$

The partial variation of the Kirchhoff stress deviator $\mathbf{s}$ depends on the evolution of the internal variables, viz.

$$\delta_u \mathbf{s} = \frac{\partial \mathbf{s}}{\partial \mathbf{s}^{\mathrm{tr}}} : \delta_u \mathbf{s}^{\mathrm{tr}} + \frac{\partial \mathbf{s}}{\partial \overline{\mu}}\, \delta_u \overline{\mu} + \frac{\partial \mathbf{s}}{\partial \Delta\gamma}\, \delta_u \Delta\gamma + \frac{\partial \mathbf{s}}{\partial \mathbf{n}} : \delta_u \mathbf{n}, \tag{A.8}$$

with the partial derivatives

$$\frac{\partial \mathbf{s}}{\partial \mathbf{s}^{\mathrm{tr}}} = \mathbb{I}_{\mathrm{sym}}, \quad \frac{\partial \mathbf{s}}{\partial \overline{\mu}} = -2\,\Delta\gamma\,\mathbf{n}, \quad \frac{\partial \mathbf{s}}{\partial \Delta\gamma} = -2\,\overline{\mu}\,\mathbf{n}, \quad \frac{\partial \mathbf{s}}{\partial \mathbf{n}} = -2\,\overline{\mu}\,\Delta\gamma\,\mathbb{I}_{\mathrm{sym}} \tag{A.9}$$

and the partial variations of the elastic trial values

$$\delta_u \mathbf{s}^{\mathrm{tr}} = \frac{\partial \mathbf{s}^{\mathrm{tr}}}{\partial \widetilde{\mathbf{b}}^{\mathrm{tr}}_{\mathsf{e}}} : \delta_u \widetilde{\mathbf{b}}^{\mathrm{tr}}_{\mathsf{e}}, \tag{A.10}$$

$$\delta_u \overline{\mu} = \frac{\partial \overline{\mu}}{\partial \widetilde{\mathbf{b}}^{\mathrm{tr}}_{\mathsf{e}}} : \delta_u \widetilde{\mathbf{b}}^{\mathrm{tr}}_{\mathsf{e}} = G\,\mathbb{I}_{\mathrm{dev}} : \delta_u \widetilde{\mathbf{b}}^{\mathrm{tr}}_{\mathsf{e}} = \frac{1}{3}\, G\,\mathbf{I} : \delta_u \widetilde{\mathbf{b}}^{\mathrm{tr}}_{\mathsf{e}}, \tag{A.11}$$

$$\delta_u \mathbf{n} = \frac{\partial \mathbf{n}}{\partial \mathbf{s}^{\mathrm{tr}}} : \delta_u \mathbf{s}^{\mathrm{tr}} = \frac{1}{\|\mathbf{s}^{\mathrm{tr}}\|}\, (\mathbb{I}_{\mathrm{sym}} - \mathbf{n} \otimes \mathbf{n}) : \delta_u \mathbf{s}^{\mathrm{tr}}, \tag{A.12}$$

$$\delta_u \Delta\gamma = \frac{\partial \Delta\gamma}{\partial \overline{\mu}}\, \delta_u \overline{\mu} + \frac{\partial \Delta\gamma}{\partial \mathbf{s}^{\mathrm{tr}}} : \delta_u \mathbf{s}^{\mathrm{tr}} = \frac{2\,\Delta\gamma^*}{f'(\Delta\gamma^*)}\, \delta_u \overline{\mu} - \frac{\mathbf{n}}{f'(\Delta\gamma^*)} : \delta_u \mathbf{s}^{\mathrm{tr}}. \tag{A.13}$$

Here, the partial derivatives of the plastic multiplier $\Delta\gamma$ are obtained by linearization of its update formula within the local Newton-Raphson method

$$\Delta\gamma^{k+1} = \Delta\gamma^k - \frac{f(\Delta\gamma^k)}{f'(\Delta\gamma^k)}. \tag{A.14}$$

As the value of the yield function in the solution point is zero ($f(\Delta\gamma^*) = 0$), the partial variation w.r.t. any quantity $(\bullet)$ simply reads

$$\delta_{(\bullet)} \Delta\gamma = -\frac{1}{f'(\Delta\gamma^*)}\, \delta_{(\bullet)} f(\Delta\gamma^*). \tag{A.15}$$

Inserting all these partial variations and derivations into Eq. (A.8) and keeping in mind the identities

$$\mathbb{I}_{\mathrm{dev}} : \mathbb{I}_{\mathrm{sym}} = \mathbb{I}_{\mathrm{sym}} : \mathbb{I}_{\mathrm{dev}} = \mathbb{I}_{\mathrm{dev}}\,, \tag{A.16}$$

$$\mathbb{I}_{\mathrm{dev}} : (\mathbf{n} \otimes \mathbf{n}) = \mathbb{I}_{\mathrm{sym}} : (\mathbf{n} \otimes \mathbf{n}) = \mathbf{n} \otimes \mathbf{n}, \tag{A.17}$$

the partial variation of the deviatoric Kirchhoff stress tensor reads

$$\delta\mathbf{s} = G \left[\left(1 - \frac{2\,\overline{\mu}\,\Delta\gamma}{\|\mathbf{s}^{\mathrm{tr}}\|} \right) \mathbb{I}_{\mathrm{dev}} + \left(\frac{2\,\overline{\mu}}{f'} + \frac{2\,\overline{\mu}\,\Delta\gamma}{\|\mathbf{s}^{\mathrm{tr}}\|} \right) \mathbf{n} \otimes \mathbf{n} - \frac{2}{3}\,\Delta\gamma \left(1 + \frac{2\,\overline{\mu}}{f'} \right) \mathbf{I} \otimes \mathbf{n} \right] : \delta_u \widetilde{\mathbf{b}}_{\mathsf{e}}^{\mathsf{tr}}. \tag{A.18}$$

With the introduction of the factors β_0, β_2 and β_3

$$\beta_0 = 1 - \frac{2\,\overline{\mu}\,\Delta\gamma}{\|\mathbf{s}^{\mathrm{tr}}\|}, \quad \beta_1 = 1 + \frac{2\,\overline{\mu}}{f'}, \quad \beta_2 = \beta_1 - \beta_0, \tag{A.19}$$

the consistent deviatoric tangent operator can be written in compact form as

$$\delta_u \mathbf{s} = G \left[\beta_0\, \mathbb{I}_{\mathrm{dev}} - \frac{2}{3}\,\Delta\gamma\,\beta_1\, \mathbf{I} \otimes \mathbf{n} + \beta_2\, \mathbf{n} \otimes \mathbf{n} \right] : \delta_u \widetilde{\mathbf{b}}_{\mathsf{e}}^{\mathsf{tr}} = \mathbb{S} : \delta_u \widetilde{\mathbf{b}}_{\mathsf{e}}^{\mathsf{tr}}. \tag{A.20}$$

Next, the partial variation of the isochoric left Cauchy-Green deformation tensor is needed. Considering the definition of the trial state $\widetilde{\mathbf{b}}_{\mathsf{e}}^{\mathsf{tr}} = \widetilde{\mathbf{F}}\,\mathbf{c}_{\mathsf{p},n}\,\widetilde{\mathbf{F}}^{\mathsf{T}}$, its partial variation is given by

$$\delta_u \widetilde{\mathbf{b}}_{\mathsf{e}}^{\mathsf{tr}} = \frac{\partial \widetilde{\mathbf{b}}_{\mathsf{e}}^{\mathsf{tr}}}{\partial \widetilde{\mathbf{F}}} : \delta_u \mathbf{F} = \left[\overset{4}{\mathbb{I}} \overset{21}{*} (\mathbf{c}_{\mathsf{p},n}\,\widetilde{\mathbf{F}}^{\mathsf{T}}) + \widetilde{\mathbf{F}}\,\mathbf{c}_{\mathsf{p},n}\ \overset{4}{\mathbb{I}}\ \overset{12}{\mathsf{T}} \right] : \delta_u \widetilde{\mathbf{F}} = \mathbb{B} : \delta_u \widetilde{\mathbf{F}}, \tag{A.21}$$

where the ischoric projection tensor of the deformation gradient can be derived to

$$\delta_u \widetilde{\mathbf{F}} = \frac{\partial \widetilde{\mathbf{F}}}{\partial \mathbf{F}} : \delta_u \mathbf{F} = J^{-\frac{1}{3}} \left[\overset{4}{\mathbb{I}} - \frac{1}{3}\,\mathbf{F} \otimes \mathbf{F}^{-\mathsf{T}} \right] : \delta_u \mathbf{F} = \mathbb{F} : \delta_u \mathbf{F}. \tag{A.22}$$

Hence, it is possible to define a fourth order tensor $\mathbb{B}_F$ given by

$$\delta_u \widetilde{\mathbf{b}}_{\mathsf{e}}^{\mathsf{tr}} = \mathbb{B} : \mathbb{F} : \delta_u \mathbf{F} = \left[\mathbb{F} \overset{21}{*} (\mathbf{c}_{\mathsf{p},n}\,\widetilde{\mathbf{F}}^{\mathsf{T}}) + \widetilde{\mathbf{F}}\,\mathbf{c}_{\mathsf{p},n}\,\mathbb{F}^{\overset{12}{\mathsf{T}}} \right] : \delta_u \mathbf{F} = \mathbb{B}_F : \delta_u \mathbf{F}. \tag{A.23}$$

The deviatoric linearization of the First Piola-Kirchhoff stress tensor therefore reads

$$\delta_u \mathbf{P}_{\mathrm{dev}}^{\mathsf{K}} = \left[(\mathbb{S} : \mathbb{B}_F) \overset{21}{*} \mathbf{F}^{-\mathsf{T}} - \mathbf{s} \left(\mathbf{F}^{-\mathsf{T}} \otimes \mathbf{F}^{-\mathsf{T}} \right)^{\overset{24}{\mathsf{T}}} \right] : \delta_u \mathbf{F} = \mathbb{A}_{\mathrm{dev}} : \delta_u \mathbf{F}. \tag{A.24}$$

Finally, the addition of the volumetric and deviatoric contributions results in the total consistent tangent operator $\mathbb{A}$

$$\begin{aligned}\delta_u \mathbf{P}^{\mathsf{K}} &= [\mathbb{A}_{\mathrm{vol}} + \mathbb{A}_{\mathrm{dev}}] : \delta_u \mathbf{F} \\ &= \left[K\, J^2\, \mathbf{F}^{-\mathsf{T}} \otimes \mathbf{F}^{-\mathsf{T}} - \boldsymbol{\tau} \left(\mathbf{F}^{-\mathsf{T}} \otimes \mathbf{F}^{-\mathsf{T}}\right)^{\overset{24}{\mathsf{T}}} + (\mathbb{S} : \mathbb{B}_F) \overset{21}{*} \mathbf{F}^{-\mathsf{T}} \right] : \delta_u \mathbf{F} \\ &= \mathbb{A} : \delta_u \mathbf{F}.\end{aligned} \tag{A.25}$$

A.2 Constitutive sensitivity operator

In this section, derivations of important quantities in the context of constitutive sensitivities are presented. The starting point is Eq. (5.18) and the vectors of constitutive parameters and their variations are given as

$$\boldsymbol{m} := \begin{bmatrix} K & G & k \end{bmatrix}^T \quad \text{and} \quad \delta\boldsymbol{m} := \begin{bmatrix} \delta K & \delta G & \delta k \end{bmatrix}^T. \tag{A.26}$$

The partial variation of the first Piola-Kirchhoff stress tensor is demanded and reads

$$\delta_m \mathbf{P}^{\mathsf{K}} = J\, \delta_m p\, \mathbf{F}^{-\mathsf{T}} + \delta_m \mathbf{s}\, \mathbf{F}^{-\mathsf{T}}. \tag{A.27}$$

The partial variation of the volumetric stress regarding the constitutive parameters is straight forward and can be written as

$$\delta_m p = \frac{J^2 - 1}{2\, J}\, \delta K. \tag{A.28}$$

The partial derivative of the deviatoric Kirchhoff stress tensor is more complex, as the evolution of plastic flow has to be considered. The partial variation w.r.t. the constitutive parameters takes the form

$$\begin{aligned}\delta_m \mathbf{s} &= \delta_m (\mathbf{s}^{\mathrm{tr}} - 2\,\overline{\mu}\,\Delta\gamma\,\mathbf{n}) \\ &= \delta_m \mathbf{s}^{\mathrm{tr}} - 2\,\delta_m\overline{\mu}\,\Delta\gamma\,\mathbf{n} - 2\,\overline{\mu}\,\delta_m\Delta\gamma\,\mathbf{n} - 2\,\overline{\mu}\,\Delta\gamma\,\delta_m\mathbf{n}.\end{aligned} \tag{A.29}$$

The trial deviatoric Kirchhoff stress as well as the the scaling factor $\overline{\mu}$ and the flow direction $\mathbf{n}$ only depend on the shear modulus and their partial variations can be identified to

$$\begin{aligned}\delta_m \mathbf{s}^{\mathrm{tr}} &= \mathrm{dev}\, \widetilde{\mathbf{b}}_{\mathsf{e}}^{\mathsf{tr}}\, \delta G, \\ \delta_m \overline{\mu} &= \frac{\overline{\mu}}{G}\, \delta G, \\ \delta_m \mathbf{n} &= \frac{\partial \mathbf{n}}{\partial \mathbf{s}^{\mathrm{tr}}} : \delta_m \mathbf{s}^{\mathrm{tr}} = \frac{1}{\|\mathbf{s}^{\mathrm{tr}}\|} \left(\mathbb{I}_{\mathrm{dev}} - \mathbf{n} \otimes \mathbf{n}\right) : \mathrm{dev}\, \widetilde{\mathbf{b}}_{\mathsf{e}}^{\mathsf{tr}}\, \delta G.\end{aligned} \tag{A.30}$$

The partial variation of the plastic multiplier $\Delta\gamma$ w.r.t. constitutive parameters can be obtained following the same arguments shown in App. A.2, cf. Eq. (A.14) and Eq. (A.15),

and reads

$$\delta_m \Delta\gamma = -\frac{1}{f'}\left[\left(\mathbf{n} : \operatorname{dev}\widetilde{\mathbf{b}}_{\mathsf{e}}^{\mathsf{tr}} - 2\,\Delta\gamma\,\frac{\overline{\mu}}{G}\right)\,\delta G - \sqrt{\frac{2}{3}}\,\delta k\right]. \tag{A.31}$$

With this, the partial variation in Eq. (A.29) reads

$$\begin{aligned}\delta_m \mathbf{s} = \quad & \left[\left(1 - 2\,\Delta\gamma\,\frac{\overline{\mu}}{\|\mathbf{s}^{\mathrm{tr}}\|}\right)\mathbb{I}_{\mathrm{dev}} + \left(2\,\frac{\overline{\mu}}{f'} + 2\,\frac{\overline{\mu}}{\|\mathbf{s}^{\mathrm{tr}}\|}\,\Delta\gamma\right)\mathbf{n}\otimes\mathbf{n}\right] : \operatorname{dev}\widetilde{\mathbf{b}}_{\mathsf{e}}^{\mathsf{tr}}\,\delta G \\ & - 2\,\Delta\gamma\frac{\overline{\mu}}{G}\left(1 + 2\,\frac{\overline{\mu}}{f'}\right)\mathbf{n}\,\delta G - 2\sqrt{\frac{2}{3}}\,\frac{\overline{\mu}}{f'}\,\mathbf{n}\,\delta k.\end{aligned} \tag{A.32}$$

Utilizing the factors β_0, β_1 and β_2, cf. Eq. (A.19), the second order tensor $\mathbf{H}_m$ can be defined as

$$\begin{aligned}\delta_m \mathbf{s} &= \left[(\beta_0 \mathbb{I}_{\mathrm{dev}} + \beta_2 \mathbf{n}\otimes\mathbf{n}) : \operatorname{dev}(\widetilde{\mathbf{b}}_{\mathsf{e}}^{\mathsf{tr}}) - 2\Delta\gamma\frac{\overline{\mu}}{G}\beta_1\mathbf{n}\right]\,\delta G - 2\sqrt{\frac{2}{3}}\,\frac{\overline{\mu}}{f'}\,\mathbf{n}\,\delta k \\ &= \mathbf{H}_{\mathsf{m}}\,\delta G + \sqrt{\frac{2}{3}}\,(1-\beta_1)\,\mathbf{n}\,\delta k.\end{aligned} \tag{A.33}$$

In a discrete setting the discrete vector of constitutive parameters is introduced as

$$\begin{aligned}\boldsymbol{m} &:= \begin{bmatrix} K & G & \sigma_0 & \sigma_\infty & H & d\end{bmatrix}^T, \\ \delta\boldsymbol{m} &:= \begin{bmatrix}\delta K & \delta G & \delta\sigma_0 & \delta\sigma_\infty & \delta H & \delta d\end{bmatrix}^T.\end{aligned} \tag{A.34}$$

With the partial variations of the bulk and shear moduli, as well as the hardening function

$$\begin{aligned}\delta K &:= \frac{\partial K}{\partial \boldsymbol{m}}\,\delta\boldsymbol{m} = \begin{bmatrix}1 & 0 & 0 & 0 & 0 & 0\end{bmatrix}\,\delta\boldsymbol{m}, \\ \delta G &:= \frac{\partial G}{\partial \boldsymbol{m}}\,\delta\boldsymbol{m} = \begin{bmatrix}0 & 1 & 0 & 0 & 0 & 0\end{bmatrix}\,\delta\boldsymbol{m}, \\ \delta k &:= \frac{\partial k}{\partial \boldsymbol{m}}\,\delta\boldsymbol{m} = \begin{bmatrix}0 & 0 & 1 & (1-\exp(-d\,\alpha)) & \alpha & \alpha\sigma_\infty\exp(-d\,\alpha)\end{bmatrix}\,\delta\boldsymbol{m},\end{aligned} \tag{A.35}$$

the third order array $\underline{\mathbf{M}}$ connecting the first Piola Kirchhoff stress tensor with changes in the discrete vector constitutive parameters of the underlying mechanical model can be defined

$$\delta_m \boldsymbol{P}^{\mathsf{K}} = \left[\frac{J^2-1}{2}\,\mathbf{F}^{-\mathsf{T}}\otimes\frac{\partial K}{\partial\boldsymbol{m}} + \mathbf{H}_{\mathsf{m}}\,\mathbf{F}^{-\mathsf{T}}\otimes\frac{\partial G}{\partial\boldsymbol{m}} + \sqrt{\frac{2}{3}}\,(1-eta_1)\,\mathbf{n}\,\mathbf{F}^{-\mathsf{T}}\otimes\frac{\partial k}{\partial\boldsymbol{m}}\right]\,\delta\boldsymbol{m} = \underline{\mathbf{M}}\,\delta\boldsymbol{m}, \tag{A.36}$$

of which, in conjunction with the conventions introduced in Sec. 2.1.2, see especially Eq. (2.9), the matrix form can be found

$$\delta_m \boldsymbol{P}^{\mathsf{K}} = \left[\frac{\partial \boldsymbol{P}^{\mathsf{K}}}{\partial \boldsymbol{m}}\right] \delta \boldsymbol{m} = \boldsymbol{M}\, \delta \boldsymbol{m}, \tag{A.37}$$

where the matrix $\boldsymbol{M}$ has the following structure

$$\boldsymbol{M} := \begin{bmatrix} \frac{\partial \boldsymbol{P}^{\mathsf{K}}_{11}}{\partial K} & \frac{\partial \boldsymbol{P}^{\mathsf{K}}_{11}}{\partial G} & \frac{\partial \boldsymbol{P}^{\mathsf{K}}_{11}}{\partial \sigma_0} & \frac{\partial \boldsymbol{P}^{\mathsf{K}}_{11}}{\partial \sigma_\infty} & \frac{\partial \boldsymbol{P}^{\mathsf{K}}_{11}}{\partial H} & \frac{\partial \boldsymbol{P}^{\mathsf{K}}_{11}}{\partial d} \\ \frac{\partial \boldsymbol{P}^{\mathsf{K}}_{21}}{\partial K} & \frac{\partial \boldsymbol{P}^{\mathsf{K}}_{21}}{\partial G} & \cdots & & \cdots & \frac{\partial \boldsymbol{P}^{\mathsf{K}}_{21}}{\partial d} \\ \vdots & \vdots & \ddots & & & \vdots \\ & & & & & \\ \vdots & \vdots & & & \ddots & \vdots \\ \frac{\partial \boldsymbol{P}^{\mathsf{K}}_{33}}{\partial K} & \frac{\partial \boldsymbol{P}^{\mathsf{K}}_{33}}{\partial G} & \cdots & & \cdots & \frac{\partial \boldsymbol{P}^{\mathsf{K}}_{33}}{\partial d} \end{bmatrix}. \tag{A.38}$$

A.3 History sensitivity

A.3.1 History sensitivity operator

In this section, the history sensitivity operator is derived. The starting point is Eq. (5.23), i.e. the partial variation of the First Piola-Kirchhoff stress tensor w.r.t. the internal history variables. Due to the J_2 elastoplasticity, the volumetric stress is independent of plastic flow, and thus the partial variation w.r.t. the internal variables consists solely on the deviatoric stress contribution, viz.

$$\delta_{h_n} \mathbf{P}^{\mathsf{K}} = \delta_{h_n} \mathbf{s}\, \mathbf{F}^{-\mathsf{T}}. \tag{A.39}$$

Here, the partial variation of the Kirchhoff stress tensor can be written as

$$\delta_{h_n} \mathbf{s} = \frac{\partial \mathbf{s}}{\partial \mathbf{s}^{\mathrm{tr}}} : \delta_{h_n} \mathbf{s}^{\mathrm{tr}} + \frac{\partial \mathbf{s}}{\partial \overline{\mu}} : \delta_{h_n} \overline{\mu} + \frac{\partial \mathbf{s}}{\partial \Delta\gamma} : \delta_{h_n} \Delta\gamma + \frac{\partial \mathbf{s}}{\partial \mathbf{n}} : \delta_{h_n} \mathbf{n}. \tag{A.40}$$

Basically, the derivation follows the same arguments as the derivation of the consistent elastoplastic tangent operator, cf. App. A.1. Thus, most of the partial derivatives are already known, cf. Eqs. (A.9) to (A.13), and the partial variations of the elastic trial

values read

$$\delta_{h_n}\mathbf{s}^{\mathrm{tr}} = \frac{\partial \mathbf{s}^{\mathrm{tr}}}{\partial \widetilde{\mathbf{b}}_{\mathsf{e}}^{\mathsf{tr}}} : \delta_{h_n}\widetilde{\mathbf{b}}_{\mathsf{e}}^{\mathsf{tr}} = G\,\mathbb{I}_{\mathrm{dev}} : \delta_{h_n}\widetilde{\mathbf{b}}_{\mathsf{e}}^{\mathsf{tr}}, \tag{A.41}$$

$$\delta_{h_n}\overline{\mu} = \frac{\partial \overline{\mu}}{\partial \widetilde{\mathbf{b}}_{\mathsf{e}}^{\mathsf{tr}}} : \delta_{h_n}\widetilde{\mathbf{b}}_{\mathsf{e}}^{\mathsf{tr}} = G\,\mathbb{I}_{\mathrm{dev}} : \delta_{h_n}\widetilde{\mathbf{b}}_{\mathsf{e}}^{\mathsf{tr}} = \frac{1}{3}\,G\,\mathbf{I} : \delta_{h_n}\widetilde{\mathbf{b}}_{\mathsf{e}}^{\mathsf{tr}}, \tag{A.42}$$

$$\delta_{h_n}\mathbf{n} = \frac{\partial \mathbf{n}}{\partial \mathbf{s}^{\mathrm{tr}}} : \delta_{h_n}\mathbf{s}^{\mathrm{tr}} = \frac{1}{\|\mathbf{s}^{\mathrm{tr}}\|}\,(\mathbb{I}_{\mathrm{sym}} - \mathbf{n}\otimes\mathbf{n}) : \delta_{h_n}\mathbf{s}^{\mathrm{tr}}, \tag{A.43}$$

$$\begin{aligned}\delta_{h_n}\Delta\gamma &= \frac{\partial \Delta\gamma}{\partial \overline{\mu}}\,\delta_{h_n}\overline{\mu} + \frac{\partial \Delta\gamma}{\partial \mathbf{s}^{\mathrm{tr}}} : \delta_{h_n}\mathbf{s}^{\mathrm{tr}} + \frac{\partial \Delta\gamma}{\partial \alpha_n}\delta\alpha_n \\ &= \frac{2\,\Delta\gamma^*}{f'(\Delta\gamma^*)}\,\delta_{h_n}\overline{\mu} - \frac{\mathbf{n}}{f'(\Delta\gamma^*)} : \delta_{h_n}\mathbf{s}^{\mathrm{tr}} + \sqrt{\frac{2}{3}}\,\frac{k'}{f'}\,\delta\alpha_n.\end{aligned} \tag{A.44}$$

Inserting these partial variations, as well as the known partial derivatives and scaling factors β_0, β_1 and β_2 into Eq. (A.40), one ends up with the following expression

$$\begin{aligned}\delta_{h_n}\mathbf{s} &= G\left[\beta_0\,\mathbb{I}_{\mathrm{dev}} - \frac{2}{3}\,\Delta\gamma\,\beta_1\,\mathbf{I}\otimes\mathbf{n} + \beta_2\,\mathbf{n}\otimes\mathbf{n}\right] : \delta_{h_n}\widetilde{\mathbf{b}}_{\mathsf{e}}^{\mathsf{tr}} - 2\sqrt{\frac{2}{3}}\,\overline{\mu}\,\frac{k'}{f'}\,\mathbf{n}\,\delta\alpha_n \\ &= \mathbb{S} : \delta_{h_n}\widetilde{\mathbf{b}}_{\mathsf{e}}^{\mathsf{tr}} + \sqrt{\frac{2}{3}}\,k'\,(1-\beta_1)\,\mathbf{n}\,\delta\alpha_n\end{aligned} \tag{A.45}$$

for the partial history variation of the deviatoric Kirchhoff stress tensor. The partial variation of the isochoric trial left Cauchy-Green tensor can further be identified to

$$\delta_{h_n}\widetilde{\mathbf{b}}_{\mathsf{e}}^{\mathsf{tr}} = \frac{\partial\left(\widetilde{\mathbf{F}}\,\mathbf{c}_{\mathsf{p},n}\,\widetilde{\mathbf{F}}^{\mathsf{T}}\right)}{\partial \mathbf{c}_{\mathsf{p},n}} : \delta\mathbf{c}_{\mathsf{p},n} = \left(\widetilde{\mathbf{F}}\,\mathbb{I}_{\mathrm{sym}}\overset{21}{*}\widetilde{\mathbf{F}}^{\mathsf{T}}\right) : \delta\mathbf{c}_{\mathsf{p},n} = \mathbb{B}_c : \delta\mathbf{c}_{\mathsf{p},n}. \tag{A.46}$$

Finally, Eq. (A.39) can be written in compact form, viz

$$\begin{aligned}\delta_{h_n}\mathbf{P}^{\mathsf{K}} &= \frac{\partial \mathbf{P}^{\mathsf{K}}}{\partial \boldsymbol{h}_n}\,\delta\boldsymbol{h}_n = \frac{\partial \mathbf{P}^{\mathsf{K}}}{\partial \mathbf{c}_{\mathsf{p},n}} : \delta\mathbf{c}_{\mathsf{p},n} + \frac{\partial \mathbf{P}^{\mathsf{K}}}{\partial \boldsymbol{\alpha}_n}\,\delta\boldsymbol{\alpha}_n \\ &= (\mathbb{S} : \mathbb{B}_c)\overset{21}{*}\mathbf{F}^{-\mathsf{T}} : \delta\mathbf{c}_{\mathsf{p},n} + \sqrt{\frac{2}{3}}\,k'\,(1-\beta_1)\,\mathbf{n}\,\mathbf{F}^{-\mathsf{T}}\,\delta\alpha_n \\ &= \mathbf{q}_{\mathsf{c}} : \mathbf{c}_{\mathsf{p},n} + \mathbf{q}_{\alpha}\,\delta\alpha_n.\end{aligned} \tag{A.47}$$

A.3.2 Partial history sensitivities

For the update of the variations of the internal history variables, some important partial derivatives and variations have to be derived. This section shows a step by step derivation of the important quantities.
In Eq. (5.29) the partial derivatives of internal variables $\mathbf{c}_{\mathsf{p}}$ and α w.r.t. the deformation

gradient are demanded. For the internal variable $\mathbf{c}_\mathrm{p}$ the partial derivative takes the form

$$\frac{\partial \mathbf{c}_\mathrm{p}}{\partial \mathbf{F}} = \frac{\partial \left(\widetilde{\mathbf{F}}^{-1} \widetilde{\mathbf{b}}_\mathrm{e} \widetilde{\mathbf{F}}^{-\mathsf{T}} \right)}{\partial \mathbf{F}} = \frac{\partial \widetilde{\mathbf{F}}^{-1}}{\partial \mathbf{F}} \overset{21}{*} \left(\widetilde{\mathbf{b}}_\mathrm{e} \widetilde{\mathbf{F}}^{-\mathsf{T}} \right) + \widetilde{\mathbf{F}}^{-1} \frac{\partial \widetilde{\mathbf{b}}_\mathrm{e}}{\partial \mathbf{F}} \overset{21}{*} \widetilde{\mathbf{F}}^{-\mathsf{T}} + \widetilde{\mathbf{F}}^{-1} \widetilde{\mathbf{b}}_\mathrm{e} \frac{\partial \widetilde{\mathbf{F}}^{-\mathsf{T}}}{\partial \mathbf{F}}. \tag{A.48}$$

Here, the the partial derivatives of the inverse and inverse transpose deformation gradient w.r.t. the deformation gradient itself are lengthy, but straight forward and can be identified to

$$\frac{\partial \widetilde{\mathbf{F}}^{-1}}{\partial \mathbf{F}} = -\left(\widetilde{\mathbf{F}}^{-1} \otimes \widetilde{\mathbf{F}}^{-\mathsf{T}} \right)^{\overset{23}{\mathsf{T}}} : \mathbb{F} \qquad \text{and} \qquad \frac{\partial \widetilde{\mathbf{F}}^{-\mathsf{T}}}{\partial \mathbf{F}} = -\left(\widetilde{\mathbf{F}}^{-\mathsf{T}} \otimes \widetilde{\mathbf{F}}^{-\mathsf{T}} \right)^{\overset{24}{\mathsf{T}}} : \mathbb{F}, \tag{A.49}$$

respectively, where the isochoric projection tensor for the deformation gradient $\mathbb{F}$ has been used, cf. Eq. (A.22). The partial derivative of the isochoric elastic left Cauchy-Green tensor takes the form

$$\frac{\partial \widetilde{\mathbf{b}}_\mathrm{e}}{\partial \mathbf{F}} = \frac{\partial \widetilde{\mathbf{b}}_\mathrm{e}}{\partial \mathbf{s}} : \frac{\partial \mathbf{s}}{\partial \mathbf{F}} + \frac{\partial \widetilde{\mathbf{b}}_\mathrm{e}}{\partial \overline{\mu}} \otimes \frac{\partial \overline{\mu}}{\partial \mathbf{F}} = \frac{1}{G} \mathbb{I}_\mathrm{dev} : \frac{\partial \mathbf{s}}{\partial \mathbf{F}} + \frac{1}{G} \otimes \frac{\partial \overline{\mu}}{\partial \mathbf{F}}. \tag{A.50}$$

The partial variations of the deviatoric Kirchhoff stress tensor and the scaling factor $\overline{\mu}$ w.r.t. the deformation gradient are already known from App. A.1, as the partial variations needed for the derivation of the consistent tangent operator only depend on the displacements via the deformation gradient. Thus, considering Eqs. (A.11), (A.20) and (A.21) one arrives at

$$\frac{\partial \widetilde{\mathbf{b}}_\mathrm{e}}{\partial \mathbf{F}} = \left(\frac{1}{G} \mathbb{S} + \frac{1}{3} \mathbf{I} \otimes \mathbf{I} \right) : \mathbb{B}_F =: \mathbb{C}. \tag{A.51}$$

Consequently, Eq. (A.48) becomes

$$\begin{aligned} \frac{\partial \mathbf{c}_\mathrm{p}}{\partial \mathbf{F}} &= \widetilde{\mathbf{F}}^{-1} \mathbb{C} \overset{21}{*} \widetilde{\mathbf{F}}^{-\mathsf{T}} - \left[\left(\widetilde{\mathbf{F}}^{-1} \otimes \widetilde{\mathbf{F}}^{-\mathsf{T}} \right)^{\overset{23}{\mathsf{T}}} \overset{21}{*} \left(\widetilde{\mathbf{b}}_\mathrm{e} \widetilde{\mathbf{F}}^{-\mathsf{T}} \right) + \widetilde{\mathbf{F}}^{-1} \widetilde{\mathbf{b}}_\mathrm{e} \left(\widetilde{\mathbf{F}}^{-\mathsf{T}} \otimes \widetilde{\mathbf{F}}^{-\mathsf{T}} \right)^{\overset{24}{\mathsf{T}}} \right] : \mathbb{F} \\ &=: \mathbb{A}_c. \end{aligned} \tag{A.52}$$

The partial derivative of the isochoric hardening variable α w.r.t the deformation gradient is comparatively simple and takes the form

$$\frac{\partial \alpha}{\partial \mathbf{F}} = \frac{\partial \alpha}{\partial \Delta\gamma} \frac{\partial \Delta\gamma}{\partial \mathbf{F}} = \sqrt{\frac{2}{3}} \frac{\partial \Delta\gamma}{\partial \mathbf{F}}. \tag{A.53}$$

Here, again, the partial derivative of the plastic multiplier increment is already known, cf. Eq. (A.13). Hence, one obtains

$$\frac{\partial \alpha}{\partial \mathbf{F}} = \sqrt{\frac{2}{3}} \frac{G}{f'} \left(\frac{2}{3} \Delta\gamma \mathbf{I} - \mathbf{n} \right) : \mathbb{B}_F =: \mathbf{A}_\alpha. \tag{A.54}$$

Partial history variations. The partial variations of the internal history variables w.r.t. the history variables of the prior load step are required for the update of their variations. The partial variation of the internal history variable $\mathbf{c}_\mathsf{p}$ takes the form

$$\delta_{h_n}\mathbf{c}_\mathsf{p} = \frac{\partial \mathbf{c}_\mathsf{p}}{\partial \widetilde{\mathbf{b}}_\mathsf{e}} : \delta_{h_n}\widetilde{\mathbf{b}}_\mathsf{e}. \tag{A.55}$$

Here, The partial derivative of the internal variable $\mathbf{c}_\mathsf{p}$ w.r.t. the isochoric elastic left Cauchy-Green tensor can be resolved to

$$\frac{\partial \mathbf{c}_\mathsf{p}}{\partial \widetilde{\mathbf{b}}_\mathsf{e}} = \widetilde{\mathbf{F}}^{-1}\mathbb{I}_s \overset{21}{*} \widetilde{\mathbf{F}}^{-\mathsf{T}} =: \mathbb{B}_c^{-1}. \tag{A.56}$$

The partial variation of the isochoric elastic left Cauchy-Green tensor can be expressed in terms of the partial variations of the deviatoric Kirchhoff stress tensor $\mathbf{s}$ and the scaling factor $\overline{\mu}$

$$\delta_{h_n}\widetilde{\mathbf{b}}_\mathsf{e} = \frac{\partial \widetilde{\mathbf{b}}_\mathsf{e}}{\partial \mathbf{s}} : \delta_{h_n}\mathbf{s} + \frac{\partial \widetilde{\mathbf{b}}_\mathsf{e}}{\partial \overline{\mu}}\,\delta_{h_n}\overline{\mu}. \tag{A.57}$$

Making use of Eq. (A.42), Eq. (A.45) and Eq. (A.46) yields

$$\delta_{h_n}\widetilde{\mathbf{b}}_\mathsf{e} = \frac{1}{G}\left(\mathbb{S} + \frac{1}{3}\,\mathbf{I}\otimes\mathbf{I}\right) : \mathbb{B}_c : \delta\mathbf{c}_{\mathsf{p},n} + \sqrt{\frac{2}{3}}\,k'\,(1-\beta_1)\,\mathbf{n}\,\delta\alpha_n \tag{A.58}$$

and thus,

$$\begin{aligned}\delta_{h_n}\mathbf{c}_\mathsf{p} &= \frac{1}{G}\,\mathbb{B}_c^{-1} : \left(\mathbb{S} + \frac{1}{3}\,\mathbf{I}\otimes\mathbf{I}\right) : \mathbb{B}_c : \delta\mathbf{c}_{\mathsf{p},n} + \sqrt{\frac{2}{3}}\,k'\,(1-\beta_1)\,\mathbb{B}_c^{-1} : \mathbf{n}\,\delta\alpha_n \\ &= \mathbb{C}_c : \delta\mathbf{c}_{\mathsf{p},n} + \mathbf{C}_c\,\delta\alpha_n.\end{aligned} \tag{A.59}$$

The partial history variation of the isochoric hardening variable α takes the form

$$\delta_{h_n}\alpha = \frac{\partial \alpha}{\partial \alpha_n} : \delta\alpha_n + \frac{\partial \alpha}{\partial \Delta\gamma}\,\delta_{h_n}\Delta\gamma = \delta\alpha_n + \sqrt{\frac{2}{3}}\,\delta_{h_n}\Delta\gamma, \tag{A.60}$$

which by means of Eq. (A.44) can be expressed as

$$\delta_{h_n}\alpha = \delta\alpha_n + \sqrt{\frac{2}{3}}\left[\frac{2\Delta\gamma}{f'}\,\delta_{h_n}\overline{\mu} - \frac{1}{f'}\,\mathbf{n} : \delta_{h_n}\mathbf{s}^{\mathrm{tr}} + \sqrt{\frac{2}{3}}\,\frac{k'}{f'}\,\delta\alpha_n\right]. \tag{A.61}$$

As the partial variations of the trial deviatoric Kirchhoff stress tensor $\mathbf{s}^{\mathrm{tr}}$ and the scaling factor $\overline{\mu}$ are already known, cf. Eq. (A.41) and Eq. (A.42), one finally arrives at

$$\begin{aligned}\delta_{h_n}\alpha &= \sqrt{\frac{2}{3}}\,\frac{G}{f'}\left(\frac{2}{3}\,\Delta\gamma\,\mathbf{I} - \mathbf{n}\right) : \mathbb{B}_c : \delta\mathbf{c}_{\mathsf{p},n} + \left(1 + \frac{2}{3}\,\frac{k'}{f'}\right)\delta\alpha_n \\ &= \mathbf{T}_c : \delta\mathbf{c}_{\mathsf{p},n} + T_\alpha\,\delta\alpha_n.\end{aligned} \tag{A.62}$$

Constitutive history variations. The partial variations of the internal history variables w.r.t. the constitutive parameters are needed in the case of constitutive design sensitivity analysis. Most of the necessary variations and derivatives are already known from the previous sections. By means of Eq. (A.56), the constitutive variation of the internal variable $\mathbf{c}_\mathsf{p}$ takes the form

$$\delta_m \mathbf{c}_\mathsf{p} = \frac{\partial \mathbf{c}_\mathsf{p}}{\partial \widetilde{\mathbf{b}}_\mathsf{e}} : \delta_m \widetilde{\mathbf{b}}_\mathsf{e} = \mathbb{B}_c^{-1} : \delta_m \widetilde{\mathbf{b}}_\mathsf{e}. \tag{A.63}$$

Here, the constitutive variation of the elastic isochoric left Cauchy-Green tensor is given by

$$\begin{aligned} \delta_m \widetilde{\mathbf{b}}_\mathsf{e} &= \frac{\partial \widetilde{\mathbf{b}}_\mathsf{e}}{\partial G}\, \delta_m G + \frac{\partial \widetilde{\mathbf{b}}_\mathsf{e}}{\partial \mathbf{s}} : \delta_m \mathbf{s} + \frac{\partial \widetilde{\mathbf{b}}_\mathsf{e}}{\partial \overline{\mu}}\, \delta_m \overline{\mu} \\ &= -\frac{1}{G^2}\,(\mathbf{s} + \overline{\mu}\,\mathbf{I})\,\delta_m G + \frac{1}{G}\,\mathbb{I}_{\mathrm{sym}} : \delta_m \mathbf{s} + \frac{1}{G}\mathbf{I}\,\delta_m \overline{\mu} \end{aligned} \tag{A.64}$$

and can, by means of Eqs. (A.30) and (A.33), easily identified to

$$\delta_m \widetilde{\mathbf{b}}_\mathsf{e} = \frac{1}{G^2}\,(G\,\mathbf{H}_m - \mathbf{s})\,\delta_m G + \frac{1}{G}\sqrt{\frac{2}{3}}\,(1-\beta_1)\,\mathbf{n}\,\delta_m k. \tag{A.65}$$

Finally, the resulting constitutive variation of the internal variable $\mathbf{c}_\mathsf{p}$ reads

$$\delta_m \mathbf{c}_\mathsf{p} = \frac{1}{G^2}\,\mathbb{B}_c^{-1} : \left[(G\,\mathbf{H}_m - \mathbf{s})\,\delta_m G + G\sqrt{\frac{2}{3}}\,(1-\beta_1)\,\mathbf{n}\,\delta_m k\right]. \tag{A.66}$$

The derivation of the constitutive variation of the internal variable α is even simpler and takes the form

$$\delta_m \alpha = \frac{\partial \alpha}{\partial \Delta\gamma}\,\delta_m \Delta\gamma. \tag{A.67}$$

The only needed variation is already known from Eq. (A.31). After insertion and straight forward transformations, the constitutive variation of the internal variable α reads

$$\delta_m \alpha = \sqrt{\frac{2}{3}}\left[\frac{\Delta\gamma}{G}\,(\beta_1 - 1) - \frac{1}{f'}\,\mathbf{n} : \operatorname{dev}\widetilde{\mathbf{b}}_\mathsf{e}^{\mathsf{tr}}\right]\delta_m G + \frac{2}{3\,f'}\,\delta_m k. \tag{A.68}$$

In a discrete setting, with the discrete vectors of constitutive parameters and their variations and by means of Eq. (A.35), the discrete matrix forms of Eq. (A.66) and Eq. (A.68) can be found and read

$$\begin{aligned} \delta_m \boldsymbol{c}^\mathsf{p} &= \left[\frac{1}{G^2}\,\boldsymbol{B}_c^{-1}\left((G\,\boldsymbol{H}_m - \boldsymbol{s}) \otimes \frac{\partial G}{\partial \boldsymbol{m}} + G\sqrt{\frac{2}{3}}\,(1-\beta_1)\,\boldsymbol{n} \otimes \frac{\partial k}{\partial \boldsymbol{m}}\right)\right]\delta \boldsymbol{m} \\ &= \boldsymbol{m}_\mathsf{c}\,\delta \boldsymbol{m}, \end{aligned} \tag{A.69}$$

$$\begin{aligned}\delta_m \alpha &= \left[\sqrt{\frac{2}{3}} \left(\frac{\Delta\gamma}{G} \left(\beta_1 - 1\right) - \frac{1}{f'} \boldsymbol{n} : \operatorname{dev} \boldsymbol{b}_{\mathsf{e}}^{\mathsf{tr}} \right) \otimes \frac{\partial G}{\partial \boldsymbol{m}} + \frac{2}{3\, f'} \otimes \frac{\partial k}{\partial \boldsymbol{m}} \right] \\ &= \boldsymbol{m}_\alpha \, \delta \boldsymbol{m}.\end{aligned} \tag{A.70}$$

Here, $\boldsymbol{B}_{\mathsf{c}}^{-1}$ is the symmetric matrix form of the fourth order tensor $\mathbb{B}_c^{-1}$ following Eq. (2.12) the symmetric matrix forms of the tensors $\boldsymbol{H}_m$, $\boldsymbol{s}$, $\boldsymbol{n}$ and $\operatorname{dev} \boldsymbol{b}_{\mathsf{e}}^{\mathsf{tr}}$ result in column matrices corresponding to Eq. (2.10).

Appendix B

Details on Numerical Implementation

B.1 Finite element discretization

This section briefly summarizes important basics regarding the discretization of continuous quantities using finite elements considering all three space dimensions. Further details can be found in the relevant literature, see e.g. [21, 31, 80, 172, 190, 199] among others. In the context of the finite element method (FEM), a continuous domain Ω, as well as its boundary $\partial\Omega$ is approximated by a mesh Ω^h consisting of a finite number nel of finite elements Ω_e, viz.

$$\Omega \approx \Omega^h = \bigcup_{e=1}^{\mathsf{nel}} \Omega_e \quad \text{and} \quad \partial\Omega \approx \partial\Omega^h = \bigcup_{e=1}^{\mathsf{nboun}} \partial\Omega_e, \tag{B.1}$$

where nboun denotes the number of elements located at the boundary of Ω_h. Each finite element consists of nnode finite element nodes. Further, let ndofe denote the number of degrees of freedom per element, i.e. $\mathsf{ndofe} = 3 \cdot \mathsf{nnode}$. Additionally, approximations of field quantities constituting the solution of the underlying boundary value problem have to be defined. Following the isoparametric concept, approximations of the geometric domain, as well as the field quantities are carried out using the same shape functions. In accordance with the Bubnov-Galerkin method, also the test functions are approximated using the same shape functions. The approximations read

$$\boldsymbol{X}^h = \sum_{i=1}^{\mathsf{nnode}} N_i(\boldsymbol{\xi})\, \boldsymbol{X}_i, \quad \boldsymbol{u}^h = \sum_{i=1}^{\mathsf{nnode}} N_i(\boldsymbol{\xi})\, \boldsymbol{u}_i, \quad \boldsymbol{v}^h = \sum_{i=1}^{\mathsf{nnode}} N_i(\boldsymbol{\xi})\, \boldsymbol{v}_i, \quad \in \mathbb{R}^{\mathsf{nnode}\times 1}. \tag{B.2}$$

Here, nnode denotes the number of nodes per element. The shape functions N_i are defined on a fixed parameter space $\Omega_\square$ that is a regular hexahedron with coordinates $\boldsymbol{\xi} = \{\xi, \eta, \zeta\}$ and edge length of 2. The column vectors $\boldsymbol{X}_i$, $\boldsymbol{u}_i$, $\boldsymbol{u}_i$ are the discrete values of the geometry, displacements and test functions

$$\boldsymbol{X}_i = \begin{bmatrix} X_i^1 & X_i^2 & X_i^3 \end{bmatrix}^T, \quad \boldsymbol{u}_i = \begin{bmatrix} u_i^1 & u_i^2 & u_i^3 \end{bmatrix}^T, \quad \boldsymbol{v}_i = \begin{bmatrix} v_i^1 & v_i^2 & v_i^3 \end{bmatrix}^T. \tag{B.3}$$

Within the scope of this thesis, the finite elements require C^0-continuity, i.e. simple continuity of the displacement field across the element edges. C^0 shape functions have to

fulfil polynomial completeness, i.e. with $i \neq j$

$$N_i(\boldsymbol{\xi}_i) = 1, \quad N_i(\boldsymbol{\xi}_j) = 0, \quad \sum_{i}^{\text{nnode}} N_i(\boldsymbol{\xi}) = 1, \quad \text{and} \quad \sum_{i}^{\text{nnode}} N_{i,\boldsymbol{\xi}} = 0. \tag{B.4}$$

Considering the simple 8-node hexahedron finite element, the linear shape functions of the form

$$N_i(\boldsymbol{\xi}) = \frac{1}{8}\,(1 + \xi_i\,\xi)\,(1 + \eta_i\,\eta)\,(1 + \zeta_i\,\zeta) \tag{B.5}$$

fulfil these requirements and are used in this work. By means of a Jacobian transformation, it is possible to determine the gradient of the shape functions regarding the discrete referential coordinates $\boldsymbol{X}$, viz.

$$\boldsymbol{L}_i := \operatorname{Grad} N_i = \boldsymbol{J}^{-T} \begin{bmatrix} N_{i,\xi} \\ N_{i,\eta} \\ N_{i,\zeta} \end{bmatrix} = \begin{bmatrix} N_{i,1} \\ N_{i,2} \\ N_{i,3} \end{bmatrix}, \tag{B.6}$$

with the transformation (Jacobi) matrix

$$\boldsymbol{J} = \begin{bmatrix} X_{1,\xi} & X_{1,\eta} & X_{1,\zeta} \\ X_{2,\xi} & X_{2,\eta} & X_{2,\zeta} \\ X_{3,\xi} & X_{3,\eta} & X_{3,\zeta} \end{bmatrix} = \begin{bmatrix} X_1\,N_{,\xi} & X_1\,N_{,\eta} & X_1\,N_{,\zeta} \\ X_2\,N_{,\xi} & X_2\,N_{,\eta} & X_2\,N_{,\zeta} \\ X_3\,N_{,\xi} & X_3\,N_{,\eta} & X_3\,N_{,\zeta} \end{bmatrix}. \tag{B.7}$$

Consequently, Eq. (B.6) represents a discrete gradient operator regarding the referential coordinates and one obtains the discrete gradients and divergence of the field quantities

$$\begin{aligned} \operatorname{Grad} \boldsymbol{u}^h &= \sum_{i=1}^{\text{nnode}} \boldsymbol{u}_i\,\boldsymbol{L}_i^T, \quad \operatorname{Grad} \boldsymbol{v}^h = \sum_{i=1}^{\text{nnode}} \boldsymbol{v}_i\,\boldsymbol{L}_i^T \quad \in \mathbb{R}^{3\times 3}, \\ \operatorname{Div} \boldsymbol{u}^h &= \sum_{i=1}^{\text{nnode}} \boldsymbol{L}_i^T\,\boldsymbol{u}_i, \quad \operatorname{Div} \boldsymbol{v}^h = \sum_{i=1}^{\text{nnode}} \boldsymbol{L}_i^T\,\boldsymbol{v}_i \quad \in \mathbb{R}^{1\times 1}. \end{aligned} \tag{B.8}$$

With the definition of the nodal gradient operator matrix $\boldsymbol{G}_i$

$$\boldsymbol{G}_i = \begin{bmatrix} \operatorname{diag}(N_{i,1}) & \operatorname{diag}(N_{i,2}) & \operatorname{diag}(N_{i,3}) \end{bmatrix}^T \in \mathbb{R}^{9\times 3}, \tag{B.9}$$

the gradients of vector valued field quantities can directly be expressed as a column matrix

$$\operatorname{Grad} \boldsymbol{u}^h = \sum_{i=1}^{\text{nnode}} \boldsymbol{G}_i\,\boldsymbol{u}_i, \quad \operatorname{Grad} \boldsymbol{v}^h = \sum_{i=1}^{\text{nnode}} \boldsymbol{G}_i\,\boldsymbol{v}_i \quad \in \mathbb{R}^{9\times 1}. \tag{B.10}$$

Further, defining the element coordinate, displacement and test function vectors

$$\boldsymbol{X}_e = \begin{bmatrix} \boldsymbol{X}_1 \\ \boldsymbol{X}_2 \\ \vdots \\ \boldsymbol{X}_{\mathsf{nnode}} \end{bmatrix}, \quad \boldsymbol{u}_e = \begin{bmatrix} \boldsymbol{u}_1 \\ \boldsymbol{u}_2 \\ \vdots \\ \boldsymbol{u}_{\mathsf{nnode}} \end{bmatrix}, \quad \boldsymbol{v}_e = \begin{bmatrix} \boldsymbol{v}_1 \\ \boldsymbol{v}_2 \\ \vdots \\ \boldsymbol{v}_{\mathsf{nnode}} \end{bmatrix} \quad \in \mathbb{R}^{\mathsf{ndofe}\times 1} \tag{B.11}$$

and the element interpolation matrix

$$\boldsymbol{N} = \begin{bmatrix} \mathrm{diag}(N_1) & \mathrm{diag}(N_2) & \dots & \mathrm{diag}(N_{\mathsf{nnode}}) \end{bmatrix} \quad \in \mathbb{R}^{\mathsf{ndofe}\times 3}, \tag{B.12}$$

the summations in Eq. (B.2) can be replaced by matrix multiplications, viz.

$$\boldsymbol{X}^h = \boldsymbol{N}\,\boldsymbol{X}_e, \quad \boldsymbol{u}^h = \boldsymbol{N}\,\boldsymbol{u}_e, \quad \boldsymbol{v}^h = \boldsymbol{N}\,\boldsymbol{v}_e. \tag{B.13}$$

This can also be done for approximations of gradients by means of the element gradient operator matrix $\boldsymbol{G}$ of the form

$$\boldsymbol{G} = \begin{bmatrix} \boldsymbol{G}_1 & \boldsymbol{G}_2 & \dots & \boldsymbol{G}_{\mathsf{nnode}} \end{bmatrix}^T \quad \in \mathbb{R}^{9\times \mathsf{ndofe}}, \tag{B.14}$$

where $\mathsf{ndofe} = 3 \cdot \mathsf{nnode}$ is the number of degrees of freedom per element. Herewith, Eq. (B.10) can easily be written as

$$\mathrm{Grad}\,\boldsymbol{u}^h = \boldsymbol{G}_e\,\boldsymbol{u}_e, \quad \mathrm{Grad}\,\boldsymbol{v}^h = \boldsymbol{G}_e\,\boldsymbol{v}_e \quad \in \mathbb{R}^{9\times 1}. \tag{B.15}$$

The discrete weak form of equilibrium and its variations that have to be computed for structural and sensitivity analysis must be integrated in each finite element. The integration is done numerically by means of the Gauss quadrature. For any function $f(\boldsymbol{x})$ the integration reads

$$\int_{\Omega_e} f(\boldsymbol{X}^h)\,\mathrm{d}V = \int_{\Omega_\square} f(\boldsymbol{X}^h(\boldsymbol{\xi}))\,\det\boldsymbol{J}\,\mathrm{d}V_\square \approx \sum_{i=1} f(\xi_i,\eta_i\zeta_i)\,w_i\,\det\boldsymbol{J}, \tag{B.16}$$

where $\det\boldsymbol{J}$ is the determinant of the transformation matrix in Eq. (B.7) and w_i are weighting factors corresponding to the coordinates of the Gaussian integration points with coordinates $\boldsymbol{\xi}$.

B.2 MATLAB specifics

In this section, in view of replication of the results presented in this work, some implementation details specific to MATLAB are given.

Compilation of element routine. Within the finite element method, usually the routine computing the element contributions of global system matrices has to be called most frequently. Considering sensitivity analysis, even more evaluations on element level are necessary. Thus, fast execution of the element routine is very convenient. MATLAB provides the opportunity to compile standard `.m` files using the built in compiler to so-called `.mex`

files. This can be done either using a script in batch mode, or using the graphical user interface (GUI) provided by `MATLAB`. Routines compiled to `.mex` usually execute much faster than standard `MATLAB` routines, as the just in time interpretation of the source code is omitted. Additionally, `.mex` files can be used for compilation of `C/C++` or `Fortran` routines to be run in `MATLAB`. Details can e.g. be found in [52].

Parallel element evaluations. The `MATLAB` Parallel Computing Toolbox [179], among others, provides the possibility to execute `for` loops in parallel. In this work, for this purpose the `parfor` construct is utilized. Hereby, it is very important to pass arguments in a *sliced* manner. That is, the parallel workers have to be served with one unique slice of the argument based on the current value of the control variable. This ensures that multiple workers cannot write into the same memory. However, utilizing `parfor` loops broadcast variables, i.e. entire variables that are shared by all workers, should be avoided, as each worker has to receive a copy of the variable, which leads to unnecessary memory overhead and slow execution times.

Utilization of cell arrays. Slicing of variables can easily be done utilizing cell arrays. This data type can contain any other type of data, including the cell array data type itself, in each of the indexed data containers called cells. That is, different data types can be mixed, or same data types of different dimension can be stored in just one variable. Depending on the containing data, cell arrays can be *homogeneous* or *heterogeneous*. More information can be found e.g. in [178].

Geometric modeling using the NURBS Toolbox. Using the NURBS Toolbox [137], geometry descriptions based on NURBS and B-Splines can easily be constructed and used for mesh generation and manipulations within a shape optimization procedure. Hereby, the essential functions are `nrbmak` and `nrbeval`. Providing control point coordinates and corresponding knot vectors, `nrbmak` builds up the NURBS structure. Subsequently, `nrbeval` evaluates corresponding mesh coordinates based on the chosen discretization. An example is given in Fig. B.1 that creates the geometry and mesh shown in Fig. 6.6 of Chap. 6. Furthermore, the function `nrbeval_der_p` is used to evaluate the first derivative of the mesh coordinates w.r.t. the control point coordinates, i.e. the design velocity matrix as shown in Fig. B.1.

```
% Control point coordinates
CP = [
0 25  0 25  0 25 12.5 25 12.5 25  0 25  0 25  0 25 12.5 25 12.5 25
0  0 40 40 90 60 90   90 100  100 0  0 40 40 90 60 90   90 100  100
0  0  0  0  0  0  0    0   0    0 2  2  2  2  2  2  2    2   2    2
]';
% Knot vectors
knt{1} = [0 0 1 1];                % x-direction
knt{2} = [0 0 0 0.5 0.5 1 1 1 ];   % y-direction
knt{3} = [0 0 1 1];                % z-direction
% Number of control points
% x-dir.    y-dir.      z-dir.
ncp{1} = 2; ncp{2} = 5; ncp{3} = 2;
% Number of elements
% x-dir.    y-dir.        z-dir.
nel{1} = 6; nel{2} = 30;  nel{3} =  6;
% Utilizing the NURBS toolbox
coefs = reshape(CP',ndim,ncp{1},ncp{2},ncp{3});
coefs(4,:,:) = 1;  % Weights: 1 --> B-Spline
%% NURBS volume
nrb = nrbmak(coefs,Knots);
% Convert the number of elements in number of points
subd = cell2mat(nel)+1; pnts = cell(1,3); order = nrb.order;
for i=1:3
 pnts{i} = linspace(knt{i}(order(i)),knt{i}(end-order(i)+1),subd(i));
end
% Build FE mesh
p = nrbeval (nrb, pnts);
x1=squeeze(p(1,:,:)); x2=squeeze(p(2,:,:)); x3=squeeze(p(3,:,:));
coord = [x1(:) x2(:) x3(:)];
nelem = nel{1}*nel{2}*nel{3};
elem = zeros(nelem,8); % 8-node hexahedron elements
for i=1:nel{1}
 for j=1:nel{2}
  for k=1:nel{3}
   ie = (k-1)*nel{1}*nel{2}+(j-1)*nel{1}+i;
   elem(ie,1) = (j-1)*(nel{1}+1)+i +(nel{1}+1)*(nel{2}+1)*(k-1);
   elem(ie,2)=(j-1)*(nel{1}+1)+i+1 +(nel{1}+1)*(nel{2}+1)*(k-1);
   elem(ie,4)=j*(nel{1}+1)+i +(nel{1}+1)*(nel{2}+1)*(k-1);
   elem(ie,3)=j*(nel{1}+1)+i+1 +(nel{1}+1)*(nel{2}+1)*(k-1);
   elem(ie,5)=elem(ie,1)+(nel{1}+1)*(nel{2}+1) ;
   elem(ie,6)=elem(ie,2)+(nel{1}+1)*(nel{2}+1) ;
   elem(ie,7)=elem(ie,3)+(nel{1}+1)*(nel{2}+1) ;
   elem(ie,8)=elem(ie,4)+(nel{1}+1)*(nel{2}+1) ;
  end
 end
end
```

Figure B.1: MATLAB code example: NURBS geometry and FE mesh construction.

```
% Design velocity matrix
ndim=3;
pncp = prod([ncp{:}]); der = zeros(prod(subd),pncp);
for i=1:pncp
[der(:,i)] = nrbeval_der_p (nrb, i, pnts);
end
Dv=zeros(prod(subd)*ndim,ndim*pncp);
Dv(1:3:end,1:3:end) = der;
Dv(2:3:end,2:3:end) = der;
Dv(3:3:end,3:3:end) = der;
```

Figure B.2: MATLAB code example: Computation of design velocity matrix.

Appendix C

Scanning Electron Microscopy Evaluations

In Chap. 7 representative SEM images of the fracture surfaces of the initial and optimized X0-specimen geometries are presented for a specific magnification factor. In this appendix further evaluated SEM images at different magnification factors are presented to improve the overall impression of the microscopic texture of the fracture surfaces. The images are taken at magnification factors of 500 x, 2 000 x and 10 000 x and three different evaluation areas located on the left (L), at the center (C), and on the right (R) of the fracture surfaces.

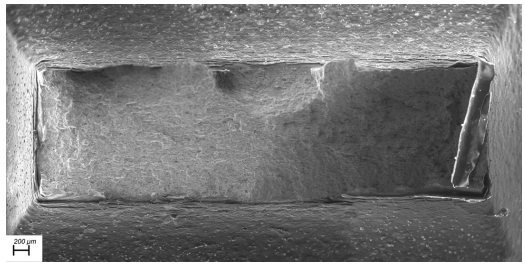

(a) Full fracture surface

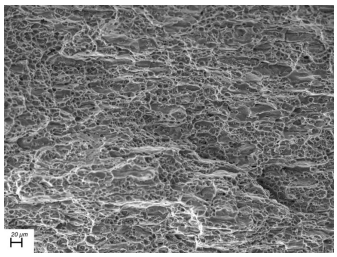

(b) L 500 x

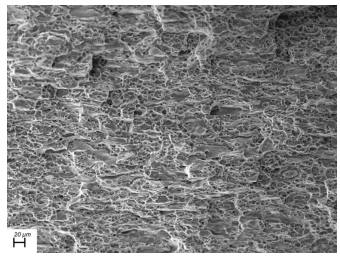

(c) C 500 x

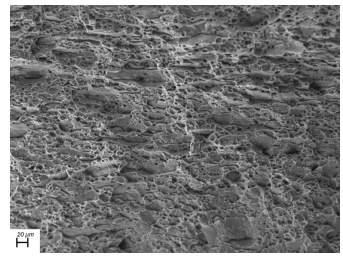

(d) R 500 x

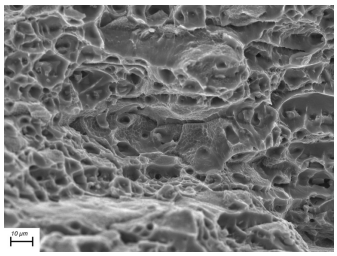

(e) L 2 000 x

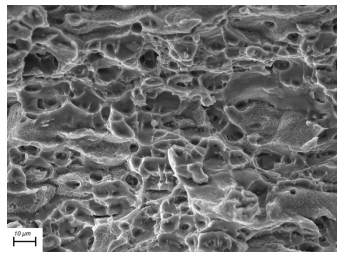

(f) C 2 000 x

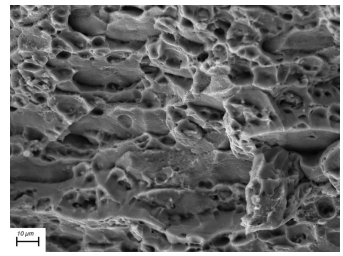

(g) R 2 000 x

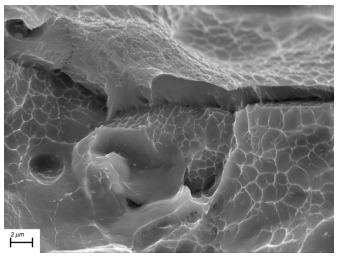

(h) L 10 000 x

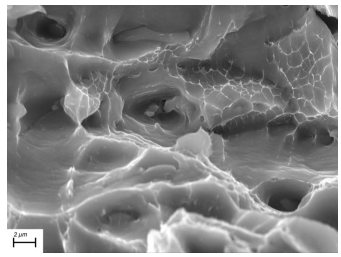

(i) C 10 000 x

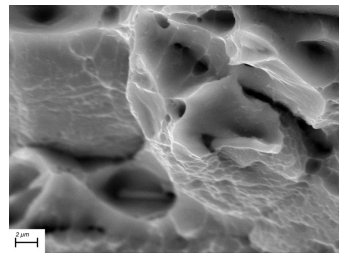

(j) R 10 000 x

Figure C.1: SEM images: Initial geometry, load case 1/1.

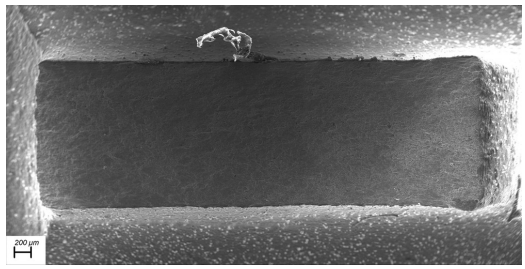

(a) Full fracture surface

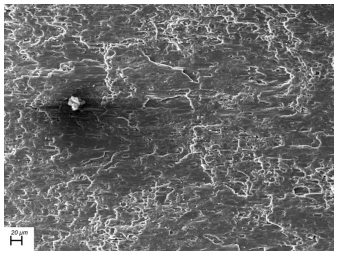

(b) L 500 x

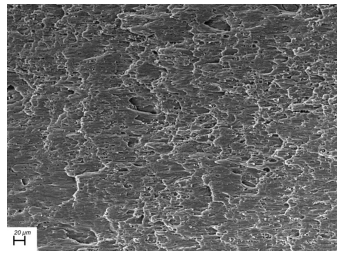

(c) C 500 x

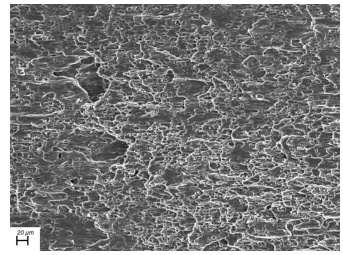

(d) R 500 x

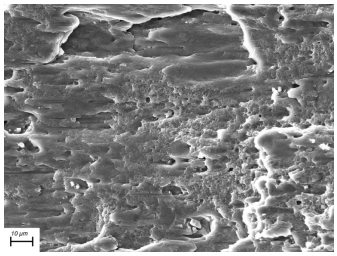

(e) L 2 000 x

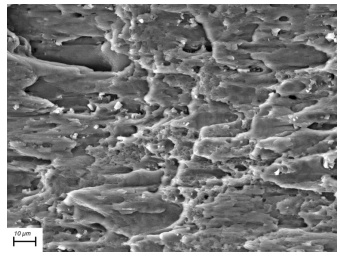

(f) C 2 000 x

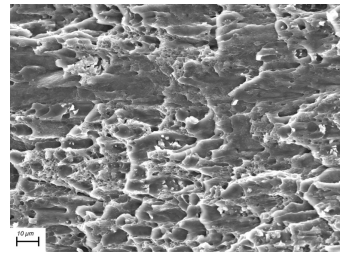

(g) R 2 000 x

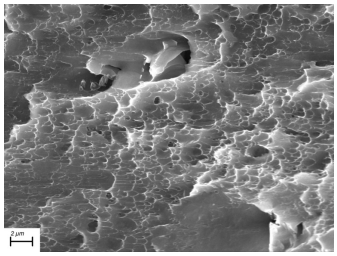

(h) L 10 000 x

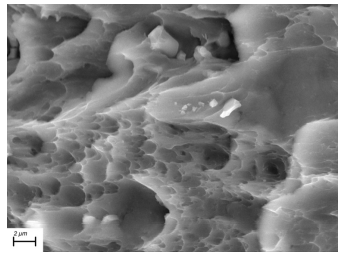

(i) C 10 000 x

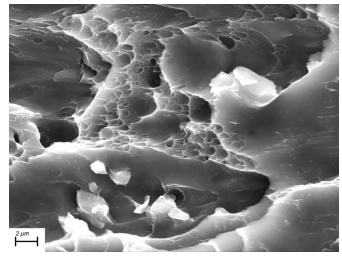

(j) R 10 000 x

Figure C.2: SEM images: Initial geometry, load case -1/1.

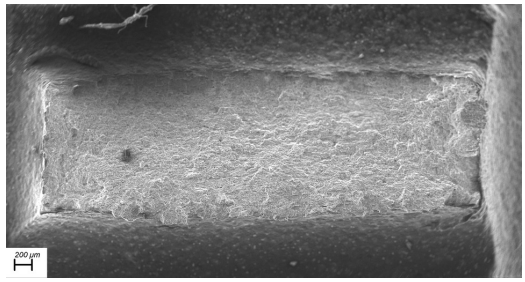

(a) Full fracture surface

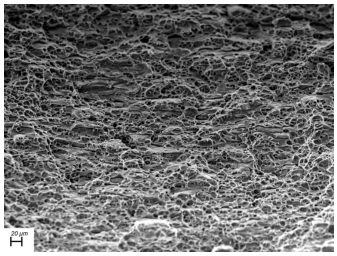

(b) L 500 x

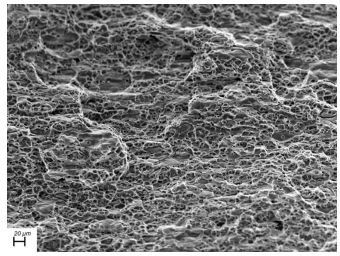

(c) C 500 x

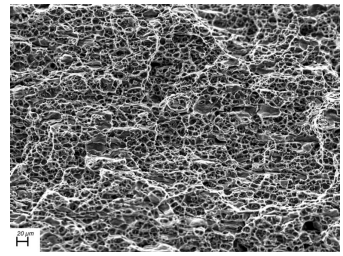

(d) R 500 x

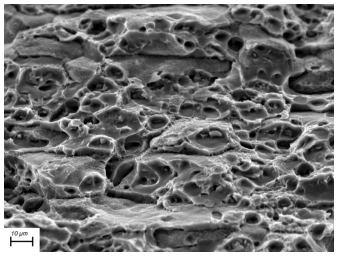

(e) L 2 000 x

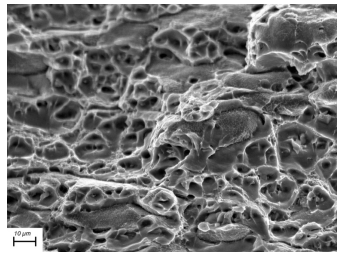

(f) C 2 000 x

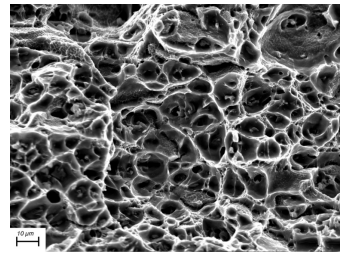

(g) R 2 000 x

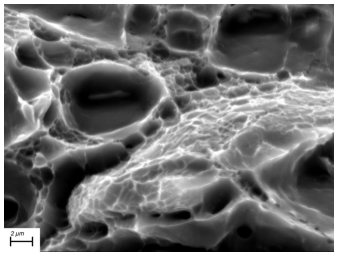

(h) L 10 000 x

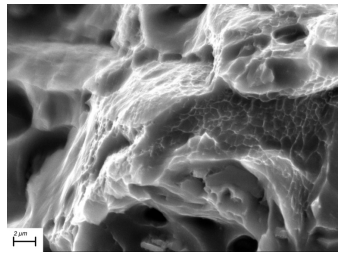

(i) C 10 000 x

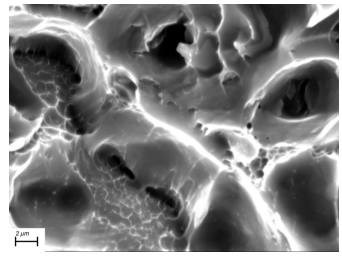

(j) R 10 000 x

Figure C.3: SEM images: V_{11} geometry, load case 1/1.

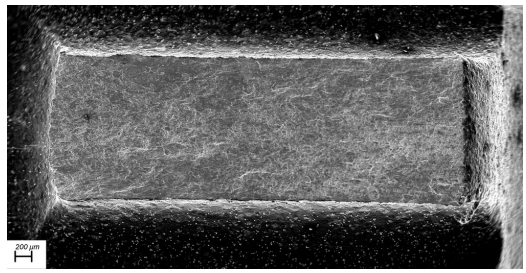

(a) Full fracture surface

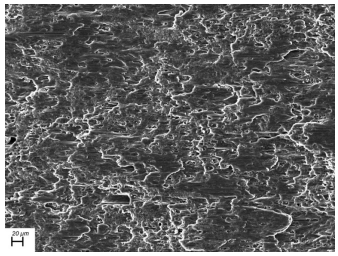

(b) L 500 x

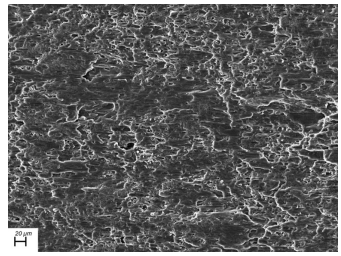

(c) C 500 x

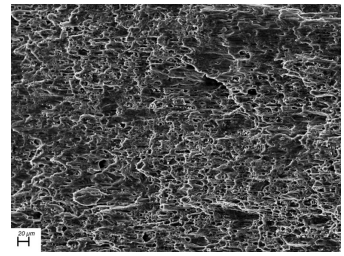

(d) R 500 x

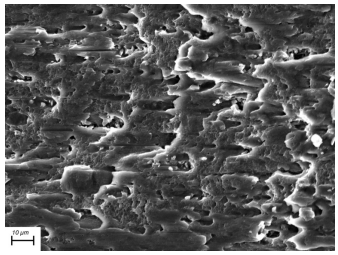

(e) L 2 000 x

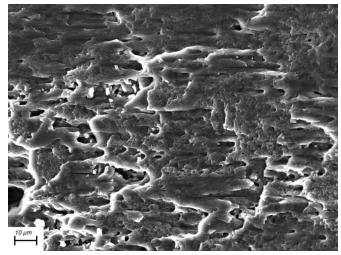

(f) C 2 000 x

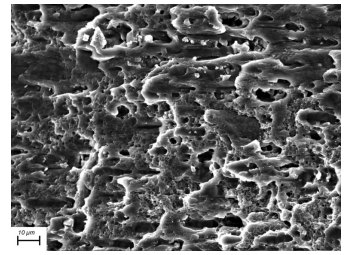

(g) R 2 000 x

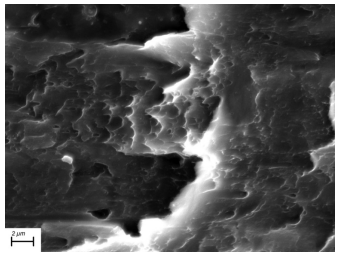

(h) L 10 000 x

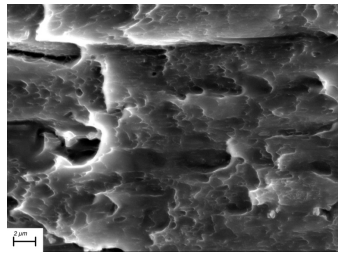

(i) C 10 000 x

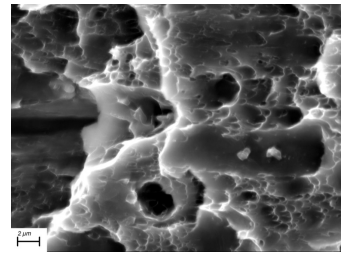

(j) R 10 000 x

Figure C.4: SEM images: V_{11} geometry, load case -1/1.

(a) Full fracture surface

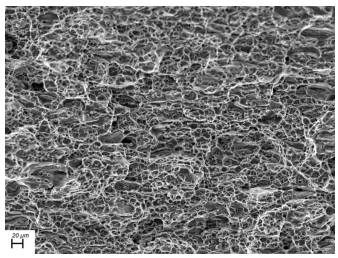

(b) L 500 x

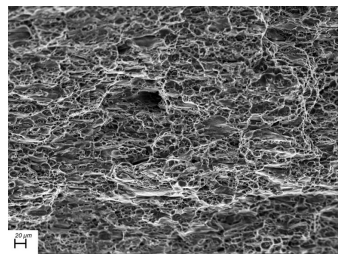

(c) C 500 x

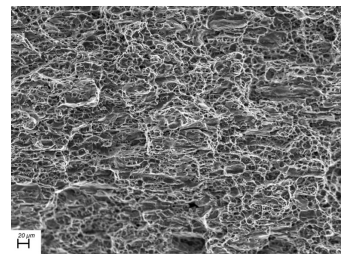

(d) R 500 x

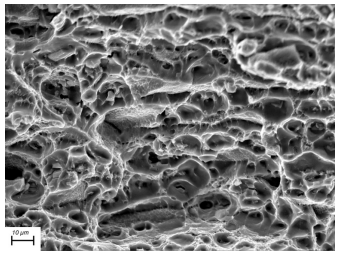

(e) L 2 000 x

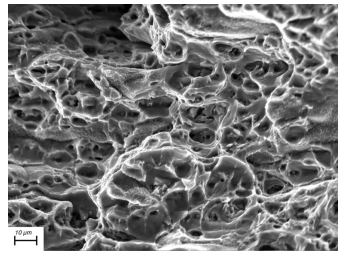

(f) C 2 000 x

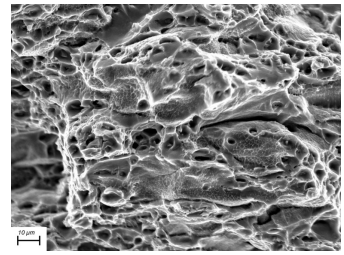

(g) R 2 000 x

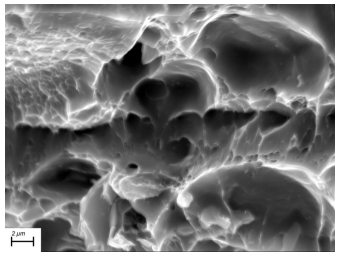

(h) L 10 000 x

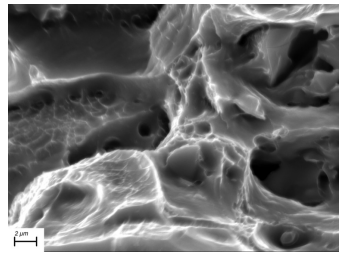

(i) C 10 000 x

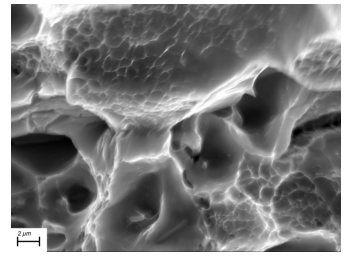

(j) R 10 000 x

Figure C.5: SEM images: $V_{\text{-}11}$ geometry, load case 1/1.

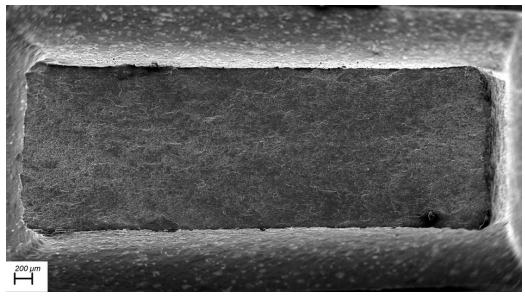

(a) Full fracture surface

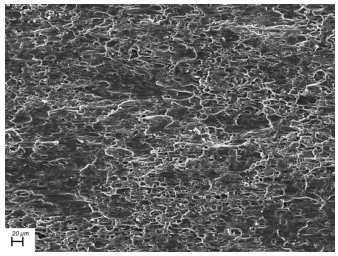

(b) L 500 x

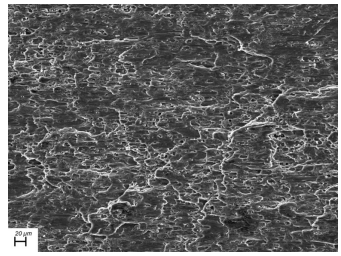

(c) C 500 x

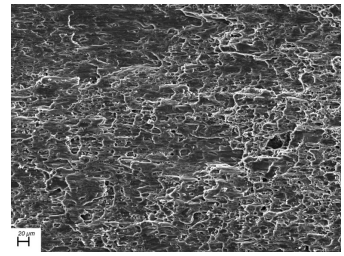

(d) R 500 x

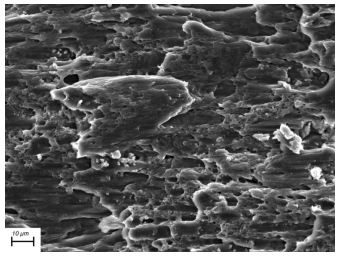

(e) L 2 000 x

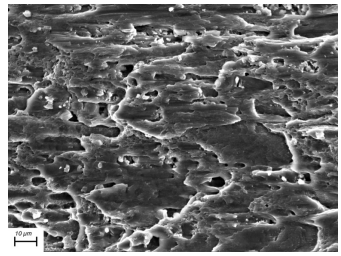

(f) C 2 000 x

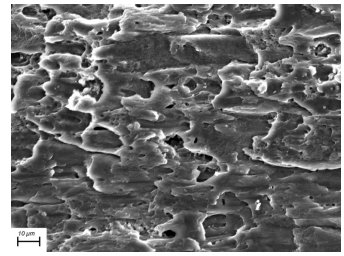

(g) R 2 000 x

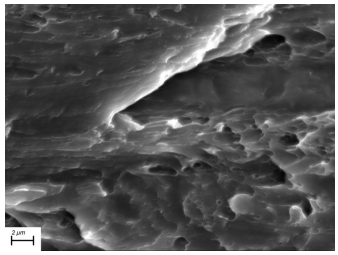

(h) L 10 000 x

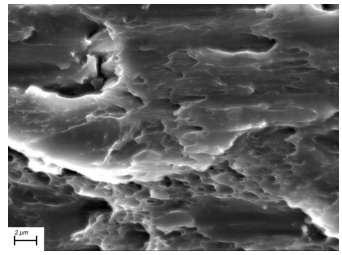

(i) C 10 000 x

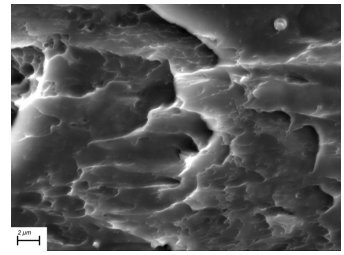

(j) R 10 000 x

Figure C.6: SEM images: $V_{\text{-}11}$ geometry, load case -1/1.